Universidade Federal de Minas Gerais

Probing exciton-phonon coupling and two phonon processes in transition metal dichalcogenides by Resonance Raman scattering

Rafael Nunes Gontijo

Supervisor: Cristiano Fantini Leite
Co-supervisor: Ariete Righi

Tese apresentada ao programa de pós-graduação em Física do Instituto de Ciencias Exatas da Universidade Federal de Minas Gerais como requerimento parcial para obtenção do título de Doutor em Ciências.

Universidade Federal de Minas Gerais

Probing exciton-phonon coupling and two phonon processes in transition metal dichalcogenides by Resonance Raman scattering

Rafael Nunes Gontijo

Trabalho aprovado

Belo Horizonte

____

Cristiano Fantini Leite
Orientador

____

Ariete Righi
Co-Orientadora

____

____

____

____

Universidade Federal de Minas Gerais
Instituto de Ciências Exatas
Programa de Pós-Graduação em Física
Caixa Postal 702
30.123-970 Belo Horizonte - MG - Brasil

Telefone (xx) (31) 3409 5637
(xx) (31) 3409 5633
Fax (xx) (31) 3409 5688
(xx) (31) 3409 5600
e-mail pgfisica@fisica.ufmg.br

ATA DA SESSÃO DE ARGUIÇÃO DA 362ª TESE DO PROGRAMA DE PÓS-GRADUAÇÃO EM FÍSICA, DEFENDIDA POR Rafael Nunes Gontijo orientado pelo professor Cristiano Fantini Leite e coorientado pela professora Ariete Righi, para obtenção do grau de **DOUTOR EM CIÊNCIAS, área de concentração Física**. Às 09:00 horas de onze de dezembro de dois mil e dezenove, na sala 4129 do Departamento de Física da UFMG, reuniu-se a Comissão Examinadora, composta pelos professores **Cristiano Fantini Leite** (Orientador - Departamento de Física/UFMG), **Ariete Righi** (Coorientadora - Departamento de Física/UFMG), **Hélio Chacham** (Departamento de Física/UFMG), **Leandro Malard Moreira** (Departamento de Física/UFMG), **Pedro Paulo de Mello Venezuela** (Instituto de Física/UFF) e **Marcos Henrique Diniz Guimarães** (University of Groningen) para dar cumprimento ao Artigo 37 do Regimento Geral da UFMG, submetendo o Mestre **Rafael Nunes Gontijo** à arguição de seu trabalho de Tese de Doutorado, que recebeu o título de **"Probing exciton-phonon coupling and two phonon processes in transition metal dichalcogenides by resonance Raman scattering"**. Às 14:00 horas do mesmo dia, o candidato fez uma exposição oral de seu trabalho durante aproximadamente 50 minutos. Após esta, os membros da comissão prosseguiram com a sua arguição, e apresentaram seus pareceres individuais sobre o trabalho, concluindo pela aprovação do candidato.

Belo Horizonte, 11 de Dezembro de 2019.

Prof. Cristiano Fantini Leite
Orientador do estudante
Departamento de Física/UFMG

Prof. Leandro Malard Moreira
Departamento de Física/UFMG

Profa. Ariete Righi
Coorientadora do estudante
Departamento de Física/UFMG

Prof. Pedro Paulo de Mello Venezuela
Instituto de Física/UFF

Prof. Hélio Chacham
Departamento de Física/UFMG

Prof. Marcos Henrique Diniz Guimarães
University of Groningen

Candidato

Dados Internacionais de Catalogação na Publicação (CIP)

G641 Gontijo, Rafael Nunes.
Probing exciton-phonon coupling and two phonon processes in transition metal dichalcogenides by Resonance Raman scattering / Rafael Nunes Gontijo. – 2019.
162f., enc. : il.

Orientador: Cristiano Fantini Leite.
Coorientadora: Ariete Righi.
Tese (doutorado) – Universidade Federal de Minas Gerais, Departamento de Física.
Bibliografia: f. 136-162.

1. Espectroscopia Raman. 2. Fotoluminescência. 3. Fônons. I. Título. II. Leite, Cristiano Fantini. III. Universidade Federal de Minas Gerais, Departamento de Física.

CDU – 535.333 (043)

Ficha catalográfica elaborada por Romário Martins – CRB6 3595
Biblioteca Professor Manoel Lopes de Siqueira – Departamento de Física - UFMG

Agradecimentos

Devido ao tempo que passei neste departamento e ao convívio com tantas pessoas que contribuíram de alguma forma tanto para a minha formação como um profissional quanto para a minha formação pessoal, tenho muito a agradecer a muitas pessoas. Como são muitas pessoas, receio que seja impossível agradecer a todos, mas farei o possível para lembrar de todos os que contribuíram para a finalização deste trabalho e desta etapa da minha vida, que é tão importante para o ingresso na carreira profissional.

Em primeiro lugar, agradeço aos meus pais Lázaro e Débora que me guiaram por toda a minha vida até que entrei no curso de Física e que me apoiaram durante toda a minha formação. Meus queridos pais me forneceram o apoio necessário para passar por todo esse processo de formação e por isso sou eternamente grato. Agradeço também a minha irmã Raíssa pelo apoio durante esses anos todos.

Agradeço aos membros do laboratório de espectroscopia Raman imensamente por todo o conhecimento e experiência que adquiri durante os anos que trabalhei ali. Foram muitos trabalhos com grande relevância científica que tive a oportunidade de participar e contribuir, me levando a aprender mais e mais sobre os temas que são relevantes a este trabalho. Agradeço aos meus orientadores, Cris e Chefa, que tiveram a paciência de me ensinar todo o processo de funcionamento do laboratório, da parte de funcionamento dos equipamentos do laboratório até analise e o relato dos dados obtidos a partir das medidas. Ao professor Marcos que colaborou muito com discussões relevantes para a minha formação, além de todos os *insights* para a realização destes trabalhos. Aos antigos membros do laboratório, Lu, Sangram, Eliel, Bruno e Rogério, agradeço muito pela amizade, discussões e por tudo que aprendi com eles durante o tempo que pudemos trabalhar juntos. Aos membros atuais, Vivi, Geovani, Jéssica e Tiago, agradeço a todos os momentos de amizade e cooperação que tivemos e que espero carregar pelo futuro, quando estivermos já trabalhando em nossos possíveis futuros cargos.

Here, I would like to thank the members of the Terrones Group in PennState. First, I would like to thank prof. Mauricio Terrones for the opportunity to learn something new and also for the support when I was working there. I would also Like to thank Dr. Ana Laura Elías and Dr. Néstor for the patience and support as well. I would like to thank Dr. Kazu and Tianyi for all the helpful discussions and for all the help during my stay. I would also like to thank all the other members of the group, George, Fu, Mingzu, Yu Lei, Tomotaroh, Ethan and Tim for the friendship and the good times I had in there.

Agradeço a todos os amigos que tive tanto na graduação, mestrado e doutorado por todos os momentos de curtição na universidade e fora dela. Foram bons tempos de aprendizado e de boas experiências que contribuíram muito para que eu pudesse chegar aonde cheguei. Para o pessoal da graduação, agradeço ao Mateus, à Mih, à Fabi, à Hayssa e também ao pessoal do DA na minha época. Ao pessoal do mestrado e doutorado que caminharam junto comigo, Wesclin, Mateus, Bruno, Cobra, Tati, Alana, Julinha, Henrique, Dani, Barbara, Samuca, entre tantos outros, sou grato pela amizade e por todos os momentos que passamos juntos. Tomo a oportunidade de agradecer também ao corpo técnico do departamento, o pessoal da oficina mecânica que sempre foi muito prestativo quando precisei do apoio deles e o pessoal da criogenia, que também sempre fez todo o possível para apoiar o nosso trabalho.

Por fim, agradeço aqui às agências de fomento Capes, CNPq, FAPEMIG, Finep, e o Instituto Nacional de Ciência e Tecnologia em nanomateriais de carbono que permitiram que este trabalho fosse realizado.

Resumo

Os materiais bidimensionais, caracterizados pela espessura atômica e baixa dimensionalidade ao longo do eixo z, são materiais que mostram grande promessa para o futuro, com grande potencial de aplicação em áreas como microeletrônica, sensores de gás, fotodetectores, catalisadores e outros. Dentre os materiais bidimensionais, podemos destacar a família dos dicalcogenetos de metais de transição, que são materiais lamelares cuja camada mais fina é formada de uma folha de um metal de transição localizada entre duas folhas de átomos da família dos calcogênios. Esses materiais possuem uma grande gama de propriedades eletrônicas, variando desde metálicos e semimetálicos até semicondutores com bandgap óptico no infravermelho e visível que pode ser direto ou indireto dependo do número de camadas.

A presença do gap na região do visível e infravermelho próximo faz com que técnicas ópticas sejam de fundamental importância no estudo de propriedades físicas desses materiais. Entre essas técnicas destaca-se a espectroscopia Raman que é a medida da luz espalhada inelasticamente por um material devido à interação entre luz e a matéria, que cria ou aniquila um quanta de vibração. Quando a luz incidente ou espalhada está em ressonância com um nível eletrônico do material temos o fenômeno de espalhamento Raman ressonante, onde a eficiência do processo é extremamente amplificada, o que permite obter informações sobre os estados eletrônicos a partir das suas interações com os fônons, assim como observar o fenômeno de espalhamento por dois ou mais fônons do material.

Neste trabalho, buscamos entender os processos de combinações de fônons no espectro Raman de Dicalcogenetos de metais de transição semicondutores, assim como os processos de interação éxciton-fônon nesses materiais. Para isso foram realizadas medidas de espalhamento Raman ressonante com variação da energia do laser de excitação e variação *insitu* da temperatura da amostra. Como técnica complementar foram realizadas também medidas de fotoluminescência com variação da temperatura da amostra. Foi mostrado como a variação de temperatura afeta a energia dos níveis eletrônicos e como essa variação pode sintonizar a ressonância dos processos de combinação de dois fônons. Mostramos também como a temperatura pode afetar a interação entre camadas em heteroestruturas formada pela combinação de dois Dicalcogenetos de metais de transição. Neste caso, foi possível observar a partir dos experimentos processos de interação éxciton-fônon e fônon-fônon entre camadas. A partir desse trabalho, conseguimos extrair informações sobre as propriedades optoeletrônicas desses materiais, importantes para futuras aplicações tecnológicas.

Palavras-chave: Dicalcogenetos de metais de transição, espectroscopia Raman, dupla ressonância, temperatura.

Abstract

Two-dimensional materials, characterized by their atomic thickness and low dimensionality along the z axis, are materials that show great promise for the future, with great potential for application in areas such as microelectronics, gas sensors, photodetectors, catalysts, and others. Among the two-dimensional materials, we can highlight the family of transition metal dichalcogenides, which are lamellar materials whose thinner layer is formed of a transition metal sheet sandwiched by two sheets of chalcogen. These materials have a wide range of properties, ranging from metallic and semi-metallic materials to semiconductors with an optical bandgap in infrared and visible regions that is temperature-dependent.

Raman spectroscopy is the measurement of light inelastically scattered by a material due to the interaction between light, or laser, and matter, which generates or annihilates a quantum of vibration, a phonon, in the material and causes the incident photon to lose or gain energy. Due to the nature of the scattering process, the Raman process is inefficient, except when the energy of the laser used resonates with the material's electronic levels, increasing the likelihood that the Raman process will occur. When the laser resonates with the electronic level, however, the Raman process can involve more than one phonon, and the scattering of light by two phonons becomes more likely. In this context, there are selection rules that filter out possible phonon combinations for the Raman process, which must even depend on the temperature at which the measurement is made.

In this work, we seek to understand the processes of phonon combinations in the Raman spectrum of semiconducting transition metal dichalcogenides, both as a function of the laser energy used and as a function of the sample temperature, in which we explore the laser resonances with the energy of the electronic transitions of each sample. We show how the temperature variation affects the energy of electronic levels and how this variation can tune the resonance of the two-phonon combination processes. We also show how temperature can affect the interaction between layers in the heterostructure formed by the combination of two transition metal dichalcogenides. From this work, we are able to extract information about the properties of these materials, which allow their applications in future technologies.

Keywords: Transition metal dichalcogenides, Raman spectroscopy, double-resonance, temperature.

Summary

1. INTRODUCTION 1

2. TRANSITION METAL DICHALCOGENIDES 5

2.1 CRYSTAL STRUCTURE AND SYMMETRY CONSIDERATIONS OF MONOLAYER, FEW-LAYERS AND BULK TRANSITION METAL DICHALCOGENIDES 5

2.1 ELECTRONIC PROPERTIES OF TRANSITION METAL DICHALCOGENIDES 8

2.2 VIBRATIONAL PROPERTIES OF TMDS FROM MONOLAYER TO BULK 13

2.3 OPTICAL TECHNIQUES FOR THE CHARACTERIZATION OF TMDS 19

2.3.1 OPTICAL ABSORPTION BY 2D MATERIALS WITH EXCITONIC COMPLEXES 20

2.3.2 PHOTOLUMINESCENCE SPECTROSCOPY AND ITS APPLICATION TO THE TRANSITION METAL DICHALCOGENIDES 22

2.3.3 RAMAN SPECTROSCOPY 24

3. THE RESONANCE RAMAN SCATTERING PROCESS IN 2D MATERIALS 27

3.1 RAMAN SPECTROSCOPY AND 2D MATERIALS 27

3.2 FIRST-ORDER RESONANCE RAMAN PROCESS IN TRANSITION METAL DICHALCOGENIDES 32

3.3 DOUBLE RESONANCE RAMAN PROCESS 34

3.3.1 TRANSITION METAL DICHALCOGENIDES 36

3.3.2 DEFECTIVE 2D MATERIAL PRODUCTION 41

3.3.3 DEFECTS IN TMDS 42

4. SAMPLE PRODUCTION METHODS AND EXPERIMENTAL SETUP FOR SPECTROSCOPIC MEASUREMENTS 47

4.1 PRODUCTION OF TMDS VIA MICROMECHANICAL EXFOLIATION AND CHEMICAL VAPOR DEPOSITION 47

4.2 SPECTROSCOPIC SETUP 50

4.3 OPTICAL CHARACTERIZATION OF THE SAMPLES 54

4.3.1 MICROMECHANICAL EXFOLIATION OF MoS_2 54

4.3.2 CVD GROWN MoS_2 SAMPLES BY THE SODIUM CHOLATE ASSISTED METHOD 55

4.3.3 CVD GROWN WS_2 AND $MoSe_2$ SAMPLES 56

5. MOS_2 59
5.1 Monolayer MoS_2 59
5.1.1 First-order, second-order and Double-resonance Raman bands 59
5.1.2 Temperature dependence of the first-order and double-resonance bands. . 63
5.1.3 Effects of temperature on the photoluminescence spectrum. 65
5.1.4 Effects of strain induced by the different thermal expansions of sample and substrate 68
5.1.5 Determination of the temperature dependence of the acoustic mode near the zone edges 68
5.1.6 Combining the temperature and laser energy effects on the double-resonance bands 70
5.1.7 Conclusions 71
5.2 Few layers and Bulk MoS_2 72
5.2.1 The spectral region between 140 and 275 cm^{-1} 73
5.2.2 The spectral region between 350 and 480 cm^{-1} 75
5.2.3 Bulk MoS_2 with several laser energies and Temperatures 79
5.2.4 Conclusions 90
5.3 Temperature study of defect induced Raman bands in MoS_2 samples under laser resonance 90
5.3.1 Defect induced bands in the Raman spectra of natural MoS_2 at low temperatures 91
5.3.2 The behavior of the defect induced and Δ bands as a function of temperature for 1L93
5.3.3 Defect induced bands in defective samples under resonance at low temperatures 94
6. $MOSE_2$ AND WS_2 AND THEIR HETEROSTRUCTURE 99
6.1 WS_2 99
6.2 $MoSe_2$ 103
6.3 Heterostructure of WS_2/$MoSe_2$ 108
7. CONCLUSION 119
APPENDIX A: TEMPERATURE EFFECTS IN THE OPTICAL SPECTRA 121

APPENDIX B: DOUBLE RESONANCE RAMAN PROCESSES IN GRAPHENE.....125

APPENDIX C: PHONON DISPERSION AND LIST OF CRITICAL POINTS FOR WS_2 AND $MOSE_2$ 130

REFERENCES 135

1. Introduction

The development of the production and utilization of silicon in large scale as a standard for the use in semiconducting based devices was one of the biggest advances for the miniaturization and consequent global distribution of electronic devices. Some of these devices are part of media players, televisions, smartphones, computers, refrigerators, microwave ovens, among so many others that make use of the transistors, like the MOSFET (Metal-Oxide-Semiconductor field-effect transistor) in special. Transistors are frequently used to amplify or interrupt electric signals in a circuit and are used for the logic operations in modern microprocessors. The first processor developed by Intel could run on a clock of 740 kHz while performing up to 93 thousand instructions, meaning that in about 11 microseconds, it could make simple addition, subtraction, multiplication and division calculations very fast. However, computers nowadays are used for much more than simple calculations, where they deal with different user interfaces, data processing software, graphical content creation, and reproduction, and of course, much more complex calculations than the ones allowed by the use of a CPU made in the 1970s.

The advances brought by the development of the technology of the microdevices also allowed the integration of several electronic devices into the smartphone, such as video cameras capable of photographing and recording videos in ultra-high definition, GPS, messaging, all sorts of communication methods, and simple chores, that needed to be done in a full desktop computer before and can be done in a device that fits into the hand today. Most of these advances come from enhancements in the production and application of semiconducting technologies.

That is one of the motivations for the study and research of materials, which will present alternatives for materials better suited for a variety of applications in the near future. In special, we want to see how new types of materials, such as the two-dimensional materials, can be explored for future technologies.

Two-dimensional (2D) materials are characterized by the breaking of the translational symmetry of the crystal in the z axis, leading to atomically thin materials extending in the xy plane. Therefore, crystal lattices composed of layered structures are good candidates for the production of 2D materials. The first 2D materials isolated was graphene, which was exfoliated from a highly oriented pyrolytic graphite with the help of Scotch tape [1]. Before graphene, it was thought that 2D materials could not be made due to instabilities in the material properties that would come from thermal fluctuations [2]. However, after graphene, several other 2D

materials were reported in the literature as theoretically stable [2–4] and with very different properties as well [5].

Among the 2D materials, one very interesting group is the family of the transition metal dichalcogenides (TMDs) [6]. They come in a variety of electronic properties, and can also present interesting possibilities of applications [7] due to the strong spin-orbit interaction presented by them. Among the application possibilities, we can highlight flexible electronics and wearables, photodetectors, light-emitting diodes, gas sensors, hydrogen evolution catalysis, spintronics and many other applications [8,9,18–27,10,28–37,11,38–42,12–17].

The possibility of stacking 2D materials also offers a tremendous advantage to these materials, since we could now use their individual properties in the coverage same area, opening the possibility of creating multiple devices in the same stack.

However, it is necessary to understand the behavior and characteristics of these materials under different types of environments and loads. One way of obtaining reliable information about the properties of a material is to study its interaction with light, which can originate several processes in the material interface, such as the emission and scattering of light. In both cases, it is possible to obtain important pieces of information regarding the electronic structure and the vibrational structure of the material.

The emission of light by the material is related to the recombination of electrons in the conduction band minimum and holes in the valence band maximum, such that the optical bandgap of the material can be extracted. The inelastic scattering of light by the material can be used to probe the interaction between electrons and the lattice vibrations, called phonons. Both phenomena allow us to obtain important information about optical, electronic and structural properties of the material investigated. The knowledge of these properties is fundamental to assert the right applications of a determined material. Finally, we are also interested in observing how heterostructures formed by the stacking of different 2D materials can change the inelastic light scattering phenomenon.

In this work, we explore the optical properties of transition metal dichalcogenides by measuring the Raman and photoluminescence spectra of monolayers, bilayers, and bulk materials, as well as the heterostructures formed by the stacking of two transition metal dichalcogenides.

In chapter 2, we begin introducing the basic properties of TMDs, both electronic and vibrational, and how the number of layers can affect the basic properties of these materials. We also introduce the optical techniques used in this work to characterize the properties of these materials as well, where we cover the basic information needed to understand the information

provided by each technique. In chapter 3, we review the resonance Raman spectra for 2D materials, where we discuss the effects of resonance in the Raman spectra of TMDs and the observation of bands resulting from the combination of phonons. In chapter 4, we introduce the experimental methods used in our work, where we discuss sample preparation methods, the experimental setup for the collection of the Raman and PL spectra and the optical characterization of the samples used in our work. In chapter 5 we focus on the experimental results obtained for the MoS_2 samples, where we show how the thermal effects can affect the Raman spectrum of the monolayer and bulk samples. In chapter 6 we present the experimental results of the monolayers of WS_2 and $MoSe_2$ monolayers along with the results from the heterostructure formed by the stack of these two materials. In chapter 7 we present the conclusions of our works.

2. Transition Metal Dichalcogenides

2.1 Crystal structure and symmetry considerations of monolayer, few-layers and bulk transition metal dichalcogenides

Transition metal dichalcogenides (TMDs) are layered materials analogous to graphite. Due to the weak bonding between the layers (van der Waals), they can be exfoliated until the monolayer regime. The monolayer consists of three atomic layers, a layer of transition metals (M) such as molybdenum or tungsten arranged in a triangular lattice, sandwiched between two chalcogen layers, again in a triangular lattice. Transition metals and chalcogens are bonded by covalent bonding, and most TMDs are very stable in a monolayer regime even in standard laboratory environmental conditions [3]. Some phases are more stable though, and easier to explore than others. The monolayer phase of a given TMD can be one of three: (i) *H* in which the top of bottom chalcogen layers are aligned and the top view of the structure resembles the honeycomb structure of graphene (Figure 2.1(a)); (ii) *T* in which the bottom chalcogen layer is rotated by 30° with respect to the top layer (Figure 2.1(b)); (iii) *T*' which is similar to *T* phase, but with interactions between the metals, leading to a deformation in the structure (Figure 2.1(c)) [43]. Just a simple observation from Figure 2.1(a), (b) and (c) can uncover that each phase has completely different symmetry operations, with the symmetry decreasing from (a) to (c).

The different structures with the same atomic composition can lead to different properties. MoS_2, for instance, is a semiconductor in the *H* phase, while it is semi-metallic in the *T* phase [44]. The *T'* phase can be even more interesting presenting a conductance that varies according to the orientation of the crystal [45]. Other combinations of atoms and the formation

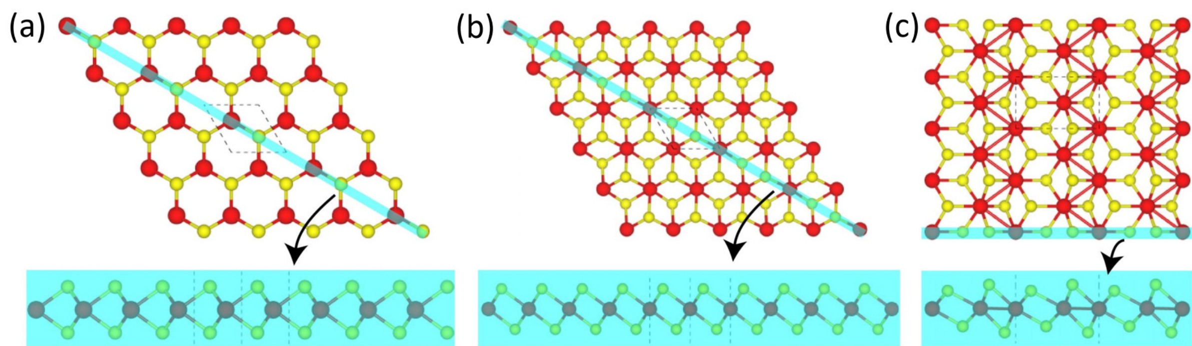

Figure 2.1. Possible phases for the honeycomb-like structure of TMDs, where the red balls represent the transition metals and the yellow balls represent the chalcogens. (a) The *H* phase, (b) the *T* phase and (c) the *T'* phase. Adapted from ref. [43].

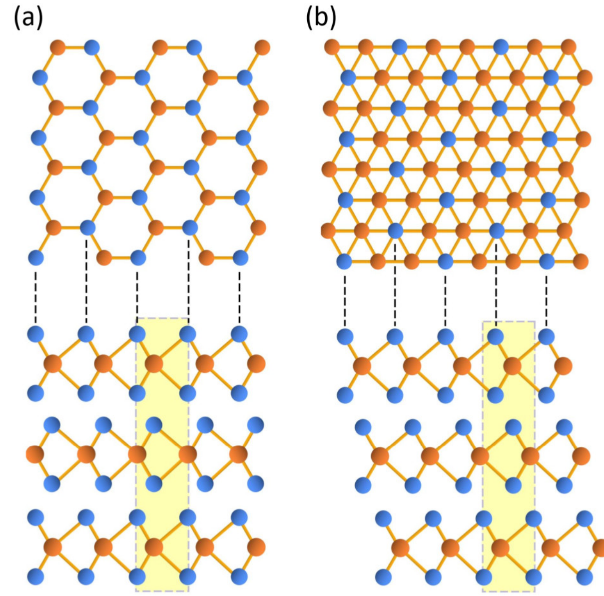

Figure 2.2. Bulk phases of TMDs, where the blue balls represent chalcogens and the orange balls represent transition metals. (a) 2H phase and (b) 3R phase. Adapted from ref. [46].

of alloys can help tune the electronic properties of these materials to suit the needs of different applications.

Although the properties of monolayers such as those presented above will be extremely important for the development of the electronics field, monolayers are not found in nature. These crystals are found naturally in their bulk form, with several thousands of layers piled one on top of the other in an organized fashion. Following the *H* phase of the monolayer, the piling of the monolayers can take one of two forms: (i) 2H with two monolayers forming a unit cell; (ii) 3R with three monolayers forming a unit cell.

The 2H bulk phase (Figure 2.2(a)) consists of two monolayers stacked with the bottom layer rotated by 60° with respect to the top layer. They are stacked in such a way that the metals in the top layer are on top of the chalcogens in the bottom layer and vice versa. This configuration is repeated through the entire crystal, forming the bulk arrangement of the 2H phase. The 3R phase (Figure 2.2(b)) is a configuration in which three monolayers are stacked and it is such that the bottom layer is displaced with respect to the middle layer, which is again displaced with respect to the top layer. This is repeated through the entire lattice. The bulk phase is important for the characterization of the material since different bulk phases will present different vibrational properties and possibly different electronic properties as well [46].

In this work, we will explore monolayer, few-layers and bulk 2H-MX_2, with M = Mo and W and X = S and Se. We introduce the concepts of the monolayer, few-layers and bulk phases to talk about symmetry operation and group theory applied to the crystal phase relevant to our problems. A monolayer H-MX_2 like the one presented in Figure 2.1(a) belongs to the

point group D_{3h}, with a C_3 located at the center of a hexagon in Figure 2.1(a), and the horizontal mirror applied to the xy plane that inverts the top and bottom chalcogen layers. If we slowly increase the number of layers and observe the applicable symmetry operations, we can see that a bilayer MX_2 with a stacking similar to a bulk crystal, named AB, belongs to D_{3d}, with a C_3 rotation axis and an inversion operation instead of a horizontal mirror plane. A trilayer MX_2 recovers the D_{3h} symmetry, but a tetralayer recovers the D_{3d} symmetry, and thus we conclude that following the 2H stacking order, for an odd number of layers the point group representing the crystal has D_{3h} symmetry, while for an even number of layers the crystal has D_{3d} symmetry. Some of the vibrational and optical properties of these materials are affected by this change in the crystal symmetry, such as the number of Raman active modes [46–48] and also second harmonic generation [49–51]. Bulk 2H-MX_2, on the other hand, has D_{6h} symmetry, containing both horizontal plane mirror and inversion symmetries.

Since the crystal structure of TMDs is honeycomb-like, similar to the case of graphene, its reciprocal space is also similar to that of graphene. Therefore, the high symmetry points in the reciprocal space are also the same, and the first Brillouin zone for TMDs is presented in Figure 2.3. Thus, there is a point with the highest symmetry of the unit cell, the **Γ** point, at the center of the Brillouin zone ($\mathbf{q} = \mathbf{0}$). At the edges of the Brillouin zone are located the other high symmetry points, at the vertexes of the hexagon, the **K** and **K'** points, and between the vertexes, the **M** point. Another important point for our consideration is the one point approximately mid-range between the **K** (**K'**) and the **Γ** points, which we will call **Q** point. The other low symmetry points will be considered further in the text.

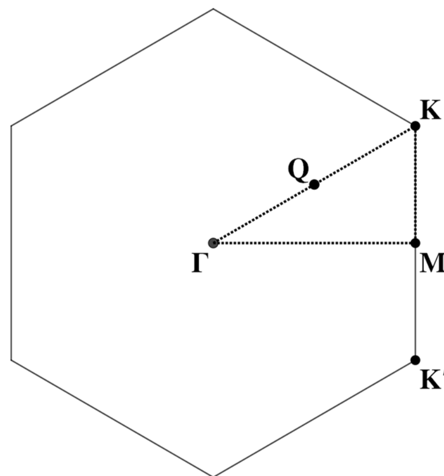

Figure 2.3. First Brillouin zone of a two-dimensional hexagonal lattice, where the main high symmetry points can be observed.

With these considerations in mind, we begin exploring the electronic and optical properties of TMDs. We will use here MoS_2 as the main example since it is the most studied TMD, but all the physics from this material can be extrapolated to the other H-MX_2 materials presented here.

2.1 Electronic properties of transition metal dichalcogenides

The 2H-MX_2 family with M = Mo, W and X = S, Se are predominantly semiconducting, with a bandgap that reduces as the mass of the chalcogen is increased. Close to the bandgap, the electronic structure can be described by a Tight binding approach that considers the atomic orbital basis as a combination of *d* orbitals from the transition metals and *p* orbitals from chalcogens [54]. Far from the bandgap, a more accurate approach is needed, such as density functional theory (DFT) calculations that can correctly reproduce the shape of the band structure [55]. The electronic band structure of monolayer MoS_2 is shown in Figure 2.4(a), which also reveals the presence of a direct bandgap located at the **K** point. This is also true for all the other monolayer H-MX_2. When we leave the monolayer regime, however, an indirect

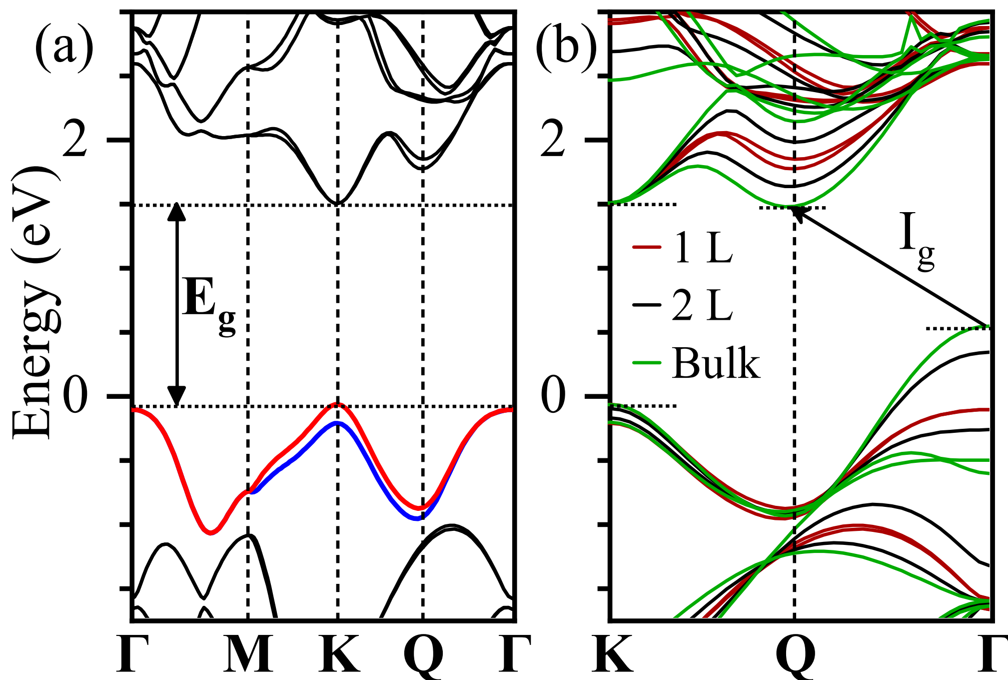

Figure 2.4. Electronic structure of TMDs. (a) The electronic structure of MoS_2 calculated by DFT. The top valence band has been colored to show the spin-orbit split. Adapted from ref. [52]. (b) Band structure of monolayer (1 L), bilayer (2 L) and bulk MoS_2 along the **K-Γ** path, showing the direct to indirect bandgap transition from monolayer to bulk MoS_2. The bands in the bilayer and bulk are displaced to show the comparison between monolayer, bilayer and bulk, where the original 0 corresponding the Fermi energy should be located at the maximum of the valence band. The indirect bandgap of bulk is illustrated as the arrow labeled I_g. Adapted from ref. [53].

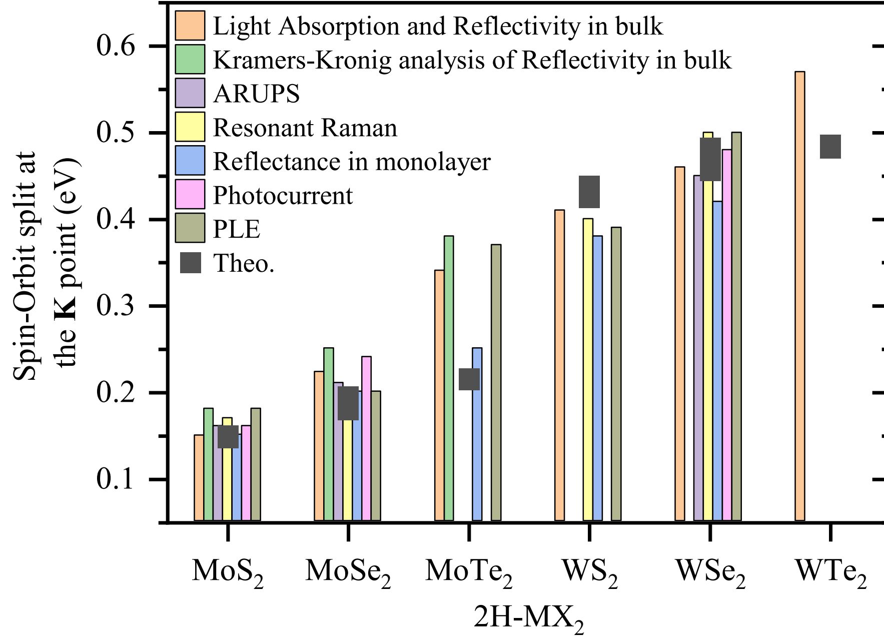

Figure 2.5. Spin-Orbit coupling for the various monolayer and bulk (Mo, W) (S, Se, Te)$_2$ compounds. Light absorption and reflectivity in bulk crystals were obtained from [6]. Kramers-Kronig analysis of reflectivity in bulk crystals was done by [57]. Angle-resolved ultraviolet photoemission spectroscopy (ARUPS) was studied by [58]. Resonant Raman in 1L-MoS_2, 1L-$MoSe_2$ and 1L-WS_2 was done by [59], [60] and [61], respectively, while in bulk-WSe_2 it was done by [62]. The data from monolayer reflectance were obtained by [63]. Photocurrent experiments were carried by [64]. Photoluminescence Excitation (PLE) was done in 1L-MoS_2, 1L-$MoSe_2$ and 1L-$MoTe_2$, and 1L-WS_2 and 1L-WSe_2 by [65], [66] and [67], respectively. The theoretical data can be found in references [68–73].

bandgap appears, connecting the top of the valence band at the **Γ** point to the bottom of the conduction at the **Q** point. The indirect bandgap decreases in energy for an increasing number of layers. The indirect bandgap for monolayer, bilayer and bulk MoS_2 can be seen in Figure 2.4(b).

The contributions of atomic orbitals near the bandgap are mostly due to the *d* orbitals from the transition metal, while the contributions from the chalcogens are more apparent closer to the **Γ** point, along with equal contributions from the transition metal as well [56]. These contributions will help understand the exciton-phonon interactions for these materials.

Due to the massive transition metals, strong spin-orbit interactions are observed for MX_2 TMDs [58]. The spin-orbit interaction splits the top valence band close to the **K** and **K’** points according to the spin projection of the electron. For monolayer MoS_2, the valence band spin-orbit split is approximately 160 meV. For massive crystals like WSe_2, however, the spin-orbit coupling can reach almost 500 meV [6,57,66–75,58,76,59–65]. The conduction band is also affected, but in a much lower degree, allowing us to neglect the spin-orbit interaction in the conduction band. The values of the spin-orbit splits for each TMD are presented in Figure 2.5,

where both theoretical and experimental data obtained by different methods can be seen. The experimental data are presented in the shape of columns and the theoretical values are presented as gray squares. The general trend of increased spin-orbit coupling can be easily observed as the masses of the constituent transition metal and chalcogens increase. The spin-orbit coupling can also be tuned by temperature [76] or by a suitable combination of chalcogens and transition metals [71,75,77].

The main contributions to the optical bandgap, or the measured value of the first electronic transition by light absorption, comes from many-body interactions due to the presence of excitonic transitions. Excitons are formed when the material is excited from the valence band to the conduction band by a photon with energy equal or higher than the bandgap energy. The excited electron leaves a hole in the valence band, which acts as a positively charged particle. The electron and hole are attracted via a coulomb-like potential, similar to a hydrogen atom. The attractive force between electron and hole is in contrast to the repulsive forces from the surrounding electrons in the valence band, which provides a balance between the forces, creating a stable state. The Hamiltonian that describes the electron-hole interaction is given by

$$H = \frac{p_e^2}{2m_e^*} + \frac{p_h^2}{2m_h^*} - \frac{q^2}{\varepsilon_r |\boldsymbol{r_e} - \boldsymbol{r_h}|} \qquad (2.1),$$

Where $p_{e(h)}$ and $m_{e(h)}^*$ are the momentum and effective mass of the electron (hole), ε_r is the relative permittivity of the material and q is the electron charge. We rewrite the Hamiltonian in terms of the relative motion of the electron and hole, defining a new variable $\boldsymbol{r} = \boldsymbol{r_e} - \boldsymbol{r_h}$ for the distance between the electron and hole pair and using the coordinate of the center of mass $\boldsymbol{\rho} = \frac{(m_e^* \boldsymbol{r_e} + m_h^* \boldsymbol{r_h})}{(m_e^* + m_h^*)}$

$$H = \frac{p_\rho^2}{2(|m_e^*| + |m_h^*|)} + \frac{p_r^2}{2\mu^*} - \frac{q^2}{\varepsilon_r |\boldsymbol{r}|} \quad , \qquad \frac{1}{\mu^*} = \frac{1}{m_e^*} + \frac{1}{m_h^*} \qquad (2.2).$$

We define the new momentum of the relative motion of the electron and hole, p_r, and the new momentum of the center of mass, p_ρ. We now treat the total wavefunction as a product of two wavefunctions for (i) the motion of the center of mass of the electron-hole pair and (ii) the relative motion between electron and hole. (i) will have the solution

$$E(\boldsymbol{K}) = \frac{\hbar^2 K^2}{2\left(|m_e^*| + |m_h^*|\right)} \tag{2.3},$$

with $\boldsymbol{K}$ being a wavevector pertaining to the first Brillouin zone of the material. This solution implies that electron and hole will move together in the band structure of the material. The relative motion between electron and hole, (ii), will present a discrete energy dispersion similar to the hydrogen problem

$$E(n) = \frac{-\mu^*}{m_e \varepsilon_r^2} \frac{R_H}{n^2} \equiv -\frac{R_X}{n^2} \tag{2.4},$$

where n is the principal quantum state number and $R_H = (m_e q^4)/(64\pi^3 \varepsilon_0^2 \hbar^3 c)$ is the Rydberg constant. We also define the value of the exciton binding energy, $R_X = \frac{-\mu^*}{m_e \varepsilon_r^2} R_H$, which is the difference between the n = 1 state and the $n \rightarrow \infty$ case, or the difference between the discrete energy spectrum and the continuum energy spectrum. One could also calculate the Bohr radius, $r(n)$ associated with the exciton as well through the relation $a(n) = \left(\frac{m_e \varepsilon_r}{\mu}\right) a_H n^2 \equiv a_X n^2$, where a_H is the hydrogen Bohr radius. For hydrogen, the value of R_H is known to be approximately -13.6 eV, the required energy to dissociate the electron from the proton. For bulk semiconductors like GaAs, for example, the exciton binding energy is approximately 4.2 meV, about 3000 times lower than that of the hydrogen level. This low binding energy is due to the fact that bulk materials present large dielectric constants and small effective masses. Therefore, it is extremely difficult to observe the excitonic effects at room temperature, where the difference between the electronic bandgap and the excitonic transition is of a few meV, smaller than the energy associated with the particles at room temperature of approximately 25 meV.

When the dimensionality of the system is reduced, quantum confinement becomes relevant along with the reduction on the dielectric constant. These factors change the binding energy of the exciton leading to an increase of almost 6 to 8 times [78,79]. Since TMDs are layered materials with a strong in-plane bond and only a weak van der Waals connecting each layer, there is a strong binding energy of the excitonic transitions in these materials. The binding energy is big enough that even at room temperature the excitonic transitions can be observed [6]. While bulk MoS_2 has an exciton binding energy near 50 meV [6], recent reports indicate that monolayer MoS_2 has an exciton binding energy of more than 400 meV [80].

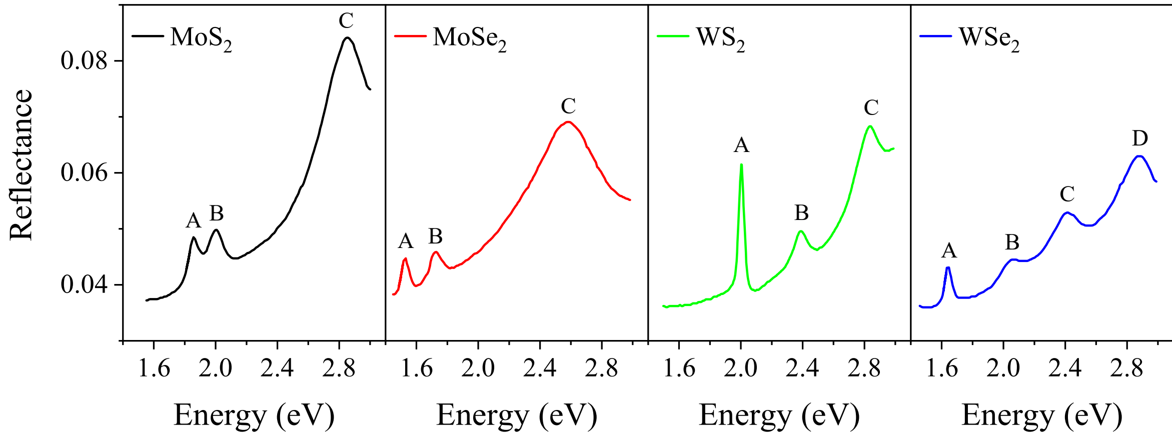

Figure 2.6. Reflectance spectra of the TMDs that are the focus of this work. Data obtained from reference [63].

Figure 2.6 shows the reflectance spectra of TMDs [63]. In thin films, the reflectance spectra will be directly proportional to the extinction coefficient [81], and thus, Figure 2.6 reveals a series of excitonic peaks. The three main features, frequently called in the literature of A, B and C excitons, are easily distinguished in the spectra, and the D exciton can also be observed in the case of WSe_2. They are important components of the optical response of these materials and are relevant to the observation of their photoluminescence and Raman spectra.

The A and B excitonic transitions occur close to the direct bandgap of the TMDs at the **K** or **K'** points (see Figure 2.4(a)) [55]. Due to the split in the valence band induced by the strong spin-orbit coupling, the A and B excitons are formed, with the difference that the first one, with lower absorption energy, comes from the transition from the top valence band (red curve in Figure 2.4(a)), while the second one, with higher energy, comes from the bottom top (blue curve in Figure 2.4(a)). The C exciton comes from vertical transitions close to the **Γ** point,

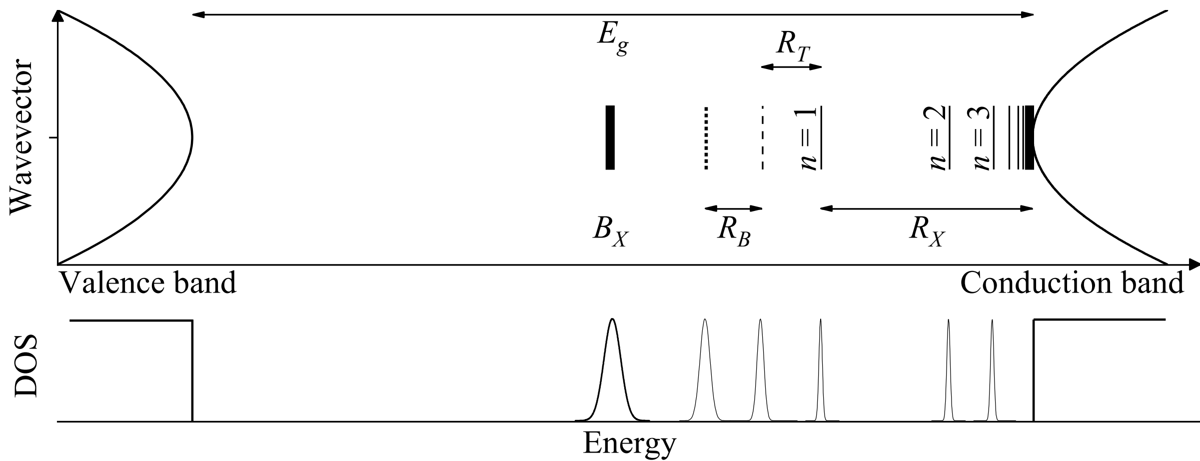

Figure 2.7. Representation of the excitonic complexes and their contributions to the density of states (DOS). E_g is the bandgap, R_X is the already defined exciton binding energy, R_T is the Trion binding energy and R_B is the biexciton binding energy. B_X represents the bound exciton energy. This is a simple sketch, with no real values.

and therefore, it is heavily affected by the number of layers, which can be observed in Figure 2.4(b) [55].

Since the electronic transitions related to these excitons occur at points in the electronic band where different orbitals are relevant, the character of the exciton may change as well.

Besides the excitonic features described above, there are other excitonic complexes in these materials as well, comprised of charged excitons like the trion or a combination of excitons such as the biexciton. They are identifiable by low-temperature spectra measurements [76,82–89], chemically treated samples [90–93], gated devices [82,94–101], defective samples [102–104], and the simple control of the excitation laser power on the sample [84,96,97,99,105,106]. These excitonic complexes have even smaller binding energy than that of the excitonic transitions, appearing very close to the excitonic transition itself, as will be presented further in the text. Also, when the sample is defective, there is the contribution of bound excitons, which appear as a very broad band below the contributions from the excitonic complexes at lower temperatures [87,91,104]. Figure 2.7 presents a simple representation of the multi-excitonic transitions and bound excitons in the bandgap of the material, along with a representative density of states for each transition, where R_X is the exciton binding energy, defined in equation 2.4, R_T, R_B, and B_X are the trion, biexciton, and bound exciton binding energies, respectively.

We finish this section commenting that the hydrogen-like treatment of the excitonic transitions is qualitatively good, but the model is wrong for small n [107,108]. That is, for the excitonic levels with a small radius, there is a big difference between the expected behavior and the measured value. This is due to the fact that the $n = 1$ and $n = 2$ transitions present a strong dielectric screening from the sample, whereas for bigger n the screening is mostly due to the surrounding environment [107]. A simple way to correct this is to consider a correction to the electron-hole interaction [107]. But this is beyond the scope of this text since we will only focus on the $n = 1$ transition.

2.2 Vibrational properties of TMDs from monolayer to bulk

Although we frequently assume that the atoms forming the crystal lattice in any material are static, they are actually moving in the lattice in a periodic motion formed by the combination of all the normal vibrational modes of the material. The vibrational motion of the crystal is responsible for most of its mechanical and thermal properties and also some of its electronic properties as well, as it will be discussed later. In order to start the discussion about vibrational properties, we will employ the adiabatic approximation, where the motion of the ions

composing the crystal is much slower than the motion of electrons. In fact, the velocity of the electrons is in the order of 10^8 cm/s, while the ions move at approximately 10^5 cm/s [109]. Thus, the energy spectra related to vibration and electronic energies can be considered separately in a first approximation.

Since the total number of atoms in the unit cell of an H or T phase TMD is 3, the resulting number of vibrational modes will be 9. Among the vibrational modes, 3 branches are acoustic, representing the x, y and z displacement of the crystal, and 6 modes are optic. The phonon dispersion for monolayer MoS_2 is presented in Figure 2.8(a), where we see the six optic branches and the three acoustic branches. At the high symmetry points **Γ**, **K,** and **M**, we observe local maxima or minima in the phonon branches, and thus the high symmetry points are also critical points to the dispersion relation. As such, the phonon density of states (pDOS) for monolayer and bulk MoS_2 in Figure 2.8(d) and (e) will present local maxima related to the phonon branch at the critical points.

Monolayer H phase TMDs belong to the D_{3h} symmetry group and from group theory, the representation of the vibrational modes at the **Γ** point is described in irreducible representations by [110]

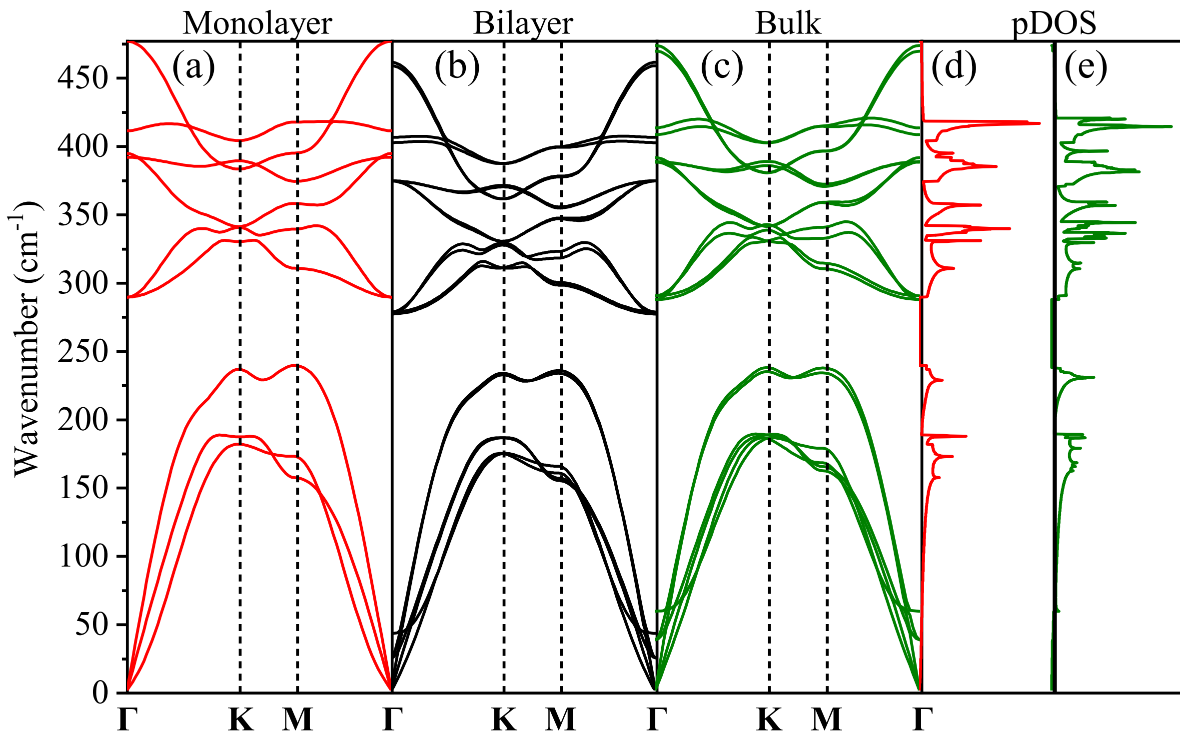

Figure 2.8. Calculated phonon dispersions for (a) monolayer, (b) bilayer and (c) bulk MoS_2. (d) and (e) are the phonon density of states for monolayer and bulk MoS_2 respectively. Adapted from refs. [52,53].

$$\Gamma_{vib} = \Gamma_{eq} \otimes \Gamma_{vec} = A_1^{'} \oplus 2E^{'} \oplus 2A''_2 \oplus E'',$$

Where Γ_{eq} is the equivalence representation of the atomic sites and Γ_{vec} is the representation for the x, y, and z real space vectors. From the nine phonon branches we see in Figure 2.8(a), at the **Γ** point, six will be two-fold degenerate optical branches, two will be degenerate at the **Γ** point, with irreducible representations E' and E", and the other three branches will have irreducible representations A_1' and A_2". From these, the A_2" and E' representations are IR active, while the A_1', E' and E" representations are Raman active. During Raman scattering experiments in a backscattering configuration, only the irreducible representations with square base functions involving x and y components will be active. Therefore, only the A_1' and E' modes will be observable in the back-scattering configuration, which are the generally observed Raman modes for monolayer and few-layers TMDs.

The A_1' mode corresponds to the out-of-plane vibrational motion in which the chalcogen planes move in opposite directions while the metal plane remains static. This motion can be approximated by a spring-mass system, where the entire chalcogen plane is a single mass

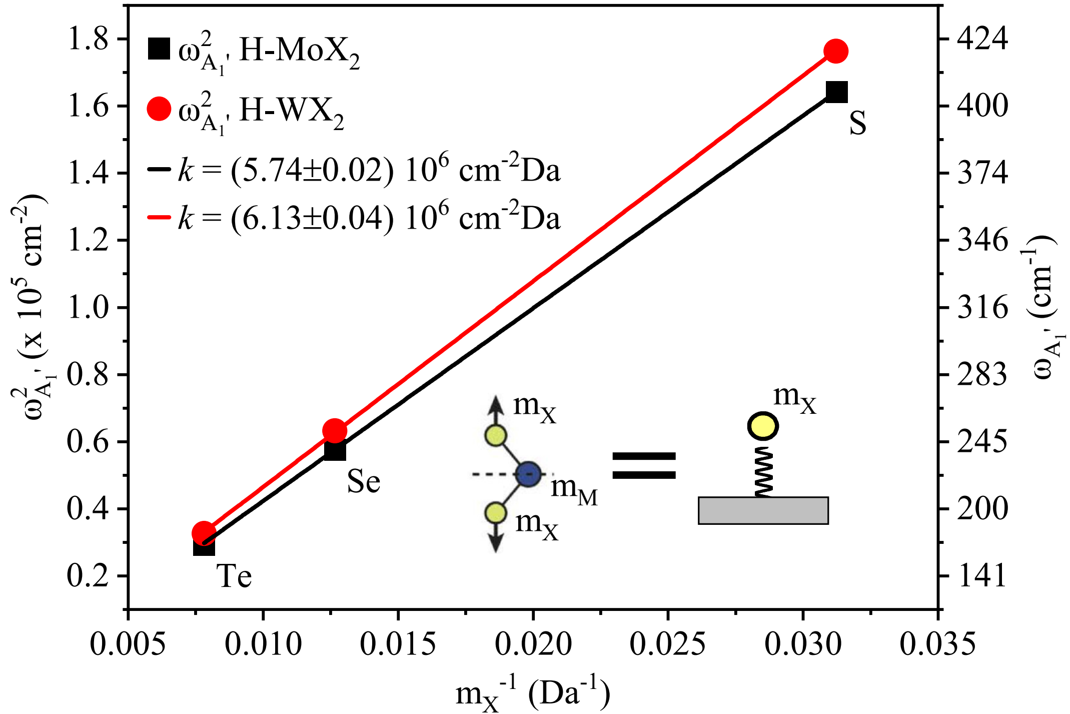

Figure 2.9. Fitting of the square of the A_1' vibrational mode frequency as a function of the chalcogen mass for the H-MoX_2 and H-WX_2 families. The right axis presents the value of ω. The inset depicts the eigenvector of the A_1' mode in the unit cell, and how it is comparable to the spring-mass problem. m_X stands for the chalcogen mass, while m_M stands for the transition metal mass. WSe_2 values are taken from [111], $MoTe_2$ values are taken from [112] and WTe_2 theoretical values are taken from [113].

while the metal plane would work as a wall. Therefore, we can use the simple harmonic motion equation to relate the mass of the chalcogen in the TMD to the A_1' frequency mode, shown in Figure 2.9. Figure 2.9 presents the square of the frequency of the A_1' mode, $\omega^2_{A_1'}$, as a function of the inverse of chalcogen mass, $\frac{1}{m_X}$, for the H-MoX_2 and H-WX_2 families of TMDs. Since $\omega^2_{A_1'} = \frac{k}{m_X}$, the linear fit of the data presented in Figure 2.9 gives the spring constant k, which is related to the lattice bonding strength of the vibrational mode. Since in our model the metal sheet should behave like a wall, it would be reasonable that k should be independent of the metal mass, which is in reasonable accordance with the observed results of 5.74 and 6.13 x 10^6 $cm^{-2}Da^{-1}$ for MoX_2 and WX_2 compounds, respectively. Since H-WTe_2 is not found in nature, we use the calculated phonon dispersion as a reference for the frequency of the A_1' and E' modes [113].

For the in-plane E' mode, the chalcogens move in one direction, while the metal goes in the opposite direction. This motion can be approximated by two masses connected by a spring, where one mass will be equal to two chalcogen masses while the other mass will be equal to the mass of the metal. Again, this is a simple mechanics problem, and the vibrational

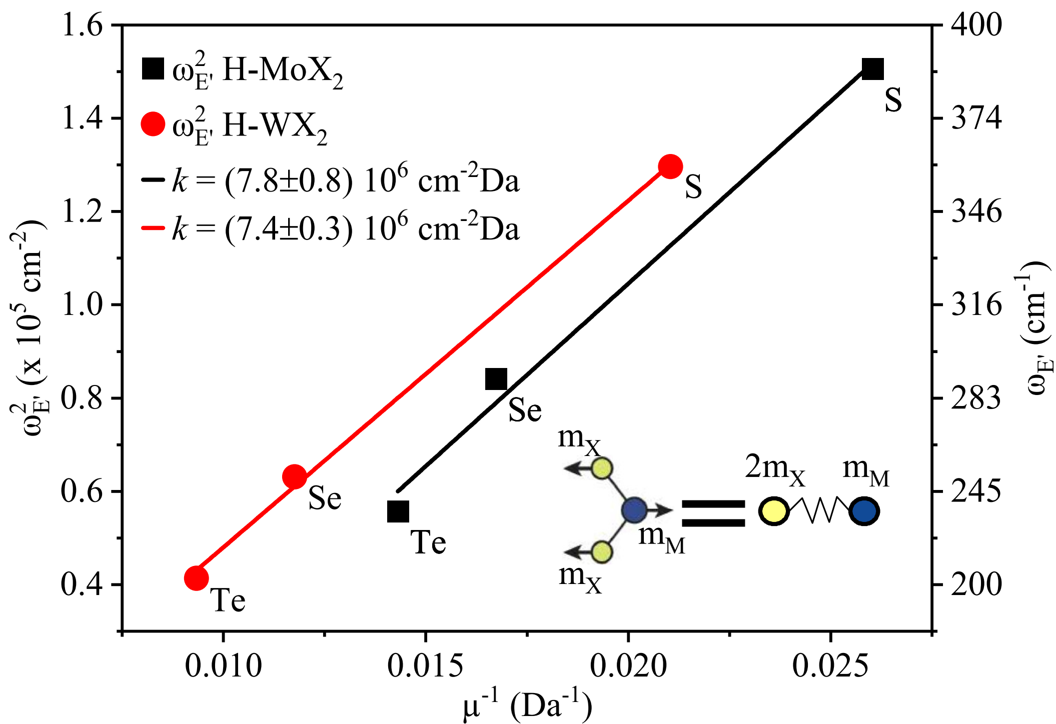

Figure 2.10. Square of the E' frequency as a function of μ^{-1}, as it is defined in the text for the H-MoX_2 and H-WX_2 families. The inset shows the eigenvector of the E' vibration represented in the unit cell, and how it is comparable to a problem of two masses connected by a spring. WSe_2 values are taken from [111], $MoTe_2$ values are taken from [112] and WTe_2 theoretical values are taken from [113].

frequency of the system will be connected to masses of chalcogen and metal via $\omega_{E'}^2 = \frac{k}{\mu}$, where $\mu = \frac{2m_X m_M}{2m_X + m_M}$. Figure 2.10 shows the square of the frequency of the E' mode as a function of μ^{-1} for the H-MoX_2 and H-WX_2 compounds. Again, we obtain a relatively reasonable fit for both families, with k = 7.8 and 7.4 x 10^6 $cm^{-2}Da^{-1}$ for MoX_2 and WX_2 compounds, respectively. The reason this simple spring model works so well is due to the fact that we are analyzing zone-center phonons. Otherwise, due to the distortion of the band structure, the model does not work so well.

As we have already discussed, when the number of layers is odd, the point group to which the crystal belongs is the D_{3h}. When the number of layers is even (for a 2H-like stack), the point group will be the D_{3d}, and for a bilayer, the number of branches doubles in comparison with a monolayer since the number of atoms in the unit cell is also doubled. The phonon dispersion for a bilayer MoS_2 is shown in Figure 2.8(b), and we see some similarities between the phonon dispersion for monolayer and bilayer MoS_2. The critical points will still be the same, and the pDOS is also similar. From group theory, we can again predict the representation of the vibrational modes at the **Γ** point, given by the irreducible representations [110]

$$\Gamma_{vib} = \Gamma_{eq} \otimes \Gamma_{vec} = 3\left(A_{1g} \oplus E_g \oplus A_{2u} \oplus E_u\right).$$

The total number of vibrational modes will be 18 since the number of atoms in the unit cell has doubled, but the number of acoustic modes is still 3, giving 15 optical branches. Among the 15 optical branches, 3 are of A_{1g} irreducible representation (totally symmetric out-of-plane vibrations), 3 are of E_g representation (in-plane vibrations), 2 are of E_u representation (in-plane vibrations) and the remaining 2 are of A_{2u} representations (out-of-plane vibrations). Of these irreducible representations, the A_{1g} and E_g representations are Raman-active, while the others are IR-active.

The increasing number of layers introduces the quasi-acoustic branches, modes with low frequency representing the vibrations between layers (interlayer vibrations). Since these modes are related to the weak van der Waals bonding between layers, the expected frequencies are small, especially compared to the frequency of the intralayer vibrations, around 40 to 60 cm^{-1} as can be seen in Figure 2.8(b) at the **Γ** point. Although the quasi-acoustic vibrations present a big difference at the **Γ** point, such difference drops very fast for the rest of the vibrational structure, where the difference is mostly in the order of a few wavenumbers. The optical branches present a small shift compared to a monolayer though, which can be easily measured by Raman spectroscopy. Increasing the number of layers to three returns the system

to a D_{3h} symmetry, and increases the number of branches to 27, and increasing the number of layers to 4 returns to a D_{3d} symmetry, with 36 branches, and so on when the number of layers is alternating between odd and even. We can summarize the number of phonon branches in the phonon dispersion for the *n*-layers problem by using the relations in Table 2.1 [110].

When the number of layers is big enough, we can consider a bulk 2H crystal, where the unit cell is similar to the unit cell of a bilayer stack and a translational symmetry along the z axis appears. The translational symmetry along the z axis will introduce another symmetry operation, the screw axis C_6^{τ}, where the unit cell can be recovered for a 60° rotation followed by a translation of $\frac{c}{2}\hat{z} = \tau$. Therefore, the system will belong to a D_{6h} symmetry, and we can use group theory, again, to predict the irreducible representations of the vibrational modes at the **Γ** point, presented in table 1, where a total of 18 vibrational modes are expected, as can be seen in Figure 2.8(c). From the 18 phonon branches, three correspond to the acoustic modes, with representations A_{2u} and E_{1u}. There are two IR active modes with representations A_{2u} and E_{1u}, and four Raman-active modes with representations A_{1g}, E_{1g}, and two E_{2g}. The remaining phonon branches do not present light activity. In the backscattering configuration, only the A_{1g} and E_{2g} modes will be observed, and they correspond to the out-of-plane intralayer vibration (A_{1g}) and the intralayer and interlayer shear modes (E_{2g}).

One of the interesting observations of the vibrations in TMDs is that the frequency of the intralayer out-of-plane A_{1g} (for simplicity, we use the irreducible representation of bulk) mode increases as the number of layers increases, while the in-plane E_{2g} mode decreases in frequency [114–121]. For the A_{1g} mode, the frequency increase with the number of layers can be thought of as a consequence of an increasing force coming from effective springs connecting the layers due to the van der Waals force that increases the strength of the out-of-plane vibration. The in-plane E_{2g} modes are affected by the dielectric screening from the chalcogens interfacing in the layers, which decreases the vibrational strength of this mode [114].

Table 2.1. Irreducible representations for the vibrational modes at the Γ point for *n*-layers and bulk.

n odd	$\Gamma_{vib} = \left(\frac{3n-1}{2}\right)(A_1{}' \oplus E") + \left(\frac{3n+1}{2}\right)(E' \oplus A_2")$
n even	$\Gamma_{vib} = \left(\frac{3n}{2}\right)\left(A_{1g} \oplus E_g \oplus A_{2u} \oplus E_u\right)$
bulk	$\Gamma_{vib} = A_{1g} \oplus 2B_{2g} \oplus E_{1g} \oplus 2E_{2g} \oplus 2A_{2u} \oplus B_{1u} \oplus 2E_{1u} \oplus E_{2u}$

Here, we comment that although the decoupling of the electronic and atomic motions in the crystal is a good approximation, it does not account for the electron-phonon interactions, which are extremely relevant for the thermal dependence of the electronic transitions, as we will discuss further. We also comment that the harmonic approximation is still a flawed model, which is not able to explain the thermal expansion of a material. At room temperature, we are near the Debye temperature of the TMDs (between 200 and 300 K) and thermal effects become more relevant. Considering a simple harmonic oscillator as an example, as the temperature of the system is raised, the thermal agitation increases, and the harmonic approximation would not be sufficient to explain the thermal expansion for instance, which can be thought of as a change in the equilibrium position of the oscillator. Thus, the anharmonic effects that are responsible for these phenomena must be considered in the full picture, especially since these effects are responsible for the softening of the vibrational modes, which will be discussed further in this text. In the following sections, we will discuss the techniques that enable the observation of the optical features in TMDs, such as photoluminescence and Raman spectroscopies, and their impact on the characterization and investigation of fundamental properties of TMDs.

2.3 Optical techniques for the characterization of TMDs

When treating the optical properties of a material, that means, its interaction with visible (400 to 700 nm), near-infrared (NIR) (700 to 1400 nm) or near-ultraviolet (UV) (300 to 400 nm) radiation, few approximations must be considered in order to simplify the treatment and modeling of the experimental data.

The first is regarding the momentum carried by light, that is proportional to its wavevector (inversely proportional to the wavelength of light) and is in the order of 10^6 to 10^7 m^{-1} for the visible, NIR and UV ranges. An electron subject to the periodic potential of a crystal will carry the momentum of the crystal. Therefore, the electron wavevector can range from the Brillouin zone center to the zone edges and will be inversely proportional to the distance between the ions forming the crystal. In the case of TMDs, that distance is about 3.2 Å and the electron wavevector in the edges of the Brillouin zone will be of order 3 x 10^9 m^{-1}, which is about 100 to 1000 times bigger than the wavevector of light. In consequence, for excitations near the visible, NIR and UV ranges the crystal electron can only be excited vertically, which means that the initial and final states of the electron must have almost the same wavevector, or $k_i \approx k_f$. This approximation is known as the electric dipole approximation and it has some interesting implications for absorption, photoluminescence and Raman spectroscopies.

Consider an electron in a periodic lattice potential where there is an incident monochromatic electromagnetic wave. The Hamiltonian for this system can be written as (using the Coulomb gauge and neglecting $|\boldsymbol{A}|^2$ terms)

$$H = \frac{\mathbf{p}^2}{2m_e} + V(\boldsymbol{x}) - \frac{q}{m_e c}\mathbf{A} \bullet \mathbf{p} + H_{e-ph} + H_{ph-ph} \cdots \quad (2.5).$$

The first two terms refer to the unperturbed Hamiltonian, including the periodic lattice potential. The third term is related to the electron-radiation interaction term which can be extracted from classical electromagnet theory, where **A** is the magnetic potential vector. The fourth and fifth terms are related to the interaction between the electron and the lattice and the interaction of the lattice with itself. The last term is related to anharmonic effects. In this section, we treat just the third term to describe optical absorption. The following terms are discussed in the next sections. They will be relevant for the photoluminescence and Raman scattering phenomena.

2.3.1 Optical absorption by 2D materials with excitonic complexes

We explore light absorption first due to its simplicity compared to the other optical processes, and we use the simple approach proposed in ref. [122]. To describe the light absorption by a photon, we need to consider Fermi's Golden rule for the transition rate between all states in the electronic structure of the material. The transition rate, $W_{i\to f}$, is given by

$$W_{i\to f} = \frac{2\pi}{\hbar}\left|\left\langle f\left|H'\right| i\right\rangle\right|^2 \rho(\hbar\omega) \quad (2.6),$$

where $\left|\left\langle f\left|H'\right| i\right\rangle\right|^2$ is the matrix element of the perturbation Hamiltonian $H' = -q/m_e c\,\mathbf{A} \bullet \mathbf{p}$, i and f denote the ground state and excited state, and $\rho(\hbar\omega)$ is the joint density of states (jDOS) for a photon of energy $\hbar\omega$ between the conduction and valence bands. If we write the vector potential **A** as $A\hat{\mathbf{r}}e^{-i\omega t}$, using the dipole approximation, the term $|\langle f|(-q/m_e c\,\mathbf{A} \bullet \mathbf{p} \mid i\rangle|^2$ can be reduced to $(qA/m_e c)^2|\langle f \mid \hat{\mathbf{r}} \bullet \mathbf{p} \mid i\rangle|^2$. This approximation means that we need to consider light polarization for absorption, which is extremely important for some materials that present anisotropic properties.

Monolayer TMDs can be described as 2D parabolic band direct bandgap semiconductor, and the jDOS can be calculated considering the energy of an electron with wavevector $\boldsymbol{k}$ excited from the valence band to the conduction band by a photon with energy $\hbar\omega$. We can write

$$\hbar\omega = \frac{\hbar^2 k^2}{2m_e^*} + E_g - \frac{\hbar^2 k^2}{2m_h^*} = \frac{\hbar^2 k^2}{2\mu^*} + E_g, \quad (2.7),$$

where the μ^* term represents the reduced mass of the effective masses of the electron, m_e^*, and hole, m_h^*, and E_g is the bandgap. Thus, the jDOS will be given by

$$\rho(E)dE = \begin{cases} 2\frac{1}{(2\pi)^2}(2\pi k)dk = \frac{(2\mu^*)^{\frac{1}{2}}}{2\pi\hbar}dE, \text{when } E \geq E_g \\ 0, \text{when } E < E_g \end{cases} \quad (2.8),$$

which leads to the transition rate

$$W_{i\to f} = \frac{(2\mu^*)^{\frac{1}{2}}}{\hbar^2}\left(\frac{qA}{m_e c}\right)^2 |\langle f\,|\,\hat{\boldsymbol{r}}\bullet\boldsymbol{p}\,|\,i\rangle|^2 \quad (2.9),$$

meaning that for photon energies above the bandgap of the material, the transition rate is constant.

The extinction coefficient is taken as the energy of the photon times the number of transitions per unit volume per unit time, given by $W_{i\to f}$, over the incident electromagnetic flux. The electromagnetic flux is given by the absolute value of the Poynting vector, which is conveniently found for a non-magnetic material as:

$$S = \frac{\omega^2 c\varepsilon_0 n}{2}A^2 \quad (2.10),$$

where n is the real part of the complex index of refraction. Combining the definition of the extinction coefficient with equations (2.9) and (2.10) yields:

$$\alpha(\hbar\omega) = \begin{cases} \frac{(8\mu^*)^{\frac{1}{2}}}{\hbar\omega c^3 n}\left(\frac{e}{m_e}\right)^2 |\langle f|p|i\rangle|^2 \equiv \alpha_{2D}(\hbar\omega), \text{when } E \geq E_g \\ 0, \text{when } E < E_g \end{cases} \quad (2.11).$$

Equation (2.11) means that the absorption should increase as a function of the photon energy right after the energy of the photon becomes bigger than the energy of the bandgap. The presence of excitonic transitions with strong binding energy affects the extinction coefficient greatly, and strong absorption peaks are observed experimentally at specific photon energies. In this case, we should correct equation (2.8) to include the contributions from the excitonic transitions. We will do so via the inclusion of a δ function, such that:

$$\rho(E)dE = \frac{(2\mu^*)^{\frac{1}{2}}}{2\pi\hbar}\left\{1 + \delta\left[\hbar\omega - \left(E_g - \frac{R_X}{n^2}\right)\right]\right\} dE \qquad (2.12),$$

leading to a new extinction coefficient:

$$\begin{aligned}\alpha(\hbar\omega) &= \frac{(2\mu^*)^{\frac{1}{2}}}{\hbar\omega}\frac{8\pi}{cn^*}\left(\frac{e}{m_e}\right)^2 |\langle f|r|i\rangle|^2\left\{1 + \delta\left[\hbar\omega - \left(E_g - \frac{R_X}{n^2}\right)\right]\right\} \\ &= \alpha_{2D}(\hbar\omega)\left\{1 + \delta\left[\hbar\omega - \left(E_g - \frac{R_X}{n^2}\right)\right]\right\}\end{aligned} \qquad (2.13).$$

A finite lifetime has to be included as well, which can be done by means of the definition of the δ function as a Lorentzian:

$$\alpha(\hbar\omega) = \alpha_{2D}(\hbar\omega) + \frac{\alpha_{2D}(\hbar\omega)C_n}{\left\{\left[\hbar\omega - \left(E_g - \frac{R_X}{n^2}\right)\right]^2 + \left(\frac{\gamma}{2}\right)^2\right\}} \qquad (2.14),$$

where the constant C_n is introduced as a fitting parameter for the oscillator strength of the n-th transition and γ is the full width at half-maximum. Therefore, we expect a small background contribution together with the contributions from the excitons in the absorption spectra. Equation (2.14) also reveals that it is possible to observe the higher valued n, though their oscillator strength is extremely reduced when compared to the $n = 1$ case.

For TMDs, there are also excitonic transitions above the bandgap identified as the C and D excitons observed in Figure 2.6 for MoS_2, WS_2, $MoSe_2$, and WSe_2. But the treatment we'll use in this text regards the excitonic contribution below the bandgap for the optical properties since the other excitonic transitions are beyond the scope of this work.

2.3.2 Photoluminescence spectroscopy and its application to the transition metal dichalcogenides

The photoluminescence is known as the spontaneous emission of light by a material, where the electron decays from the minimum in the conduction band to the maximum in the valence band. Thus, photoluminescence provides a direct measurement of the optical band-gag of a material.

When a semiconductor with a direct bandgap E_g is illuminated by a photon with energy above E_g, an electron-hole pair is created and the electron is promoted to the conduction band above the minimum. Through non-radiative decays, by the emission of phonons and other lattice processes, the electron and hole pair are scattered to the minimum of the conduction

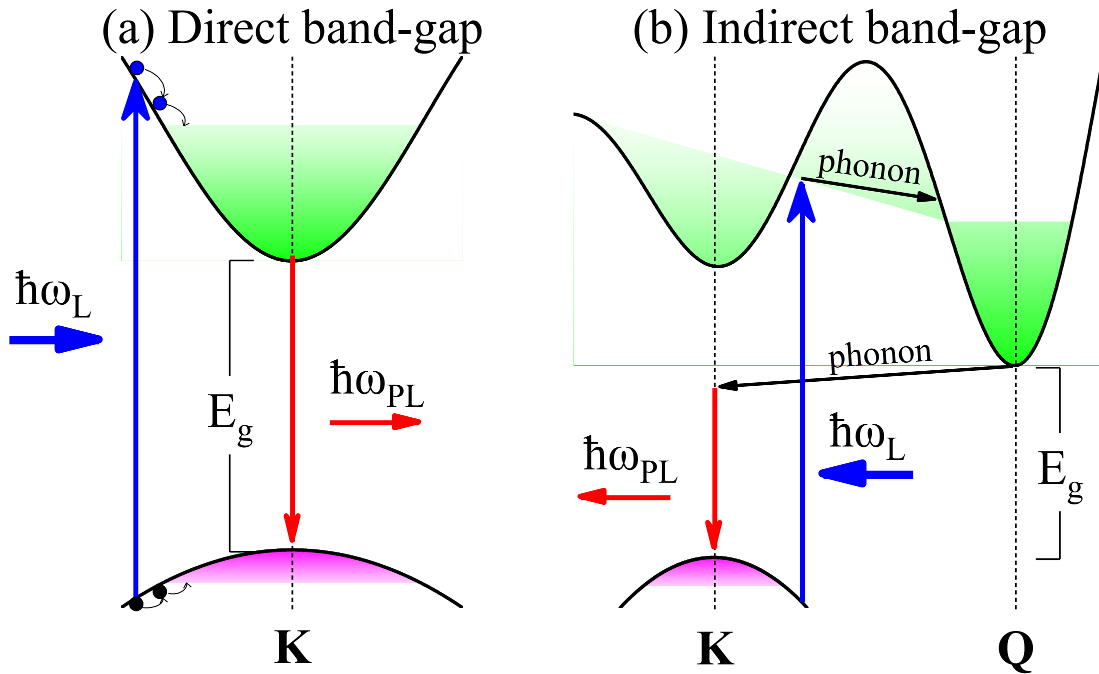

Figure 2.11. Sketch of the photoluminescence process for (a) Direct bandgap and (b) indirect bandgap semiconductors. The high symmetry points are those of TMDs.

band and maximum of the valence band. The electron-hole pair recombines, with the emission of a photon corresponding to the bandgap. A simple sketch of this process is depicted in Figure 2.11(a).

When the material possesses an indirect bandgap, however, the process of emission is slightly different, as it is illustrated in Figure 2.11(b), because light does not carry enough momentum to promote the recombination of the electron-hole pair. Thus, a phonon with large momentum and small energy is required to allow the recombination between the electron-hole pair. Since this process depends on the available population of phonons, its intensity is heavily influenced by the material temperature. The intensity is also very weak compared to the emission of a direct bandgap material since there must be a correction to the transition rate which accounts for the electron-phonon interaction, which is much weaker than the electron-radiation term.

Since monolayer TMDs are direct bandgap semiconductors, the emission is a very efficient process where the quantum yield reaches almost 100% in some specific cases [123]. From bilayers up to bulk, the TMDs present an indirect bandgap, similar to the one shown in Figure 2.4(b), and the emission efficiency reduces drastically. A comparison between the photoluminescence of monolayer MoS_2 and bilayer MoS_2 is presented in Figure 2.12(a) [124]. Bulk TMDs present almost no emission in the region of the direct bandgap, thus, most of its emission comes from the indirect bandgap at approximately 1.3 eV. The indirect bandgap

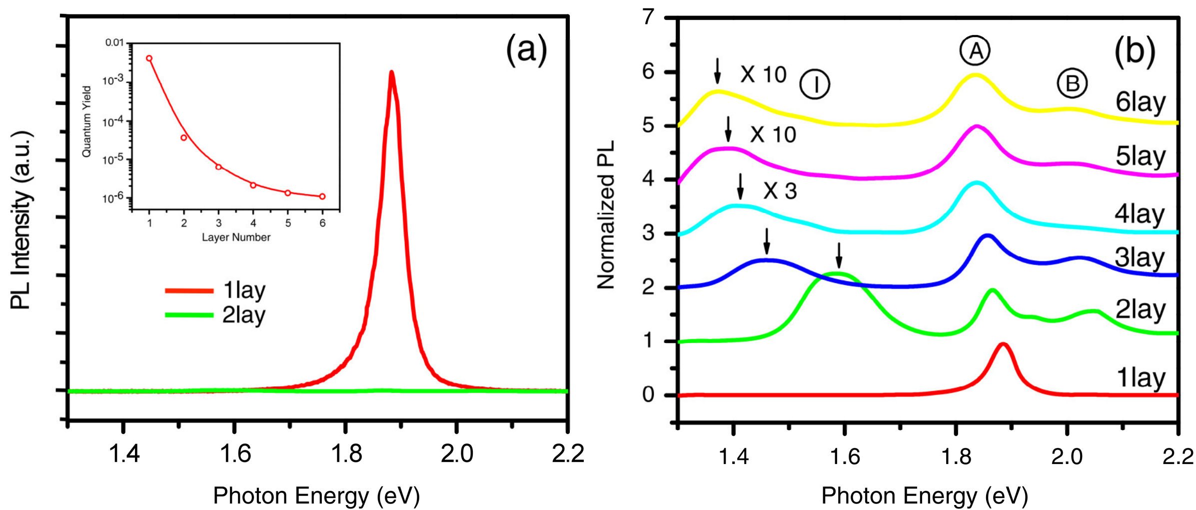

Figure 2.12. (a) Comparison between the PL from a monolayer MoS_2 and a bilayer MoS_2. The inset shows how the quantum yield varies with the number of layers. (b) Normalized PL from a monolayer up to six layers MoS_2. The peak marked by I is the indirect bandgap and the peaks marked by A and B are the A and B excitons. Adapted from ref. [124].

energy and consequently the emission energy decreases for an increasing number of layers, as can be observed in Figure 2.12(b) [124].

For a monolayer TMD, the PL intensity and lineshape are affected by several factors such as the power used [97,106], the density of carriers [82,84,94,95,97,98,105], defects [103,125] and also temperature [87]. Resonances with the electronic transitions are also incredibly relevant to the emission of these materials, influencing the observed intensity by up to 2 orders of magnitude. The study of the PL intensity as a function of the laser energy is known as photoluminescence excitation (PLE), and it has been used in the study of TMDs for the characterization of their energy levels [65,108]. We also add here that due to strong exciton-phonon coupling in TMDs, their PL presents strong resonances with phonon levels, especially the acoustic phonons [126,127].

2.3.3 Raman spectroscopy

Among the possible processes of light-matter interaction, one of the most interesting is the scattering of light, which can be either elastic or inelastic. Elastic scattering is the phenomenon responsible for the blue color of the sky and also the white color of the clouds. Light scattering plays an important role in the way we see the world and also in its applications for the characterization of materials. Here, we will present a quick overview of the topic of inelastic scattering of light by a crystal.

Suppose a coherent monochromatic light source of frequency ω with an electric field component $\boldsymbol{E}(t)$described by $\boldsymbol{E}(t) = \boldsymbol{E}_0 \cos(\omega t)$, interacts with a crystal. The light electric field will induce a polarization $\boldsymbol{P}$ in the crystal such that

$$\boldsymbol{P} = \chi \boldsymbol{E} = \chi \boldsymbol{E}_0 \cos(\omega t) \qquad (2.15),$$

where χ is the electric susceptibility of the crystal. The electric susceptibility can be expanded in terms of the normal vibrational modes of the crystal, q_k, such that

$$\chi = \chi_0 + \sum_k \left(\frac{\partial \chi}{\partial q_k}\right)_0 q_k + \cdots \qquad (2.16),$$

where the under script 0 means at $q_k = 0$. Since the normal vibrational coordinates describe the approximate harmonic vibrational motion of the crystal, q_k can be rewritten as $q_k \cos(\omega_k t)$, with ω_k being the frequency of vibration of this mode. After some minor changes, the combination of 2.15 and 2.16 yields

$$\boldsymbol{P} = \chi_0 \boldsymbol{E}_0 \cos(\omega t) + \sum_k \left(\frac{\partial \chi}{\partial q_k}\right)_0 \frac{\boldsymbol{E}_0 q_k}{2} \left[\cos(\omega t - \omega_k t) + \cos(\omega t + \omega_k t)\right] \qquad (2.17).$$

Since the observed intensity is proportional to the square of $\boldsymbol{P}$, we expect to see three different scattering phenomena: (i) the elastic scattering of light, the first term in the right-hand-side of equation 2.17; (ii) the Stokes inelastic scattering of light, where the scattered light loses energy via an interaction with the material; (iii) the anti-Stokes inelastic scattering of light, where the scattered light gains energy via the interaction with the material. The elastic scattering of light is called the Rayleigh scattering, named after Rayleigh first introduced the theory for the elastic scattering of light. The inelastic scattering of light is called Raman scattering after C. V. Raman first observed the inelastic scattering of light in molecules in 1928.

In the classical treatment of light scattering, the intensity of this process is proportional to the fourth power of the light frequency (or inversely proportional to the fourth power of the wavelength), thus, for light with high frequency such as blue or violet, the probability of scattering is much higher than that of red or yellow light. The scattering intensity is still very low compared to other processes such as reflection or even the emission of light by a crystal. The inelastic scattering of light is even weaker than the elastic scattering. Thus, a very sensitive setup along with high-intensity coherent light sources are better suited for the detection of the Raman scattering of materials.

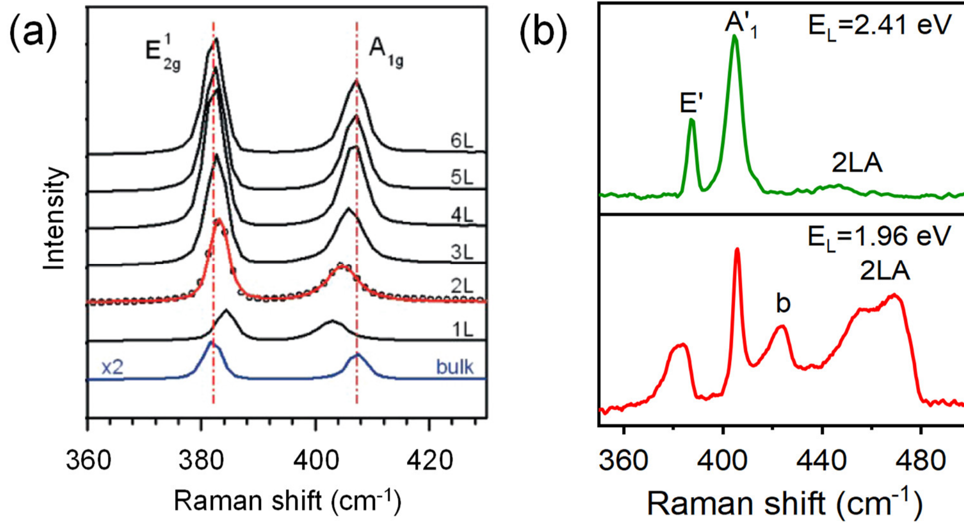

Figure 2.13. (a) Raman spectra of a monolayer (1L) up to six-layers (6L) and the bulk of MoS_2 measured with a 2.41 eV laser. Adapted from ref. [114]. (b) Raman spectra of monolayer MoS_2 collected with a 2.41 eV laser (top) and a 1.96 eV laser (bottom).

Out of resonance with the excitonic transitions, the Raman spectra of TMDs is generally composed of two main peaks in the backscattering configuration. One peak corresponds to the totally symmetric vibrational out-of-plane optical mode, and the other corresponds to the doubly degenerate in-plane longitudinal and transverse optical modes. As we discussed before in section 2.2, the number of layers in the crystal affects the frequency of the vibrational modes due to the interlayer interactions. Raman spectroscopy can measure the shifts due to the interlayer interactions of the Raman active vibrational modes, which we show in Figure 2.13(a) for a monolayer, few-layers, and bulk of MoS_2.

To finish this chapter, we comment that although the classical treatment is correct for the case where the laser energy is less energetic than the electronic transition energy, it is wrong for the case of the laser energy matching the electronic transition energy. When the laser energy is close to the transition energy, also called a resonance with the electronic transition, the overall intensity of the Raman process is increased by many folds, and also higher-order scattering processes appear as well. In TMDs specifically, the proximity of the resonance with the A and B excitons strongly affects the intensity of the bands resulting from combinations of acoustic phonons, like the 2LA and *b* bands in Figure 2.13(b). To properly understand the mechanism behind these two bands, we treat the resonance Raman processes in chapter 3, where we review the resonances with the excitonic levels for the H-MX_2 family. We’ll see how the resonances with different excitons can affect the intensities of the Raman bands involving one phonon, and also the processes involving two phonons.

3. The resonance Raman scattering process in 2D materials

3.1 Raman spectroscopy and 2D materials

In the last years, Raman spectroscopy has presented itself as a key tool to obtain information about the structure and physical properties of 2D materials. It can provide a better understanding of the electronic and vibrational properties in several types of 2D systems such as graphene [128–130], black phosphorus [131], hexagonal boron nitride [132–134] and transition metal dichalcogenides (TMDs) [135,136]. The analysis of the first-order Raman spectrum of TMDs, for instance, allows us to gather information about the interlayer interactions [137], exciton-phonon interactions [60,61,138], as well as dependence of the phonon frequencies with the number of layers [48,114,115,117,118,121,139,140], among many other relevant characteristics that are fundamental to unveil the underlying physics in these systems [137,141–144]. The second-order and double resonance bands have been used in the literature to obtain important information from III-V group semiconductors [145–147], Cadmium Telluride alloy [148], graphite and graphene [129,130,157–159,149–156], and extensive studies from bulk to monolayer regimes of TMDs as well [53,60,164–172,74,117,119,121,160–163]. The double resonance process arises from the intervalley or intravalley scattering where two phonons or one phonon and one defect participate in the scattering of the excited electron. The double resonance bands can help us characterize both the electronic and vibrational properties of these materials. These contributions can aid the understanding of changes in basic properties brought by defects, which could, in turn, allow the application of 2D materials to new relevant technologies [173,174].

In the electric dipole approximation, the first-order Raman scattering only allows the observation of phonons at the Brillouin zone center (the $\mathbf{\Gamma}$ point). This is justified by the fact that the momentum carried by light is much smaller than the size of the Brillouin zone and, consequently, much smaller than the momentum required to reach phonons away from the $\mathbf{\Gamma}$ point. Therefore, optical transitions can be regarded as strictly vertical [175].

The full equation that describes the first-order Raman scattering process can be deduced from third-order time-dependent perturbation theory [175], but in the interest of simplicity, we use the Feynman diagrams in order to deduce the Raman intensity equation, proportional to the transition rate. The terms composing the transition rate equation take into account that the

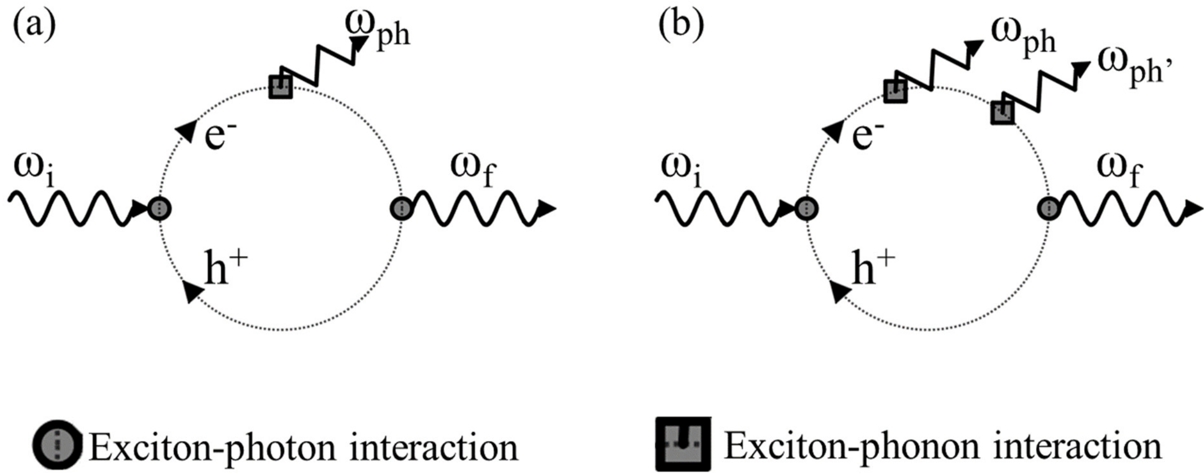

Figure 3.1. Feynman diagrams for the Raman scattering process involving (a) one phonon and (b) two phonons.

numerator represents the product of interaction terms and the denominators come from corrections to the energy states of the system due to the transitions.

Figure 3.1(a) displays the Feynman diagram for the first-order Raman process, which involves one phonon. First, a photon with energy $\hbar\omega_i$ interacts with the material, promoting an electron from the valence band to the conduction band and leaving a hole in the valence band. Second, the electron-hole pair, or the exciton, will interact with the crystal lattice, creating a phonon with energy $\hbar\omega_{ph}$. Finally, the exciton will decay, emitting a photon with energy $\hbar\omega_f$.

In order to construct the equation, we need to travel back in time to analyze the interaction vertexes that integrate the equation. We also use the band structure diagram in Figure 3.2(a) to help visualize the construction. The final term reflects the exciton-photon interaction, which takes place during the recombination of the electron-hole pair. This interaction will contribute a matrix element of the form $\langle f|H_{e-R}|b\rangle$ to the transition rate, where f is the final state and b is an intermediate state (see Figure 3.2(a)). The second term comes from the exciton-phonon interaction, that creates a vibration due to the interaction of exciton and crystal lattice, which will contribute a matrix element of the form $\langle b|H_{e-Ph}|a\rangle$, where a is another intermediate state (see Figure 3.2(a)). The final term in the numerator comes from the creation of the exciton, which contributes a term of the form $\langle a|H_{e-R}|i\rangle$, where i is the ground state.

The term in the denominator comes from the correction to the energy of each state after the transitions. The first transition connects the ground state i to the intermediate state a, and the correction to the energy will have the form $\left[\hbar\omega_i - (E_{e^-} + E_{h^+})\right]$, where E_{e^-} is the energy of the electron in the conduction band and E_{h^+} is the energy of the hole in the valence band. The second transition connects the intermediate states a and b, and the correction will have the

form $\left[\hbar\omega_i - (E_{e^-} + E_{h^+}) - \hbar\omega_{ph}\right]$. The third and last term does not have a correction, but we use the total energy to construct the joint density of states, $g(\omega_f) = g\left[\hbar\omega_i - (E_{e^-} + E_{h^+}) - \hbar\omega_{ph}\right]$. Combining every term, we can reach

$$I_{\omega_f}(\omega) = C\omega^4 \left| \sum_{a,b} \frac{\langle f|H_{e-R}|b\rangle\langle b|H_{e-Ph}|a\rangle\langle a|H_{e-R}|i\rangle}{\left[\hbar\omega_i - (E_{e^-} + E_{h^+})\right]\left[\hbar\omega_i - (E_{e^-} + E_{h^+}) - \hbar\omega_{ph}\right]} \right|^2 \times g\left[\hbar\omega_i - (E_{e^-} + E_{h^+}) - \hbar\omega_{ph}\right]. \tag{3.1}$$

The summation is made over all possible intermediate states. Since $E_{e^-} + E_{h^+} = E_g + \frac{\hbar^2 k^2}{2\mu^*}$, we see right away that for states where $\hbar\omega_i \ll E_g$, we recover the classical behavior of the intensity. For $\hbar\omega_i \gg E_g$, the behavior is also recovered, since the terms in the denominator will be very large. When $\hbar\omega_i \approx E_g$, we would need to consider the resonance with the electronic level, especially when $\hbar\omega_i = E_g$, where the photon energy matches the electronic transition energy, and equation 3.1 would diverge. Since we are dealing with physical quantities, the transition between the levels have finite lifetimes, therefore, a constant must be introduced in equation 3.1 to correct the lifetime of the electronic levels. Combining the results of section 2.3.1 with equation 3.1, yields

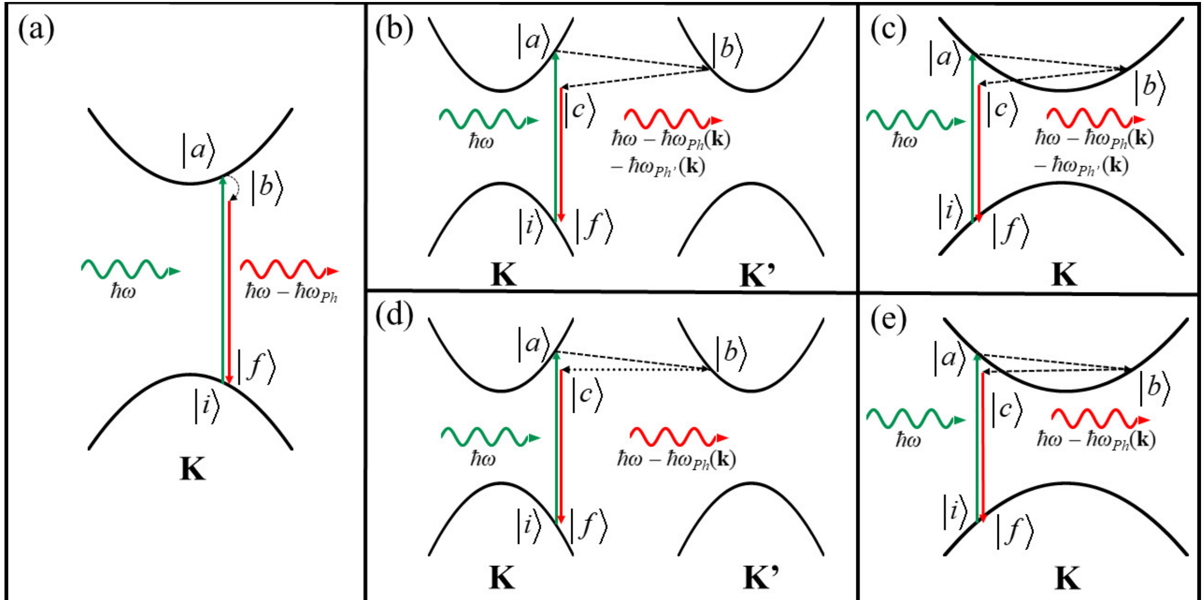

Figure 3.2. The first and second-order Raman scattering processes illustrated in a parabolic band semiconductor. (a) First-order Raman scattering. (b) Intervalley two-phonon electron-electron double-resonance scattering process. (c) Intravalley two-phonon electron-electron double-resonance scattering process. (d) Intervalley phonon-defect electron-electron double-resonance scattering process. (e) Intravalley phonon-defect electron-electron double-resonance scattering process. Adapted from ref. [176].

$$I_{\omega_f}(\omega) = C\omega^4 \left(\frac{q}{cm_e}\right)^4 \left| \sum_{a,b} \frac{\langle f|\boldsymbol{A} \bullet \boldsymbol{p}|b\rangle\langle b|H_{e-Ph}|a\rangle\langle a|\boldsymbol{A} \bullet \boldsymbol{p}|i\rangle}{\left[\hbar\omega_i - \left(E_g + j\Gamma\right)\right]\left[\hbar\omega_i - \left(E_g + j\Gamma\right) - \hbar\omega_{ph}\right]} \right|^2. \quad (3.2)$$

Where E_g is the measured optical bandgap, or for TMDs, the exciton transition energy and $j\Gamma$ is the product between the pure imaginary number and damping constant related to the lifetime of the Raman process. We neglected the jDOS term because its purpose is mainly to give the lineshape of the photon distribution. Since the only phonons that can be accessed are the optical phonons at the zone center, the expected distribution would be similar to a Dirac delta function. However, since there are anharmonic effects, and also due to the dampening, the expected lineshape of the Raman peaks will be Lorentzian.

A closer look into equation 3.2 reveals a very important selection rule for the scattering of a photon by a phonon, the fact that the parity of the wavefunction must be conserved at the end of the process. Since the Raman process involves two dipole transitions, the parity of the wavefunction changes during the first transition, but it changes again after the second transition. In the end, the parity is conserved through the scattering. The Raman scattering is different from infrared (IR) absorption, where there is only one dipole transition. Therefore, in order to observe the Raman scattering via a specific phonon, the irreducible representation of said phonon must transform as a quadratic function. For the IR absorption, however, the irreducible representations of the phonon must transform as a linear function.

Semiconducting monolayer TMDs such as MoS_2, with trigonal prismatic symmetry, belongs to the D_{3h} point group which predicts two Raman active modes, A_1' and E', in the backscattering configuration [136]. Thus, only two peaks can be seen in their first-order Raman spectrum. Bilayer MoS_2 would present six Raman active modes, 3 A_{1g}, and 3 E_g. Trilayers would present eight Raman active modes, 4 A_1' and 4 E'' modes, and bulk presents three Raman active modes, A_{1g}, and 2 E_{2g}.

The two-phonon Raman bands obey different selection rules, which do not only consider vertical transitions but also the scattering of the excited electron throughout the entire reciprocal lattice as long as momentum conservation is achieved [53,128,149]. The intensity of the two-phonon bands can be described by the following equation

$$I(\omega) = D\omega^4 \left(\frac{q}{cm_e}\right)^4 \times \left| \sum_{a,b,c} \frac{\langle f|\boldsymbol{A} \bullet \boldsymbol{p}|c\rangle\langle c|H_{e-ph'}|b\rangle\langle b|H_{e-ph}|a\rangle\langle a|\boldsymbol{A} \bullet \boldsymbol{p}|i\rangle}{\left(\hbar\omega - \left(E_g + j\Gamma\right)\right)\left(\hbar\omega - \left(E_g + j\Gamma + \hbar\omega_{ph}\right)\right)\left(\hbar\omega - \left(E_g + j\Gamma + \hbar\omega_{ph} + \hbar\omega_{ph'}\right)\right)} \right|^2. \quad (3.3)$$

Notice the presence of a second electron-phonon interaction and a third intermediate state, $|c\rangle$, due to the creation of a second phonon with energy $\hbar\omega_{Ph'}$, in contrast with Equation 3.2. We can construct equation 3.3 using the same principles used for equation 3.2, and the Feynman diagram present in Figure 3.1(b). Figure 3.2(a) illustrates a two-phonon process. First, similar to the first-order process, the electron is promoted from the valence band (state $|i\rangle$) to the conduction band (state $|a\rangle$) and it interacts with the lattice to create a phonon with energy $\hbar\omega_{Ph}$ (state $|b\rangle$). However now, instead of a zone center phonon, the emitted phonon has enough momentum to scatter the electron from one point in the Brillouin zone to another (**K** to **K'** in our example). To guarantee momentum conservation, the electron at **K'** must emit another phonon with the same amount of momentum that the first phonon had and energy $\hbar\omega_{Ph'}$ (state $|c\rangle$). Finally, the excited electron-hole pair recombine and a photon with energy equal to $\hbar\omega - \hbar\omega_{Ph} - \hbar\omega_{Ph'}$ is emitted. Due to the scattering of the electron from one valley to the other, this process is frequently called intervalley scattering [53]. Another example of a two-phonon process could be the intravalley scattering, where instead of the electron being scattered from the **K** valley to the **K'** valley, the electron is scattered in the same valley, following the same trajectory as Figure 3.2(b). The same procedures from the intervalley process can be applied, just the length of the wavevector changes.

The following question is how would defects change the Raman process. Figure 3.2(d) and Figure 3.2(e) present the defect induced Raman process expected for a low-defective material (a material with a defect density low enough that its basic properties are not very affected by defects). In this case, the same process for intervalley and intravalley scatterings occur, but the transition from state $|b\rangle$ to state $|c\rangle$ is carried by a defect instead of a phonon. Then, the energy of the scattered photon will be $\hbar\omega - \hbar\omega_{Ph}$, like in the case of the first order bands, but the phonon participating in the Raman process is not a zone center phonon. The intensity of this process can be explained by means of Equation (2) as well [159], after some minor changes to include the electron-defect interaction.

The processes illustrated in Figure 3.2(b-d) have only shown the scattering of the electron from one point to another in the electronic structure. As a matter of fact, the electron is not the only entity that can be scattered, but the hole in the valence band can be scattered as well [74,155]. For the case where the electron is the only entity scattered in an intervalley or intravalley process, we call it electron-electron scattering. If both electron and hole are scattered, we call it electron-hole scattering and the case where just the hole is scattered can be called hole-hole scattering.

Unfortunately, the two-phonon or the phonon-defect bands have a very low probability of happening, such that their intensity is much smaller than that of first-order modes. Nevertheless, when the incoming laser energy reaches resonance with the electronic transition of the material, or when the defect density is high enough in a defect induced process, the intensity becomes comparable or even higher than that of the first-order modes [53,156,177,178]. When it happens, the bands approach a resonant behavior like that of the first-order modes. But, since the choices are not limited to the zone center phonons, other terms in the denominator of Equation 3.3 can be null at the same time. That is why these bands are called double-resonance bands or even triple-resonance bands in some cases [53,179].

In this chapter, we present some of the recent advances in the resonance Raman process in transition metal dichalcogenides and make a comparison with graphene. We also discuss some information that can be obtained from the analysis of the double resonance Raman bands and its applications, e.g. investigation of defects in 2D materials.

3.2 First-order resonance Raman process in transition metal dichalcogenides

In this section, we present a quick overview of the resonance Raman process involving only the zone center phonons of TMDs. As discussed in the last section, the first order Raman-active modes of TMDs have representations belonging to the totally symmetric irreducible representations A_1' or A_{1g}, or the degenerate E', E_g or E_{2g} irreducible representations for the Raman spectrum measured in the backscattering configuration. The totally symmetric irreducible representations A_1' or A_{1g} represent the out of plane vibration where the chalcogen sheets vibrate in opposite directions maintaining the metal sheet fixed. The degenerate E', E_g and E_{2g} representations represent the LO and TO vibrations where the chalcogen sheets vibrate in one direction while the metal sheet vibrates in a different direction. In this section, we use the irreducible representations of bulk, A_{1g}, and E_{2g}, for simplicity.

Considering only the transition energy in equation 3.2, we would expect that the enhancement observed for the Raman bands associated with the A_{1g} and E_{2g} modes would be equal as a function of the laser energy, except for a constant. Figure 3.3(a) shows the Raman spectrum of monolayer (1L), bilayer (2L), trilayer (3L) and bulk MoS_2 collected under several laser energies, where it can be observed that for the laser energies close to the A and B excitons, 1.92 and 2.18 eV, the intensity of the A_{1g} band is stronger than the intensity of the E_{2g} band. In the meanwhile, for laser energies closer to the C exciton, at 2.71 and 2.81 eV, the intensities of both A_{1g} and E_{2g} bands are similar. Figure 3.4(a) shows the intensity of the A_{1g} and E_{2g} bands

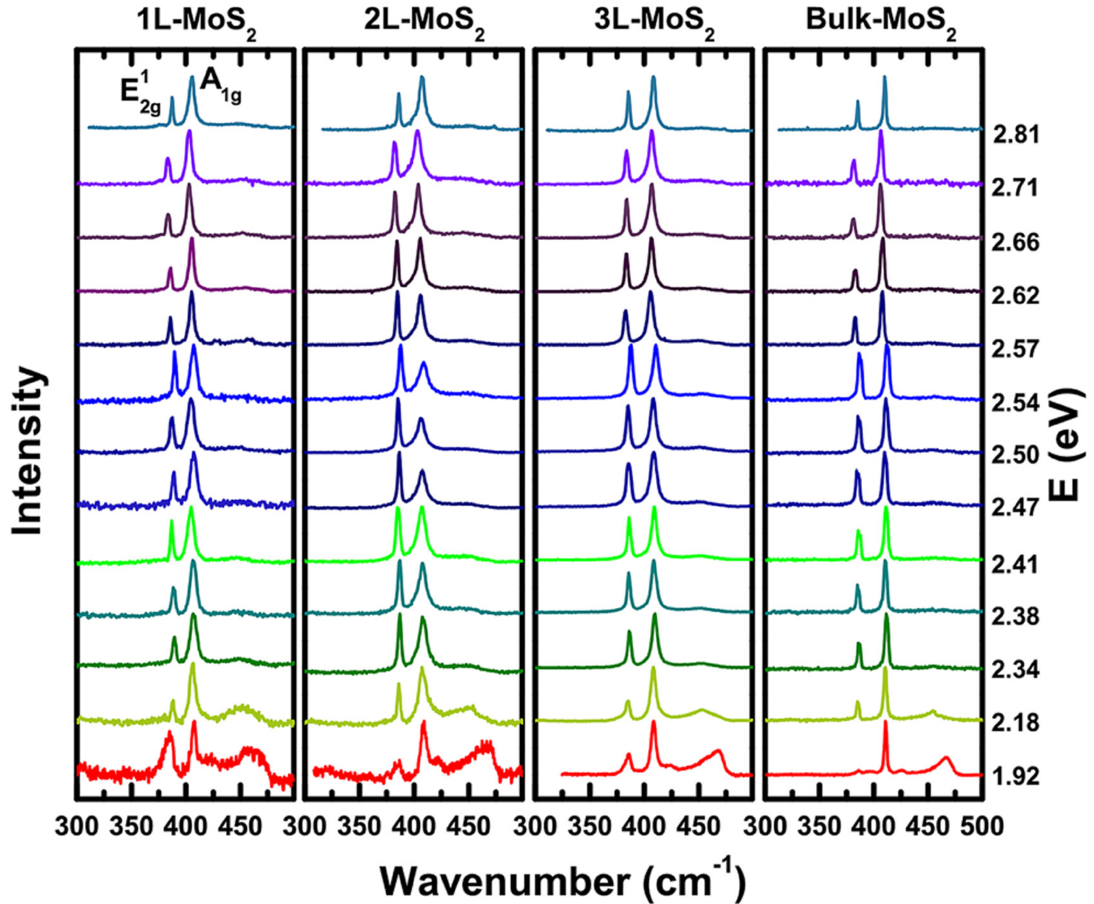

Figure 3.3. The Raman spectrum of a monolayer (1L), bilayer (2L), trilayer (3L) and bulk MoS_2 collected under the laser energies ranging from 1.92 to 2.81 eV. Adapted from ref. [180].

as a function of the laser energy, where the resonance with the A and B excitons around 1.9 and 2.1 eV is clear for the A_{1g} band, while the resonance with the C exciton affects both A_{1g} and E_{2g} bands. The observed behavior also affects the other TMDs, as it was observed in several works in the literature [60–62,118,162,164,180,181].

The explanation for such anomalous behavior comes from the interaction between the vibrational modes and the atomic orbitals involved in the electronic transition. For the A and B excitons, the transitions are around the direct bandgap at the **K** point.

As we discussed before, the atomic orbitals around the direct bandgap are mostly constituted by the *d* orbitals of the transition metal [55,182,183]. The *d* orbitals, in turn, have a similar character to the vibrational motion of the out-of-plane A_{1g} mode, which couples with this electronic transition very well, increasing the intensity of this mode [180]. The C and D excitons come from transitions close to the **Γ** point, where both *d* orbitals from transition metals and *p* orbitals from the chalcogens are present. In this case, the zone center phonons are highly enhanced, and the intensities of both A_{1g} and E_{2g} bands are enhanced [60,61,118,180].

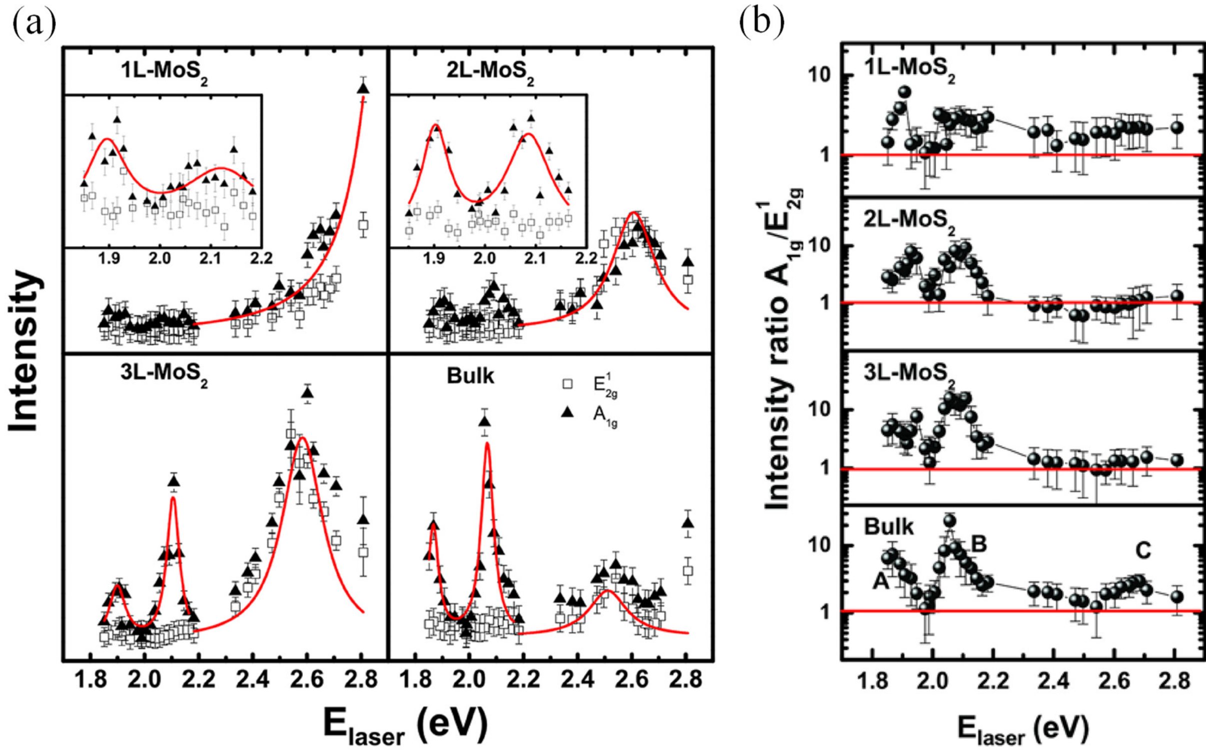

Figure 3.4. (a) The Raman intensity for the A_{1g} (solid triangles) and E_{2g} (empty squares) bands as a function of the laser energy for 1L, 2L, 3L, and bulk. Adapted from ref. [180] (b) The intensity ratio of the A_{1g} and E_{2g} bands as a function of the laser energy. The intensity is displayed on a logarithmic scale. Adapted from ref. [180].

One important implication of the enhancement of the just the A_{1g} mode around the excitonic levels is the fact that we can use the intensity of the E_{2g} mode as a standard for calibration since it will not couple with the A and B excitons. Therefore, around the A and B excitons, we may use the intensity ratio between the A_{1g} and E_{2g} modes to observe these excitonic transitions, which is illustrated in Figure 3.4(b). However, this reasoning only applies in the proximity of the A and B excitonic transitions, because at the C exciton level the intensity of both A_{1g} and E_{2g} bands is enhanced.

3.3 Double Resonance Raman Process

The appearance of double resonance Raman bands can be originated from an intervalley or intravalley scattering of the excited electron by a combination of two phonons of the same wavevectors but with opposite signs. The Raman process is resonant if at least one of the states accessed by the electron is a real electronic state. However, the double resonance process is characterized by two real states connecting each other [129,151]. It can be either a band state in the conduction band, such as in the case of graphene (see appendix B), or it can be an excitonic state, such as in the case of TMDs. The phonons that participate in the process will be limited to those with wavevectors that can connect states with similar energy of the excited

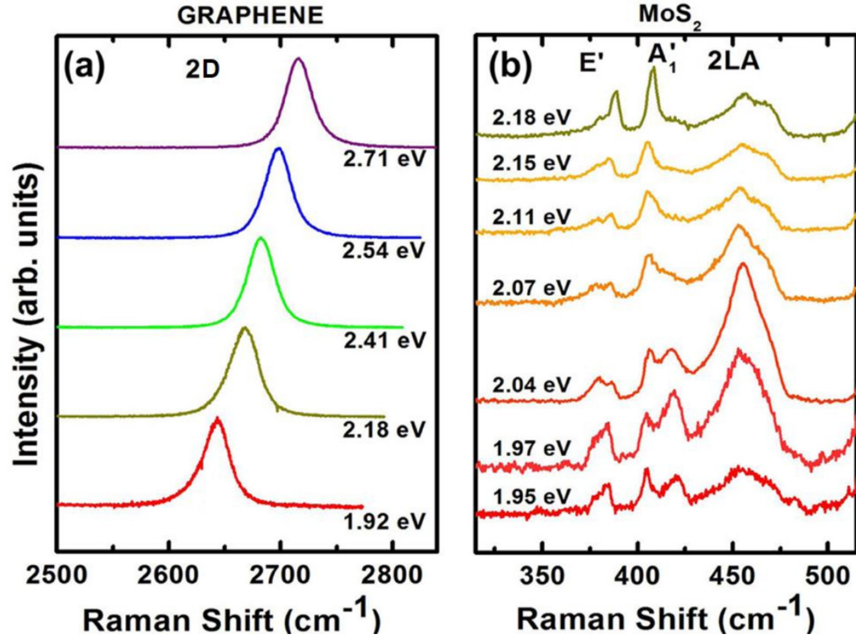

Figure 3.5. The two-phonon Raman bands originated from the double-resonance intervalley scattering in (a) graphene and (b) monolayer MoS_2. Adapted from ref [135].

electron [129,151]. Such is the case for the 2D band in the Raman spectrum of graphene (see Figure 3.5(a)), which arises from the contributions of the TO branch around the **K** point. In the case of the MoS_2, a semiconducting TMD, it has been recently demonstrated that the double resonance band in the material has contributions from the longitudinal acoustic (LA) and transversal acoustic (TA) phonon branches in the vicinities of the **K** and **M** points (see Figure 3.5(b)) [8,49]. The aforementioned considerations help us to understand some rules regarding the double resonance process and, the information that it can provide, such as the electron or phonon velocity along a certain region in the electron or phonon dispersion [130].

Before discussing the double-resonance process for TMDs, we make some important considerations here about graphene as they will act as a guide for the other materials. A complete review of the double and triple-resonance processes in graphene is presented in Appendix B, where we discuss the important features observed and their attributions to the phonon dispersion. The most intense feature in the Raman spectra of monolayer graphene is the 2D band (Figure 3.5(a)). From the process introduced before, we can infer that not only the triple resonance due to Equation 3.1 is important, but also a strong interaction between electron and phonons can play a big role in the probability of the process. In fact, the electron-phonon interaction has been found to be twice as strong for LO phonons close to the **K** point than for phonons close to the **Γ** point [159]. This relatively small difference becomes rather strong when we remember that Equation 3.1 has a product of two electron-phonon interaction terms that are squared. Thus, an intensity difference of at least eight times can be expected from the 2D and

2D' bands [159], which are originated from the same phonon branch at the **K** and **Γ** points, respectively. Graphene can be considered a semimetal, meaning that it has electronic states available everywhere, except at $E = 0$. Looking at Equation 3.1, we realize that there is a term for the electronic transition energy, which is null for graphene. This means that while the linear behavior of the electronic structure is satisfied, graphene is always in resonance, which is true for the NIR and visible spectral regions. This fact also remotes to another important point in the characteristics of the double or triple resonance process, the fact that it is coupled with the position of the electron in the electronic band. Finally, the phonons that participate in the process must conserve momentum, as we have previously mentioned. But, as long as momentum is conserved, any combination of phonons is possible, though the final intensity varies due to the electron-phonon interaction.

3.3.1 Transition metal dichalcogenides

As discussed before, the non-resonant Raman spectrum of semiconducting TMDs, collected in the backscattering configuration, are mostly restricted to first-order modes, which are known in the literature as the out-of-plane A_1' (A_{1g} for bulk) and the in-plane degenerate E' (E_{2g} for bulk) mode [135,136] (see top of Figure 3.6(a)). On the other hand, when the incoming laser energy closely matches the *A* and *B* excitonic transitions, new contributions arise in the Raman spectrum of the material (see bottom of Figure 3.6(a)). The new features can be associated with the intervalley scattering mediated by acoustic phonons [53,74,160,165,168,169,172,184]. For instance, in MoS_2, two bands are mainly observed in its resonant Raman spectrum: a band at approximately 420 cm^{-1} commonly known in the literature as "*b*" band [53,160,172], and a broad and asymmetric band at approximately 460 cm^{-1} which is related to two LA phonons (Figure 2.8) [53,161,164,166,185,186]. A detailed discussion about the origin of these bands will be presented in the sequence.

Before that, to understand the physical meaning of the double resonance bands involving the acoustic phonons, it is necessary to separate the simple second-order Raman process and double resonance process that overlap in a resonant Raman spectrum of TMDs.

Second-order bands are present in the Raman spectrum of several materials, and their main characteristic is the fact that they are the reflection of the phonon density of states of the material with twice the original frequency. This means that their position does not change with the laser energy in contrast to double-resonance bands. Recent theoretical work for silicon has shown that the Raman intensity of the second-order bands is highly affected by the many-body effects that come into play [187]. Thus, the second-order bands are greatly enhanced when the

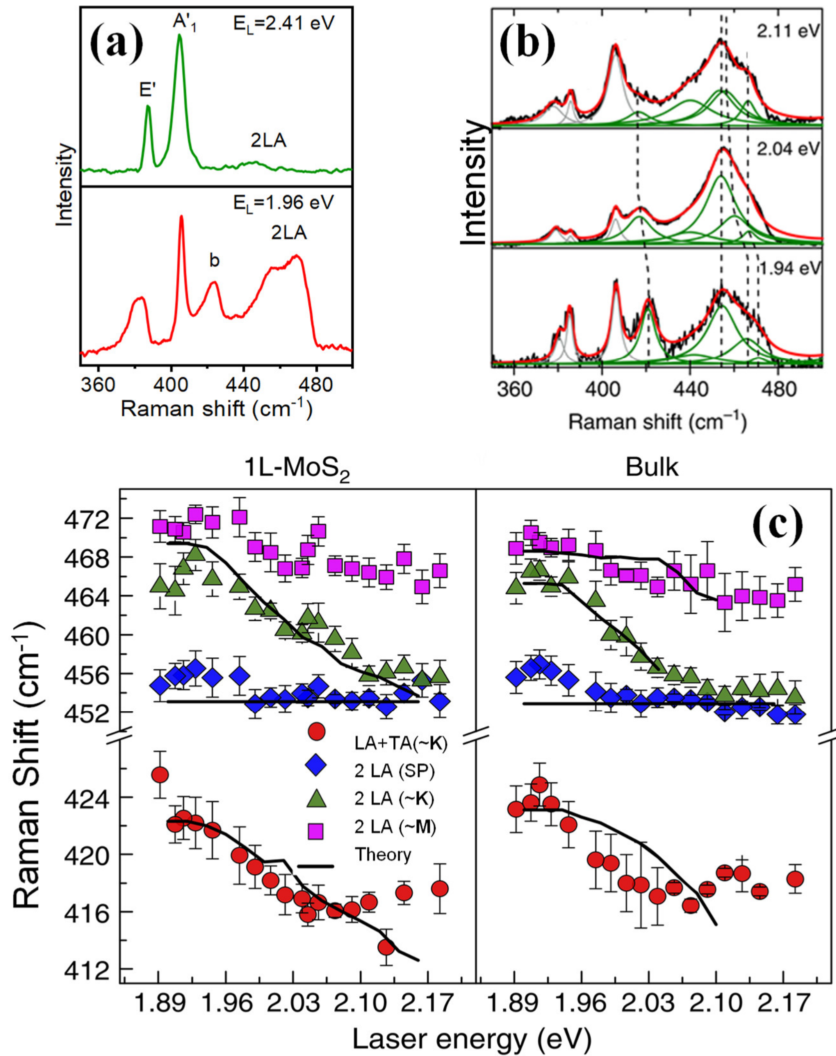

Figure 3.6. The Raman scattering process MoS_2. (a) Raman spectra of monolayer MoS_2 off-resonance (top) and on-resonance (bottom) with the excitonic transition. (b) Raman spectra of monolayer MoS_2 collected at different laser energies across the A and B excitons. (c) Frequencies of the LA+TA (~**K**) band and the components of the 2LA band: singularity, 2LA(~**K**) and 2LA(~**M**) as a function of the laser energy. Adapted from refs. [53] and [176].

laser energy matches the electronic transition of the material. The difference between second-order and double resonance bands, however, can be observed when several laser lines are employed to measure the Raman spectra close to the electronic transition, revealing the pattern where the dispersion of the bands can be observed.

Several works have reported the study of the double resonance process in TMDs [53,168,169,178,184,188,189]. These reports show that the double resonance bands observed in TMDs are mostly due to intervalley scattering. As it can be seen in Figure 3.6(b), the peak at around 460 cm^{-1} associated with a double resonance band is asymmetric and its shape strongly depends on the excitation laser energy and the number of layers, thus more than one process may be participating in this band [130,156,159].

The first observation of a double resonance band in bulk MoS_2 was reported by Sekine *et al.*, where the authors observed a dispersive Raman feature named as "*b*" band located at approximately 420 cm^{-1} [160]. This feature presented a high dispersion of 82 cm^{-1}/eV with the laser energy close to the *A* and *B* excitons. To explain such high dispersion, the authors proposed a mechanism considering a two-phonon scattering of one quasi-acoustic phonon and an optical phonon, parallel to the *c* axis of the crystal [160]. A similar mechanism was later proposed for the "*b*" band by taking into account the explanation of the anti-stokes process [165]. However, these models were not compatible with the observed resonant Raman spectrum of a monolayer MoS_2, which had a similar band but lacked a quasi-acoustic phonon branch. Additionally, Chen *et al.* and later Stacy *et al.* reported another band in the resonant Raman spectrum of bulk MoS_2 located at 460 cm^{-1}, the intensity, and shape of which strongly changes as the excitation energy is tuned [161,185]. This band has been attributed to a combination of two LA phonons at the **M** point. Henceforth, few other works have tried to associate this band to different combinations of phonons [186,190], but none of these works presented a satisfactory explanation of the origin of this band.

Using graphene as a starting point (appendix B), we can start to propose a better explanation based not only on the rules observed but also on other known features of the TMDs, such as their phonon dispersion and electronic structure. Considering an electron-electron two-phonon intervalley scattering from **K** to **K'** in the conduction band of MoS_2, we can ask which phonons could participate in such a process. Since, from graphene, the phonons must present strong interaction with the electron, we can suppose that the phonons involved in the intervalley scattering must be acoustic phonons, due to the strong correlation between the excitonic transitions in MoS_2 and the acoustic phonons [191–194]. This is especially true since the phonon energy that we observe experimentally is very close to double the frequencies of the LA phonons in the **K** and **M** points (Figure 2.8). This means that there could be a double resonance process occurring that actually involves those phonons.

Using the train of thought above, it was proposed in ref. [53] a model based on theoretical and experimental results to explain the origin of both *b* and 2LA bands (see Figure 3.6(b) and (c)) [53]. The authors have performed resonant Raman measurements across the *A* and *B* excitons levels on monolayer and bulk MoS_2. By tracking the behavior on frequency and intensity of the *b* and 2LA Raman bands and calculating the on-resonance electrons and phonons that participate in the scattering process, it was shown that the *b* band could be associated with a combination of phonons from the LA and TA phonon branches around the **K** point due to a double-resonance electron-electron intervalley scattering process, i.e.

LA+TA(~**K**). This process is analogous to the D+D'' band in graphene (see Appendix B), where two different phonons with the same wavevector participate in the electron scattering process.

For the 2LA band, the authors deconvoluted this broad and asymmetric band by a set of Lorentzian peaks and showed that it is composed of at least three components that can be assigned as two double resonance bands and one second-order band (see Figure 3.6(b)). The two double resonance features are associated with the electron scattering by two LA phonons at the proximities of the **K** and **M** points, which were assigned as 2LA(~**K**) and 2LA(~**M**) located around 460 cm^{-1} and 470 cm^{-1}, respectively. The second-order band is located at 452 cm^{-1} related to a singularity in the phonon density of states present due to a saddle point in the LA phonon branch between the **K** and **M** points. The above assignment was proposed due to the analysis of the observed difference in intensity band from bulk to monolayer, where the 2LA(~**M**) phonon has a higher contribution in the few-layers and bulk samples than in a monolayer sample since this process is mediated by the indirect bandgap [49,56].

The wavenumber of 2LA(~**K**) and 2LA(~**M**) decreases as the laser energy increases, this negative dispersive behavior is contrary to the observed for the 2D band of graphene but resembles the behavior of the D+D" band. The negative dispersion is a result of the wavevectors that are accessed by the excited electron as it is scattered from **K** to **K'**. The frequency of the LA branch decreases for wavevectors further from the **K** or **M** points (Figure 2.8), which will both contribute to the double resonance bands, hence resulting in a negative dispersion. To this date, the dispersive behavior in TMDs has only been reported for semiconducting MoS_2 [53].

Some works have reported the study of the Raman spectrum of MoS_2 in the UV range to gain further information about other high-order resonance processes. Sun *et al*. observed that the Raman spectrum of MoS_2 in bulk, mono-, bi- and tri-layer samples, collected with an excitation energy of 3.81 eV (see Figure 3.7(a)), present three strong bands in the 750 to 840 cm^{-1} spectral range, which were associated to combinations of E_{2g} and A_{1g} modes [74]. It was proposed that these bands are originated by a triple-resonant hole-hole Raman scattering process, where the hole would be scattered from the bottom of the spin-orbit split at the valence band to the top valence band and later recombines with the electron (see Figure 3.7(b)). Liu *et al.* have observed the presence of several new peaks between 560-820 cm^{-1} spectral range in the Raman spectrum of monolayer MoS_2 collected with a 3.50 eV laser energy [168] (see Figure 3.7(c)). The observed bands were related to intervalley scatterings between points at halfway from **Γ** to **K**, where the absorption of this laser energy is strongest according to the theoretical calculations reported (see inset of Figure 3.7(c) and Figure 3.7(d)). The observed phonons were

associated with their correct wavevectors in the phonon dispersion (see Figure 3.7(e)) [168]. A similar study has also been done recently for WS_2 [189].

Guo *et al*. investigated the Raman spectra of $MoTe_2$ using three laser lines of energy 1.58, 1.96 and 2.33 eV [169] (see Figure 3.7(f)). A set of new Raman bands were observed and associated with intervalley scattering between the proximities of **M** point (see Figure 3.7(g)). The contribution of each laser energy to the observed bands was calculated, and connected to their correct wavevectors (see Figure 3.7(h)). Although these works are promising, they are still

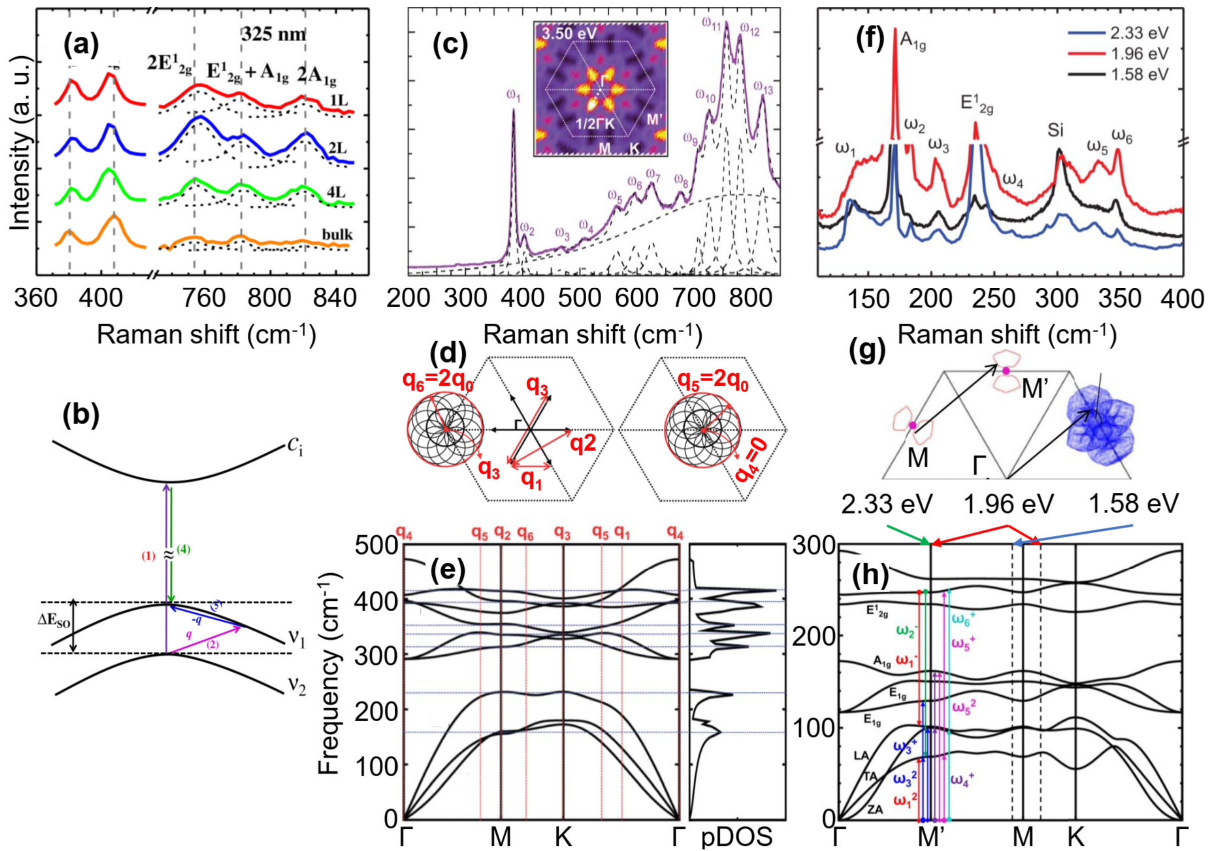

Figure 3.7. Double-resonance Raman bands above the excitonic transitions. (a) Raman spectrum of monolayer, bilayer, trilayer and bulk MoS_2 collected with a UV laser of 3.81 eV and (b) Proposed triple-resonance process. (c) Raman spectrum of monolayer MoS_2 collected with a UV laser of 3.50 eV. The inset shows the calculated absorption probability for this laser energy. (d) Proposed scattering process near the **Γ** point responsible for the observed Raman bands in (c). (e) Complete phonon dispersion of MoS_2 with the different contributions of the double-resonance bands in (c) and (d) ascribed to their respective points in the Brillouin zone. (f) Raman spectra of monolayer $MoTe_2$ collected with three different laser energies. (g) Proposed electron scattering near the **M** points for a laser energy of 1.96 eV. (h) Phonon dispersion of $MoTe_2$ with observed contributions to the Raman spectra from the three laser energies ascribed to their respective points in the Brillouin zone. Adapted from ref. [176].

in infancy since further probe by tuning the excitation laser energy and the number of layers (that helps to unveil the Raman scattering process) need to the performed for the 2D family.

Most of the works in the literature investigate the Raman spectrum of TMDs by tuning the excitation laser energy to probe the resonance effects. However, a closer inspection at the Raman intensity equations (see Equations 3.2 and 3.3) can provide more insightful thoughts regarding the Raman scattering process. The intensity can be tuned not only by changing the excitation laser energy but also by changes in the excitonic transition energy itself. Such changes in the excitonic transition energy can be achieved, for example, by in-situ variation of the sample's temperature or pressure. For instance, tuning the exciton energy for bulk MoS_2, either by temperature or pressure changes, affects the double resonance processes just as if the excitation laser energy is being tuned [165].

Recent works on monolayer MoS_2 have shown that under temperature variation the frequency position of the double resonance LA+TA(~**K**) band (i.e. the *b* band), shifts by a rate of $(\Delta\omega/\Delta T)_b$ = -0.035 cm^{-1}/K, while the first-order A'_1 mode shifts $(\Delta\omega/\Delta T)_{A'_1}$ = -0.008 cm^{-1}/K [172]. This represents a dispersive rate ratio of around 4.4 times between the double resonance and first-order bands, which is a good indicator of changes in the excitonic effects leading to the strongly dispersive behavior of the *b* band.

We end this section reminding that the strong enhancement of the double resonance Raman bands in MoS_2-like TMDs comes from resonance with the excitonic transitions. Therefore, out of resonance, the Raman bands should show little intensity, and would barely be observable, which is the case shown in Figure 3.6(a), where we compare the spectra of monolayer MoS_2 at a laser far from resonance (2.41 eV) and a laser very close to resonance with the *A* exciton (1.96 eV). These are important considerations since in the next section we will discuss defects in 2D systems, and resonance with the electronic levels of the material is fundamental to measure the contributions of defect induced bands to the Raman spectra.

3.3.2 Defective 2D material production

Controlling defects in materials is of utmost importance for the development of technology due to its role on tuning the doping concentration or carrier types, reducing contact resistance in electronic devices, and improving the responsivity, speed and operation wavelength of photodetectors in novel optoelectronic devices, such as photodetectors and LEDs [174]. Therefore, a quantitative way to control the density of defects in 2D materials is a key ingredient for the development of 2D materials technology. In this aspect, Raman

spectroscopy is a simple and non-destructive tool that allows the characterization and quantification of defects in 2D materials.

Defects can be generated either during (in-situ defects) or after (ex-situ defects) the synthesis process [173], where the latter is extended to exfoliated samples. Several kinds of in-situ defects can be generated such as vacancies of chalcogens and metals (usually accompanied by their bonds) in TMDs, anti-sites, grain boundaries, edges and line defects [195]. These in-situ defects are not controllable. However, ex-situ defects can be created in a controllable way due to the improvement of defect engineering in 2D materials. For example, electron beam irradiation [196,197] and ion (Mn+ and Ar+) bombardment [103,177] have been used to create chalcogen vacancies in TMDs, where the distance among vacancies can be controlled by the beam dosage. The same approach can also be used to create MoS_2 nanocrystallites [198]. Additionally, the introduction of vacancies by electron irradiation can be followed by doping [199]. Indeed, oxygen substitution of chalcogenides may occur in normal ambient conditions despite the slow rate of the reaction and difficulties to be controlled [200]. However, oxygen passivation of chalcogen vacancies using laser annealing has been performed in WSe_2 as an alternative, improving its conductivity and photoconductivity [200]. Besides, doping by potassium [201] was achieved before theoretical studies for alkali metals (Li, K, and Cs) doping in TMDs [202] while lithium doping has been recently done [203]. This brief defect production discussion highlights the importance of probing defects in 2D materials and how the presence of defects impacts the Raman spectra of TMDs.

Before we dive into the analysis of the defect induced processes in TMDs, we define a way to quantify the number of defects in the sample, since the Raman spectrum is affected by the number of defects present in the sample. We can use the defect density related to the fluence of ions into the samples (in order of 10^{11} to 10^{14}) [204], but most works in the literature quantify the amounts of defects by the average defect distance, $L_D = \frac{1}{\sqrt{\eta}}$ where η is the defect density [130,156,159,177,205–207].

3.3.3 Defect-induced Raman processes in TMDs

The presence of defects can impact the Raman spectrum of TMDs, but the observed impact in TMDs is far less sensitive than those observed for graphene (appendix B). For graphene, the D band can be directly observed in the Raman spectrum with L_D up to 25 nm [156,206]. Graphene is always in resonance on the NIR and the visible range, thus, most of the double resonance processes involving defects are fairly strong, in special when L_D is low enough that we can expect a big enhancement of the defect induced bands. For semiconducting

TMDs, unless the sample is resonantly excited [53,170] across the excitonic transitions, the disorder-induced bands can be barely observed. These bands are associated with the acoustic branches and can only be observed when a small L_D is reached, meaning a high defect density [170,177,198].

As the size of the analyzed crystal decreases, the selection rule for zone center phonons can be dropped. Therefore, a new domain size where L_D needs to be taken into account must be considered for confinement effects. The uncertainty principle states that the momentum uncertainty of the electron will be proportional to $(L_D)^{-1}$, which will involve phonons away from the **Γ** point. As a result, the shape of the Raman bands changes from a regular Lorentzian, related to a forced damped harmonic oscillator, to a broader and asymmetric shape. This new shape can be described by a weighted sum over all the phonons in the Brillouin zone within a Gaussian distribution related to the mean defect distance [177,198]

$$I(\omega) = \int_{BZ} \frac{\exp\left(-\left(\frac{qL_D}{2\alpha}\right)^2\right)}{\left(\omega - \omega_{Ph}(\boldsymbol{q})\right)^2 + \left(\frac{\gamma}{2}\right)} d\boldsymbol{q} \quad (3.4).$$

The α parameter is a constant that relates the mean defect distance to the phonon confinement length by defects or microcrystalline size, $\omega_{Ph}(\boldsymbol{q})$ is the phonon branch frequency and γ is a broadening factor that increases as the defect mean distance decreases. This model can be used to describe the disorder in several systems other than TMDs, as it has already been used for graphene and graphite [204,205], silicon [208,209] and GaAs [210].

The first-order bands are also affected by increasing the disorder density. The effects observed are frequency shifts and an increased broadening in contrast to pristine samples. Figure 3.8(a) shows the non-resonant Raman spectrum of semiconducting MoS_2 monolayers with different L_D. We can clearly observe how the first order E' and A_1' modes are altered. A new peak associated with the defect induced LA-mode is also observed [163,164]. This defect induced peak is located at around 230 cm^{-1}, half the frequency of the 2LA band [163,164].

The shift and increased broadening observed in the Raman spectrum of MoS_2 are related to a smaller phonon correlation length L_C, which is a measure of the phonon confinement by defects or microcrystallite size, and it is proportional to the L_D parameter.

In order to relate L_D with the intensity ratio between the LA band and the first-order E' band, it was used a formula based on the works done on defective graphene [177] (see Appendix B):

$$\frac{I(LA)}{I(E')} = \frac{C(E')}{L_D^2}, \quad (3.5)$$

Where $C(E')$ is a fitting parameter equal to 1.11±0.08 nm². Similar to graphene, the intensity ratio of the disorder-induced LA band and the first-order modes A₁' and E', i.e. $\frac{I(LA)}{I(E')}$ and $\frac{I(LA)}{I(A_1')}$, can provide a way to quantify the amounts of defects (see Figure 3.8(b)) [177]. This has also been observed by Li-doped MoS_2 monolayer samples, where the LA band is rapidly intensified for increasing lithium exposure time [203].

One important remark is that the disorder-induced LA band is composed of at least three components: LA(~**K**), LA(~**M**) and a band associated with a singularity from the phonon density of states (Figure 3.8(c)). The peak position of these Raman bands presents half the frequency of the bands composing the 2LA band. Therefore, the LA(~**K**) and LA(~**M**) modes

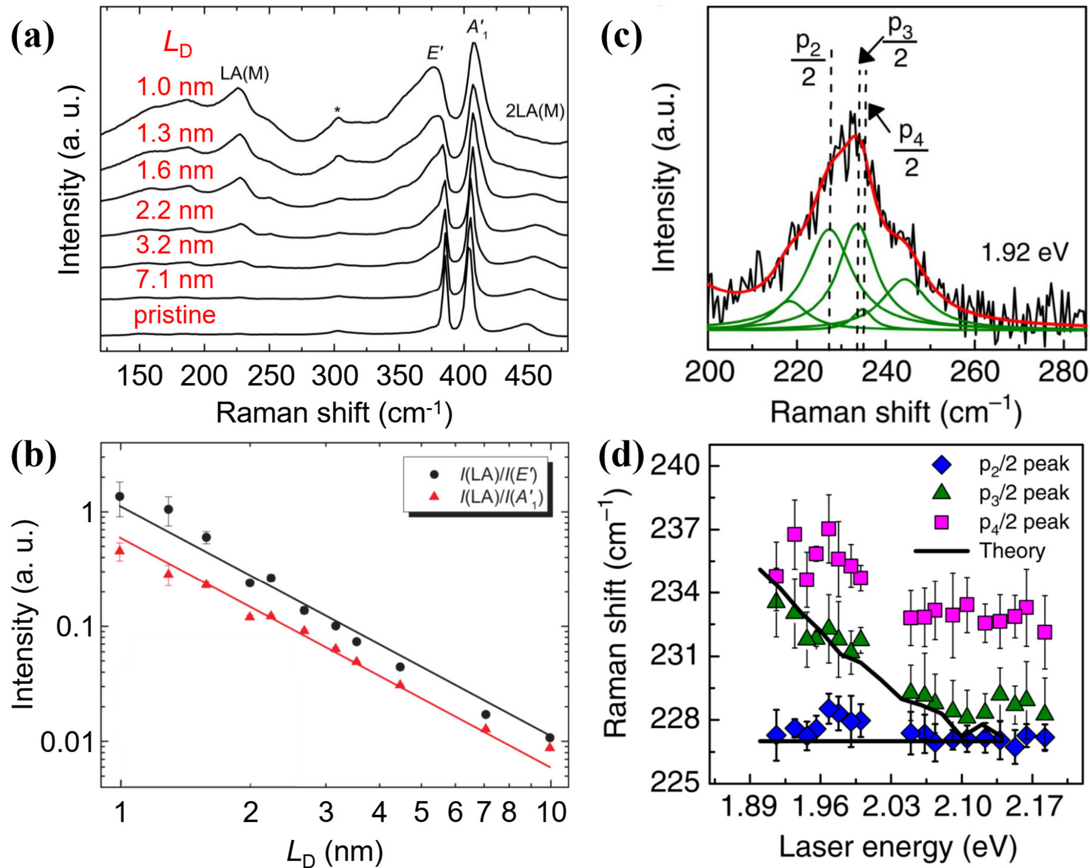

Figure 3.8. Phonon-defect Raman spectrum of monolayer MoS_2. (a) Raman spectrum of monolayer MoS_2 for different values of L_D collected with a 2.41 eV laser. (b) Intensity ratio between the LA band and the A' and E' bands as a function of L_D. The observed line is a fit with a curve proportional to $(L_D)^{-2}$. Deconvolution of the defective LA band in monolayer MoS_2. (d) Frequencies of the LA band components in (c) as a function of the laser energy. Adapted from ref. [176].

also present a dispersive behavior with the excitation laser energy, following a similar trend as the dispersive two-phonon features composing the 2LA band [53]. The observation of these three components in the defect induced LA band, and the fact that these components present half of the calculated dispersion of the 2LA(~**K**) and 2LA(~**M**) bands, further strengthens the intervalley double resonance scattering model claim proposed in ref. [53] for semiconducting MoS_2 (see Figure 3.8(d)).

To the best of our knowledge, such a detailed analysis of the double resonance process in defective TMDs sample was only explored for the MoS_2. Recently, however, it was reported the presence of two new bands in the tip-enhanced Raman spectrum of a defective WS_2 sample, called D and D' [211]. The appearance of these new bands was related to an increased number of sulfur vacancies, and the D band was associated with the A_1' phonon branch. The D' band was associated with the infrared active A_2" [211]. This study, however, was a single laser line study of the Raman spectrum of WS_2, and the only one so far about this material where defect induced bands appear.

There are a few other works that have measured the contribution of the defect induced bands in the Raman spectrum of semiconducting TMDs [170,177,198]. These works reported changes to the observed spectra related to different wavevectors accessed by the high density of defects present the samples. More importantly, they have observed mainly changes around the first-order modes, which means that the main contributions are related to optical phonons.

In this chapter, we have discussed the double resonance Raman bands in 2D materials. We have focused on the state-of-art among the 2D materials, semiconducting MoS_2. We have explained the most pronounced bands that arise from the electron-electron, electron-hole and hole-hole Intra and Intervalley scattering process. These scattering processes allow phonons at the Brillouin zone edge to participate in the scattering where the momentum conservation is preserved by a two-phonons or phonon-defect processes. Such processes allow the observation of the D, D', D+D", 2D and 2D' Raman bands of graphene mediated by phonons at the vicinity of the **K** and **Γ** points (appendix B). Whereas the electron-electron intervalley scattering allows the observation of the LA, *b* and 2LA Raman bands in MoS_2 mediated by phonons near the **K** and **M** Brillouin zone edge points.

There are other few works on the study of the double resonance Raman bands in other TMDs providing insights on the scattering process. However, up to this date, the detailed analysis of the double resonance Raman process has been described only for the semiconducting MoS_2. The latter has shown that a more in-depth resonant Raman study for the other materials is still needed to properly observe the possible double resonance contributions

in the Raman spectrum of the other TMDs. In particular, the study of other classes of TMDs is lacking, especially those with high anisotropic optical properties such as ReS_2 and $ReSe_2$ [212,213]. It could be very interesting to observe the possible behavior of double resonance bands of these materials, even though their optical transitions are very far from the most common lasers used in the collection of the Raman spectrum at 1.3 to 1.5 eV [212,213].

A recent study of bulk black phosphorous has observed the presence of several small intensity bands that were ascribed to two-phonon bands [214]. The intensity of these bands reaches a maximum close to a laser excitation energy of 2.4 eV, indicating the presence of an electronic transition [214]. It remains to be seen whether the same effect will be visible in a single layer, or even few-layers samples. One study has observed the presence of new bands in defective mono and few-layers of black phosphorus which were assigned to phonon-defect intravalley processes [215]. Although, in comparison with graphene, more works should be done in order to asses some other possible effects that could be present.

The emerging of new 2D materials shows that the field on double-resonant Raman process is still in progress and more work needs to be done for a deeper understanding of the underlying physics of the double resonance process in other materials. The double resonance Raman mechanism provides important information for the understanding of the photo-physics of 2D materials, the quantification of defects and to describe the inter- and intra-valley scattering of electrons essential for the development of the spintronics and valleytronics.

In chapter 5, we deal with the double resonance processes in TMDs changing both the laser and temperature, where the resonance with the excitonic transition is tuned in order to observe a similar phenomenon as the laser tuning. We also observe how the excitonic transition affects the double resonance processes and how the defect induced bands in TMDs are severely affected by temperature.

4. Sample production methods and experimental setup for spectroscopic measurements

In this chapter, we present the experimental methods for the development of this thesis including the sample preparation methods and details about the optical measurements. We begin with a brief explanation of the micromechanical exfoliation and chemical vapor deposition processes and move to describe the experimental setups used for the resonant Raman and photoluminescence experiments. We finish this chapter with the optical characterization of the samples investigated in this work.

4.1 Production of TMDs via micromechanical exfoliation and chemical vapor deposition

Samples used in the experiments carried in our work were produced by two different methods, micromechanical exfoliation and chemical vapor deposition (CVD). From the two possible sample fabrication processes, we start with micromechanical exfoliation since it provides the samples with the best quality possible, and there is the possibility of observing samples with more than one layer. The disadvantage of micromechanical exfoliation is the size of the samples obtained by this method, which are generally no bigger than a few tens of micrometers.

Starting from a bulk crystal, an adhesive tape is used to remove a thinner piece from the crystal, which is still much thicker than a single layer from the TMDs and can be considered a bulk crystal. The thin crystal stays in the adhesive tape due to the weak van der Waals binding energy between the layers composing the crystal. Afterward, the piece of the crystal in the adhesive tape is subjected to several cycles like the one presented in Figure 4.1(a), where the tape is used continuously glued to the thin crystal to further exfoliate the layers. After some cycles, some few-layers can be isolated from the thin crystal, such as it is represented in Figure 4.1(b). The few-layers are glued to a suitable substrate, like silicon with a 300 nm silicon oxide layer, which is presented in Figure 4.1(c). After the tape is removed from the substrate, a single layer can be isolated and the sample is ready for optical characterization and applications. Figure 4.1(d) presents an exfoliated sample of WS_2, where we see that a small portion of the exfoliated sample is actually the monolayer, while the biggest portion of the exfoliated sample is a multilayer crystal that behaves similarly to a bulk crystal. Samples produced via this method present properties compared to pristine bulk crystals, since they come directly from a bulk crystal. However, the samples are small for large scale applications, about tens of micrometers,

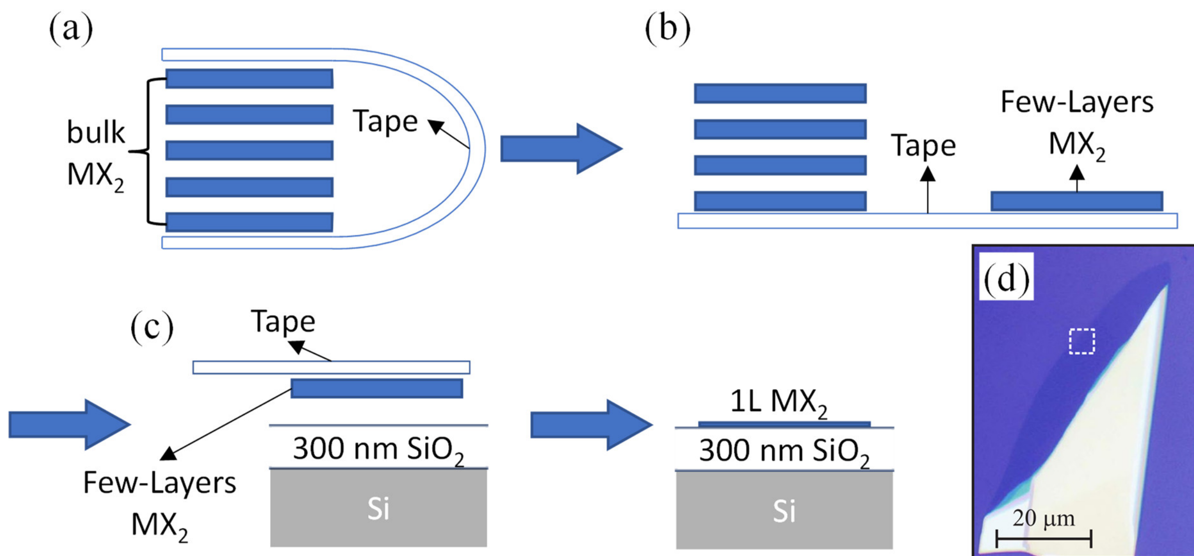

Figure 4.1. Micromechanical exfoliation from a bulk crystal. (a) A thin crystal is placed in adhesive tape, and the tape is continuously glued on top of the crystal in order to exfoliate the thin further, until a single layer from the crystal is isolated, like it is shown in (b). (c) The isolated crystal in (b) is transferred to the silicon substrate with a 300 nm thick SiO_2 layer and we are left with a single layer on top of the Si/SiO_2 substrate. (d) Representative exfoliated sample of WS_2, where the dotted square is a monolayer, while the yellow crystal would be a multi-layer sample, comparable to a bulk crystal. (d) is adapted from ref. [219].

since the interaction between TMDs and substrates like silicon with silicon oxide is not as strong as it is for graphene, for instance [216]. Going to other substrates like gold can improve the size of the exfoliated monolayers greatly though [217,218], but the method is not as easily available as the adhesive tapes generally used.

The CVD method, on the other hand, can produce monolayers of an average size above 50 μm, but the crystals produced are not of as good quality as the ones obtained via micromechanical exfoliation. There are several methods for the CVD growth of TMDs [220–226], but they are generally based on the same process, where a transition metal precursor is reacted with a chalcogen precursor in the surface of a substrate to produce atomically thin TMDs.

We illustrate in Figure 4.2 the processes used for the sample growth procedures in this work. First, the transition metal source is placed in a substrate, either in a powder form, molybdenum (MoO) or tungsten oxides (WO), or as a small drop of a solution made with a water-soluble precursor, ammonium Heptamolybdate (AHM) or ammonium Metatungstate (AMT), such as it is shown in Figure 4.2(a). The solution-based method also involves an additional step where the substrate is first covered in a growth promoter solution of a sodium-based surfactant such as sodium cholate (SC) or sodium dodecyl sulfate. The substrate is loaded

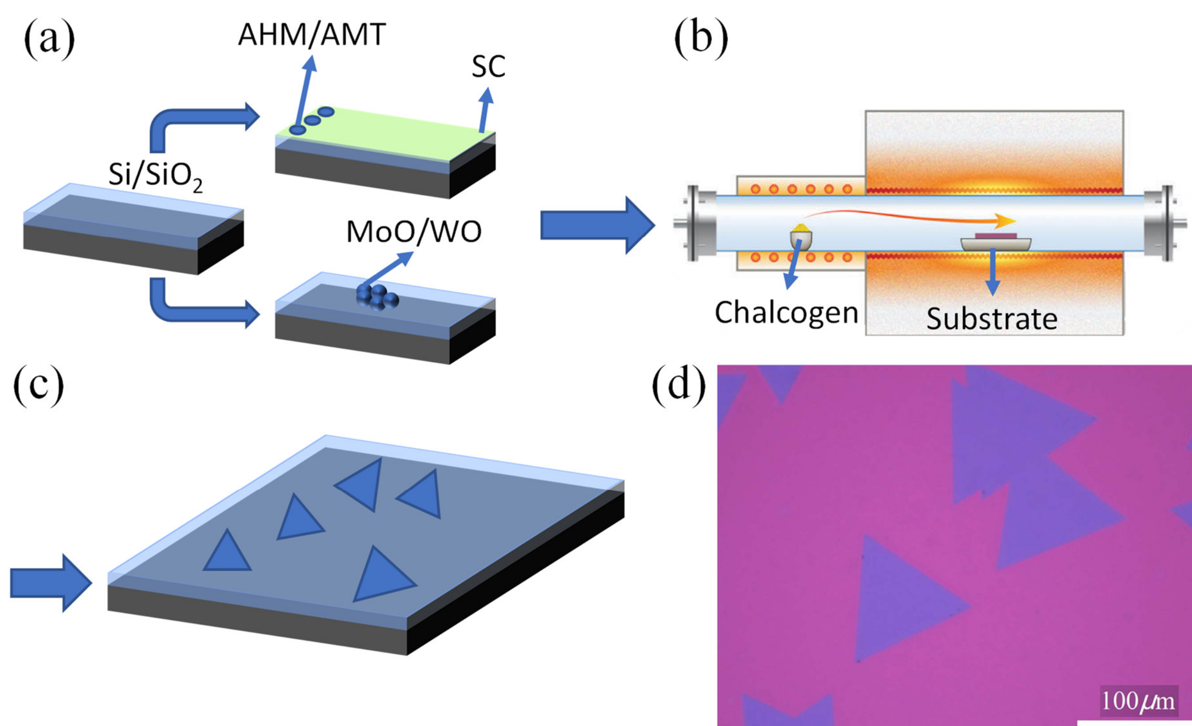

Figure 4.2. CVD growth methods used in this work. (a) The silicon with a 300 nm silicon oxide layer can be covered with SC, and then a small amount of an AHM or AMT solution may be dropped on it, or a solid precursor can be placed onto the substrate directly. (b) Following the substrate preparations, the substrate is loaded into a quartz tube, which is placed in a furnace such that the substrate is located in the hot zone of the furnace. The chalcogen precursor is placed at the edge of the quartz tube, and it is transported toward the substrate as it sublimates during heating. (c) After the heating phase, the triangles are formed in the substrate with different sizes and orientations. (d) Representative image of a CVD growth of WS_2 monolayers. (d) is adapted from ref. [227].

in an alumina boat, which is placed in the center of a quartz tube with approximately 2 cm of diameter, which is loaded in a furnace, such that the alumina boat is centered in the furnace hot zone. At this stage, the chalcogen precursor is placed near the edge of the quartz tube, which is sealed from both sides in order to be purged with an inert gas such as argon or nitrogen. Finally, both the substrate and the chalcogen precursor are heated, in order to allow the reaction between the transition metal and the chalcogen, which is transported via the gas flow, which is illustrated in Figure 4.2(b). The temperatures reached by the substrate and the chalcogen vary according to each case, as we will discuss further on. In the end, triangles of the TMDs are grown with random orientations as it is illustrated in Figure 4.2(c), and the lateral sizes of the triangles depend on a diversity of parameters that are beyond the scope of this work. Figure 4.2(d) shows triangles of WS_2 grown by a CVD method, where the lateral size of the sample is about ten times bigger than the lateral size of the monolayer sample obtained by micromechanical exfoliation Figure 4.1(d).

The CVD method allows us to obtain grains, or flakes, much bigger than the ones we would be able to obtain via micromechanical exfoliation. Recent works have even made it possible to cover whole silicon wafers 2.5 to 10 cm in diameter [228–230].

4.2 Spectroscopic setup

In order to measure the Raman and photoluminescence spectrum of our samples, we need to use a spectrometer since the Raman, PL and elastic scattering signals are all mixed, as it is illustrated in Figure 4.3(a). The spectrometer will divide the signal coming from the sample due to the elastic scattering of the laser used, from the PL emission and Raman scattering. We used either a Horiba T64000 or a LabRAM HR spectrometers, where the T64000 spectrometer can be set up to work in either single grating or triple grating configurations. We briefly explain the mechanism behind the spectrometer operation.

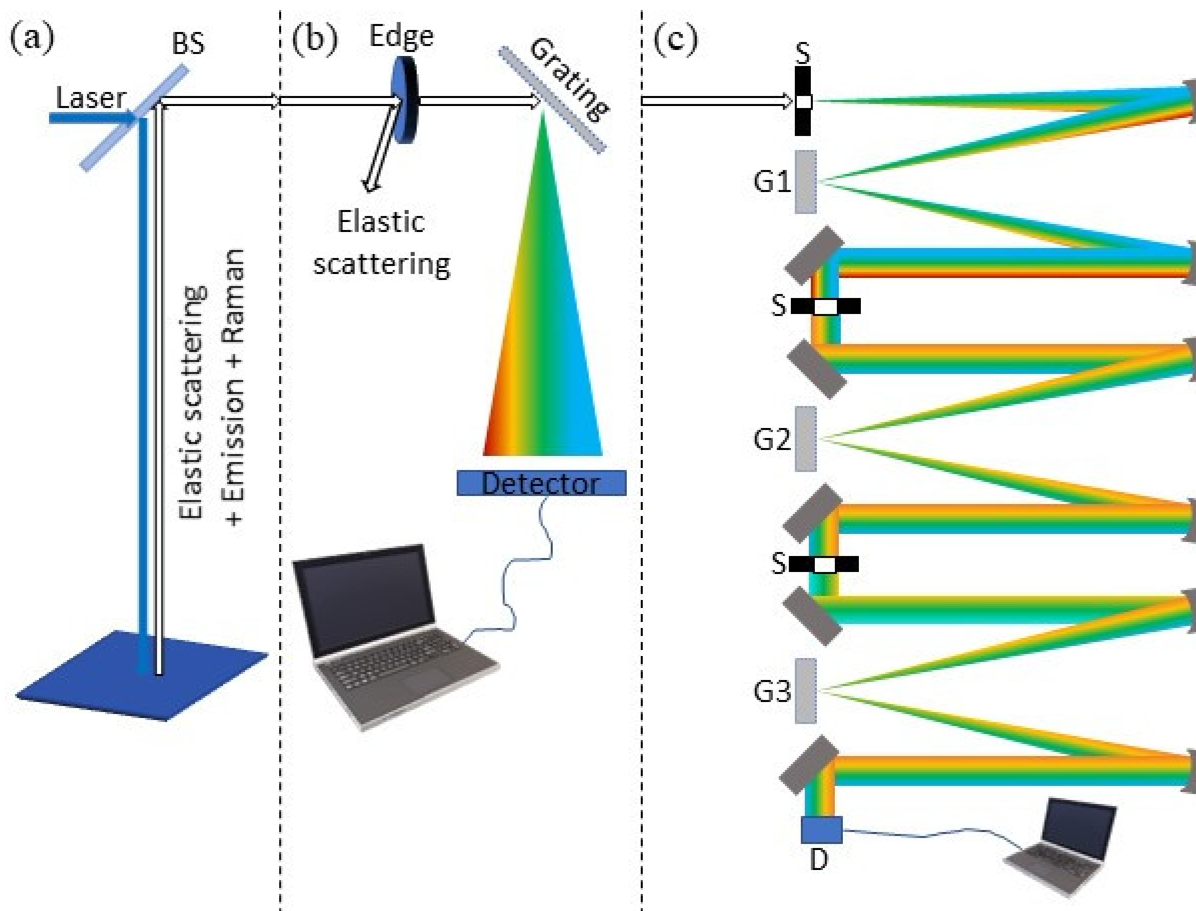

Figure 4.3. The functioning mechanism for a spectrometer. (a) The light emission coming from a sample illuminated with a high energy laser will generate three signals, mostly, the elastic and Raman scatterings and the PL emission from the sample. The signals are mixed and need to be separated in order to be analyzed. (b) Single grating configuration, where the light coming from the sample is filtered with either an edge filter or a notch filter to remove the elastic scattering of light, and it is directed to the diffraction grating. (c) Triple grating configuration, which is used in the case where the laser line cannot be filtered with an edge or notch filter.

In the single grating configuration, illustrated in Figure 4.3(b) the light goes from the sample directly to the grating before the CCD, called the spectrograph. The signal that reaches the CCD detector in this configuration is stronger than in a triple grating configuration but edge filters are necessary to reduce the excitation laser due to the reflection and elastically backscattered light from the sample, much stronger effects than the signal emitted by the sample. Therefore, the single grating configuration limits the use of any laser available to only those that have appropriate edge filters. There is also the commitment to the low-frequency range of measurements since the edge filter will also filter a small range of wavelengths bigger than the excitation wavelength. The anti-stokes range is also affected since it is not possible to cut only the laser line with edge filters. An alternative to edge filters would be the super notch filters, which can cut only the laser wavelength and work at up to a 5 cm^{-1} frequency range, which was used in the LabRAM HR spectrometer for a He-Ne laser. But it is a very expensive filter not available for every laser.

In order to filter the light near the excitation laser for any laser that does not have an edge filter, the most reliable way is to use a triple grating setup, illustrated in Figure 4.3(c). In this case, the two gratings are used to separate the light coming from the sample, which is filtered spacially via slits present in the spectrometer, in such a way that the excitation laser is filtered by these gratings. In a triple grating configuration, we can use any available laser without any compromises to the low-frequency range or anti-Stokes scattering. The intensity will be affected though, which will increase the time required to measure the Raman spectrum. Thus, we use the available edge filters when convenient, especially with the Ar-Kr laser, and in case it is not possible, such as the tunable lasers, we use a triple grating configuration.

The type of gratings used for each experiment also varies from case to case. In order to measure the Raman spectrum, we want the best possible resolution. The resolution of a spectrometer, $\delta\lambda$, can be defined in terms of the following equation

$$\delta\lambda = \frac{W \times d}{f} \tag{4.1}$$

Where W is the pixel size in the detector which is about 26 μm, d is the distance between two consecutive grooves and f is the focal length of the spectrometer. Since the entrance slits of the T64000 and LabRAM HR spectrometers are the same, about 100 μm, the only difference between them will be the focal distance and the gratings used in each one. The T64000 spectrometer has a 64 cm focal length, while the LabRAM HR spectrometer has an 80 cm focal length. A bigger focal length will increase the distance that light travels in order to reach the

CCD, increasing the line separation due to diffraction. Thus, the LabRAM HR spectrometer provides a better resolution than the T64000 spectrometer for the same grating. The gratings used in our work have a groove density of 600 gr/mm and 1800 gr/mm, translating to about a 0.07 and 0.02 nm resolution, respectively, for the T64000 spectrometer. The resolution is slightly better for the LabRAM HR spectrometer since the focal length is also bigger. These resolutions in the wavelength domain can be translated to a resolution of about 2.8 cm^{-1} and 0.8 cm^{-1} for a laser wavelength of 500 nm in the frequency domain for the 600 and 1800 gratings, respectively. The advantage of using 600 gr/mm grating is the spectral range covered by the grating compared to the 1800 gr/mm grating, which should be about 3 times bigger. Therefore, for experiments where a high spectral coverage is needed while the spectral resolution is not a priority, such as PL measurements, the 600 grooves/mm is a better choice than the 1800 grooves/mm. On the other hand, if a high spectral resolution is necessary, such as Raman spectroscopy, the 1800 grooves/mm grating is the obvious choice. Therefore, except where we explicitly indicate, the PL measurements were carried with the 600 grooves/mm grating while Raman experiments were carried with the 1800 grooves/mm.

Table 4.1. Laser sources with the models in parenthesis and the respective wavelengths used. We also convert the laser wavelengths into energy, which we use in the following chapters.

Laser source	Wavelength (nm)	Energy (eV)
Ar-Kr (Coherent Innova 70C)	647.1	1.92
	568.2	2.18
	530.9	2.34
	514.5	2.41
	488	2.54
	457.9	2.71
He-Ne (REO)	632.8	1.96
He-Cd (Kimmon IK5751I-G)	441.2	2.81
Coherent 899 ring Dye laser (DCM)	640 - 628	1.94 - 1.97
Coherent 899 ring Dye laser (Rhodamine 6G)	610 - 562	2.03 - 2.21
Ti-Sapphire (Spectra-Physics model 3900S)	747	1.66

The laser energies that were used in this work vary from 1.66 eV to 2.81 eV, corresponding to wavelengths of 747 to 441.6 nm. Thus, we use several laser sources listed in table 4.1. The Coherent Innova 70C Ar-Kr laser provides a wide range of laser energies from 1.92 to 2.73 eV. The REO He-Ne laser provides a 632.8 nm laser line. The Kimmon IK5751I-G He-Cd provides the 441.6 and 325 nm laser lines. We also use a Coherent 899 ring dye laser optically pumped with a Coherent Verdi V6 laser emitting at 532 nm with 6 W, that can be combined with solutions based in the DCM and Rhodamine 6G dyes to provides a continuum selection of lasers ranging from 650 to 560 nm, which depends on the dye solution used. A Spectra-Physics model 3900S Ti-Sapphire laser pumped by a Verdi G with 10 W is also used for an IR emission.

In order to change the sample temperature, we used a Linkam THMS600, which uses liquid nitrogen as a cooling source. The samples were placed on top of a silver ceramic holder, which is cooled by the liquid nitrogen flow due to a pump, cooling the sample on top. In order to remove the humidity around the sample, the sample container is purged using nitrogen that comes from the liquid nitrogen pump, in such a way that the sample is under a nitrogen atmosphere during the low-temperature measurements.

For the intensity calibration of the Raman spectrum of the samples, we use two possible procedures. The first procedure used for MoS_2 is to normalize the intensity of the Raman spectra obtained at different laser energies and temperatures with the intensity of the E' or the E_{2g} band. This procedure is validated since we are only concerned with laser energies close to the energy of the A and B excitonic transitions, that only couple with the A_1' band and show no intensity enhancement for the E' band in MoS_2, as we discussed in section 3.2. The second procedure, that we use for the other samples, is to normalize the spectra by the intensity of the silicon peak at 521 cm^{-1}. The intensity of this mode was previously studied under the illumination of several laser energies in the range between 1.58 and 2.81 eV, and it was found that its intensity increases at a rate different from the expected ω^4 [231]. In fact, the intensity of the first-order silicon peak increases following the increasing value of the dielectric constant, which has a peak at 3.4 eV according to the values presented in ref. [232], but it was found at slightly smaller energy, at 3.35 eV, in ref. [231]. Nonetheless, the absolute cross-section of the first-order Raman peak of silicon was measured in this range. It can be used as a standard for calibration by normalizing the spectra acquired by the intensity of the silicon Raman peak, followed by the multiplication of the intensity by the absolute Raman cross-section obtained by ref. [231].

4.3 Optical characterization of the samples

The samples used in this work were first characterized by optical images, PL and Raman spectroscopy, which are usual techniques for the optical characterization of monolayers of TMDs. We present a brief characterization section of the samples used in this work.

4.3.1 Micromechanical exfoliation of MoS_2

For the sample obtained via micromechanical exfoliation, we proceeded with the optical characterizations via Raman and PL spectroscopies. The samples of exfoliated MoS_2, monolayer, few-layers and bulk were provided in collaboration with the Laboratory of Nanomaterials and were produced by the student Andreij Gadelha.

Our monolayer samples were prepared via mechanical exfoliation from bulk MoS_2 crystals and transferred to silicon substrates with a 285 nm oxide layer. The monolayer is confirmed due to the separation of 19 cm^{-1} between the A_1' and E' Raman bands located at 406 and 387 cm^{-1}, in contrast to the separation of 22 cm^{-1} observed in bilayers, where the A_1' and E' bands are located at 408 and 385 cm^{-1}, observed in Figure 4.4(a). The strong PL signal, observed in Figure 4.4(b), also confirms the monolayer attribution. An optical image of the exfoliated monolayer can be observed in the inset of Figure 4.4(b), where the position of our measurements is marked by the black dot.

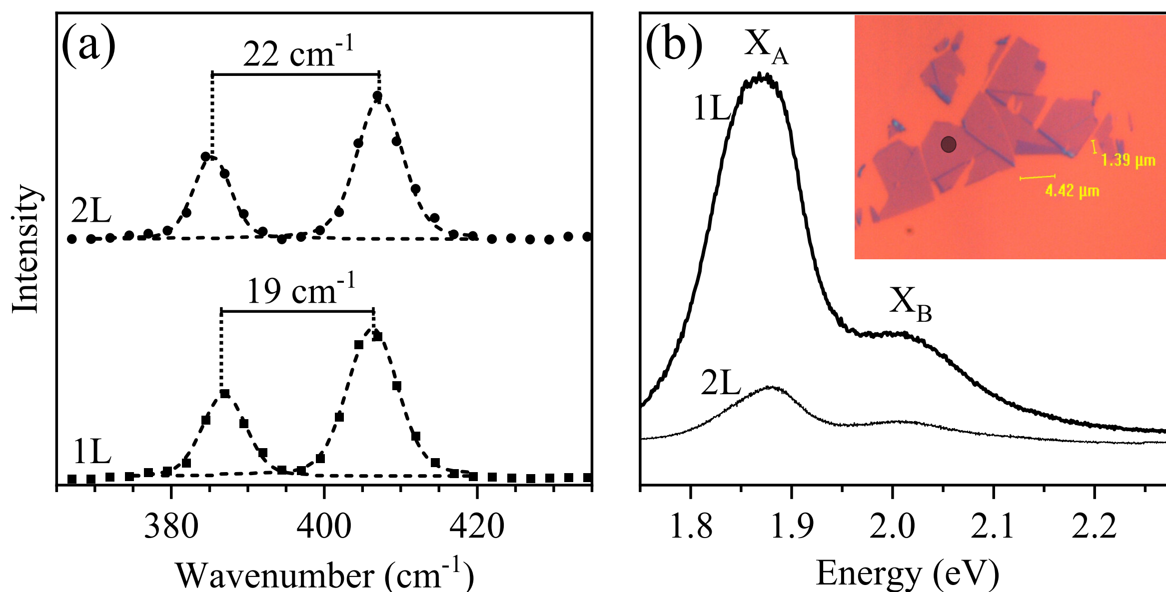

Figure 4.4. (a) Raman spectrum of the monolayer MoS_2 measured in this work (1L) in comparison with the spectrum of a bilayer MoS_2 (2L) obtained with a 2.41 eV laser. (b) PL spectrum obtained with a 2.41 eV laser and optical image (inset) of the exfoliated monolayer (1L) and bilayer (2L) samples. Both measurements were carried at room temperature and standard laboratory conditions.

Our few-layers and bulk samples were exfoliated from bulk crystals of MoS_2 to flakes approximately 50 nm high in adhesive tape and transferred to silicon substrates with 285 nm oxide layers.

4.3.2 CVD grown MoS_2 samples by the sodium cholate assisted method

The CVD grown MoS_2 monolayers of MoS_2 used in this work were produced during my sandwich internship period in the Pennsylvania University in collaboration with the Terrones Group.

The CVD growth procedure for our MoS_2 samples consists of spin-coating the substrate (1 cm x 1 cm silicon with 300 nm oxide layer) with a 2% wt sodium cholate solution at approximately 3000 RPMs. Following, 3 µL of a 60 µM solution of ammonium Heptamolybdate is dropped at the corner of the substrate. The substrate is put in the middle of a quartz tube with a boat containing approximately 300 mg of sulfur at the edge. The tube is then placed in a furnace and a sealed to permit argon flow through the tube for approximately 15 minutes. Afterward, the furnace is set to heat to 800 °C, for approximately 30 minutes, heating the substrate, while the boat containing sulfur is set to reach 220 °C. Following the 30 minutes, the furnace is set to cool down to room temperature. We end up with MoS_2 flakes varying in diameter between 10 to 60 µm, as presented in Figure 4.5(a).

Figure 4.5(a) presents the PL measured of one of the flakes grown with the method above. A sharp and strong peak centered around 1.82 eV can be observed. Figure 4.5(b) presents

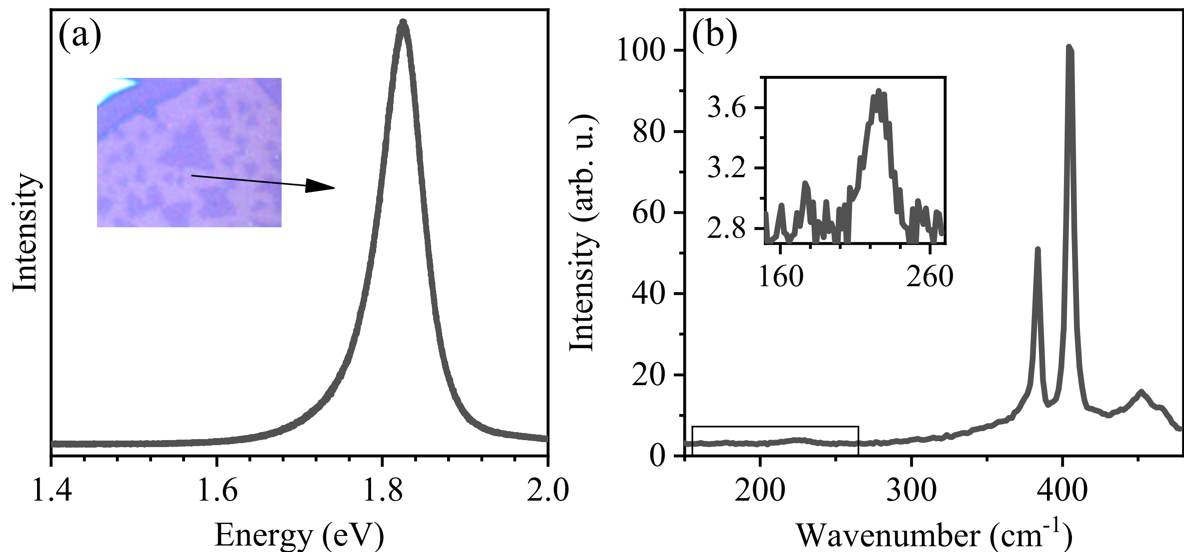

Figure 4.5. (a) PL measurement of one of the grown CVD MoS_2 flakes. The inset is an optical image of the sample in the same Si/SiO_2 substrate used for growth. (b) Raman spectrum of the monolayer measured in (a). The inset is the signal from the LA band. Both measurements were carried under a 2.41 eV laser illumination.

the Raman spectra of the monolayer sample measured in Figure 4.5(a) collected with a laser excitation energy of 2.41 eV. We observe two strong peaks centered around 386 and 406 cm^{-1}, corresponding to the E' and A_1' bands of a monolayer. We also observe a small LA band around 230 cm^{-1}. We can extract the approximate value of L_D using the relation [177]

$$L_D = \sqrt{C(E^{'}) \frac{I(E^{'})}{I(LA)}} \tag{4.2}$$

Where $I(E^{'})$ and $I(LA)$ correspond to the intensities of the E' and LA bands, respectively, and $C(E^{'}) = 1.11 \pm 0.08\ nm^2$ is a fitting parameter obtained in reference [177] for the 2.33 eV laser at room temperature. Using equation 4.2, and the intensity ratio of approximately 60, we arrive at $L_D = 8.6 \pm 0.6\ nm$, which is a small value considering the results from Figure 3.8(a) [177], where a sample with $L_D = 7\ nm$ is very similar to a pristine sample, considering the measured Raman spectrum in both cases.

4.3.3 CVD grown WS_2 and $MoSe_2$ samples

The CVD grown WS_2 and $MoSe_2$ samples were provided in collaboration with the Terrones group from the Pennsylvania University and were produced by the former student Bruno Ricardo Carvalho.

Triangular monolayers of WS_2 were grown by chemical vapor deposition (CVD) at atmospheric pressure at 700 °C on a Si substrate with a 300 nm oxide layer. 10 mg of WO_3 (Alfa Aesar, 99.998%) was placed directly onto a SiO_2 substrate, and another substrate was placed directly on top of the first one and then placed inside of a quartz tube with 2 cm diameter. 400 mg of sulfur (Alfa Aesar, 99.5%) was placed on an alumina boat at the edge of the quartz tube, where it was heated independently. The substrates at the center of the quartz tube were heated to 700 °C, while the sulfur boat was heated to 250 °C. The quartz tube was kept sealed and under argon flow at 200 standard cubic centimeters per minute (sccm) as a carrier gas. Monolayer WS_2 samples grew on both the bottom and top substrates [233]. Monolayers $MoSe_2$ were also grown by CVD at atmospheric pressure at 750 °C using selenium pellets (99.9%, Sigma Aldrich) and molybdenum oxide (99%, Sigma Aldrich) powder placed into the same alumina boat. A constant flow of 50 sccm of a mixture of argon and hydrogen was used as the carrier gas and reducing atmosphere [234]. The as-grown WS_2 flakes on a SiO_2/Si substrate were transferred onto CVD grown monolayer $MoSe_2$ on SiO_2/Si substrate by polymethylmethacrylate-assisted wet transfer [235]. Then, the WS_2/$MoSe_2$ heterostructure

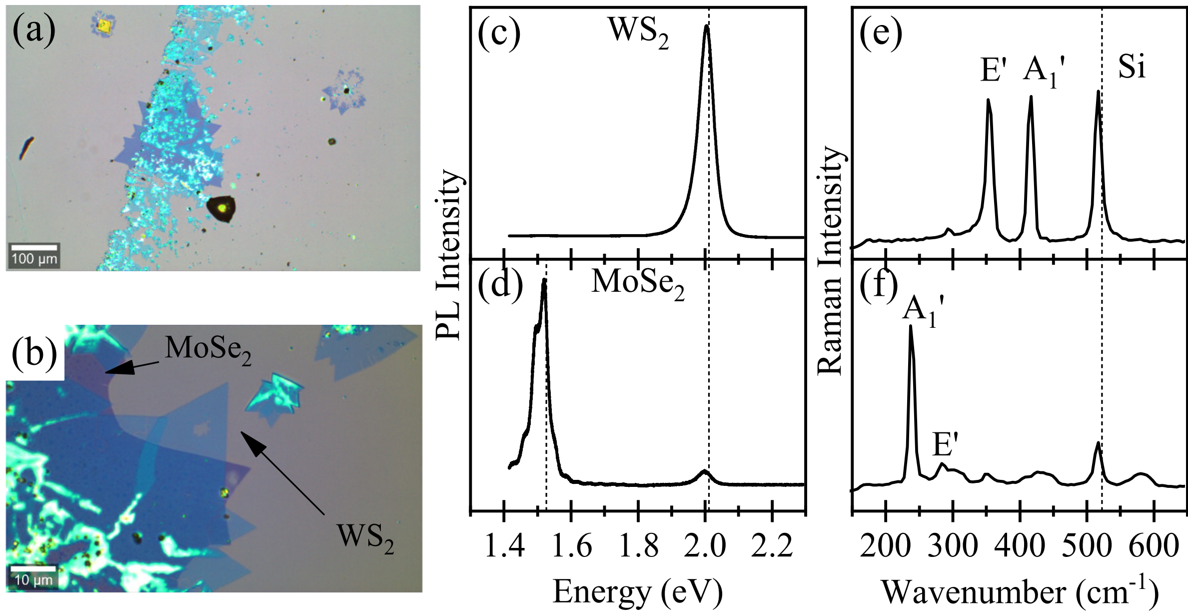

Figure 4.6. Optical characterization of the WS_2/$MoSe_2$ heterostructure. Optical image taken with (a) a 10x objective and (b) a 100x objective. PL spectra of (c) WS_2 and (d) $MoSe_2$. Raman spectra of (e) WS_2 and (f) $MoSe_2$.

sample was annealed at 700 °C for 3h in an Ar atmosphere to enhance the interlayer coupling [236,237].

Figure 4.6 shows the optical characterization of the individual WS_2 and $MoSe_2$ monolayers at room temperature using a 2.71 eV laser. In Figure 4.6(a), we see the big $MoSe_2$ flake, purple-colored, with the WS_2 flakes on top, in a light blue color. Figure 4.6(b) shows a region of the heterostructure where we can see a separate region for the single WS_2 and $MoSe_2$ flakes, indicated by the arrows.

Figure 4.6(c) and (d) show the PL of WS_2 and $MoSe_2$, respectively. For WS_2, we can clearly observe the excitonic transition corresponding to the A exciton (X_A) at approximately 2.00 eV, while for $MoSe_2$, X_A can be observed at 1.52 eV, which is in clear agreement with the values observed in the literature for these two materials grown under these experimental conditions [233,234].

Figure 4.6(e) and (f) show the Raman spectra of WS_2 and $MoSe_2$, respectively, where the first-order Raman bands can be observed. As we have discussed before in section 2.1, the frequency of the first-order out-of-plane A_1’ band depends mostly on the inverse of the mass of the chalcogen atom composing the TMD, since the vibrational motion can be reduced to a spring-mass system connected to a wall. Therefore, the A_1’ band frequency for WS_2 is more energetic than for $MoSe_2$. The first order E’ band depends on the mass of both transition metal and chalcogen, where we reduced the crystal motion to that of two masses connected by a spring, meaning that both the transition metal and chalcogen are significant for the frequency

of the E’ mode, proportional to the inverse of the reduced mass of the components. Therefore, the E’ mode for WS_2 is still more energetic than the E’ mode for $MoSe_2$.

5. Temperature dependent Resonant Raman measurements in MoS_2

In this chapter, we begin exploring the experimental results obtained in this work for monolayer, few-layers and bulk MoS_2. We introduce the results obtained for MoS_2, which has already been explored in many works and forms the basis for other similar 2D materials. First, we explore the double resonance process tuned by the laser energy and temperature in monolayer. We apply the same analysis to bulk, comparing the results for both monolayer and bulk MoS_2. In the bulk section, we also explore the subject of the other Raman bands observed, focusing mainly on the dispersive bands. We finish by approaching the effects of defect induced Raman bands and how temperature is of the utmost importance for its observation.

5.1 Monolayer MoS_2

The Raman spectrum of TMDs can be strongly affected by temperature. In fact, since the temperature will affect the excitonic transitions present in these materials, the resonance conditions observed by a certain laser energy will shift when the temperature is changed. Thus, there can be a strong effect on the spectrum of TMDs due to the resonance window shifts because of temperature effects [165]. Here, we explore this subject in depth for monolayer MoS_2.

5.1.1 First-order, second-order and Double-resonance Raman bands

Figure 5.1(a) shows the Raman spectra of monolayer MoS_2 at different temperatures and excited by a laser with an energy of 2.03 eV, in the spectral range between 350 and 485 cm^{-1}. At 93 K, the first-order modes A_1' and E' appear at 408 and 388 cm^{-1}, respectively, and they are indicated by arrows. The other bands observed in the range 420-480 cm^{-1}, and the band at 380 cm^{-1} are originated from combinations of the longitudinal and transversal acoustic (LA and TA) phonons near the zone edges, as it will be explained afterward.

Figure 5.1(b) shows the Raman spectra of monolayer MoS_2 at T = 80 K, but now using different laser excitation energies. The frequency of the first-order E' and A_1' modes for monolayer samples do not depend on the laser energy. On the other hand, the position and shape of the other features in the range 420-480 cm^{-1} are strongly dependent on the laser excitation energy. The dependence of band wavenumbers on the laser excitation energy is a signature of a double-resonance (DR) Raman process, due to the selectivity of phonon wavevectors that satisfy the DR condition [53,160,185]. Besides, there are also second-order peaks in Figure

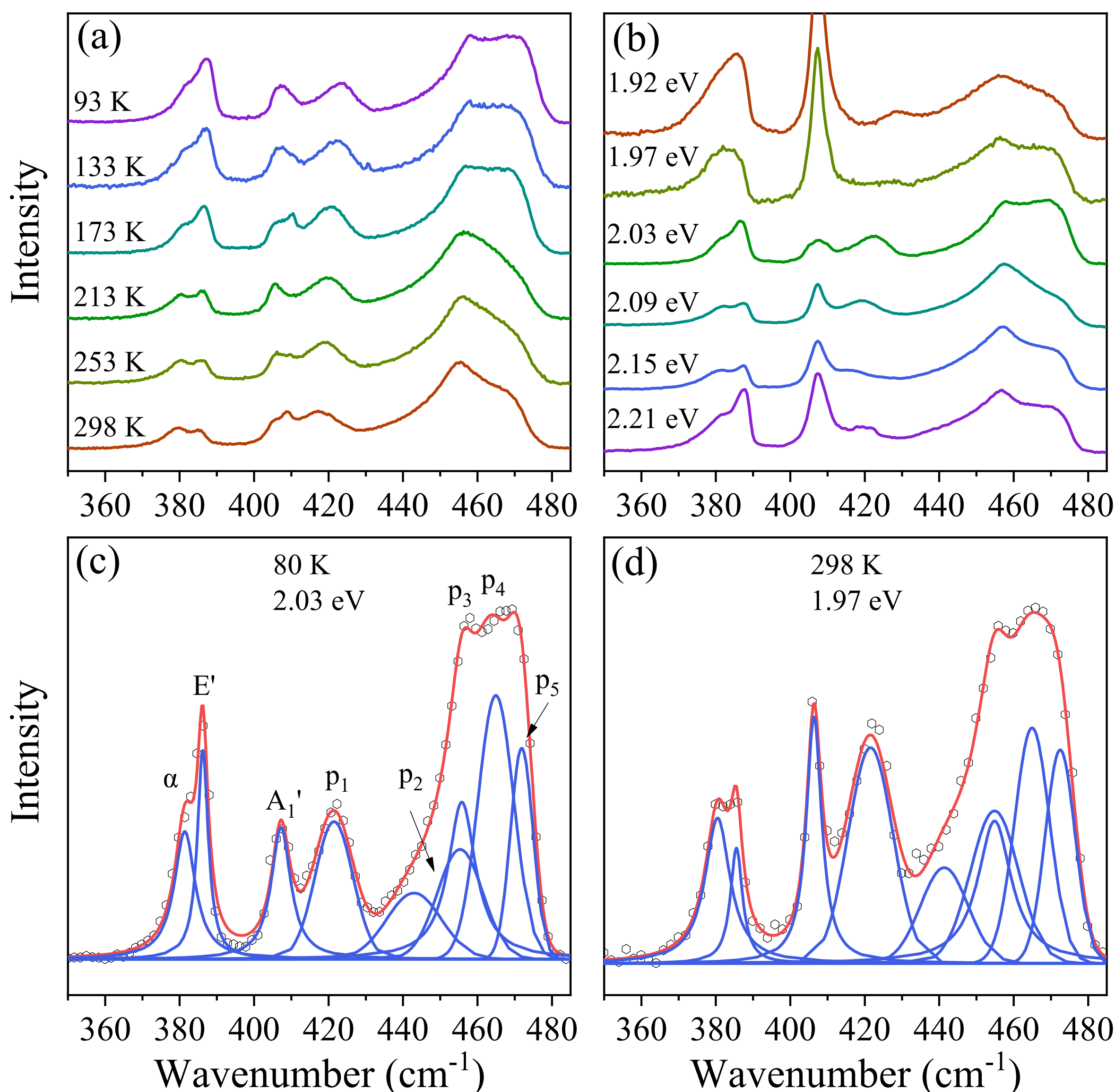

Figure 5.1. (a) Raman spectra of MoS_2 in the spectral range between 350 and 485 cm^{-1} at a laser energy of 2.03 eV for various temperatures. (b) Raman spectra of MoS_2 at a temperature of 80 K for various laser energies. (c) and (d) Similar Raman spectra obtained at two different laser energies and temperatures.

5.1(b) whose wavenumbers do not depend on the laser excitation energy. These peaks come from overtones of maxima in the phonon density of states (pDOS) and overlap with the double-resonance bands, preventing a clear distinction when we use just one laser line. The analysis of the Raman features recorded with different laser excitation lines allows the distinction between the normal second-order and the double-resonance bands [53]. Figure 5.1(c) shows the spectrum at T = 80 K using the laser energy of 2.03 eV and Figure 5.1(d) shows the spectrum of the same sample at T = 298 K using the laser energy of 1.97 eV. Notice the shapes of the double-resonance bands are similar, despite the fact that they were obtained with different laser lines and at different temperatures.

Figure 5.1(c) and Figure 5.1(d) also present the fitting of the spectra by a sum of different curves. The two first-order A_1' and E' bands can be fitted using Lorentzian functions since first-order bands involve a single phonon at the Brillouin zone center. For the other bands, the best fit was obtained by a sum of Gaussian curves, each one associated with a specific type of DR process, as it will be discussed at the end of this section.

We adopt the peak assignment for the second-order features proposed recently by Carvalho et al. [53] and summarized in Table 5.1, and the additional α band is further explored in section 5.2. The peak around ~420 cm^{-1} in Figure 5.1(c) and Figure 5.1(d) is called p_1 and involves the combination of two phonons of the LA and TA branches, close to the **K** point. Thus, it corresponds to a LA+TA(~**K**) process [53]. The broad and asymmetric band in the range 440-480 cm^{-1}, usually called the 2LA band in the literature, is, in fact, a multicomponent band with at least four features. The feature at ~456 cm^{-1} is called p_2, and it corresponds to the overtone of the van Hove singularity in the phonon DOS appearing at 228 cm^{-1} due to a saddle point (**SP**) between the **K** and **M** points in the LA phonon branch. It is the most intense peak in the calculated pDOS shown in Figure 2.8(d). The two peaks in the range 455-470 cm^{-1} are called p_3 and p_4 and they involve two LA phonons around the **K** and **M** points, respectively, giving rise to the 2LA(~**K**) and 2LA(~**M**) DR-processes. The fifth feature, called p_5, localized at approximately 472 cm^{-1}, was not reported in ref. [53]. It was evidenced by the fitting of the low-temperature spectra in this work. It is a non-dispersive band and can be assigned to a secondary maximum in the phonon density of states due to a maximum in the LA phonon branch around the **K** or **M** points [186], as shown in Figure 2.8(d).

The results presented in Figure 5.1 show that the double-resonance Raman bands in monolayer MoS_2 are strongly affected by temperature and laser energy and that we can tune

Table 5.1. Name, position, assignment, and mechanism responsible for the observed bands in the Raman spectrum of monolayer MoS_2.

Name	Position (cm^{-1})	Assignment	Process
α	380	2TA(~**K**)	Double Resonance
p_1	420	LA+TA(~**K**)	Double Resonance
p_2	454	2 LA(**SP**)	Second-order
p_3	460	2 LA(~**K**)	Double Resonance
p_4	470	2 LA(~**M**)	Double Resonance
p_5	472	2 LA(**K**) or 2 LA(**M**)	Second-order

the resonance effect. Each feature will be studied in the next section as a function of temperature and also as a function of the laser energy.

First, consider the scattering of the excited electron from **K** to **K'** for a laser energy a bit above the bandgap, just as it is illustrated in Figure 5.2(a). If a zoom is performed close to the scattering site (the red dot in Figure 5.2(a)), we can possibly observe the contribution of other phonons which can also obey the resonance condition, illustrated in Figure 5.2(b). These phonons are almost out of resonance, but they can still contribute to the scattering of the electron. Now, a simple geometry analysis reveals that the wavevector connecting the vicinities of **K** and **K'** points is close to the wavevector connecting the vicinities of **Γ** and **K**, as Figure 5.2(c) illustrates. Therefore, these are equivalent to phonons that connect **Γ** and **K**, which is greatly exaggerated in Figure 5.2(d). The first-order Raman band can be modeled as a Lorentzian lineshape because only a single phonon will participate in this process and the phonon participating has close to null momentum in the large wavelength approximation. This is a similar process to a photon emission or absorption from an atom. On the other hand, the

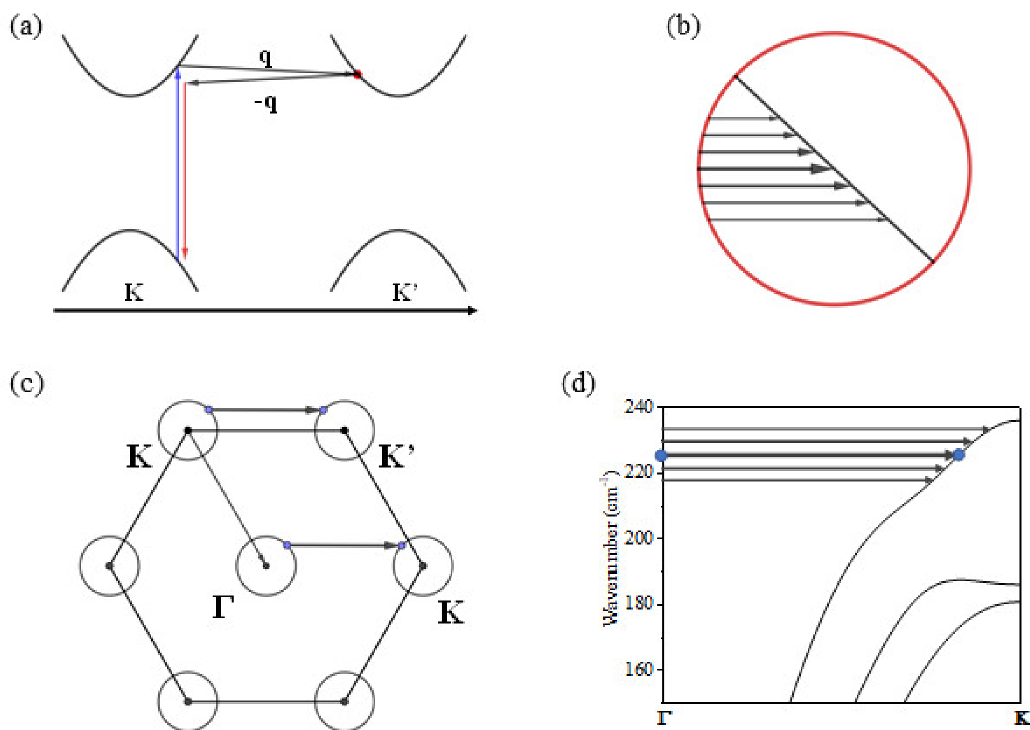

Figure 5.2. (a) Intervalley scattering process that describes the double resonance bands, all the processes are out of scale for clarity. (b) Zoom at the point in (a). (c) Wavevectors connecting **K** and **K'** and **Γ** and **K**. (d) Wavevectors of phonons connecting **Γ** and **K** through the LA phonon branch, which were greatly exaggerated for clarity. These can also connect **Γ** and **K** through the TA phonon branch as well.

second-order process involves a locus of phonons, which can be weighted by a gaussian contribution. Thus, this contribution can be used as a fitting lineshape.

5.1.2 Temperature dependence of the first-order and double-resonance bands.

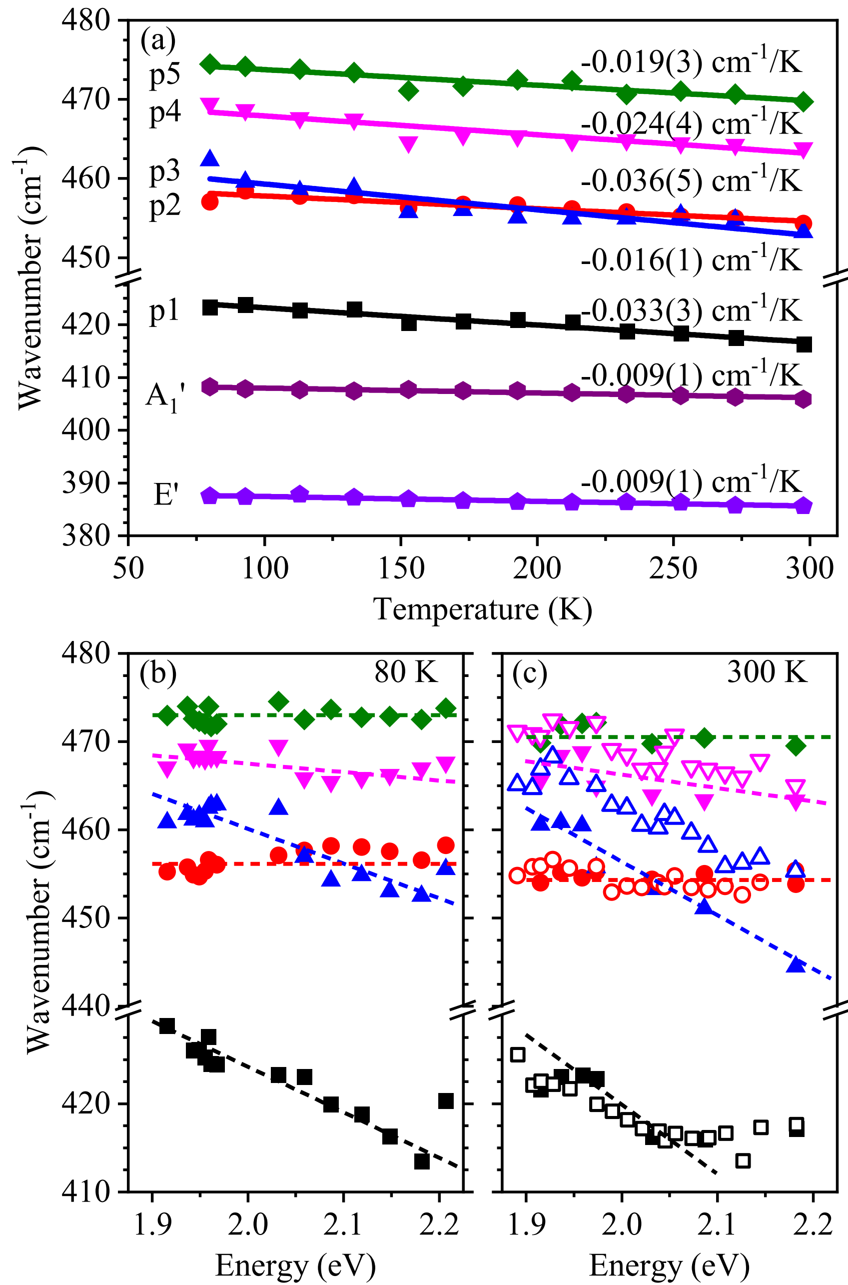

Figure 5.3. Monolayer MoS_2. (a) Frequency of each band as a function of temperature for the 2.03 eV laser energy. The values represent the slope of the line used to fit the frequencies as a function of temperature. (b) Frequency of p_1 to p_5 as a function of the laser energy at 80 K, where the colors correspond to the colors used in (a). The dashed lines are guides to the eyes. (c) Frequency of p_1 to p_5 as a function of the laser energy at 300 K, where the colors correspond to the colors used in (a). The dashed lines are guides to the eye. The open symbols represent data from Carvalho et al. adjusted with four Lorentzian curves at 298 K [53].

Figure 5.3(a) shows the frequency of the Raman features as a function of temperature. The first-order A_1' and E' modes are zone-center phonons and, therefore, the temperature dependence of their frequency is only due to the temperature dependence of the phonon energy. When the temperature is raised, phonon-phonon interactions play a major role, leading to a decrease in the phonon energy [238–240].

Our results of -0.009 ± 0.001 cm^{-1}/K for the slopes in the frequency versus temperature plots for the A_1' and E' modes are close to the previous results in the literature [241,242] within the accuracy of our measurements. In those works, samples of suspended and supported MoS_2 were measured and similar slopes of the A_1' mode frequency versus temperature were obtained [241–243], between -0.012 and -0.016 cm^{-1}/K. Notice that the accuracy 0.001 cm^{-1}/K in the temperature range 80-300 K corresponds to a frequency uncertainty of 0.2 cm^{-1}, which is below our spectrometer resolution.

The temperature dependence of the p_2 and p_5 bands is only due to the temperature effect on the phonon dispersion relations. The rate of change for the temperature dependence of the p_2 and p_5 frequencies are, respectively, -0.016 cm^{-1}/K and -0.019 cm^{-1}/K. These rates are about two times the rates of first-order bands, -0.009 cm^{-1}/K as shown in Figure 5.3(a), in good agreement with the assignment of p_2 and p_5 as normal second-order pDOS bands.

Figure 5.3(a) also shows the frequency of the double-resonance peaks p_1, p_3, and p_4 as a function of temperature. In this case, the peak frequencies of p_1, p_3, and p_4, depend both on the temperature and on the laser energy. As a matter of fact, the slopes of the DR bands p_1, p_3, and p_4 are -0.033, -0.036 and -0.024 cm^{-1}/K, respectively, and are larger than the slope of the first and second-order bands. Thus, we conclude that other effects come into play for the temperature-induced changes in the DR bands. As will be discussed below, the temperature dependence of p_1, p_3, and p_4 is indeed related to how both the phonon and electronic structures are affected by temperature.

A fundamental property of a DR feature is the fact that its frequency depends on the laser energy. Different laser energies involve different points in the valleys in the electronic structure and phonons with different momenta. This result is clearly shown in Figure 5.1(b). As already discussed, the DR bands in monolayer MoS_2 are originated from the scattering of the electron from a valley around the **K** point to other valleys around the **K'** or **Q** points. The **KK'** scattering process involves phonons in the proximity of the **K** point, whereas the **KQ** scattering process involves phonons in the proximity of the **M** point. As the laser energy increases, the optical transition occurs farther from the bottom of the conduction band, and phonons with different momenta satisfy the double-resonance condition. For TMDs, the acoustic phonon

dispersion exhibits a maximum at the **K** and **M** points, and the phonon energy decreases for wavevectors moving apart of these points. Therefore, as the laser energy increases, the frequency of the double-resonance bands decreases, leading $\left(\frac{\partial\omega}{\partial E}\right)_T$ to be negative, as shown in Figure 5.3(b) and (c), and as it was observed in ref. [53]. Assuming that ω_1, ω_3, and ω_4 are named as the frequencies of the peaks p_1, p_3, and p_4, respectively, the slopes obtained in Figure 5.3(b) and (c) are: $\left(\frac{\partial\omega_1}{\partial E}\right)_{80\ K} = -50\,\frac{\text{cm}^{-1}}{\text{eV}}$, $\left(\frac{\partial\omega_3}{\partial E}\right)_{80\ K} = -40\,\frac{\text{cm}^{-1}}{\text{eV}}$, $\left(\frac{\partial\omega_4}{\partial E}\right)_{80\ K} = -23\,\frac{\text{cm}^{-1}}{\text{eV}}$, $\left(\frac{\partial\omega_1}{\partial E}\right)_{300\ K} = -100\,\frac{\text{cm}^{-1}}{\text{eV}}$, $\left(\frac{\partial\omega_3}{\partial E}\right)_{300\ K} = -63\,\frac{\text{cm}^{-1}}{\text{eV}}$, $\left(\frac{\partial\omega_4}{\partial E}\right)_{300\ K} = -36\,\frac{\text{cm}^{-1}}{\text{eV}}$.

5.1.3 Effects of temperature on the photoluminescence spectrum.

In order to distinguish the contribution of phonons and electrons for the temperature dependence of the DR Raman features, we have performed photoluminescence measurements in monolayer MoS_2 with an in-situ variation of the sample temperature (Figure 5.4). From these measurements, we can directly obtain the temperature dependence of the optical transition energies.

Figure 5.5(a) shows the fitting of the PL spectra at T = 173 K using four Voigt components. The most intense feature, named T_A, is associated with the A trion [76,91,92,94,97,100]. The strong intensity of T_A is due to the excess of charge (possible optical doping) induced by the relatively high laser power used in our experiments [97]. The

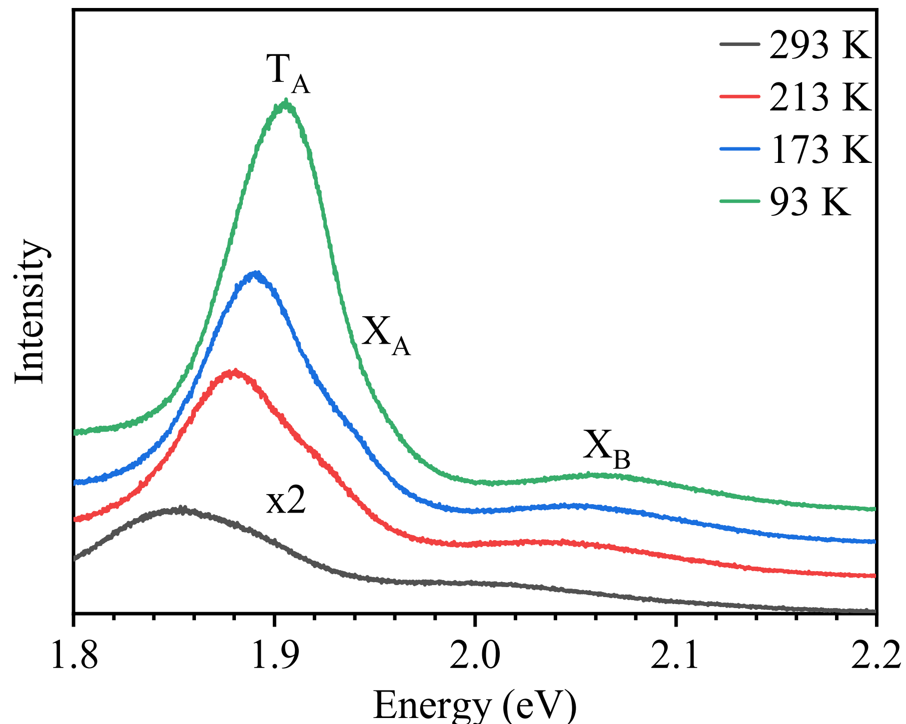

Figure 5.4. PL of monolayer MoS_2 measured for the temperature of 93, 173, 213 and 293 K.

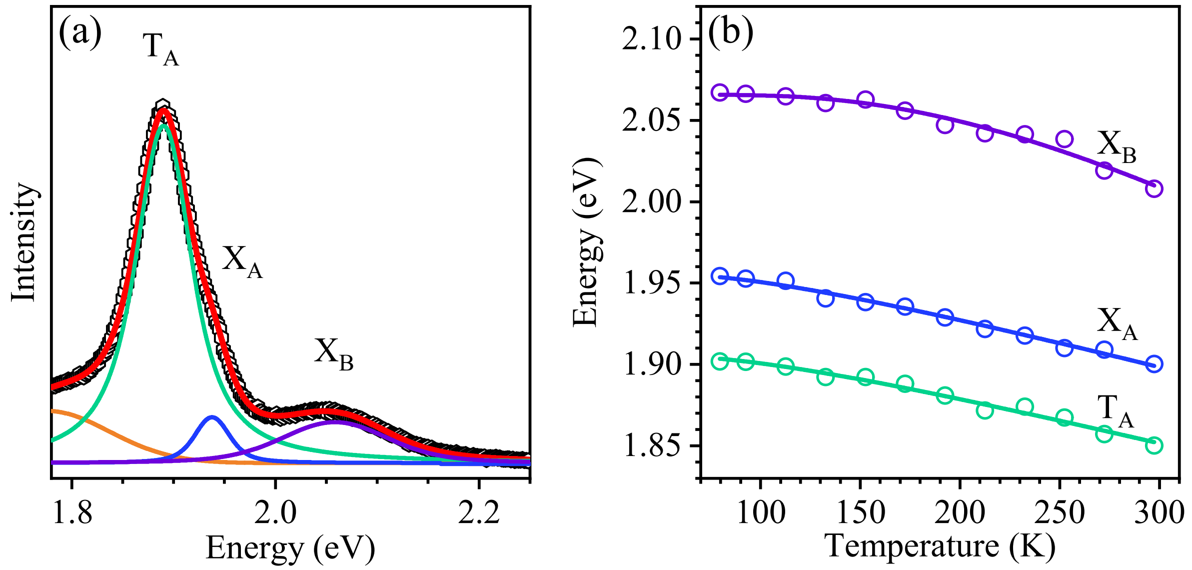

Figure 5.5. Temperature dependence of the excitonic transitions of monolayer MoS_2. (a) The observed features comprising the PL spectrum at 173 K. (b) Fitting of the positions of T_A, X_A, and X_B for the measured temperature range using Equation A.13.

two smaller bands are named X_A and X_B, and associated with the A and B excitons [76,91,92,94,100], respectively.

The positions of T_A, X_A, and X_B as a function of temperature are shown in Figure 5.5(b) and their positions and widths were fitted according to the equations (see Appendix A for the deduction) [244]

$$E(T) = E(T=0) - a\left(1 + \frac{2}{e^{\frac{\langle \hbar\omega \rangle}{K_B T}} - 1}\right), \tag{A.13}$$

$$\Gamma(T) = \Gamma(T=0) + b\left(1 + \frac{2}{e^{\frac{\langle \hbar\omega \rangle}{K_B T}} - 1}\right). \tag{A.14}$$

The values of the fitting parameters for the positions and width of T_A, X_A, and X_B peaks can be found in Table 5.2, and a deduction of the equations can be found in Appendix A. The parameters related to the properties of the material are the extrapolated optical bandgap at 0 K,

Table 5.2. Fitting parameters obtained after the mutual adjustment of equations A.13 and A.14 to the experimental PL data.

	E(0) (eV)	*a* (meV)	Γ(0) (meV)	*b* (meV)	⟨ħω⟩ (meV)
T_A	1.94 ± 0.02	34 ± 10	24 ± 8	29 ± 10	24 ± 10
X_A	1.99 ±0.03	34 ± 10	44 ± 20	3 ± 1	24 ± 10
X_B	2.16 ± 0.06	94 ± 60	66 ± 36	54 ± 20	38 ± 14

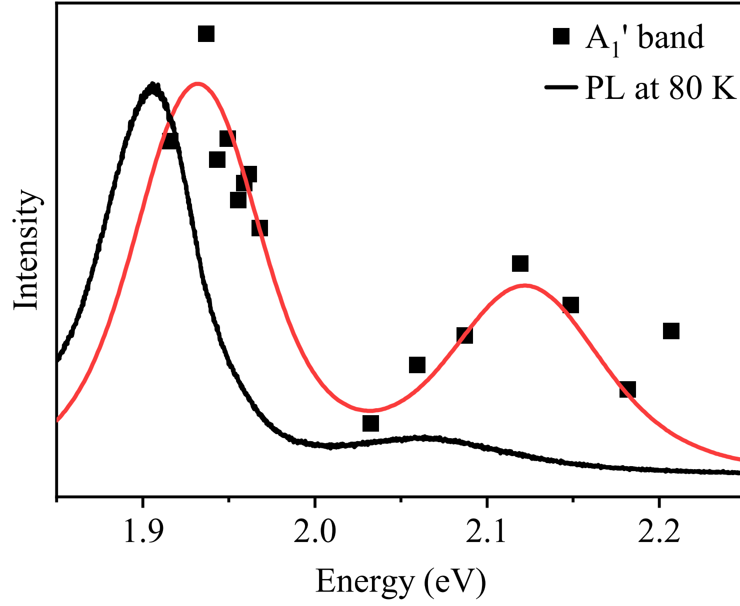

Figure 5.6. The intensity of the A_1' band at 80 K, normalized by the intensity of the E' band, as a function of the laser energy is shown as solid squares. The red line represents a fit using Equation 3.2 for the two maxima observed. The black line is the measured PL spectrum at 80 K.

$E(0)$, the average phonon energy $\langle\hbar\omega\rangle$ and the intrinsic broadening parameter $\Gamma(0)$, while a and b are fitting parameters. From the difference between $E(0)$ for X_A and T_A, we obtain a binding energy of 50 meV for the trion energy, which is in good agreement with the reported values in the literature [92]. Also, from the difference between $E(0)$ for X_A and X_B, we extract the spin-orbit coupling energy of 170 meV, in excellent agreement with the results presented in Figure 2.5.

The Raman excitation profile of the A_1' mode, i.e., the calibrated intensity of the mode as a function of the laser energy, is shown in Figure 5.6 for a temperature of 80 K. The red curve corresponds to the fitting of the Raman excitation profile (REP) using the theoretical expression for the Raman intensity given by Equation 3.2, while the black curve is the PL measured at 80 K. The fitting parameters from Figure 5.6 can be found in Table 4.2. From the REP of the A_1' mode, we extract two resonance energies at 1.907 and 2.098 eV. Notice that the actual maximum of these two curves is shifted from the value of the electronic transition by approximately 26 meV, which is half the energy of the A_1' mode. Equation 3.2 predicts two

Table 5.3. Fitting parameters for the excitation profile of the ratio of intensities of the A_1' and E' bands according to equation (3.2). The phonon frequency ω_{Ph} was fixed at 410 cm^{-1}.

E (eV)	C (eV)	Γ (eV)
1.907 ± 0.005	0.007 ± 0.004	0.053 ± 0.021
2.098 ± 0.008	0.008 ± 0.004	0.071 ± 0.020

resonances when the laser energy corresponds to the relevant electronic transition and when the laser energy corresponds to the electronic transition plus the energy of the phonon. Since T_A is 1.906 eV at 80 K and the first resonance observed in the REP is at 1.907 eV, it is reasonable to assume that T_A corresponds to the first observed resonance.

5.1.4 Effects of strain induced by the different thermal expansions of sample and substrate

It is important to comment that the strain induced by the adhesion of the sample to the substrate when the sample is cooled-down, due to the different thermal expansion coefficients of MoS_2 and the substrate, affects in principle both electronic structure and phonon energy of MoS_2. However, this effect is not strong enough to be observed in our experimental results. Considering the linear thermal expansion coefficient of 0.56×10^{-6} K^{-1} for fused quartz [245] and of 4.76×10^{-6} K^{-1} for MoS_2 [246], the cooling down process from 300 K to 80 K would induce a strain of ~0.1% in MoS_2, considering the perfect adhesion with the substrate. However, as shown in previous works of graphene and MoS_2 on SiO_2/Si [247–249], the strain transfer is usually partial and the adhesion depends on the type of the substrate, being very weak for SiO_2.

According to the Raman and PL study of strained MoS_2 [250], the induced strain of 0.1% would shift the frequency of the in-plane E' mode by ~0.5 cm^{-1} and would not affect the position of the out-of-plane A_1' mode. In fact, our observed slopes of -0.009(1) cm^{-1}/K for both the A_1' and E' modes positions as a function of temperature are very close to those observed for suspended and supported monolayer MoS_2 samples, approximately -0.013 cm^{-1}/K for both A_1' and E' modes [241,242]. On the other hand, the PL measurements as a function of strain [250] show that 0.1% of strain would shift the exciton transition by 0.005 eV. Considering that the dispersion of the DR bands is approximately 50 cm^{-1}/eV, the shift of the band induced by 0.1% strain would be smaller than 0.5 cm^{-1}. Therefore, even considering a perfect adhesion between MoS_2 and the substrate when the sample is cooled down, the changes induced by the strain in the electronic structure and phonon energy cannot be detected in our measurements, considering the spectrometer resolution and the temperature variation range.

5.1.5 Determination of the temperature dependence of the acoustic mode near the zone edges

As shown in Figure 5.3(a-c), the positions of the DR bands depend on both the temperature and the laser excitation energy, which is in resonance with the excitonic transition. Moreover, the excitonic transition also depends on temperature, as shown in Figure 5.5(b). The

rates $\frac{\partial\omega}{\partial T}$ shown in Figure 5.3(a) for the DR bands may have contributions of the temperature dependence of both the phonon and the excitonic transitions. We can distinguish these two contributions by taking into account the results shown in Figure 5.3(a-c) and Figure 5.5(b), as explained below.

Let us call ω_1, ω_3 and ω_4, the frequencies of p_1, p_3, and p_4, respectively. We can construct a function for ω_i based on light absorption and the wavevector accessed by the electron-hole pair. We refer to the DR process illustrated in Figure 5.2, where an electron in the valence band around the **K** point is excited by a photon with energy E to the conduction band at a wavevector $\boldsymbol{k}$, distant k units from the **K** point. For simplicity, we suppose that the Brillouin zone is centered at the **K** point, such that we can write for light absorption:

$$\Delta E = E - E_g = \frac{\hbar^2 k^2}{2\mu^*}, \tag{5.1}$$

where E_g is the bandgap and $\mu^* = \frac{m_e^* m_h^*}{m_e^* + m_h^*}$ is the exciton reduced effective mass. The term ΔE will be the excess energy of the electron-hole pair after the electron is promoted to the conduction band. After light absorption, the electron can be scattered to the **K'** point by a phonon with frequency ω and wavevector $\boldsymbol{q}$. Following this process, the electron is scattered back to the **K** point by another phonon with frequency ω' and wavevector $-\boldsymbol{q}$, and at the **K** point, the electron-hole pair recombine in order to emit a scattered photon. From the explanation developed so far, we can already say that $\omega(E) = \omega(\boldsymbol{k}) = \omega(\Delta E)$.

Since changing the temperature T will affect the bandgap and will also affect the phonon frequency, we may also write that $\omega(E, T) = \omega(\boldsymbol{k}, T) = \omega(\Delta E, T)$. We must remember that ΔE, as it was defined, depends on both E and T. Thus, in order to calculate the partial derivatives of ω with regards to the experimental parameters, we must also consider the electronic transition energy and the way it will affect the final result. We can calculate the derivatives of ω using the chain rule:

$$\left(\frac{\partial\omega}{\partial E}\right)_T = \left(\frac{\partial\omega}{\partial\Delta E}\right)_T \left(\frac{\partial\Delta E}{\partial E}\right)_T = \left(\frac{\partial\omega}{\partial\Delta E}\right)_T \qquad (5.2),$$

$$\begin{aligned} \left(\frac{\partial\omega}{\partial T}\right)_E &= \left(\frac{\partial\omega}{\partial\Delta E}\right)_T \left(\frac{\partial\Delta E}{\partial T}\right)_E + \left(\frac{\partial\omega}{\partial T}\right)_{\Delta E} \\ \left(\frac{\partial\omega}{\partial T}\right)_E &= -\left(\frac{\partial\omega}{\partial E}\right)_T \left(\frac{\partial E_g}{\partial T}\right)_E + \left(\frac{\partial\omega}{\partial T}\right)_{\Delta E} \end{aligned} \qquad (5.3).$$

Table 5.4. Temperature dependence of the acoustic phonons' frequencies in the proximity of the K and M points.

	LA(~**K**)	LA(~**M**)	TA(~**K**)
$\left(\frac{\partial\omega_{ph}}{\partial T}\right)_{\Delta E}$	-0.013 cm^{-1}/K	-0.009 cm^{-1}/K	-0.008 cm^{-1}/K

The term $\left(\frac{\partial\omega}{\partial\Delta E}\right)_T$, gives the rate of change of ω with ΔE at constant T, the term $\left(\frac{\partial E_g}{\partial T}\right)_E$ gives the rate of change of the bandgap with T, which is equal to the term $\left(\frac{\partial\omega}{\partial E}\right)_T$, or the slope of ω with the laser energy. The term $\left(\frac{\partial\omega}{\partial T}\right)_{\Delta E}$ gives the rate of change of ω with T at fixed ΔE, or the purely thermal coefficient of ω. The product $\left(\frac{\partial\omega}{\partial\Delta E}\right)_T\left(\frac{\partial E_g}{\partial T}\right)_E = \left(\frac{\partial\omega}{\partial E}\right)_T\left(\frac{\partial E_g}{\partial T}\right)_E$ gives the contribution of the DR process to the rate of change of ω with T.

We can evaluate the contribution $\left(\frac{\partial\omega}{\partial\Delta E}\right)_T\left(\frac{\partial E_g}{\partial T}\right)_E$ to $\left(\frac{\partial\omega}{\partial T}\right)_E$ by substituting some values from Figure 5.3 and using $\left(\frac{\partial E_g}{\partial T}\right)_E \sim \frac{2aK_B}{\Theta} = -0.25$ meV/K from the parameters of T_A in Table 5.2. The values of $\left(\frac{\partial\omega_1}{\partial\Delta E}\right)_{80\ K}\left(\frac{\partial E_g}{\partial T}\right)_E$, $\left(\frac{\partial\omega_3}{\partial\Delta E}\right)_{80\ K}\left(\frac{\partial E_g}{\partial T}\right)_E$ and $\left(\frac{\partial\omega_4}{\partial\Delta E}\right)_{80\ K}\left(\frac{\partial E_g}{\partial T}\right)_E$ are equal to -
-0.013, -0.010 and -0.006 cm^{-1}/K, respectively. Thus, the values of $\left(\frac{\partial\omega_1}{\partial T}\right)_{\Delta E}$, $\left(\frac{\partial\omega_3}{\partial T}\right)_{\Delta E}$ and $\left(\frac{\partial\omega_4}{\partial T}\right)_{\Delta E}$ will be equal to -0.020, -0.026 and -0.019 cm^{-1}/K, respectively, consistent with the values we have obtained for the second-order peaks p_2 and p_5. Considering that $\omega_1 = \omega_{LA(\sim\boldsymbol{K})} + \omega_{TA(\sim\boldsymbol{K})}$, $\omega_3 = 2\omega_{LA(\sim\boldsymbol{K})}$ and $\omega_4 = 2\omega_{LA(\sim\boldsymbol{M})}$, we can determine the rate of change of the frequency of the LA and TA phonons in the proximities of the **K** and **M** points, presented in **Table 5.4**.

5.1.6 Combining the temperature and laser energy effects on the double-resonance bands

The complete set of data comprising the second-order and DR bands of each spectrum at different laser lines and temperatures can be summarized in a single graphic by considering the difference between the excitation laser and the excitonic energies as a function of temperature [165]. As evidenced in Figure 5.5(c), the relevant optical transition for the Raman scattering was the T_A trion. The procedure employed here is based on the difference $\Delta E = (E - T_A)$ between the laser energy E and the trion energy T_A determined in Figure 5.5(b). For instance, we know that at 80 K, T_A = 1.906 eV, and if we measure the Raman spectrum with a 1.917 eV laser line, we need to consider the difference ΔE = 0.011 eV.

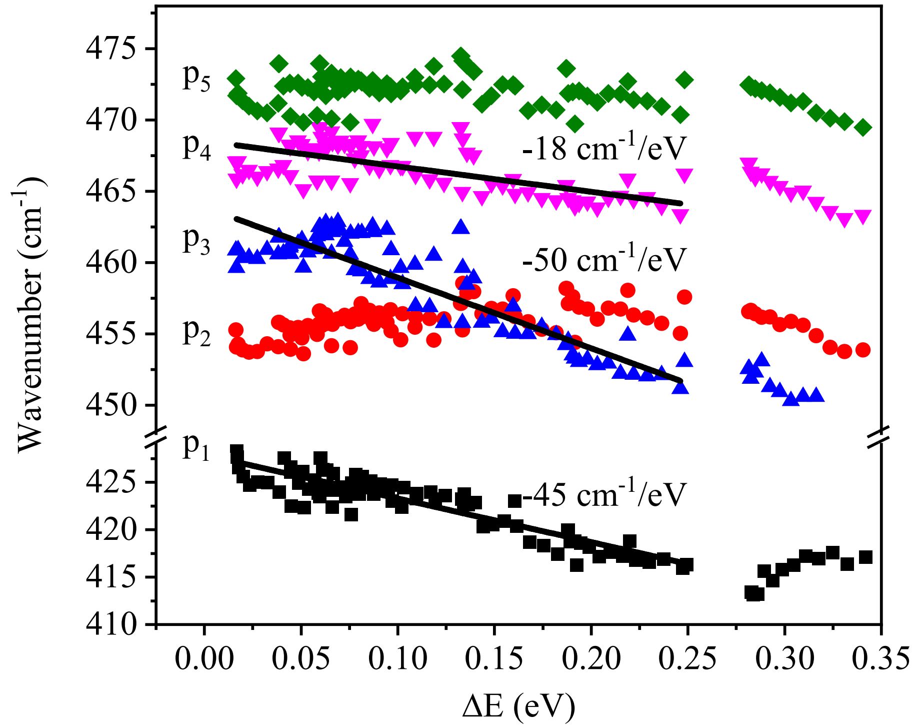

Figure 5.7. Frequency of the DR and second-order bands as a function of ΔE defined in the main text. The lines represent a linear fit with the corresponding slopes presented in the figure. The error for the slope values is 3 cm^{-1}/eV.

The simple approach of considering only the difference between laser-line and excitonic-transition energies enables us to include all data obtained in this work, at different temperatures and using different laser lines, in the same plot. The frequency of the DR bands as a function of ΔE is shown in Figure 5.7. We can clearly see the dispersive behavior of p_1, p_3, and p_4 peaks. On the other hand, the frequency of the experimental bands p_2 and p_5, which corresponds to maxima of the LA branch in the calculated pDOS, only disperses with temperature.

5.1.7 Conclusions

In conclusion, we have studied the Raman spectra of monolayer MoS_2 using many different laser lines with energies in the range 1.92-2.21 eV and at different temperatures ranging from 80 to 300 K. We have measured the dispersion of all DR features and the second-order bands by changing the laser excitation energy in the temperature range of 80 to 300 K. The dependence of the frequency of first-order bands on temperature is explained by anharmonic effects related to phonon-phonon interactions, whereas the frequency and the shape of the double-resonance bands depend not only on the temperature dependence of the phonon frequency but also on the excitonic transition energy. The excitonic transitions were measured

by PL as a function of temperature in order to distinguish these two effects. We have observed that the Raman bands are enhanced by resonances with the trion with energy T_A.

5.2 Few layers and Bulk MoS_2

Unlike the monolayer, whose electronic structure is characterized by a direct bandgap at the **K** point, bulk MoS_2 possesses an indirect bandgap (I_g) that connects the **Γ** and **Q** points as it was shown in Figure 2.4(b). It can also be observed in Figure 2.4(b) that the valleys in the conduction band around the **K** and **Q** points are in the same energy level for bulk. Therefore, in comparison with monolayer MoS_2 where the main contributions to the double resonance process come from the electron scattering from valleys near the **K** and **K'** points, in bulk MoS_2 are also possible electron scattering processes that occur from valleys near the **K** and **Q** points. Here a similar approach as that used for monolayer MoS_2 will be applied to explain temperature effects on the intervalley scattering for few-layers and bulk MoS_2. A broader spectral range

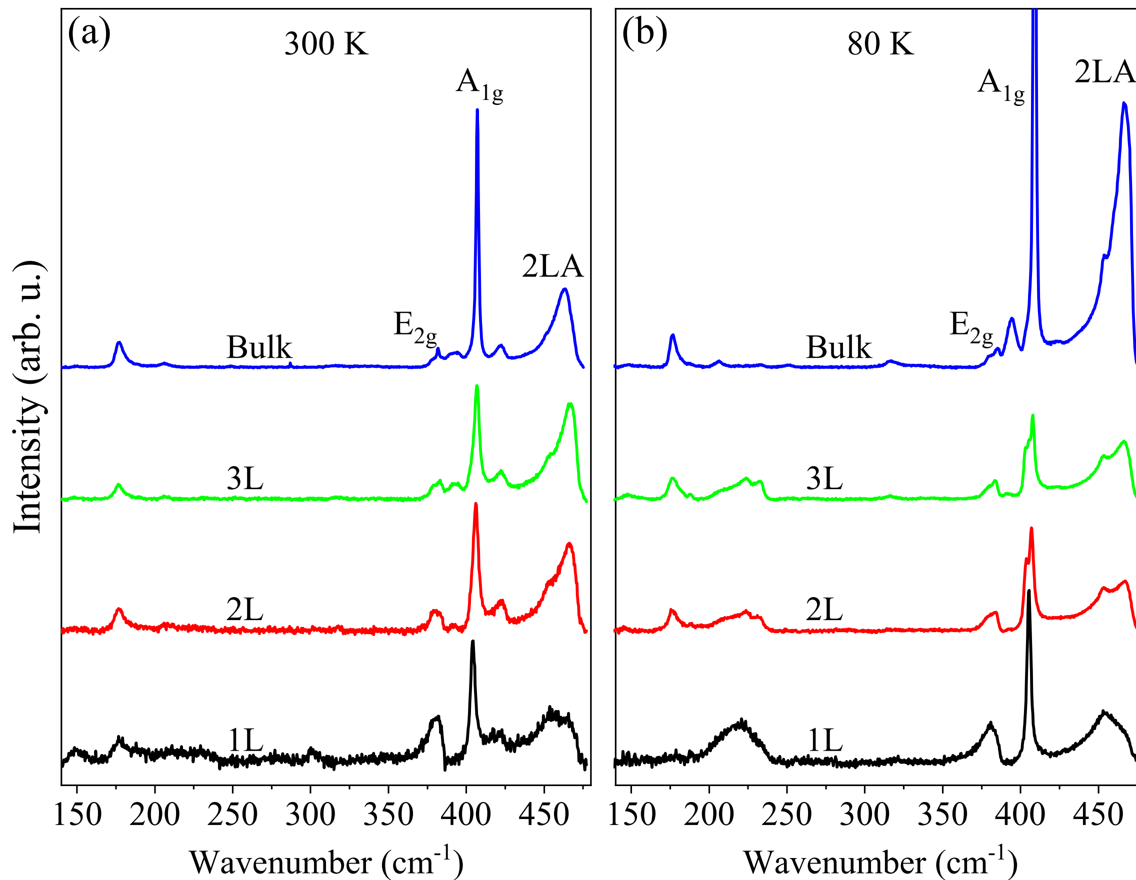

Figure 5.8. Raman spectrum of the monolayer (1L), bilayer (2L), trilayer (3L), and bulk MoS_2 collected with a 1.92 eV (647.1 nm) laser line at temperatures of (a) 300 K and (b) 80 K. The intensity is normalized by the intensity of the E_{2g} mode at approximately 382 cm^{-1}. We use the irreducible representations of bulk for simplicity. The intensity of the A_{1g} mode for bulk in (b) is cut for clarity.

from 140 to 480 cm^{-1} will be explored in order to understand the additional processes observed, for bilayer, trilayer and bulk, as compared to monolayer MoS_2.

Figure 5.8(a) and (b) show the Raman spectra of monolayer (1L), bilayer (2L), trilayer (3L) and bulk MoS_2 obtained with a laser excitation energy of 1.92 eV at temperatures of 300 and 80 K. At 300 K, the Raman spectrum of all samples is dominated by the A_{1g} mode a well as the double resonance bands p_1 and 2LA. We use the irreducible representations of bulk at this point forward for simplicity. At frequencies lower than 300 cm^{-1}, we can see some smaller bands, and the ones in the range of 140 to 275 cm^{-1} are especially enhanced at the low temperature for 1L, 2L, and 3L, as can be seen in Figure 5.8(b). The band at approximately 395 cm^{-1}, indicated by an arrow in Figure 5.8(a) and (b), is equal in intensity between 2L, 3L, and bulk at 300 K, but it is very small for 2L and 3L, and huge for bulk at 80 K. We also see that the peak corresponding to the E_{2g} mode is very broad and asymmetric, which could be explained in terms of another component that appears due to the resonance with the excitonic level. We explore these peaks in detail in the next sections, starting from the region between 140 to 275 cm^{-1} and after we move to the region between 300 to 480 cm^{-1}.

5.2.1 The spectral region between 140 and 275 cm^{-1}

Figure 5.9(a) and (b) present the Raman spectra of 1L, 2L, 3L and bulk in the range of 140 to 275 cm^{-1} collected with a 1.92 eV laser at 300 and 80 K, respectively. At 300 K, there are two components common to all four samples, at approximately 177 cm^{-1} and at 207 cm^{-1}. Both peaks are related to a phonon subtraction process, where there is the creation of a phonon,

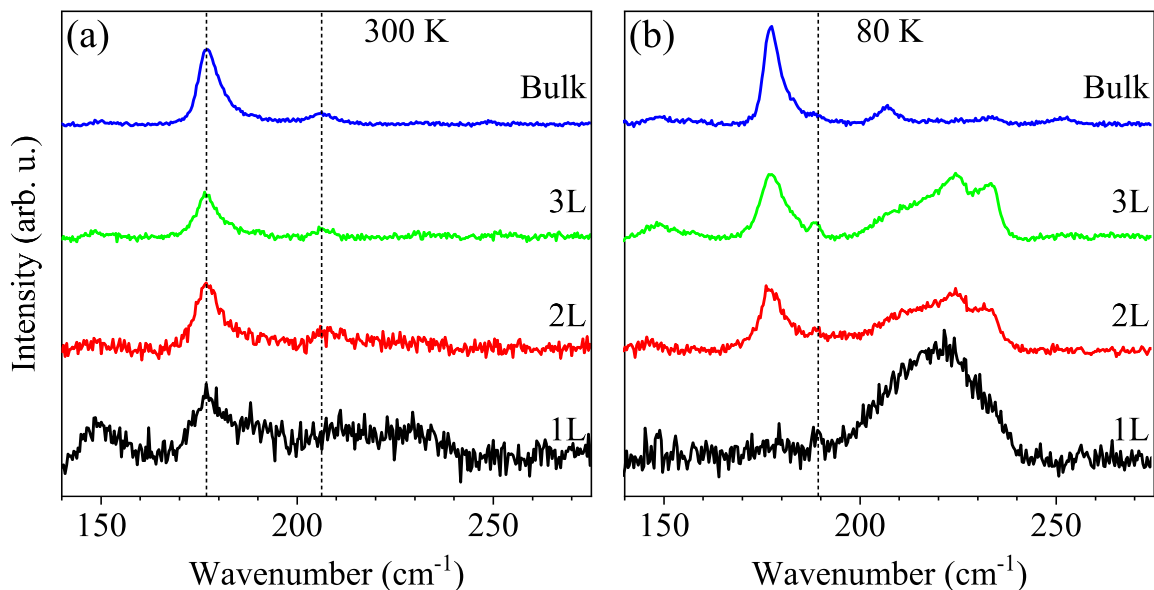

Figure 5.9. Raman spectra of 1L, 2L, 3L and bulk from bottom to top at (a) 300 and (b) 80K in the range of 140 to 275 cm^{-1}.

followed by the destruction of another phonon [251]. In order to simplify the notation, we address the phonon branches, except the acoustic at the **M** or **K** points, by their irreducible representations at the **Γ** point of bulk. The 177 cm^{-1} peak corresponds to the difference between A_{1g}(**M**) and LA(**M**) phonons, which we conveniently write as A_{1g}-LA(**M**). In the same way, the peak at 207 cm^{-1}, which is barely visible at 300 K, corresponds to E_{2g}-LA(**M**). We name these processes as Stokes/Anti-Stokes combinations since they correspond to the emission of a phonon by the lattice followed by the absorption of a different phonon by the lattice. In principle, these bands should be heavily affected by temperature, since the Stokes/Anti-Stokes process requires that the lattice is already thermally excited. However, since we did not reach temperatures below cryogenic and we are in resonance, the Stokes/Anti-Stokes process is still observed. In fact, at 80 K, the peaks are slightly more intense for 3L and bulk, than at 300 K, for 2L, the intensity is about the same, and for 1L, the intensity drops to almost zero and increases for 300 K, revealing a strong dependence with the electronic structure.

We expect that the main electron-scattering process for the 177 and 207 cm^{-1-} peaks comes from the valleys near **K** to the valleys near **Q**. Now, from Figure 2.4(b), the parabolic band near **Q** at the conduction band is above the parabolic band at the **K** point for 1L; it is slightly closer to alignment for 2L and it is aligned for bulk. Therefore, as the number of layers increases, the resonance with the valley at **Q** should come for energies closer to the direct bandgap. If instead of the laser energy we tune the electronic structure as we have done in the monolayer case, we can control the resonance energies. Therefore, at 80 K, since bulk will be closer to the resonances with the **Q** valley, the processes that come from the phonon subtraction processes will be more intense and it will be out of resonance for 1L. This is also the case for the small peak at 252 cm^{-1}, which corresponds to the difference A_{1g}-TA(**M**), which is not visible at 300 K but can be seen at 80 K. The peak at 150 cm^{-1} corresponds to the difference E_{2g}-LA(**K**) and as the other bands discussed above it is stronger when the laser is in resonance with the direct bandgap. The best instance of this is the case for 1L at 300 K, where the laser is more energetic than the trion energy, as discussed in section 5.1.3, and there is enough energy for both electron and hole to be in resonance.

The broad band centered at approximately 225 cm^{-1} and the very thin band centered at approximately 190 cm^{-1} correspond to the LA and TA bands, which are activated through the phonon-defect process. From the difference in intensity between the spectra collected at 80 and 300 K, we can conclude, especially for 1L, that the defect assisted process is intensified when the laser is in resonance with the excitonic or, for 1L, the trion transition. We will keep exploring the defect-assisted process in section 5.3, where we characterize CVD samples of

MoS_2 and show that the intensity of the defect-assisted bands is highly enhanced when the sample is excited in resonance with the electronic transition, and also that there is a trade-off between the defect-assisted bands and the subtractive bands.

5.2.2 The spectral region between 350 and 480 cm^{-1}

We now turn our attention to the region between 350 and 480 cm^{-1} from Figure 5.8, which is zoomed in Figure 5.10. A quick comparison between the spectra acquired at 80 and 300 K shows a big difference for all samples, going from the first-order modes to the double-resonance bands as well.

The first observation is regarding the first order A_{1g} mode, which is quickly discernable at 300 K in Figure 5.10. We discussed in section 2.3 about the vibrational properties of *n*-layers TMDs, and the conclusion is that the number and representation of the Raman-active modes would change according to *n* and the parity of *n* [110]. From refs. [114–116], however, only a main feature can be observed which increases in frequency as the number of layers increase as well. One observation made by ref. [114] is that the width of the A_{1g} band is maximum for 2L,

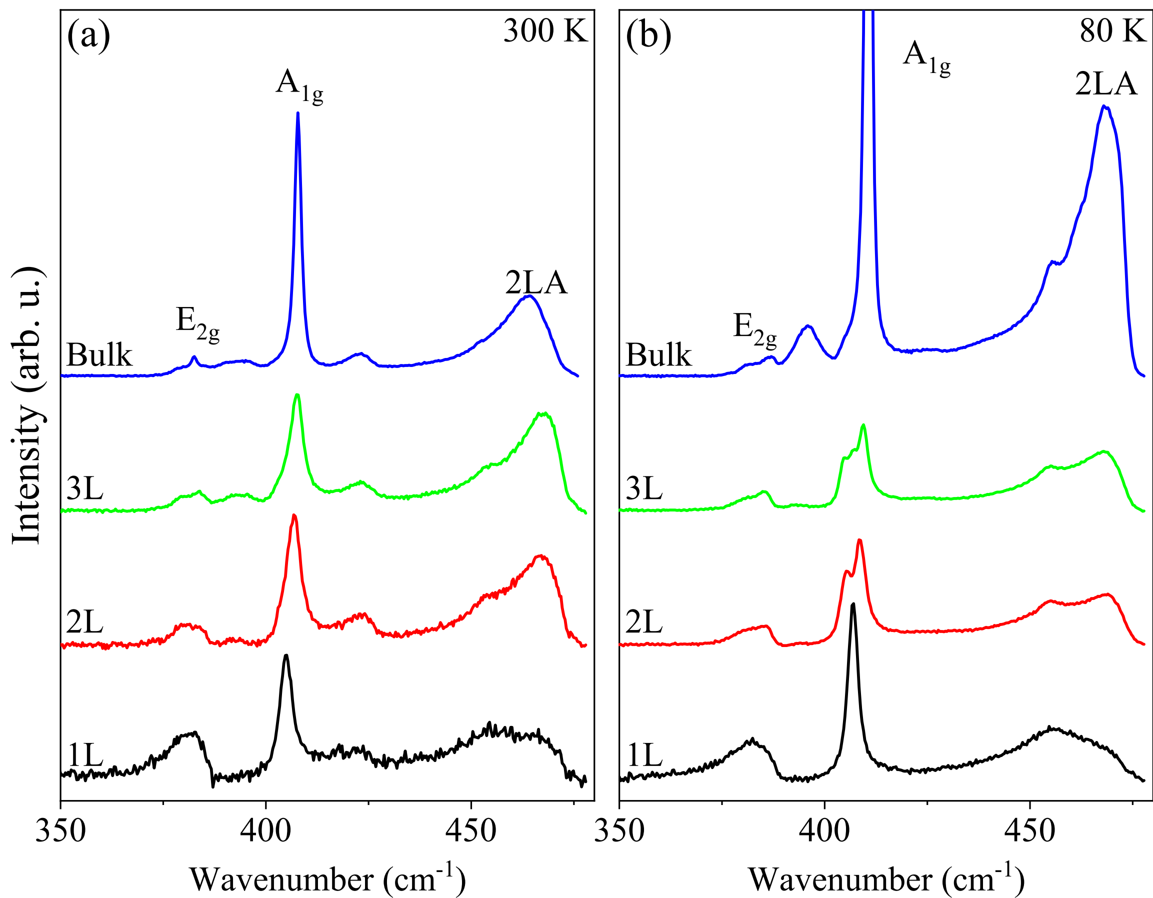

Figure 5.10. Raman spectra of 1L, 2L, 3L, and bulk for temperatures of (a) 300 and (b) 80 K in the range of 300 to 480 cm^{-1} collected with a 1.92 eV laser.

which is almost the double of 1L. A greater width could potentially mean another component with a frequency very close to the A_{1g} mode, that could not be separated due to thermal effects or due to the lack of appropriate resolution of the spectrometer. As the number of layers increases from 2L to 3L, though, the width reduces, and at 4L the width is basically the same as 1L. Therefore, we could assume that the components composing the A_{1g} band get closer and closer as the number of layers converges to bulk.

From Table 2.1, we would expect 3 modes of A_{1g} representation for 2L, while for 3L we would expect 4 modes of A_1' representation. Since the stacking of layers introduces the interlayer vibrational modes which are Raman-active, we expect that at least 1 mode of A_{1g} representation would be referent to an interlayer vibrational mode. Since the A_{1g} and A_1' modes are totally symmetric, they represent a breathing-like movement, an out-of-plane vibration. From ref. [46], the number of interlayer breathing modes is only 1 for 2L and 3L. Thus, for 2L and 3L, 1 and 2 A_{1g} modes remain unaccounted, and as it is shown in Figure 2.8(b), they must be almost degenerate. Therefore, the splitting of the A_{1g} band presented in Figure 5.10(b) for 80 K is due to both thermal effects that are lessened when temperature is decreased, and also due to a better resolution, since the red light used in this experiment is more dispersed (in the frequency domain) than green light used in [114]. We observe no clear distinction of the E_{2g} band, which can be attributed to the large contribution from the broad band that is right beside it, at approximately 380 cm^{-1}.

The band at 380 cm^{-1}, which we call α, has been attributed to a few possibilities, such as the E_{1u} phonon at the **Γ** point [160], the E_{2g} phonon at the **M** point [252], or a combination of two TA or two TA' phonons at the **K** point [186]. Based on the enhancement of the **KK'** electron-scattering process in 1L, we propose that the α band comes from the combination of two TA phonons at the **K** point. The assignment is fair since the band is very strong for 1L, which does not possess the quasi-acoustic phonons and also because it corresponds to exactly twice the frequency of the TA phonon at **K**, which was observed at 80 K in Figure 5.9(b). Since the pDOS for MoS_2 presents a very strong peak at the 190 cm^{-1} (Figure 2.8(d)), reflecting the flat dispersion of the TA branch close to the **K** point, we would expect that this peak is not very dispersive, remaining rather constant in frequency when the laser energy changes. Therefore, most of the changes we observe in the frequency of this peak are simply related to temperature effects.

The band at approximately 395 cm^{-1}, which we call β, is observed with the highest intensity for bulk at 80 K, while it is rather weak for 2L and 3L and inexistent for 1L. At 300 K, the β band presents the same intensity between 2L, 3L, and bulk, while it still remains

inexistent for 1L. Therefore, we believe the process related to this band is connected to the **KQ** scattering process, which involves phonons around the **M** point. A simple look into Figure 2.8(a) (the phonon dispersion of 1L for simplicity), reveals that the combination of phonons around the **M** point belonging to the LA (~235 cm^{-1}) and ZA (~160 cm^{-1}) branches would correspond exactly to this frequency. In the same manner, the weak band at 320 cm^{-1}, which is observable for 3L and bulk at 80 K, can be related to the combination of two TA phonons around the **M** point, which is a weak process overall since the coupling with TA phonons is much weaker than that for LA phonons.

We now turn to the 2LA band, which was deeply explored for 1L in section 4.2. A comparison between 1L, 2L, 3L, and bulk at 80 K from Figure 5.10, shows how the resonance with the valley at the **Q** point can affect the double resonance process. Since bulk has the less energetic bandgap between the samples, it would exhibit the lowest energy at the **Q** valley in the conduction band. Thus, when the laser energy is closer to the resonance with the excitonic transition, the **KQ** electron-scattering process is stronger, since the scattering channel involves real states. For 2L and 3L, although they are indirect bandgap as well since the **Q** valley is more energetic compared to the bulk, the intensity will be smaller since the real state is getting into resonance. At 300 K, however, the entire band structure is shifted to smaller energy, and the bandgaps are reduced. As a consequence, the strong resonance observed for bulk is reduced, and the maximum intensity is shifted from 469 to 464 cm^{-1}. 2L and 3L, on the other hand, present a stronger intensity for the 2LA band (when the spectra are normalized by the E_{2g} band), which means that the process is now in resonance, which is also evidenced by the fact that the frequency of the 2LA band is about the same between the 80 and 300 K, changing just 2 cm^{-1}. 1L is still coming into resonance with the **KQ** scattering process, since the "shoulder" of the 2LA band, corresponding to the p4 peak described in section 4.2, is getting stronger at 300 K.

Another way to look for the resonance with the **KQ** scattering process is to begin at a laser energy below the excitonic transition and increase the sample temperature. In this way, since the conduction band is reducing in energy, the laser energy will come into resonance with the excitonic transition, which would enhance the double resonance features.

Figure 5.11(a), (b) and (c) shows the Raman spectra of bulk collected with a laser energy of 1.66 eV at 300, 473 and 573 K. In these experiments, the bulk sample was excited with a vertically polarized laser, but the collection was optimized for the horizontal configuration, which greatly minimizes the intensity of the A_{1g} mode. Nonetheless, we can observe that at 300 K in Figure 5.11(a), only the E_{2g} band, the first-order mode, is strongly observed, which is expected since the sample is out of resonance with this specific laser energy. We can observe

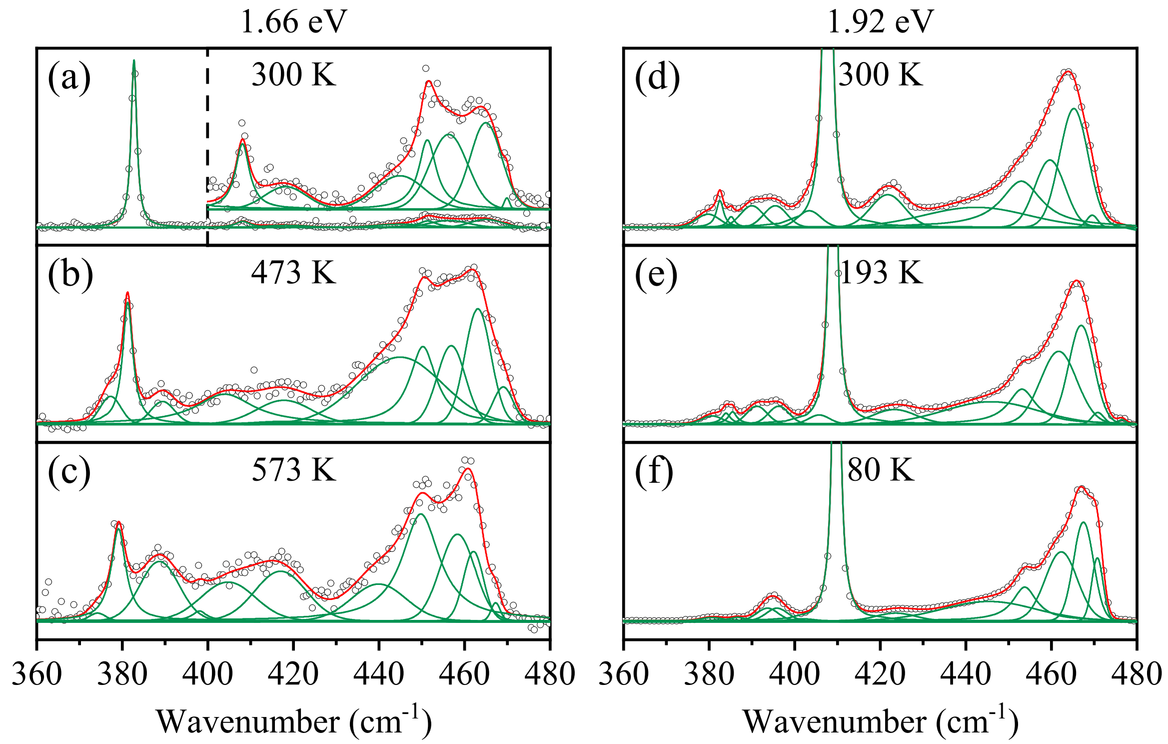

Figure 5.11. Cross-polarized Raman spectrum of bulk obtained using a laser line of 1.66 eV at the temperatures of (a) 300 K, (b) 473 K and (c) 573 K. The A_{1g} mode is attenuated because of the polarization geometry used in the experiments. It is also shown the Raman spectrum of bulk collected with the 1.92 eV laser at temperature of (d) 300 K, (e) 193 K, and (c) 80 K.

the other bands though, but they are minimized compared to the E_{2g} band. According to ref. [194], the X_A transition would have values of 1.82, 1.76 and 1.73 eV at 300, 473 and 573 K, extrapolating the results obtained in their work. Although a laser excitation energy of 1.66 eV is not exactly in resonance with X_A at any of the temperatures present in Figure 5.11, we would still need to consider the resonance window, which becomes broader as temperature increases. Therefore, we are coming into resonance with X_A as the temperature is increased from Figure 5.11(a) to Figure 5.11(c). The same effect can be achieved by beginning with a laser excitation energy above the resonance with X_A at room temperature and decreasing the temperature in order to recover the resonance. We illustrate this result in Figure 5.11(d), (e) and (f), where a laser with an energy of 1.92 eV is used to excite the sample while the temperature changes from 300 to 80 K. We observe that the components of the 2LA band change according to the measurement temperature. From Figure 5.11(a), (b) and (c), as the temperature increases, the contribution from the p_4 peak to the 2LA band becomes more apparent, which is mainly due to contributions from the **KQ** electron-scattering process. Thus, as the temperature is increased, the bulk sample is coming into resonance with X_A.

5.2.3 Bulk MoS_2 with several laser energies and Temperatures

We now turn to the double resonance processes in bulk, which were studied with the same laser energies and temperatures as the 1L sample in section 4.2. Figure 5.12(a) shows the Raman logarithmic intensity color map in the energy range between 370 and 485 cm^{-1}, for laser energies between 1.916 and 2.210 eV and a temperature of 80 K. The most prominent feature is the A_{1g} mode, which presents a strong resonance with the X_A and X_B transitions [180]. It is also observed a strong contribution from the 2LA band, covering the entire laser energy range, where the contributions to the peak can be separated according to the laser energy, being fairly easy to distinguish close to 2.09 eV.

We can extract the excitonic transition energy, E_X, by fitting the Raman excitation profile (REP) of the A_{1g} peak with respect to the laser energy, just as it was done for 1L. The REP is shown in Figure 5.12(b), where we identify X_A and X_B, with their respective fitting

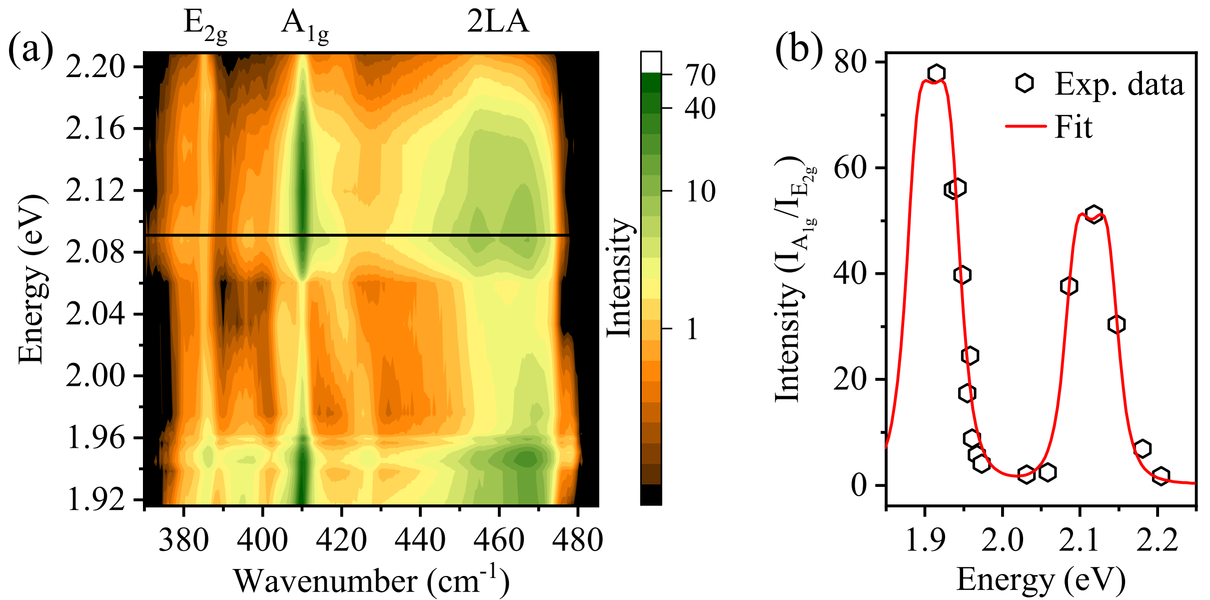

Figure 5.12. (a) Raman intensity map obtained at 80 K, where the *x* axis represents wavenumber, the *y* axis represents the laser energy and the intensity is given by the color map on a logarithmic scale. The black line at approximately 2.091 eV represents the energy of X_B, which is still in the region of measurements. (b) Raman excitation profile of the A_{1g} band in (a), located at approximately 410 cm^{-1}. The intensity is normalized by the E_{2g} band located at approximately 385 cm^{-1}.

Table 5.5. Fitting parameters of the REP in Figure 5.12(b) with equation 3.2.

	C (eV)	E_X (eV)	Γ (eV)
X_A	0.010 ± 0.002	1.887 ± 0.002	0.023 ± 0.004
X_B	0.008 ± 0.003	2.091 ± 0.003	0.022 ± 0.007

parameters presented in Table 5.5. The extracted energy transitions are 1.887 and 2.091 eV for X_A and X_B, respectively. The value obtained for X_A is very similar to the one observed in the literature of 1.884 eV at 80 K [194]. Therefore, we will use the temperature dependence of X_A observed by Dey et al. [194] in order to compare the thermal effects of X_A to the DR bands.

Figure 5.13 presents the positions of p_1 to p_5 as a function of ΔE, just like it was done for 1L in section 4.2. Again, we see a similar trend between the position of each band and ΔE, indicating a strong effect of the excitonic transition in the DR position. We observe an additional feature though, which is readily distinguished in Figure 5.12(a) at approximately 478 cm^{-1}, which we call p_6. The p_6 band is very weak even when compared to other weak features and it appears only in the X_A excitation range, ranging from 1.916 to 1.975 eV, and it was ascribed to either a combination of two LA' phonons at the K point, or to a combination of three TA' phonons at the M point [186].

Either way, p_6 is supposed to be a simple second- or third-order band, where the position of the band is unaffected by the laser energy, but it should be affected by temperature. Therefore, we can see how p_6 behaves as a function of temperature and extract the information of whether it is a combination of two or three phonons. From the fitting of the position of p_6 as a function of temperature, we obtain a thermal coefficient of -0.017±0.002 cm^{-1}/K for the 1.92 eV laser, -0.015±0.002 cm^{-1}/K for the 1.94 eV laser and -0.012±0.001 cm^{-1}/K for the 1.96 eV

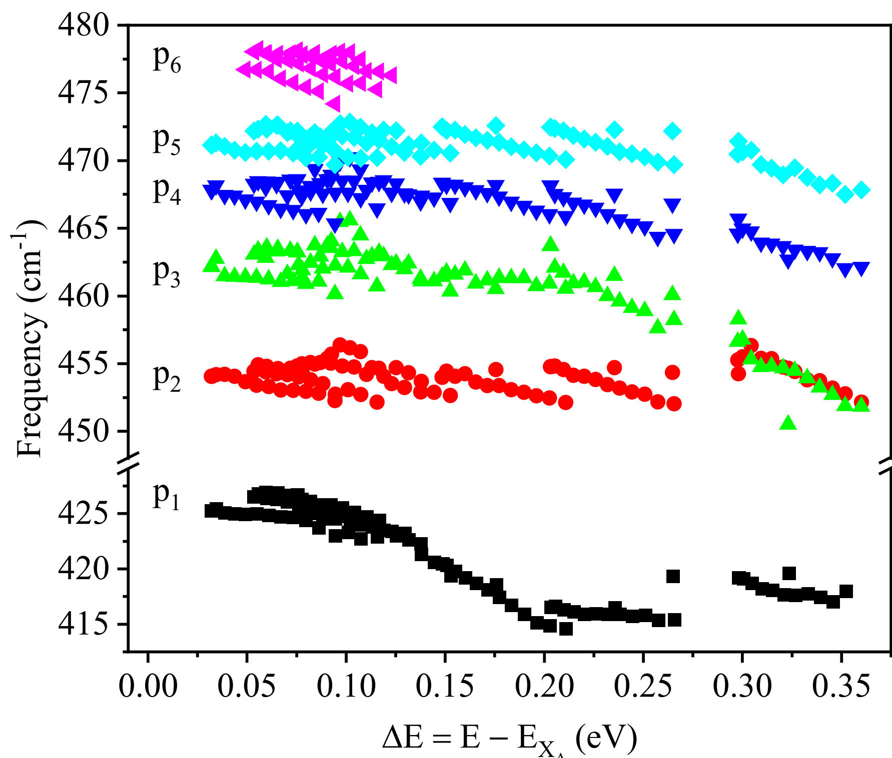

Figure 5.13. Position of the DR bands as a function of the difference between the laser energy and X_A.

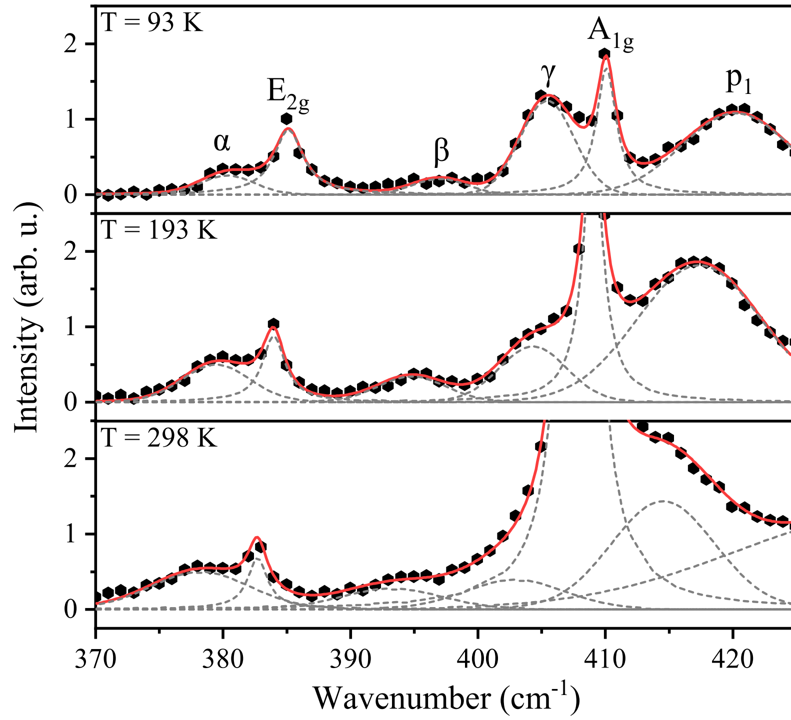

Figure 5.14. Raman spectrum of bulk MoS_2 under a laser excitation energy of 2.03 eV at 93, 193 and 298 K. The long tail contribution observed at 298 K comes from the 2LA band.

laser. These values are fairly consistent with the results we have obtained for the second-order bands of 1L, which would mean that we have a simple second-order band, instead of a third-order band.

Now, we turn the attention to the lower frequency peaks and their behavior. Figure 5.14 shows the Raman scattering of bulk collected under a laser energy of 2.03 eV for the temperatures of 93, 193 and 298 K. Besides the double resonance band p_1 observed for 1L, we observe additional features indicated in Figure 5.14, such as the aforementioned α and β bands at approximately 380 and 395 cm^{-1}, and also another band at approximately 405 cm^{-1}, which we call γ. The peak fittings were performed following a similar procedure as that for 1L, but we chose to share the width between the α, β, and γ features in order to facilitate the fitting procedure. This was justified in the sense that we need to reduce the number of fitting parameters in order to fit every spectrum correctly. Otherwise, the data will present inconsistencies with the generally expected behavior of the Raman bands, such as convoluted bands becoming thinner when the temperature increases.

The α and γ bands were previously associated with the E_{1u}^2 and B_{1u} vibrational modes [160]. However, α is strongly enhanced in 1L, as shown in Figure 5.10, and thus, we associate it with the combination of two TA phonons near the **K** point, where there is a maximum in the pDOS.

We could ask the same question of whether the γ band can be attributed to a phonon combination process as well. Since the possible processes that are active around the **K** point have already been strongly observed for 1L, we are left to associate the γ band to a possible combination of phonons in the proximities of the **M** point. A quick look into the phonon dispersion and pDOS of bulk MoS_2 in Figure 2.8(c) and (e) reveal a maximum around 167 cm^{-1} due to a saddle point in the TA phonon branch around the **M** point. Since the LA branch also presents a maximum around 238 cm^{-1}, the γ band at 405 cm^{-1} can be associated with a combination of an LA phonon and a TA phonon in the proximity of the **M** point. We can associate the γ band to the combination of one TA and one LA phonon in the proximities of the **M** point.

Figure 5.15(a) presents the frequency of all bands in the interval of 370 to 430 cm^{-1} as a function of the laser energy. The position of the A_{1g} and E_{2g} bands as a function of the laser energy remain basically unchanged, with a small variation of 1 cm^{-1}/eV, which is around the error bar for the slopes of the other bands. An interesting aspect is the observation of a very thin band alongside the E_{2g} band, which has been attributed to the E_{1u}^2 vibrational mode [165]. One important characteristic which has been reported in the literature for MoS_2 is the splitting of the degenerate LO and TO phonon branches that form the E_{2g} mode due to the polar character of MoS_2 [253]. Therefore, we use the assignment proposed by ref. [253] instead of the assignment attributed before in ref. [165].

Aside from the first order A_{1g} and E_{2g} modes, we also observe the behavior of the α, β, γ, and p_1 peaks. For the α band, the frequency decreases with the laser energy at a rate of -13 cm^{-1}/eV, which is small compared to p_1, but still relevant. However, the β and γ bands, present a positive rate of change, which is in direct contrast to p_1, p_3, and p_4. Even more interesting is the split of β into two components, one almost constant at approximately 398 cm^{-1} while the other presents an odd dispersive behavior, again increasing in frequency as the laser energy increases.

Figure 5.15(b) and (c) present the position of all the bands in the region between 370 and 430 cm^{-1} as a function of temperature for the laser energies of 1.98 eV and 2.03 eV. The first-order bands present similar behaviors as 1L, where the rate of change is -0.010 cm^{-1}/K for the A_{1g} band while it is -0.013 cm^{-1}/K for the E_{2g} mode. The p_1 band presents a rate of change of more than double the value of the A_{1g} mode, at -0.026 m^{-1}/K and -0.030 m^{-1}/K for the 1.98 and 2.03 eV lasers, respectively. The other bands present, the same (or very close) slope as the first-order bands.

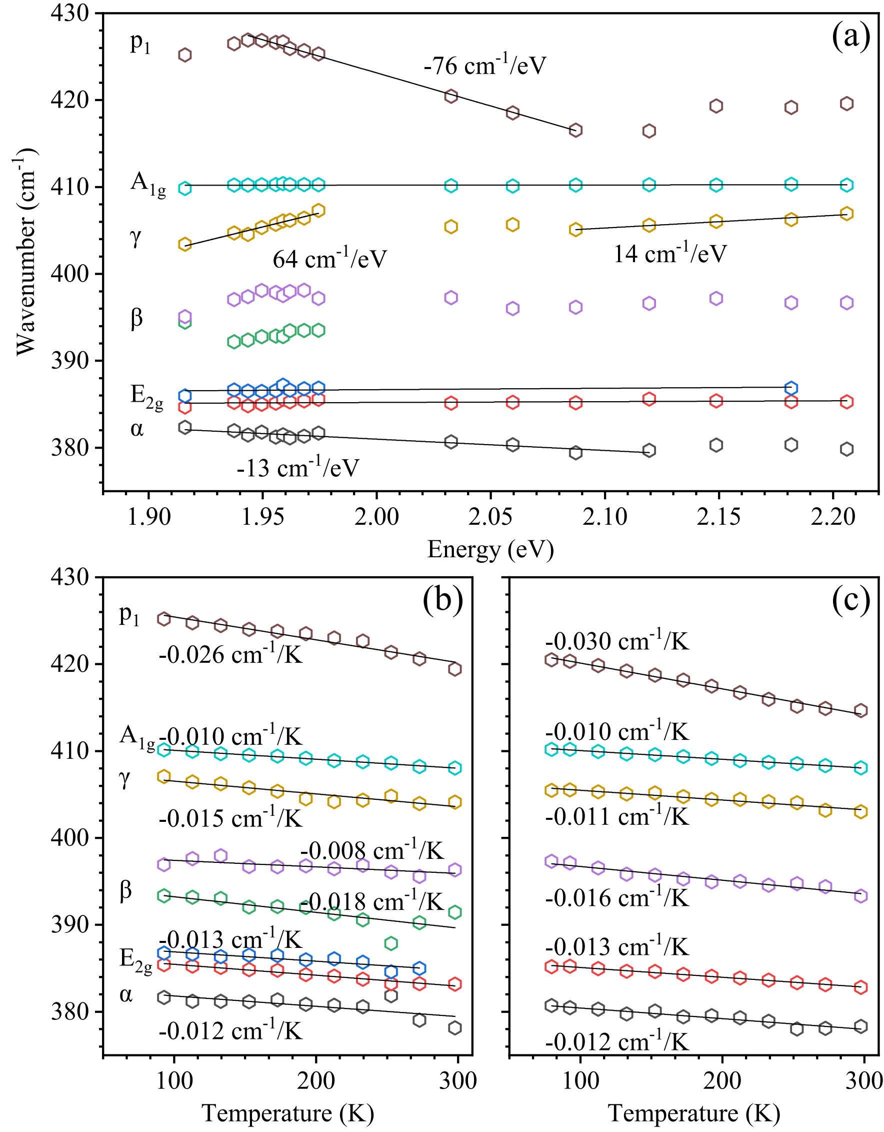

Figure 5.15. (a) Position of each band in the frequency range between 370 and 430 cm^{-1} as a function of the laser energy at 80 K. The solid lines represent a linear fit over an apparently linear behavior, and the slopes associated with each fit are next to the curves. The first order bands present a small variation (about 1 cm^{-1}/eV) which is neglected because it is within the experimental error of the measurements. (b) and (c) represent the position of each band in the range between 370 and 430 cm^{-1} as a function of temperature for the laser energy of 1.98 and 2.03 eV, respectively. In (b) and (c), the positions are linearly fit as a function of temperature and the slopes are presented next to each curve. The error for each slope is in the order of 0.001 cm^{-1}/K.

The fact that bands with such high dispersion with the laser energy as β and γ present slopes similar to the ones of first-order bands is unexpected if we consider the model proposed for 1L. According to the model that we have proposed for 1L, the band is expected to show either a small decay or a constant frequency as a function of temperature, since the $\frac{\partial \omega}{\partial E}$ is positive. In order to analyze the behavior of α, β, and γ, we use a similar process as that used for p_1 to p_6, where we plot the frequency of α, β, and γ as a function of ΔE.

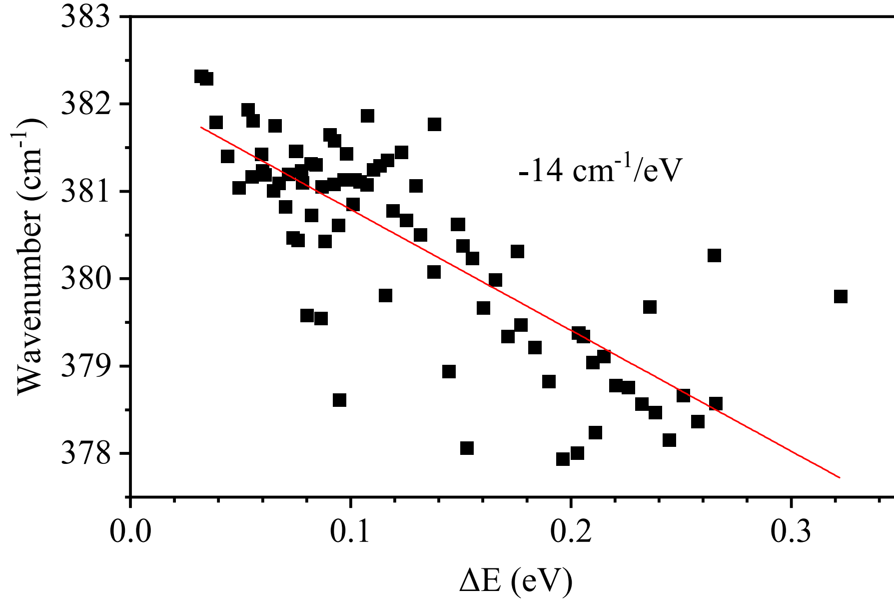

Figure 5.16. Frequency of α as a function of ΔE, the difference between the laser and X_A.

Figure 5.16 shows the position of the α band as a function of ΔE. Similar behavior is observed between the dispersion with purely the laser energy presented in Figure 5.15(a), where the slope between 1.92 and 2.1 eV is -13 cm^{-1}/eV. Since the α band presents a relatively small dispersion with the laser energy, we may apply the model from 1L, which means that this band would present a small decay of approximately -0.004 cm^{-1}/K. Combining the thermal effects of Figure 5.15(b) and (c), we would arrive at a dispersion of approximately -0.004 cm^{-1}/K for the TA phonon branch at the **K** point, which is about half of the value observed for 1L. A smaller value of the thermal slope of the phonon branch may be related to the extra interactions between the layers, which would imply that other phonon decay processes may occur for bulk, compared to 1L.

We mentioned the β band before, and we observed it as for two temperatures in Figure 5.10 measured with a laser very close to X_A. It is possible to observe that there are two components in the β band, which can be better observed in Figure 5.17. We will call the two components β'', for the lower frequency component, and β' for the higher frequency component. In the low energy regime, closer to X_A, the two components are almost degenerate, which can be seen in Figure 5.17(a) for a laser energy of 1.92 eV and in Figure 5.17(b) for a temperature of 93 K. However, as ΔE increases, meaning higher laser energies for Figure 5.17(a) or higher temperatures for Figure 5.17(b), the band splits and the two components can be distinguished. Figure 5.17(c) shows the frequency of β' and β'' as a function of ΔE, for the laser energies close to X_A measured at 80 K and for the laser energies of 1.92, 1.96, and 1.98

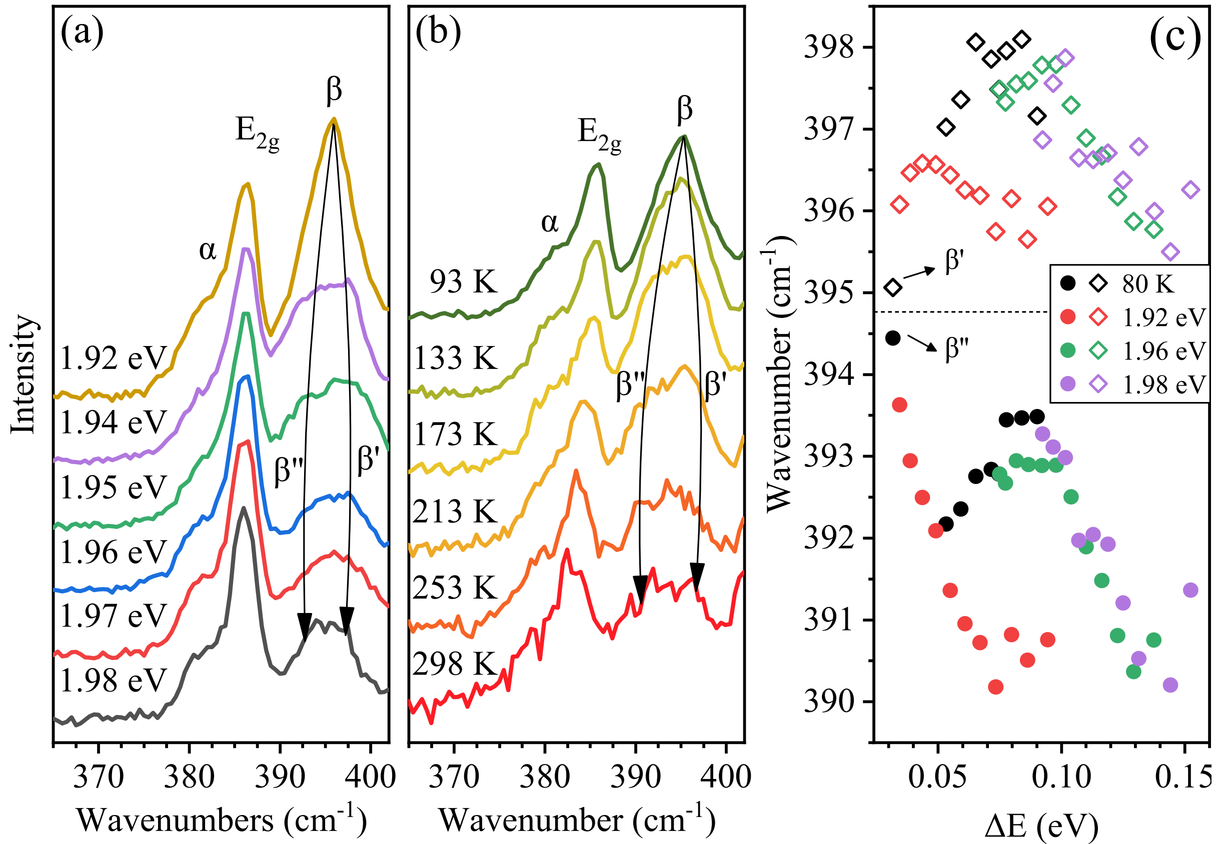

Figure 5.17. The evolution of the components of the β band for (a) laser energies between 1.92 and 1.98 eV at 80 K and (b) temperatures between 93 and 298 K with a 1.92 eV laser energy.

eV. The behavior observed of the frequency of β' and β'' as a function of ΔE is heavily dependent on the laser line utilized.

Going back to Figure 5.17(c), starting with the smaller energy laser in red of 1.92 eV, β' and β'' are nearly degenerate at 394.5 and 395 cm^{-1}. As the temperature increases, the separation between β' and β'' increases as well, until a determined limit is reached at approximately 391 and 396 cm^{-1}, where both bands remain constant. The next laser line, at 1.96 eV, begins closer to the maximum observed at 80 K for both β' and β'', but as temperature increases, both components decrease as well. Finally, the last laser line covering the X_A region at 1.98 eV, follows a similar trend as 1.96 eV, decaying as the temperature increases. After 1.98 eV, the β' component is not seen anymore, and only the β'' component is still active. However, β'' presents only a small dispersive behavior with the laser line and it is strongly affected by temperature, almost compared to a simple second-order band.

We have already associated β to the combination of LA and ZA phonons in the proximity of the **M** point. If we assume that some other scattering process may occur, such as the electron being scattered to two different valleys in the proximity of the **Q** point, we can

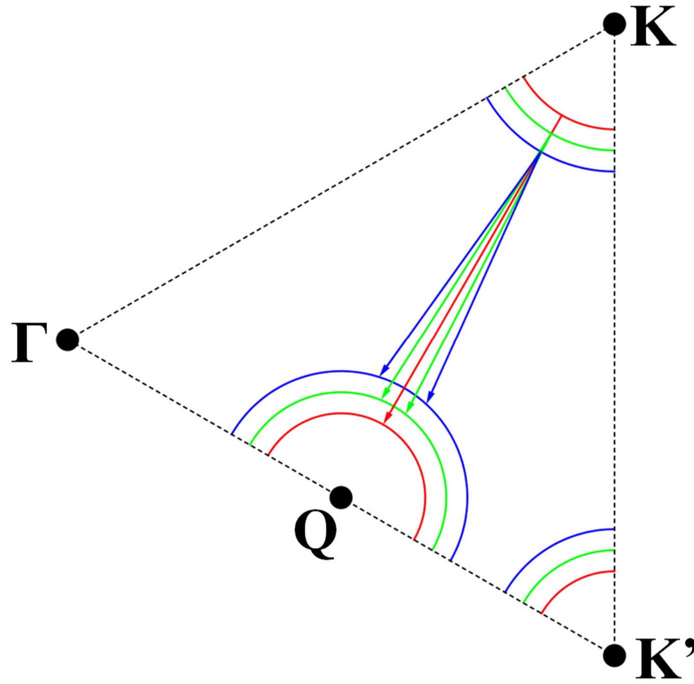

Figure 5.18. Representation of the **KQ** double resonance channel responsible for the β band for three different laser energies.

associate the splitting of β to such phenomenon, which is illustrated in Figure 5.18. For a laser energy below a certain threshold, the electron could only be scattered to the **Q** valley via a single route, since there would not be enough energy to connect the real states leading to a resonant condition, illustrated by the red arrow in Figure 5.18. However, for a laser with sufficient energy, the **K** and **Q** valleys could be connected by two possible processes, involving the LA and ZA phonons in this case, illustrated by the green arrow in Figure 5.18. For increasing laser energies, it would be possible to increase the separation of β' and β'', which is illustrated by the blue arrow in Figure 5.18.

Since bulk has a different scattering channel which involves the valleys near the **Q** point, it could have some implications in the behavior of the band as a function of temperature. It was shown recently that the indirect bandgap in bilayer MoS_2 shifts to higher energies as temperature increases [89]. We believe that a similar process may also be occurring for bulk MoS_2, where the shift of the indirect bandgap with temperature may be affecting the resonance condition for the β and γ bands, while the p_1 and α bands are tuned by the resonance with the excitonic transition.

The γ band presents an odd behavior as well, wherein Figure 5.15(a) it presented a high dispersion of 64 cm^{-1}/eV between the laser energy range of 1.92 and 1.98 eV while it showed a small dispersion of 14 cm^{-1}/eV between the laser energy range of 2.09 and 2.21 eV. Figure 5.19(a) shows the Raman spectrum of bulk collected under a 1.96 eV laser illumination at

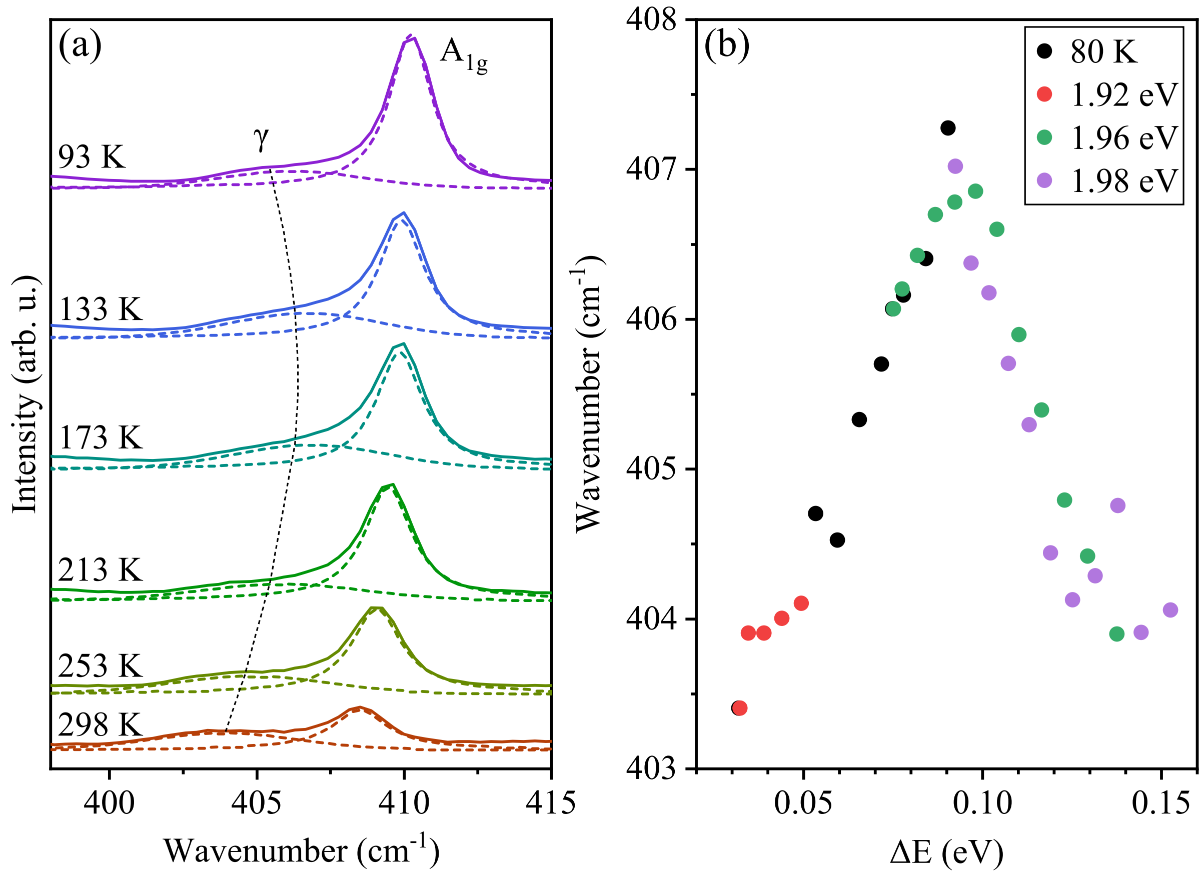

Figure 5.19. Raman spectrum of bulk under the illumination of a 1.96 eV laser obtained for different temperatures of the sample between 93 and 298 K, where the A_{1g} and γ bands are fitted. The dashed line is a guide to the eyes. (b) Frequency of the fitted positions of the γ band as a function of ΔE, for laser energies between 1.92 and 1.98 eV measured at 80 K (black dots), and collected with the 1.92 (red dots), 1.96 (green dots) and 1.98 (violet dots) at temperatures ranging from 80 to 298 K.

temperatures ranging from 93 to 298 K, where we see both the A_{1g} and γ bands. The A_{1g} band presents the known linear behavior explored before, but the γ band presents another behavior, where its position increases with temperature and it decays afterward. In Figure 5.19(b), the position of the γ band is plotted as a function of ΔE. The γ band presents an increasing linear behavior as a function of ΔE until 0.1 eV, which is the limit of our measurements at 80 K corresponding to the 1.98 eV laser. The measurements with the 1.96 eV laser mimic the observed behavior of the measurements at 80 K, but the band position decays after 0.1 eV, which can be connected to either the resonance process or to temperature effects. The measurements with the 1.98 eV laser present similar results as those of the 1.96 eV laser, however, and the decay of the band as a function of ΔE is confirmed.

We associated the γ band to a combination of LA and TA phonons close to the **M** point. Since the LA and TA phonon branches present a positive derivative leaving the **M** point and

going to the **K** point, as the laser energy increases, the wavevectors connecting the **K** and **Q** points become smaller. Therefore, the corresponding phonons become more energetic, which leads to a combination of phonons with increasing frequency, when we think only about the photon energy. When the temperature effects are considered, the dispersion of the band will be affected by the double resonance process, but it will also be affected by the thermal effects as well.

In summary, future calculations considering the behavior of the **Q** valley as a function of temperature are still needed to understand the behavior of α, β, and γ, but the general trend of the observed bands agrees well enough with the proposition of a shift in the valleys near the **Q** point.

The last important feature that we discuss for bulk, is the feature centered at approximately 177 cm^{-1}, which is associated with the difference between the A_{1g} and LA phonon branches around the **M** point, that we call δ. Figure 5.20 shows the Raman spectra of bulk collected with laser energies of 1.92 eV, 2.03 eV, and 2.09 eV, at temperatures of 93, 193 and 298 K, where we see the spectral region between 370 and 430 cm^{-1}, but also the δ band at

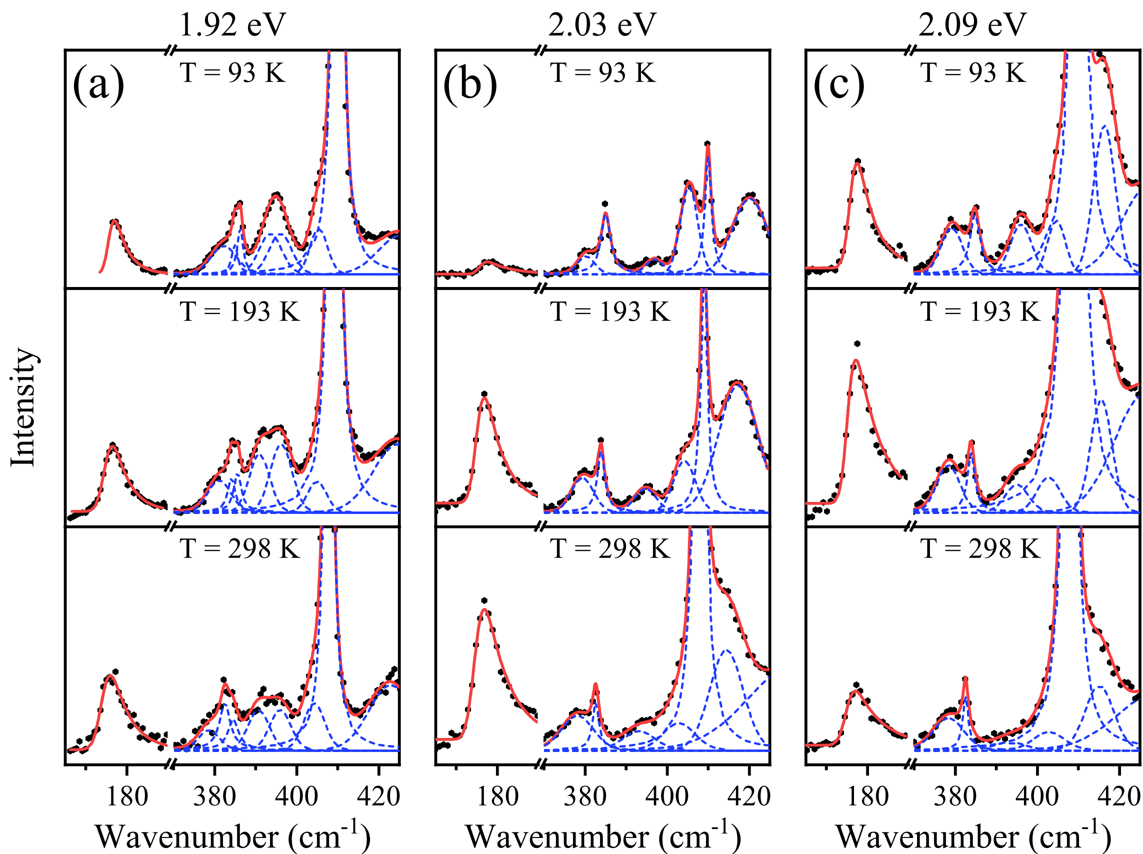

Figure 5.20. The Raman spectrum of bulk collected with laser energies of (a) 1.92, (b) 2.03 and (c) 2.09 eV at 93, 193 and 298 K.

177 cm^{-1}. The δ band presents a very small frequency increment with either the laser energy or temperature effects, and it is also asymmetric, which leads to the use of a modified Gaussian function that had an exponential decay to fit this peak. Therefore, we will not focus on the frequency of the δ band, but rather we focus on its intensity changes with both the laser energy and temperature, as it is shown in Figure 5.20. The intensities are calibrated by the intensity of the E_{2g} mode, which is not affected appreciably by the resonance with X_A and X_B.

Since the δ band comes from the difference between two phonons, its intensity depends on the probability of the lowest energetic vibrational level, the LA(**M**) phonon, being occupied, which will be destroyed in order to produce the scattered light. Since the probability of occupation of a vibrational level increases as temperature increases, it would be expected that as temperature increases, the intensity of this band would increase as well. Although this behavior is observed for the 2.03 eV laser in Figure 5.20(b), the other laser energies tell completely different stories, where the intensities decrease as the temperature increases. Therefore, this band is also tuned by the resonance condition much like all the other double resonance bands as well.

Figure 5.21 presents the intensity of δ as a function of ΔE for the measurements at 80 K and the temperature dependence of measurements with the 2.03 and 2.09 eV lasers. The intensity profile of the measurements at 80 K reveals a clear maximum near 0.2 eV, corresponding to the resonance with X_B, at 2.091 eV. The intensity of δ is greatly enhanced for the 2.03 eV laser at higher temperatures because the band is coming into resonance exactly as temperature increases and shifts X_B to lower energy at the same time that the LA(**M**) phonons become more populated. On the other side, for the 2.09 eV laser, δ is close to the maximum at

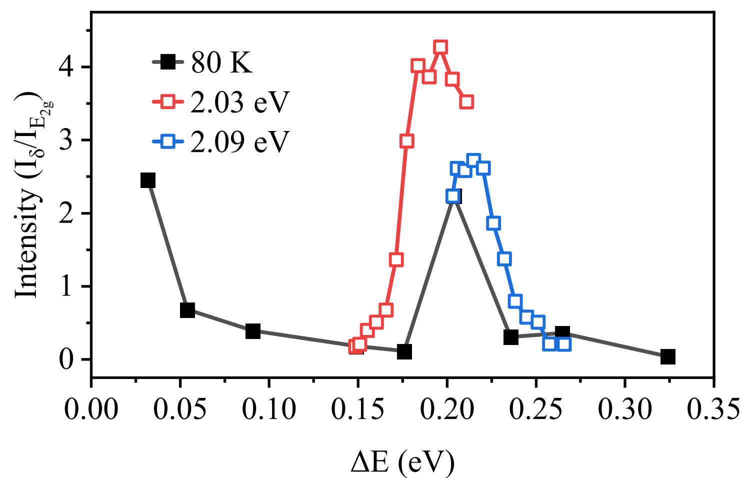

Figure 5.21. The intensity of the δ band as a function of ΔE. The black filled squares correspond to measurements at 80 K varying the laser energy, while the red and blue open squares correspond to measurements with a 2.03 and 2.09 eV laser, respectively, varying the temperature.

approximately 0.22 eV, around 130 K, and it quickly goes out of resonance as temperatures increases, due to the X_B shift to lower energies thanks to thermal effects. Therefore, even as the population of the LA(**M**) phonons increases, the intensity of δ will quickly decrease.

The knowledge provided by the δ band is important for the study of the Raman spectrum of defective TMDs since the defect induced bands have frequencies very close to those displayed by the bands resulting from the difference of frequencies.

To summarize the features observed and explored for bulk MoS_2 in this section are included in Table 5.6, where we include the names, positions, and assignments of the double resonance bands.

Table 5.6. Names, Assignments, and frequencies of the second-order features of bulk MoS_2.

Name	Assignment	Frequency (cm^{-1})	Reference
δ	A_{1g}(~**M**) - LA(~**M**)	178	[190]
α	2TA(~**K**)	380	[186]
β	LA(~**M**)+ZA(~**M**)	395	This work
γ	LA(~**M**)+TA(~**M**)	405	This work
p_6	2LA'(**K**) or 2LA'(**M**)	480	This work

5.2.4 Conclusions

In conclusion, we presented a comprehensive study of the Raman spectrum of few-layers and bulk MoS_2 covering the range between approximately 160 and 480 cm^{-1}, where we show the presence of several bands that can be related to either first or second-order/combination processes enhanced by the resonance with the excitonic transition.

This work shows the importance of the contribution of the other possible scattering channels in MoS_2, which are relevant for bulk, as much as it is for 2L, 3L and *n*L as well. We mainly show other possibilities of attributions that are not considered in the literature and also that preserve the Raman selection rules, where infrared-active modes do not need to be involved if we just consider other possibilities as well.

5.3 Temperature study of defect induced Raman bands in MoS_2 samples under laser resonance

This section is devoted to the study of the defect induced bands in the Raman spectrum of 1L and bulk MoS_2 when the laser is in resonance with the excitonic transition energy. Synthesized or natural bulk crystals of MoS_2 present a small concentration of sulfur vacancies [254], but, it is still non-negligible. We already discussed in chapter 3 the effects of

defects in the Raman spectrum of MoS_2, where the defect induced bands are very weak, even when the sample is almost in resonance with the laser energy. Therefore, we would expect that in the low defect density regime, or high L_D, the Raman spectrum of MoS_2 would be dominated by the presence of mostly the first and second-order Raman peaks.

Figure 5.8 showed that for an exfoliated sample, which is our reference for a low defect density sample quality, we only see a small contribution from the LA band at 300 K. When the temperature is reduced to 80 K, however, the intensity of the LA band increases expressively, to the point where it equals the intensity of the 2LA band and surpasses the intensity of the E' band at approximately 388 cm^{-1}.

We explore this result further, where we measured the Raman spectra of 1L using two laser lines and changing the temperature in the range of 80 to 300 K. Further, we also measure the Raman spectrum of a defective 1L using a single laser excitation energy of 1.96 eV and changing the temperature from 80 to 400 K.

5.3.1 Defect induced bands in the Raman spectra of natural MoS_2 at low temperatures

For laser energies close to X_A or T_A, the Raman signal is strongly suppressed by the PL signal, which makes the measured spectra very noisy and difficult to interpret. Therefore, instead of working close to the resonance with X_A or T_A, we move to laser energies closer to X_B, where the PL intensity is a small fraction of the X_A intensity and the spectra measured in this energy range present easily discernable features. Figure 5.22(a) shows the Raman spectrum of 1L between 140 and 260 cm^{-1} collected in the energy range between 2.03 and 2.21 eV at 80 K. In this case, we can see three main features, the δ, TA(**K**) and the LA bands.

According to references [177] and [53], the range between 140 and 260 cm^{-1} is composed of at least 10 bands altogether. The fitting procedure to converge so many peaks in such a small spectral range is highly unreliable. We also have bands presenting strong convolution, which makes it extremely difficult to analyze. Therefore, instead of fitting every single component in this range, we propose the analysis of the integrated area of the defect induced bands and also the subtractive band δ, which would produce a much more reliable and reproducible procedure.

To obtain a quantitative analysis of the integrated intensity, we fit the asymmetric δ band with a modified Gaussian function to show an exponential decay in the high-frequency range, characteristic of this band. The choice of an asymmetric function relates to the pDOS of the A_1'(~**M**) branch which is relatively sharp, and the pDOS of the LA(~**M**) branch, which is

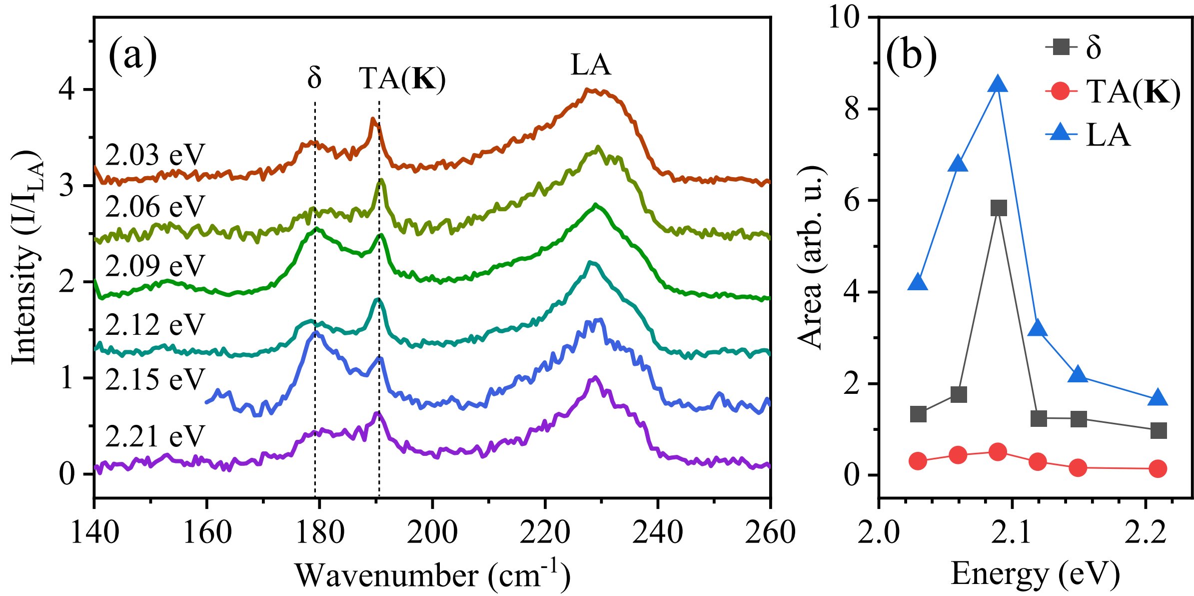

Figure 5.22. (a) Raman spectra of 1L in the spectral range of 140 to 260 cm^{-1} collected with several laser energies at 80 K. The three main features in this range are marked and named. The intensities are normalized by the LA band for clarity. (b) Integrated intensities of the δ (solid squares), TA(**K**) (solid circles) and LA (solid triangles) bands as a function of the laser energy. The intensity is normalized by the intensity of the E' band.

very asymmetric. The combination of both densities of states would lead to a line shape that is asymmetric in shape and can avoid the use of more than one function to fit this particular peak. The definition of the modded gaussian peak can be found in Appendix D. The TA(**K**) band is fitted with a single gaussian since this band presents a characteristic thin contribution. The asymmetric LA band is fitted with three components, one biGaussian at 225 cm^{-1} and two Gaussians around 230 and 235 cm^{-1}. The biGaussian represents the contribution from the van Hove singularity to the LA band, while the Gaussians curves represent the contribution from the double resonance LA(~**K**) and LA(~**M**) bands, discussed in chapter 3. The meaning for the choice of a biGaussian, which has two different widths at half maximum, is to account for the asymmetric shape of the van Hove singularity in the pDOS related to the saddle point between the **K** and **M** points in the LA branch (see Figure 2.8(d)). The definition of the biGaussian function used for the fitting is presented in Appendix D,

Figure 5.22(b) shows the integrated area of the δ, TA(**K**) and LA bands as a function of the laser energy. We see a maximum at approximately 2.09 eV, corresponding to the resonance with X_B, similar to bulk. We would expect then, that the subtractive band δ and the LA bands show a strong enhancement when the laser energy approaches the resonance with the excitonic level. Meaning that both δ and LA bands are strongly enhanced near the resonance with X_B. This is also true for X_A, as it was shown in Figure 5.8 and Figure 5.9, where the intensity of the

LA band is extremely high, however, the presence of a strong PL along with a very strong elastic scattering signal further mask the presence of the defect induced bands.

5.3.2 The behavior of the defect induced and δ bands as a function of temperature for 1L

In order to check the behavior of the Stokes/Anti-Stokes band δ and the defect induced TA(**K**) and LA bands, we have measured the Raman spectra with two laser energies close to X_B, at 2.03 and 2.09 eV, and in the temperature range between 80 and 298 K.

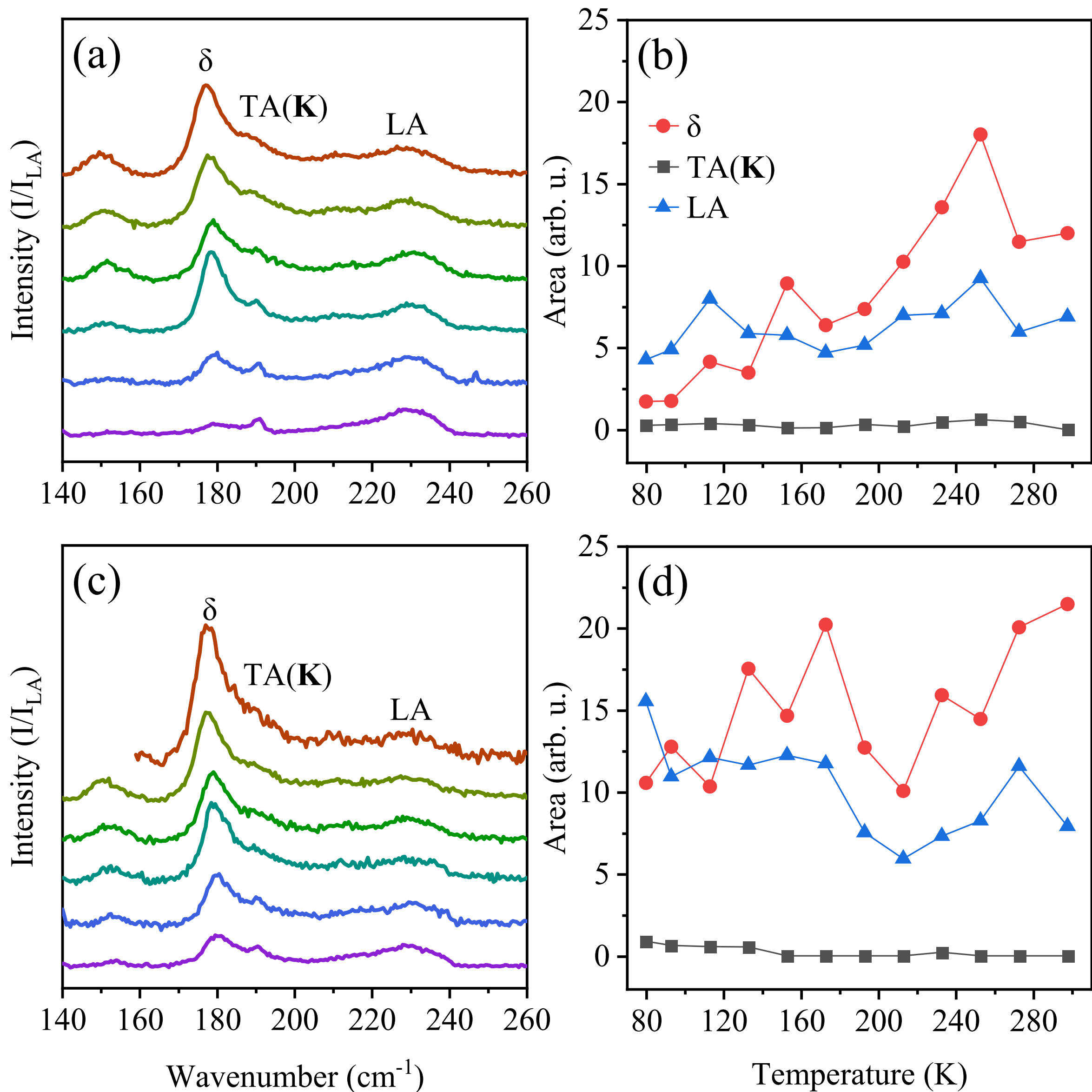

Figure 5.23. (a) Raman spectra of 1L between 140 and 260 cm^{-1} collected under a laser energy of 2.03 eV at temperatures ranging from 93 to 298 K. The spectra are normalized by the intensity of the LA band. (b) Area of the three main components from (a) (δ, TA(**K**) and LA) as a function of temperature. (c) Same as (a) but with a laser energy of 2.09 eV. (d) Same as (b) but corresponding to the spectra at (c).

Figure 5.23(a) shows the Raman spectra of 1L for temperatures from 93 to 298 K, between 140 and 260 cm^{-1} for the 2.03 laser, where the intensity is normalized by the LA band for better visualization. From the start, we observe the contribution from the δ band increasing as temperature increases, following the same trend as bulk. The TA(**K**) band disappears as temperature increases, being overwhelmed by the δ band. The LA band is not much affected by the temperature effects, however, remaining almost constant as temperature changes. We also see the band at 150 cm^{-1}, corresponding to the E'-TA(**K**) band, which is strongly affected by temperature effects.

Figure 5.23(b) shows the integrated area of the three main bands, δ, TA and LA, as a function of temperature for the 2.03 eV laser, where the intensity is normalized by the intensity of the E' band. The solid points correspond to the fitted values of each band as a function of temperature. One could easily realize that the LA and TA bands remain almost constant as temperature increases, while the δ band increases by almost five-fold.

Figure 5.23(c) shows the Raman spectra of 1L for temperatures of 93 to 298 K, between 140 and 260 cm^{-1} for the 2.09 laser, where the intensity is normalized by the LA band again for clarity. Now, similar to what we observed for bulk, the δ band is already amplified even at the very low temperature of 93 K, but, as temperature increases, the intensity of the δ band increases as well, in contrast to the results from bulk. Figure 5.23(d) shows the integrated area of the δ, TA and LA bands normalized by the E' band intensity as a function of temperature, for the 2.09 eV laser. While the intensity of the δ band increases as a function of temperature, the intensity of the defect induced bands are actually decreasing, which indicates that the defect induced bands are going out of resonance. Since the sample has a very low defect concentration, we expect that the defect induced bands would show this big intensity only when the resonance condition with X_A or X_B is achieved.

5.3.3 Defect induced bands in defective samples under resonance at low temperatures

Further, we explore the same results for a defective sample grown by Chemical Vapor Deposition assisted by sodium cholate [255,256], which was discussed in section 4.3.2. Figure 5.24(a) shows the measured Raman and PL spectra of a defective collected with a 1.96 eV laser for temperatures between 120 and 400 K in the spectral range of 1.95 to 1.55 eV. Figure 5.24(b) shows the extracted Raman spectra for each temperature as well. From Figure 5.24(a), we can observe the resonance behavior with the excitonic transition T_A. As the temperature increases, the PL center redshifts, exactly like we observed for the exfoliated sample.

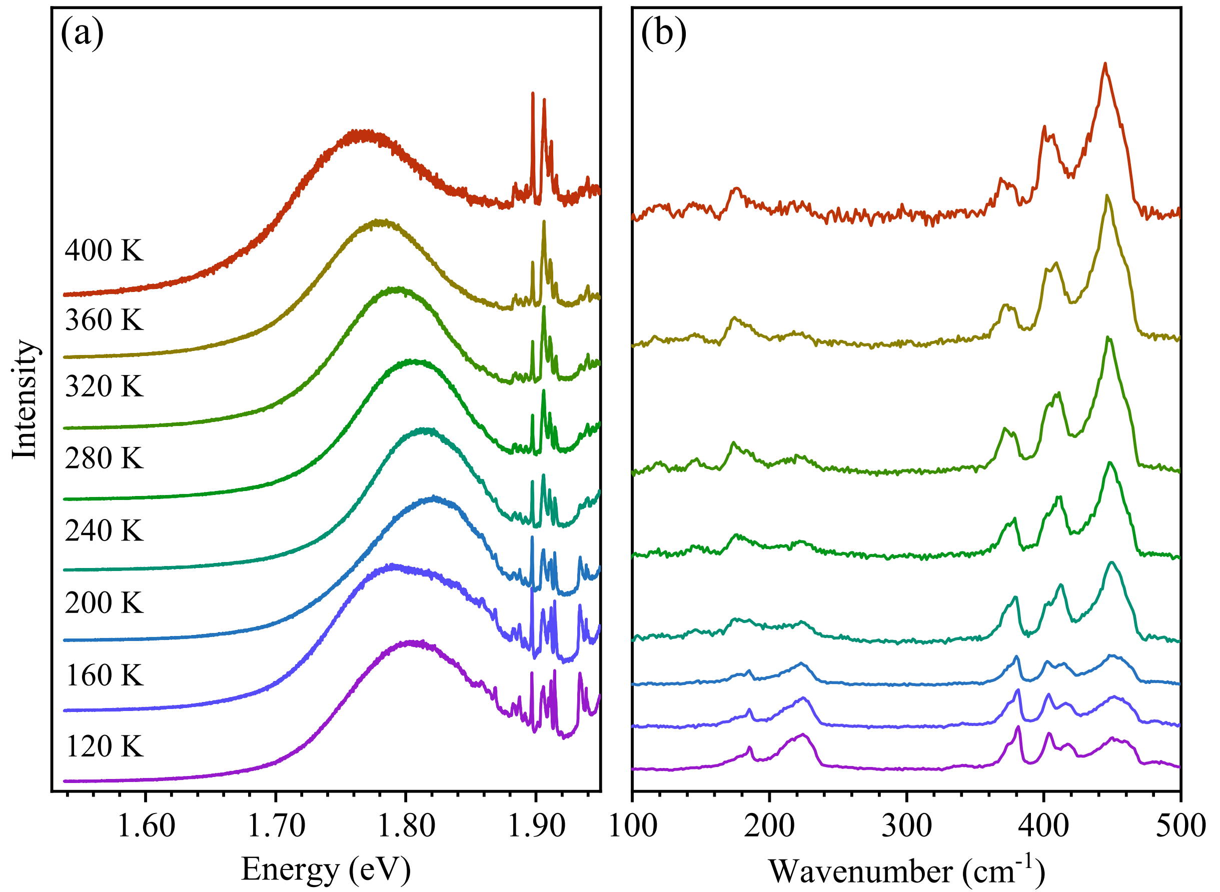

Figure 5.24. (a) Measured spectra of the defective sample for the temperature range between 120 and 400 K using a 1.96 eV laser. The intensity is normalized by the intensity of the PL peak around 1.8 eV. (b) Extracted Raman spectra from (a). The intensity is normalized by the intensity of the E' band.

Figure 5.25 shows the PL peak position from Figure 5.24(a) as a function of temperature, compared with the emission of the exfoliated monolayer in section 5.1.3. The range between 200 and 400 K is very well behaved and presents a linear decay, with a slope of -0.28 meV/K, very similar to the results from the exfoliated sample at approximately -0.25 meV/K. We do not know a reason for the anomalous behavior of the PL peak in the temperature range of 100 to 200 K, but a possible explanation may be related to the resonance with a combination of vibrational levels [126,127].

We now turn to the analysis of the defect induced and subtractive bands in the range between 170 and 260 cm^{-1}. From Figure 5.24(b), we can see that as the temperature increases, the defect induced bands become less intense, and the δ band becomes more intense. The intensity of each spectrum is normalized by the intensity of the E' band. Since the laser energy is very close to X_A and X_B, the E' band is a good normalization standard because it presents no resonance with X_A and X_B. Therefore, we can use it to quantify L_D in a more concise way.

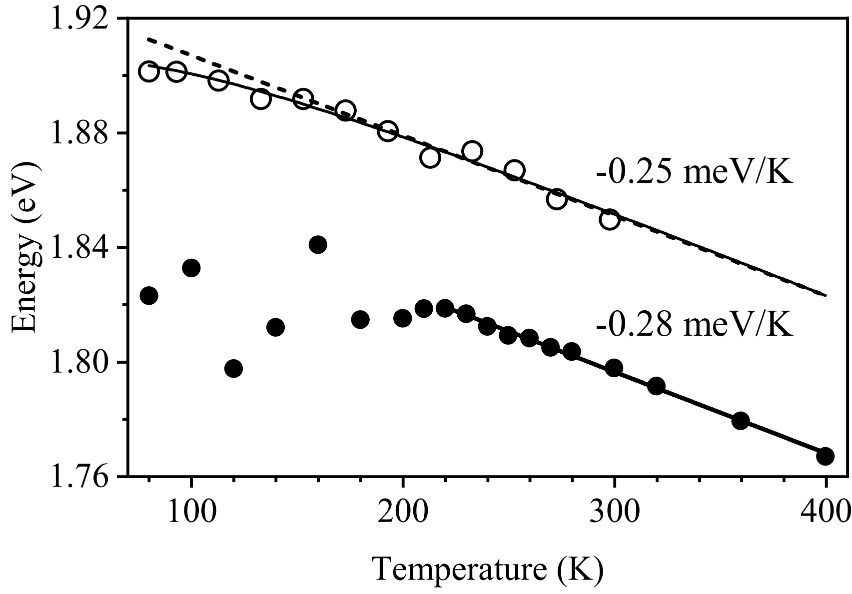

Figure 5.25. Position of the PL peak for the defective sample as a function of temperature (solid circles), compared with the position of T_A of the exfoliated sample in section 5.1.3 (empty circles). The solid line used to fit the position of T_A for the defective sample is a linear adjust with a slope of -0.28 meV/K. The solid line used to fit the position of the exfoliated sample is the same presented in section 5.1.3, while the line has a slope of -0.25 meV/K.

Figure 5.26(a) presents the intensity of the A_1', δ, TA(**K**) and LA bands normalized by the intensity of the E' band. The A_1' band slowly comes into resonance with X_B as the temperature increases, since X_B is shifted both by temperature and defect effects. On the other hand, the defect induced bands, are steadily coming out of resonance, following a similar behavior that was observed for 1L with the 2.09 eV laser. Since the laser is slowly coming out of resonance with the excitonic transition observed in Figure 5.25 as the temperature increases, we can say that the defect induced bands are still heavily dependent on the resonance with the laser energy for their observation, even when L_D is considerably low.

Now, considering the relation between L_D and the intensity ratio $\frac{I(LA)}{I(E^{'})}$ given by equation 4.4, we may now find a new constant $C(E^{'})$ for the 1.96 eV laser. Since $L_D = 8.6 \pm 0.6\ nm$, and $\frac{I(LA)}{I(E^{'})} = (0.73 \pm 0.05) - (0.0010 \pm 0.0002)T$, we can estimate the value of $C(E^{'}) = (47 \pm 4) - (0.064 \pm 0.015)\, T\, nm^2$ for the 1.96 eV laser. At 80 K, $C(E^{'}) = 42\ nm^2$, and in contrast with the value obtained for the 2.33 eV laser, this value is almost 40 times bigger, revealing the importance of a laser in resonance with the excitonic transition in order to correctly quantify the presence of defects in the sample. The contribution from temperature effects is $C(E^{'})(T) = -0.064T\, nm^2$, which can reduce the constant by up to 26 nm^2 in our temperature range. Although this would mean a new constant of 21 nm^2, this value is still 20

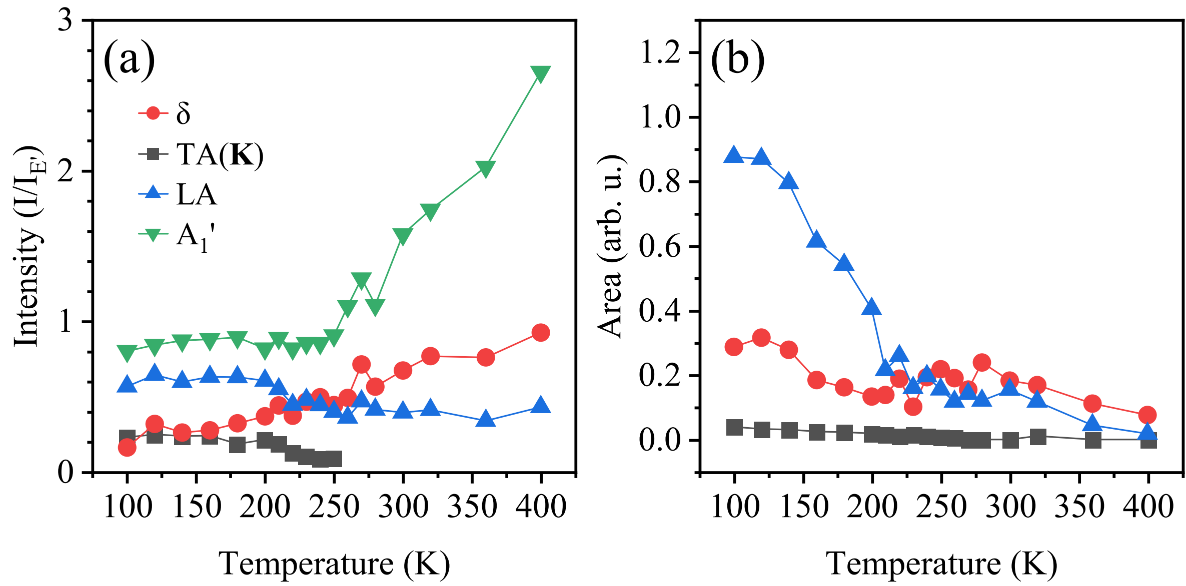

Figure 5.26. (a) Intensities of the A_1', TA(**K**), δ and LA bands normalized by the intensity of the E' band as a function of temperature. (b) Normalized area of the TA(**K**), LA and δ bands as a function of temperature.

times bigger than the one reported for the 2.33 eV laser of $C(E^{'}) = (1.11 \pm 0.08)\ nm^2$ [177], revealing that even at elevated temperatures the intensity of the defect induced bands is still much higher by a simple laser choice. We can also use the same procedure to calculate the coefficient $C(E^{'})$ for the TA band, where $\frac{I(TA)}{I(E^{'})} = (0.73 \pm 0.05) - (0.0010 \pm 0.0002)T$, and $C(E^{'}) = (28 \pm 4) + (0.064 \pm 0.015)T$.

The subtractive band δ presents a steady increase with temperature, consistent with the previous observations of 1L for the 2.03 and 2.09 eV laser energies. In this case, we can conclude that this band is more affected by temperature effects for 1L than it is for bulk samples. This is especially true since δ is always increasing in intensity regardless of the laser energy we used for 1L, in the proximities of T_A, X_A, and X_B. Since the intensity of the δ band increases as the temperature increases, the area it covers in the spectrum will also increase, due to its intrinsic asymmetric shape. Therefore, as temperature increases, the δ band will mask the presence of the defect bands, becoming the most prominent band in the region between 140 and 260 cm^{-1}, which is the result presented in Figure 5.26(b).

6. Optical properties of WS_2, $MoSe_2$, and their heterostructure

This chapter is devoted to the investigation of the optical and electronic properties of monolayers of WS_2 and $MoSe_2$ and the heterostructure formed by the stacking of these two materials. We dive into the photoluminescence spectrum of the samples first, in order to understand the interlayer interaction in the heterostructures. We investigated the characteristics of the excitonic transition as a function of the sample temperature. The PL spectrum was observed at different points in the heterostructure, to observe how the interlayer interaction can affect the electronic structure of each sample. From that point on, we deal with the resonant Raman signal of the specific points that present higher or smaller interactions between the samples and explore the topic further by comparing the PL and Raman signals at different temperatures and laser energies.

Much like the Raman spectrum of MoS_2 presents a strong resonance with X_A or T_A, the Raman spectrum of WS_2 and $MoSe_2$ presents a strong resonance with X_A and T_A as well, as it has been shown for 1L, few-layers and bulk of these materials [60–62,117,118,162,181,219]. A few important properties of WS_2 and $MoSe_2$ have not been explored though, such as the double resonance processes in these TMDs, and how temperature can affect these processes. In the next sections, we deal with these issues, starting with WS_2, and moving to $MoSe_2$. The final section of this chapter is devoted to the study of the heterostructure formed by the WS_2 and $MoSe_2$ flakes, where we measure the Raman spectrum and observe the interlayer coupling between each flake and the effects observed in the Raman spectrum.

6.1 Raman and photoluminescence measurements on WS_2

From Figure 2.6, we can extract the position of X_A, X_B, and X_C of WS_2 at room temperature, where we find that X_A = 2.0 eV, X_B = 2.4 eV and X_C = 2.8 eV. Using what we learned from MoS_2, one easy way to recover the resonance with the laser energy is to reduce the sample temperature in order to increase the electronic transition energy. This phenomenon is easily illustrated in Figure 6.1, where for two laser energies of 2.18 and 2.54 eV, slightly above X_A and X_B for this material, the Raman spectra are enhanced by several times compared to that at 320 K. One detail in particular when comparing Figure 6.1(a) and Figure 6.1(b) is the fact that the bands that show enhancement for X_A are different from the bands that show enhancement for X_B, revealing an intricate possible double resonance behavior for this material.

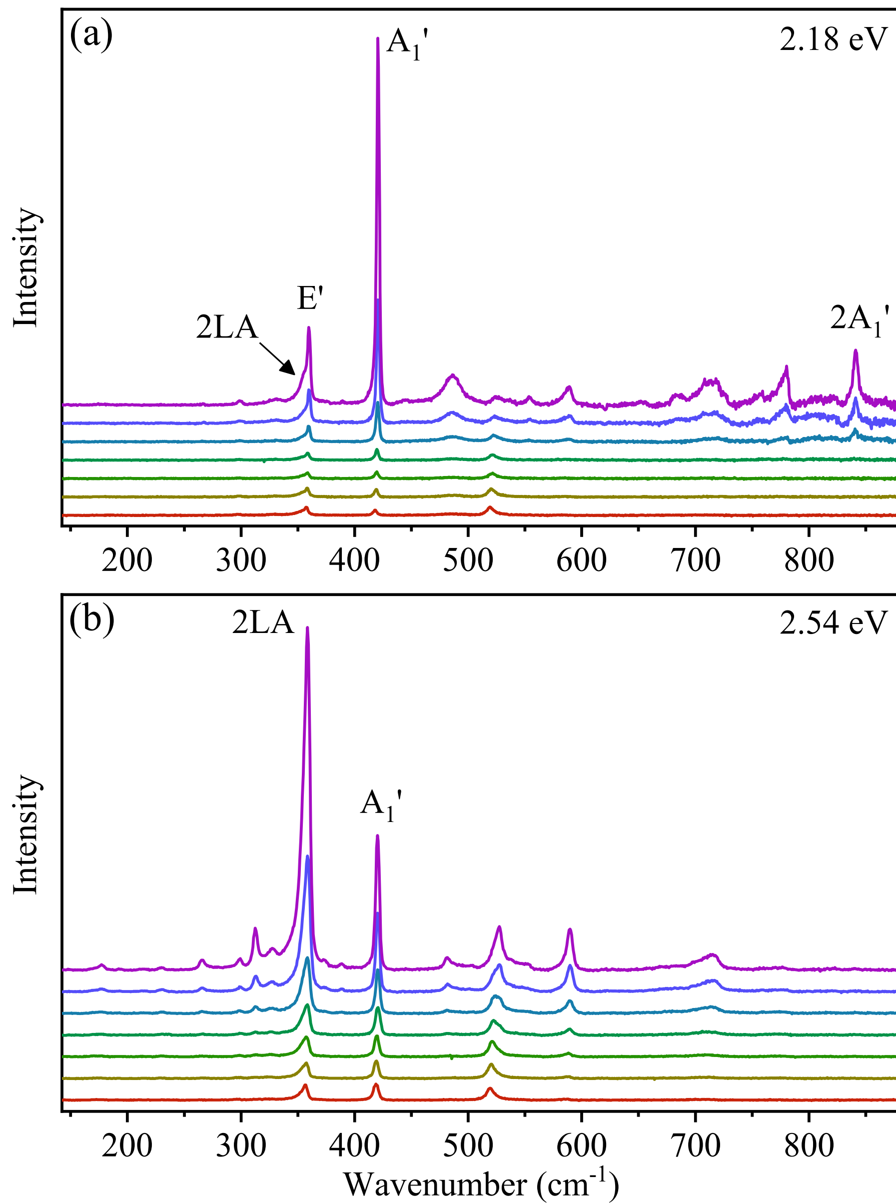

Figure 6.1. Raman spectra of WS_2 collected under (a) 2.18 eV and (b) 2.54 eV excitation for temperatures ranging from 320 K (bottom) to 80 K (top).

Recent resonance Raman measurements of WS_2 reveal a rich structure of features for laser energies in the proximities of X_A and T_A [219]. Moreover, the features related to the zone center phonons are more enhanced, especially the band associated with the combination of two A_1' phonons, $2A_1$'. The results observed in ref. [219] are similar to the results we observed here in the temperature range between 80 and 160 K in Figure 6.1(a), where the intensity of the $2A_1$' band is very intense near 80 K, and it is almost as intense as the E' band. In contrast, the bands associated with the combination of acoustic phonons in the edges of the Brillouin zone are not very intense, and even the 2LA band is diminished compared to the intensity of the A_1' band.

Figure 6.1(b) shows the Raman spectrum collected under the 2.54 eV laser for temperatures ranging from 80 to 320 K. At 80 K, the position of X_B shifts to higher energy compared to 320 K [257]. Therefore, starting from 320 K in Figure 6.1(b) and going to 80 K, we restore the resonance with X_B. We can observe the presence of several peaks, but the most enhanced bands, in this case, are associated with the combinations of acoustic phonons at the zone edges. The spectrum of WS_2 at 80 K in Figure 6.1(b) is very similar to the spectrum of WS_2 collected with a 2.41 eV laser, a common laser used to probe and characterize WS_2 [61,119], where the intensity of the 2LA band at approximately 356 cm^{-1} is extremely enhanced compared to the 2.18 eV laser. Following the assignment proposed for MoS_2, we believe that the main contribution to the 2LA band for WS_2 should come from the saddle point in the LA branch between the **K** and **M** points. Although there should be some dispersive bands for the 2LA band, it has not been reported so far in the literature, and we did not observe any dispersive behavior of the 2LA band with the laser or temperature. We summarize the position of each band and their respective assignment in Table 6.1, where we use the irreducible

Table 6.1. Assignment of all the bands observed for the 2.18 and 2.54 eV lasers at 80 K.

Band assignment	Band position (cm^{-1})	
	2.18 eV	2.54 eV
LA(**SP**)	178	177
E''_2-TA(**K**), E''_2+ZA(**K**)		193
A_1'-LA(**K**)		213
A_1'-LA(**M**)		230
2ZA(**M**)	266	266
TA+ZA(**K**)	299	299
LA+TA(**M**)		313
LA+TA(**K**), LA+ZA(**K**)	331	328
2LA(**SP**)	355	356
E’(**Γ**)	360	360
E'_1(**M**)		373
A_1'(**K**)		389
A_1'(**Γ**)	421	421
E''_2+TA(**K**), E''_2+ZA(**K**)	486	482
E'_1+TA(**K**), E'_1+ZA(**K**)		504
E''_2+LA(**K**)		528
A_1'+TA(**K**), A_1'+ZA(**K**)		538
E'_1+LA(**M**)	555	552
A_1'+LA(**M**)	589	590
2LA+2TA(**M**), 2LA+2ZA(**M**)	654	
2E'_1(**M**)	685	
E'_1+E’2(**M**)	712	715
2E’(**Γ**)	720	
?	759	
E’+A_1'(**Γ**)	781	
2A_1'(**Γ**)	842	

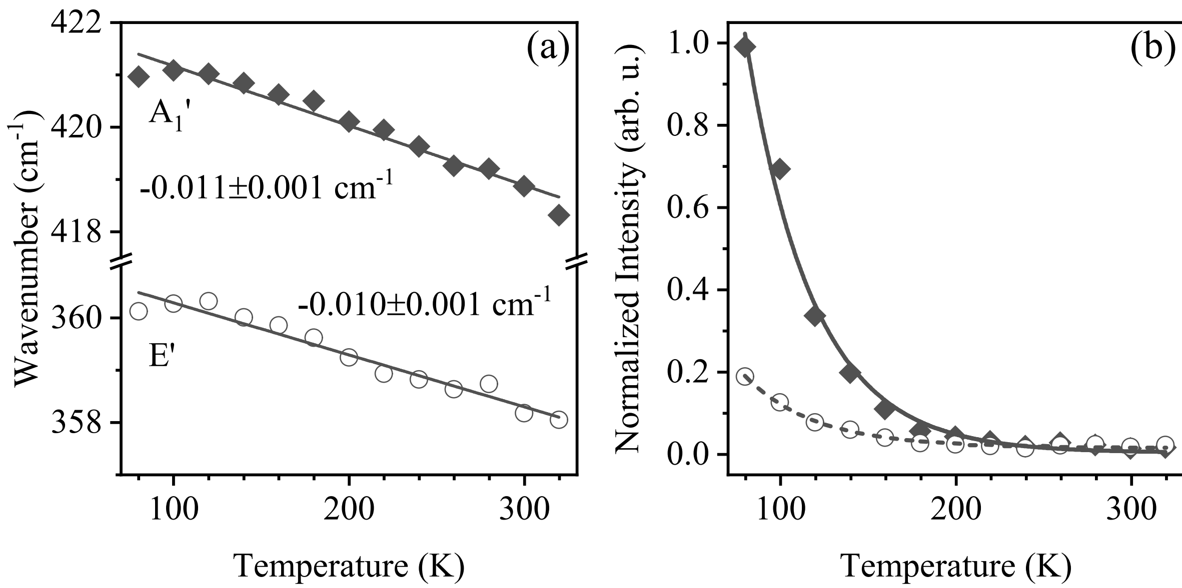

Figure 6.2. (a) Frequency of the A_1' (solid diamonds) and E' (empty circles) bands as a function of temperature. (b) The intensity of the A_1' and E' bands as a function of temperature, where the intensities of both peaks are normalized by the maximum of the A_1' band. The solid and dotted lines are a guide to the eye.

representations of the **Γ** point for clarity and treat the degenerate phonon branches as E'_1 and E'_2, for the higher and lower frequencies, respectively. The phonon dispersion and critical points in the phonon structure are listed in Appendix C.

From this point forward, we focus on the results from the laser excitation line at the absorption edge of X_A and T_A, 2.18 eV, since the Raman spectrum shows the highest resonance at lower temperatures. As we have shown for MoS_2, the position of the A_1' and E' bands of WS_2 will be affected by temperature effects as well, where the main factor for the shift induced by temperature effects comes from the anharmonic effects related to phonon-phonon and electron-phonon interactions.

Figure 6.2(a) shows the shift in the position of the A_1' and E' bands as a function of temperature for the 2.18 eV laser. The fitted slope for the frequency of the peaks as a function of temperature is -0.011±0.001 and -0.010±0.001 cm^{-1}/K for the A_1' and E' bands, respectively. The slope values are in good agreement with the observed results present in the literature [77,227,258]. The important remark we make here is about the intensity of the A_1' band, which comes into resonance with X_A as the temperature decreases, revealing a strong resonance of the A_1' band with X_A, as it is revealed in Figure 6.2(b).

Figure 6.3(a) shows the PL spectrum collected under the 2.18 eV laser with a laser power of 0.10 mW. We can observe the PL peak shifting to lower energies as temperature increases, which is in agreement with the observed PL spectra for MoS_2. The intriguing characteristic is how the center of the PL emission is shifting as a function of temperature since

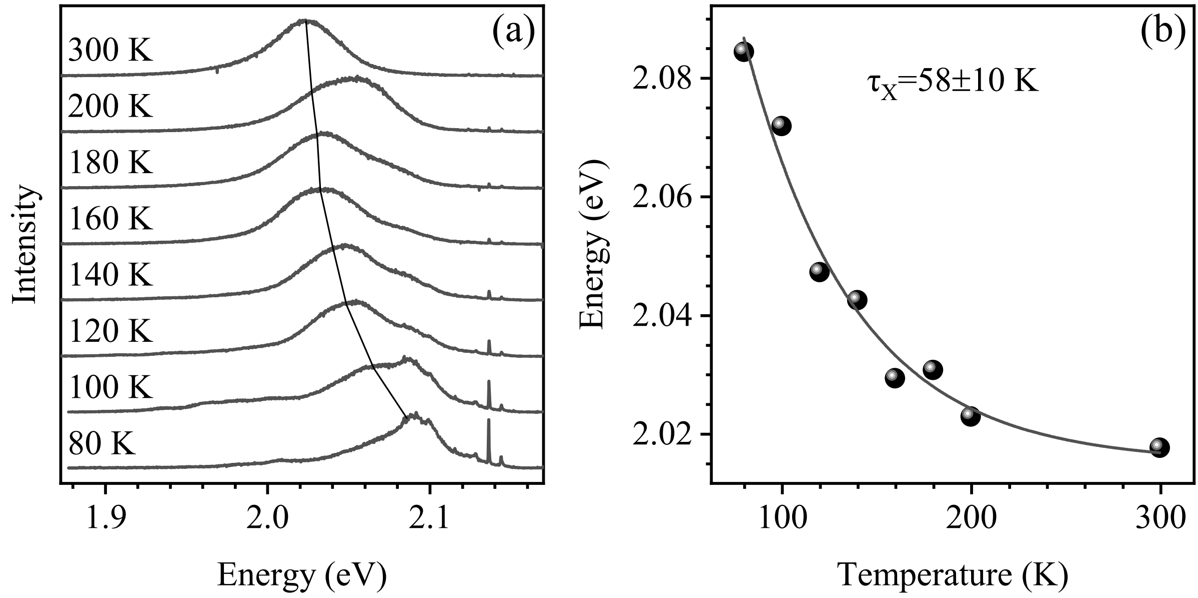

Figure 6.3. Measurement of the PL emission for a laser with energy close to the absorption peak. (a) PL spectrum collected with a 2.18 eV laser for the temperature range between 80 to 300 K. (b) Position of the less energetic components of (a) as a function of temperature shown as solid spheres, the solid line represents a fit with an exponential decay function. The fitting parameters are presented in Table 6.2.

it is in total disagreement with the expected behavior based on equation A.13 (Appendix A). The observed behavior of the peak PL emission is changing like an exponential decay. The fitting of the peak PL emission as a function of temperature is presented in Figure 6.3(b), where an exponential decay of the form $y_0 + Ae^{t/\tau}$ is used to fit the position of the PL emission as a function of temperature, and the fitting parameters can be found in Table 6.2. Although the equation that governs the intensity of the Raman spectrum is not directly proportional to the electronic energy, the peak intensity of the Raman signal comes when the laser energy is close to the electronic transition energy. Therefore, when the transition energy is being tuned by the thermal effects, the Raman signal is coming out of resonance, revealing that the intensities of these bands are related to the position of X_A.

6.2 Raman and photoluminescence measurements on $MoSe_2$

$MoSe_2$ possesses three excitonic transitions in the visible and NIR range, which can be extracted from Figure 2.6 just like we did for WS_2. The positions of X_A, X_B, and X_C are

Table 6.2. Fitting parameters of the exponential decay function used to fit the position of X_A as a function of temperature for the X_A transition of WS_2.

	A (eV)	τ (K)	y_0 (eV)
X_A	0.283 ± 0.064	58 ± 10	2.015 ± 0.005

approximately 1.55, 1.75 and 2.60 eV at room temperature. However, it has been shown in the literature that the excitonic transitions present a shift as a function of temperature as well [259]. Here, we show how the Raman spectrum of $MoSe_2$ changes for the resonance with X_C.

Figure 6.4 presents the Raman spectrum of $MoSe_2$ collected under the laser energies of 2.18, 2.54 and 2.81 eV. We observe straight away the strong resonance of the A_1' band under the three laser energies, and how the intensity changes with temperature for the two laser energies at the edges. The E' band intensity is also affected by the three different lasers shown here, but to a much lesser degree than the A_1' band.

One important detail is the behavior of the intensity as a function of temperature in the three laser energies below, above, and on resonance with the excitonic transition. Again, the excitonic transition is tuned by temperature due to the electron-phonon interaction, meaning that as temperature increases, the electronic transition energy decreases. At 80 K for the 2.18 eV laser in Figure 6.4(a), the intensity is approximately 1.5, however, as the temperature increases, the intensity of the A_1' band increases, reaching approximately 2.5 at 320 K. In the

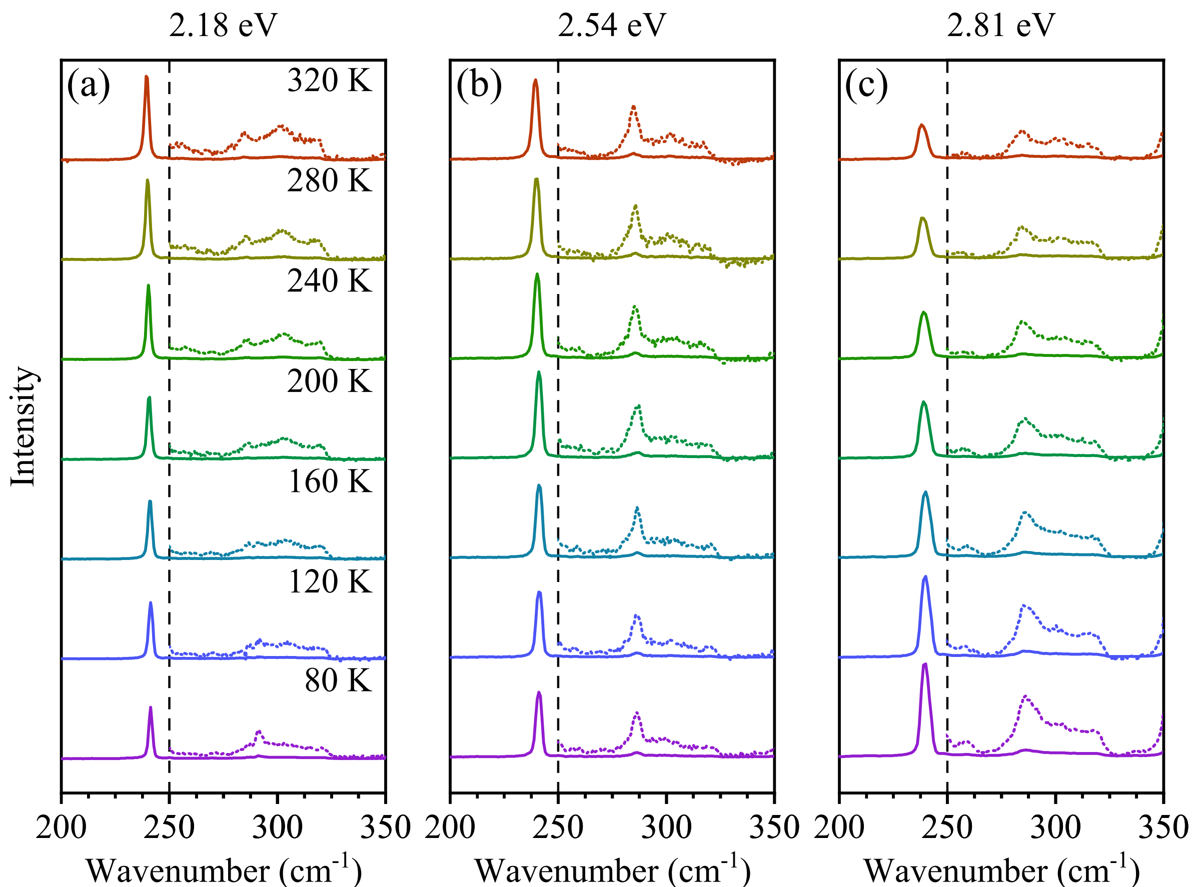

Figure 6.4. Raman spectrum of monolayer $MoSe_2$ between the temperature range of 80 to 320 K for the laser energies of (a) 2.18, (b) 2.54 and (c) 2.81 eV. The intensity in the spectral range of 250 to 350 cm^{-1} after the dotted axis is multiplied by 10 for clarity. The intensities are normalized by the intensity of the silicon peak.

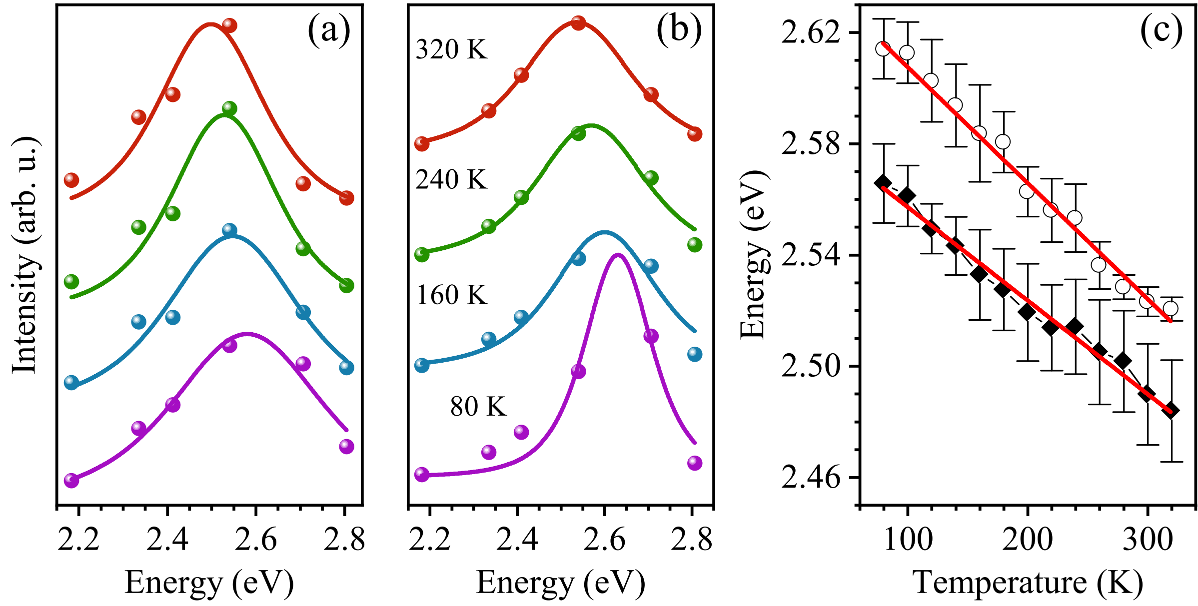

Figure 6.5. Intensities of the (a) A_1' and (b) E' bands as a function of the laser energy for the temperatures of 80, 160, 240 and 320 K. The intensities are normalized by the intensity of the silicon peak in the measured spectrum, and afterward, we used the silicon cross-section from ref. [231]. The solid lines represent a fit with equation 3.2. (c) Position of the X_C as a function of temperature taken from the fitted profile of the A_1' band (solid diamonds) and E' band (empty circles). The fitting parameters can be found in Table 6.3.

spectra obtained with excitation energy of 2.54 eV laser in Figure 6.4(b) the intensity of the A_1' band remains almost constant in the whole temperature range measured. The last measurements that are shown in Figure 6.4(c) are obtained with the 2.81 eV laser, where the intensity is actually decreasing as a function of temperature. In summary, the processes observed are actually being tuned by the resonance with X_C.

The intensity of the A_1' band as a function of the laser energy, corrected with the intensity of the silicon peak [231] (see section 4.2) is shown in Figure 6.5(a) for a few temperatures in the range of 80 to 320 K, and it is fitted with equation 3.2 in order to extract the excitonic transition energy. As temperature increases, we can see that the energy of the X_C transition shifts to lower energies. The same result can be observed for the intensity of the E' band, presented in Figure 6.5(b) which does not present an enhancement as strong as the A_1' band, but presents an enhancement with X_C nonetheless.

Table 6.3. Fitting parameters of the linear fit in Figure 6.5(c). The electronic transitions extracted from the A_1' and E' bands are marked as $X_C(A_1')$ and $X_C(E')$, respectively.

	$E(0)$ (eV)	$\frac{dE}{dT}$ (meV/K)
$X_C(A_1')$	2.591±0.002	-0.337±0.012
$X_C(E')$	2.650±0.005	-0.417±0.017

From the fitting of the intensities with equation 3.2, we can recover the electronic transition energy, presented in Figure 6.5(c) as a function of temperature. We can see that the electronic transition energy is slightly different for the A_1' and E' bands, with an apparent difference of about 60 meV at 80 K. The fitting parameters obtained by the linear fitting of both the observed electronic transitions are presented in Table 6.3. In addition to the difference in their energy, the rate of change of the electronic transition with temperature is also different between the two bands. In a recent work [259], it was shown that the dielectric function of $MoSe_2$ in the energy range of X_C is actually composed of two peaks instead of just one. The two components, called C_a and C_b in ref. [259], presented different temperature coefficients of values -0.32 meV/K and - 0.36 meV/K, which are approximately consistent with the X_C(A_1') and X_C(E') measured in this work. However, the difference between their values at 80 K was approximately 150 meV, almost 2.5 times the value we observed in our work. Nonetheless, the attributed transitions C_a and C_b are related to transitions in the proximity of the **Γ** point, but separated due to spin-orbit interactions [260]. Since the method of growth used in [259] is different from the method used here, we attribute the observed difference to probable strain or other external influences.

Coming back to the results observed specifically at 2.18 eV in Figure 6.4(a), we further analyze the dependence of the A_1' and E' bands frequencies and intensities as a function of temperature. Figure 6.6(a) shows the zoomed spectra of $MoSe_2$ measured with the 2.18 eV laser line in the spectral range between 270 and 360 cm^{-1}. Coming from the lowest temperature at 80 K, the peak corresponding to the E' band is strongest at approximately 292 cm^{-1}, called E'$_2$, while there is a small peak centered at approximately 287 cm^{-1}, called E'$_1$. As the temperature increases, the intensity of E'$_2$ decreases, while the intensity of E'$_1$ increases, to the point where we can barely distinguish the E'$_2$ band at 320 K.

In monolayer $MoSe_2$, it was reported by a few works the resonance behavior of the E' band as a function of the laser energy [60,117]. It was observed that for laser energies below 2.18 eV, the position of the E' band was located at approximately 292 cm^{-1}, while for energies above this threshold, the position of the E' band was located at approximately 289 cm^{-1}. The explanation of this behavior comes from the split of the LO-TO phonon branches at the **Γ** point due to the polar character of $MoSe_2$ [60,261], where the LO phonons, with higher energy, would be the E'$_2$ band, and the E'$_1$ band would represent the TO phonons. The exact explanation for the behavior where the E'$_2$ band comes into resonance with X_A and X_B is still lacking though, and we keep only the observation of this event. In section 5.2.3, we saw a similar behavior for

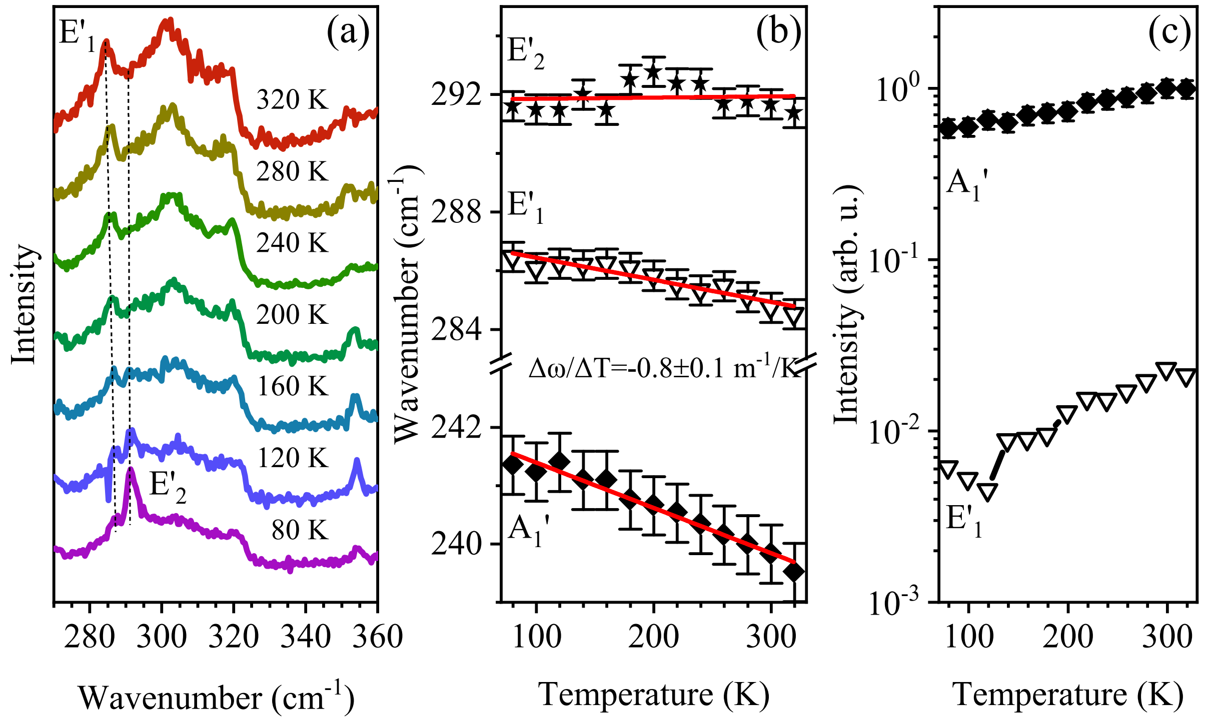

Figure 6.6. (a)Raman spectra of $MoSe_2$ in the spectral range of 270 to 330 cm^{-1} collected under 2.18 eV laser illumination for the temperature range of 80 to 320 K. The lines depict the position of the two components of the E' band, named E'_1 and E'_2, which move as a function of temperature. (b) Frequencies of the A_1' and E' bands as a function of temperature. The solid lines represent a linear fit where the slope of both A_1' and E'_1 bands is given by the $\Delta\omega/\Delta T$, while the slope of the E'_2 band is null. (c) Intensities of the A_1' band and E'_1 bands as a function of temperature. The intensities are normalized by the highest intensity of the A_1' band for clarity.

bulk MoS_2, where the band appearing at approximately 386 cm^{-1}, also comes into resonance with X_A and X_B. Which means that the assignment for the E'_1 and E'_2 bands are correct.

Figure 6.6(b) shows the position of the A_1', E'_1 and E'_2 bands as a function of temperature, where we see a linear behavior of the positions as a function of temperature, similar to the results from MoS_2 and WS_2. What has changed is the value of the slope, which is -0.008 cm^{-1}/K for both A_1' and E'_1 bands, while it is null for the E'_2 bands. Since the linear behavior is only an approximation of equation A.6, the difference observed means that the average phonon energy is different, but also the fitting parameters are different. The reported value for the slope of the A_1' band is -0.012 for a temperature range of 123 to 623 K [262,263], measured with a 2.33 eV laser. Although the reported result is bigger than the results we have found here, the temperature range is also bigger, meaning that other effects such as fourth-order terms in the potential interaction between atoms must be taken into account. Nonetheless, the authors explain the observed shift of the Raman bands in terms of thermal expansion, without taking into account the anharmonic effects due to phonon-phonon interactions. They find

thermal expansion coefficients of approximately 1 x 10^{-4} K^{-1} for $MoSe_2$, however, the reported thermal expansion coefficient for bulk $MoSe_2$ is reported to be approximately 7 x 10^{-6} K^{-1} [264], which is one order of magnitude smaller than the value obtained by ref. [262].

Considering that bulk should present a smaller expansion coefficient compared to a monolayer, we could still assume that the expansion coefficient for monolayer MoS_2 would be approximately equal for $MoSe_2$ as well. A recent work using Raman spectroscopy of a monolayer MoS_2 at different temperatures and substrates, found a thermal expansion value of approximately 7×10^{-6} K^{-1}, in good agreement with the reported value for bulk $MoSe_2$. Therefore, we assume that most of the contributions to the softening of the phonon energies are due to anharmonic interactions.

The final remark we make in this section is regarding the intensities of the A_1' and E' bands at the 2.18 eV laser as a function of temperature, which is found in Figure 6.6(c). The intensities of both the A_1' and E' bands are increasing, although at different rates, meaning that the modes are coming into resonance as temperature increases. This resonance is due to X_C, which has a rather broad width, and shifts to lower energy as temperature decreases, as it is shown in Figure 6.5(c).

Since we have an understanding of the resonance phenomena and exciton-phonon interaction in WS_2 and $MoSe_2$ we investigate the stacking effects on the heterostructures formed by monolayers of WS_2 and $MoSe_2$.

6.3 Heterostructure of WS_2/$MoSe_2$

We make two main observations, the coupling of the E' mode of $MoSe_2$ with the excitonic transition of WS_2, and also the observation of a double, triple, or higher-order process involving the combination of two phonons of WS_2 and a phonon of $MoSe_2$.

Only a few works have reported the presence of an additional peak in the Raman spectrum due to interlayer interactions [265–268]. Even fewer have reported the emergence of additional peaks due to interlayer interactions in heterostructures, where only one work reports the observation of an additional band in the Raman spectrum of a WSe_2 over hexagonal Boron Nitride (hBN) [266]. They report the presence of two additional peaks corresponding to the ZO vibrational mode of hBN at 820 cm^{-1}, and the combination of the ZO mode of hBN with the A_1' mode of monolayer WSe_2, at 1070 cm^{-1}. Due to symmetry restrictions, the ZO mode of hBN is not Raman active, however, due to the interlayer interaction between WSe_2 and hBN, the modes could be observed, and its intensity profile matches the electronic transition energy found by absorbance.

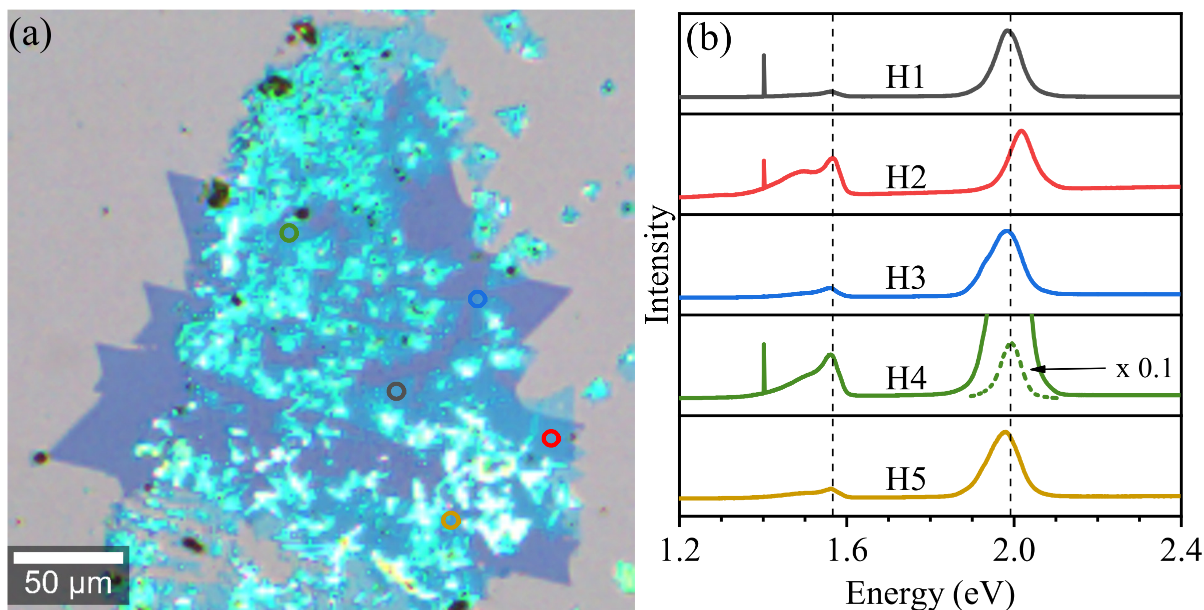

Figure 6.7. (a) Measured spots of the $WS_2/MoSe_2$ heterostructure. (b) PL spectrum of the spots presented in (a), measured with a 2.81 eV laser. The dashed lines at approximately 1.58 and 2.0 eV are the approximate positions of X_A for $MoSe_2$ and WS_2, respectively. The peak appearing at approximately 1.4 eV is the second-order diffraction from the laser. The dotted peak in H4 is the PL spectrum multiplied by 0.1, in order to show the entire data set. Measurements are carried under 80 K.

Here, we work with the heterostructure presented in Figure 4.6(a), where we measure different spots of the sample to compare their optical responses. Raman and PL measurements were taken at the different spots of the sample, presented in Figure 6.7(a).

The PL measured at the colored spots in Figure 6.7(a) are presented in Figure 6.7(b), where we can have an idea of the interlayer coupling based on the observed difference of the PL peaks intensity in the monolayers presented in Figure 4.6(b) and (c). It would be expected that changes in the interlayer coupling between the flakes in the heterostructure would lead to higher emission from one layer or the other, according to the strength of the interlayer coupling, which has been observed for other heterostructures of $MoSe_2$ and WSe_2 [269].

Basically, the interlayer interactions can be probed by the relative intensity between the PL peak of WS_2 and $MoSe_2$ [270,271]. Although it is expected that the interlayer interaction should be tuned by the angle between the layers, the domains observed in our sample are not well defined. Therefore, we can't extract the angle between the top WS_2 monolayer and the bottom $MoSe_2$ monolayer.

From the PL spectra presented in Figure 6.7(b), we can observe that the relative PL intensity between WS_2 and $MoSe_2$ is almost equal for H2, while for the other points the intensity of the PL of WS_2 is much stronger than the PL of $MoSe_2$. The laser used to acquire the PL spectra in Figure 6.7(b) is the 2.81 eV laser, which is in resonance with X_C from WS_2, but it is

coming out of resonance with X_C from $MoSe_2$. Therefore, we would expect an enhancement of the PL from WS_2, while the PL from $MoSe_2$ would be out of resonance. Since the biggest enhancement of the PL intensity of $MoSe_2$ comes from the H2 spot in Figure 6.7(b), it appears that the interlayer interaction would be strongest for H2, while the weakest would come from the other points.

In order to explore the resonant behavior of the heterostructure, instead of measuring so far into the resonance with X_C, it would be more appropriate to measure the PL closer to the resonance with X_A, where possible interlayer excitons can be observed due to the resonance condition matching the electronic level closest to the optical bandgap. In this context, we measured the PL spectrum near the X_A/T_A excitonic transition of the spots presented in Figure 6.7(a).

Figure 6.8(a), shows the PL spectrum of all spots present in Figure 4.6(a) and Figure 6.7(a) collected under a 2.18 eV laser illumination at 80 K. While the PL spectrum of $MoSe_2$ presents a strong peak related to the X_A transition, the PL spectrum of WS_2 is relatively weak, presenting a band at approximately 2.08 eV. The Raman lines can be observed at energies above 2.0 eV, where the most intense Raman band for WS_2 is the A_1' band, which presents almost 60% of the intensity of the PL peak. The Raman signal of $MoSe_2$ cannot be observed in Figure 6.8(a) due to the strong resonance observed by the PL peak. The heterostructures present a very interesting behavior, where the intensity of the PL peak of $MoSe_2$ drops drastically, becoming almost equal to the intensity of the PL peak of WS_2. In addition, a new peak at 2.0 eV starts forming in the PL spectrum of WS_2, which becomes the dominant feature as we move from H1 to H5. The apparent difference between the peak observed for WS_2 and the additional peak observed in H1 to H5 is 50 meV, which corresponds to the binding energy of T_A for WS_2 [272]. It could be suggested that the observed enhancement of the T_A emission in the heterostructure can be due to the interlayer interaction, which may transfer charges from the $MoSe_2$ layer to the WS_2 layer. And if this is indeed the case, we would see an enhancement of the contributions from the Raman spectra of $MoSe_2$ coming into resonance with the excitonic transition of WS_2 due to the resonance effect caused by the hybridization of the electronic states between the top and bottom layers.

Figure 6.8(b) shows the Raman spectrum extracted from Figure 6.8(a) for the seven spots mentioned before. In the WS_2 spectra, we see an enhancement of the A_1' and E' bands, which was discussed before. We also notice the presence of the double resonance bands listed in Table 6.1. In the $MoSe_2$ side, the most prominent band observed is the A_1' band at approximately 240 cm^{-1}, and the E' band is barely noticeable. However, moving into the Raman

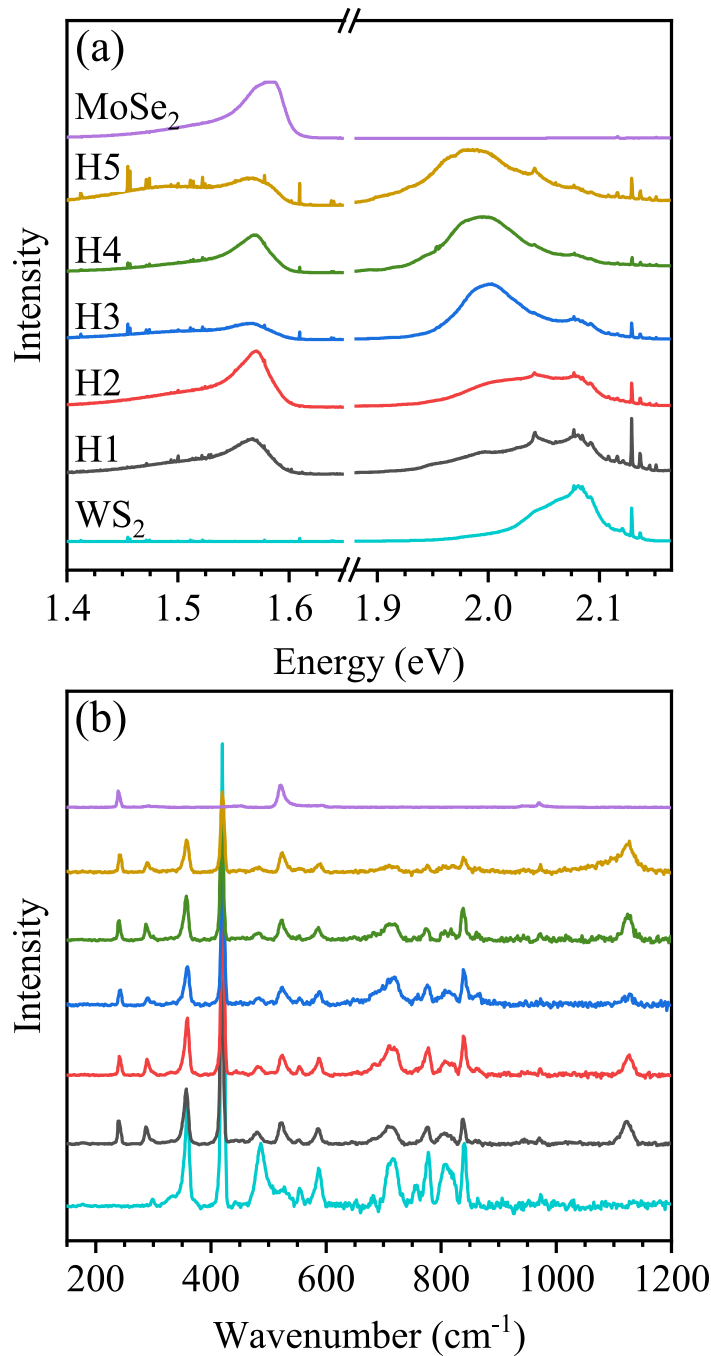

Figure 6.8. (a) PL measurements obtained with a 2.18 eV laser for the same spots presented in Figure 4.6(a) and Figure 6.7(a). The thin peaks above the energy of 2.0 eV are the Raman spectrum coming from the flakes, while the thin peaks below 1.6 eV are due to the plasma lines coming from the Ar-Kr laser. (b) Raman spectrum extracted from the measurements in (a), where the intensity is normalized by the intensity of the Si peak at approximately 525 cm^{-1}.

spectrum of the heterostructure spots, we observe the presence of two peaks that are enhanced, one at approximately 290 cm^{-1} and another one at approximately 1130 cm^{-1}.

We can attribute the peak at 290 cm^{-1} to the E’ peak of $MoSe_2$ since the frequency corresponds quite well to the frequency observed in Figure 6.6(b). But, the intensity of the E’

mode in the heterostructures is much higher than the intensity observed in the monolayer. This is indicative of the strong interlayer interaction since, in the case of weak interlayer interaction, the resulting Raman spectrum of the heterostructure would correspond to just the sum between the Raman spectrum of the individual layers.

We illustrate the interlayer interaction by comparing the Raman spectrum obtained by the sum of the spectrum of the individual layers, and the spectrum of the heterostructure itself, presented in Figure 6.9. In both of the spectra in Figure 6.9, the A_1' band of WS_2 is the dominant feature, but we can see some noticeable variations in the intensity of the other features. First, the intensity of the A_1' band of $MoSe_2$ is much stronger in the H1 spectrum than in the sum, which is also the case of the E' band. Second, the intensities of the second-order and double resonance features of WS_2 are reduced compared to the silicon peak close to 520 cm^{-1}, especially the E''-LA(**K**) band. The change in intensity of the double resonance band means that the electronic structure is being affected somehow since the intensities of these bands are strongly dependent on the resonance condition being satisfied in order to allow the combination of phonons for that specific double resonance process. Therefore, the inhibition of the energetic combination process of the E''+LA(**K**), while the other bands like the E'+LA(**M**) and

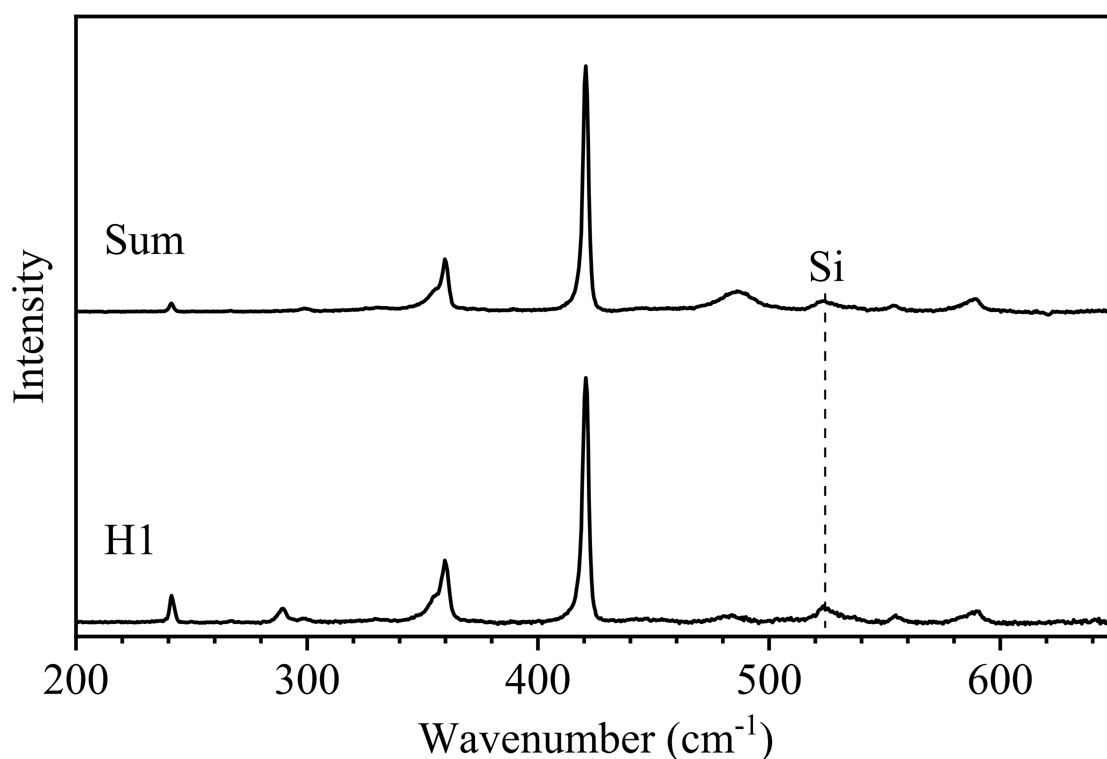

Figure 6.9. Raman spectrum of the H1 heterostructure sample compared with the sum of the spectrum of WS_2 and $MoSe_2$ obtained under a 2.18 eV laser illumination at a temperature of 80 K. The intensity of the spectra is normalized by the intensity of the highest peak for clarity.

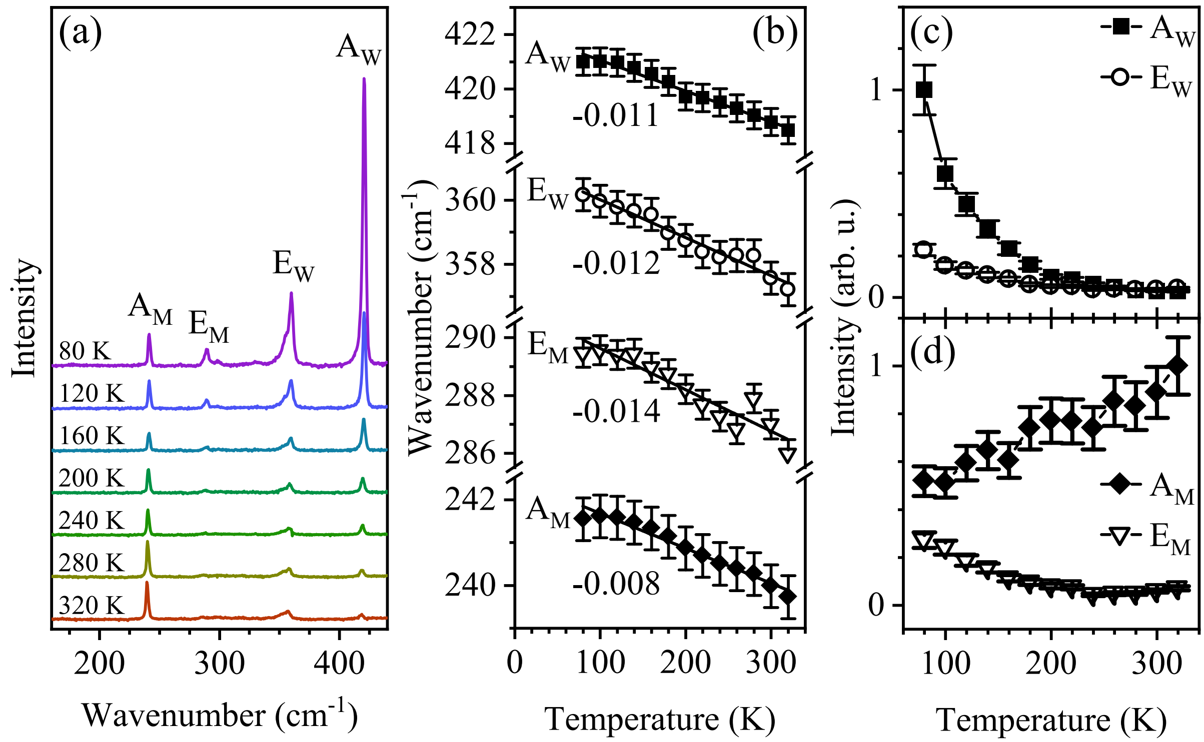

Figure 6.10. (a) Raman spectrum of H1 measured in the temperature range between 80 and 320 K under a 2.18 eV laser illumination. A_M and E_M are the A_1' and E' bands of $MoSe_2$, while A_W and E_W are the A_1' and E' bands of WS_2. (b) Position of the first-order bands as a function of temperature, where the numbers next to each curve represent the slope of the linear fit given by the solid curve. The error associated with the slope is 0.001 cm^{-1}/K. (c) and (d) are the intensities of first-order bands as a function of temperature for (c) WS_2 and (d) $MoSe_2$. Intensities are normalized by the highest intensity of the A_W and A_M bands. The solid lines are guides to the eye.

A_1'+LA(**M**) remain almost constant in intensity compared to the intensity of silicon, means that the **KK'** electron scattering process could be possibly inhibited by the **KQ** electron scattering process. As we discussed for MoS_2 in chapter 5, the **KQ** scattering process is connected to the indirect bandgap of the material. Therefore, the band structure of the heterostructure is being affected near the indirect bandgap of WS_2.

The band at approximately 1130 cm^{-1} is trickier to assign, since it does not correspond to a first-order band, due to its high frequency, neither to a second-order peak, since its frequency is higher than the sum of the highest frequency phonons of WS_2 (check Appendix C). However, we can assign it to a combination of three phonons, being two A_1' phonons from WS_2 at **Γ**, plus one E' phonon from $MoSe_2$, which is in resonance with the X_A/T_A transition from WS_2. We can call this phonon combination $2A_W+E_M$. The sum of these three phonons would correspond to exactly 1130 cm^{-1}, matching the position of the additional band observed in the Raman spectrum of H1 to H5. From this point forward, for simplicity, we call the A_1' and E' bands of WS_2 of A_W and E_W, and the A_1' and E' bands of $MoSe_2$ are called A_M and E_M.

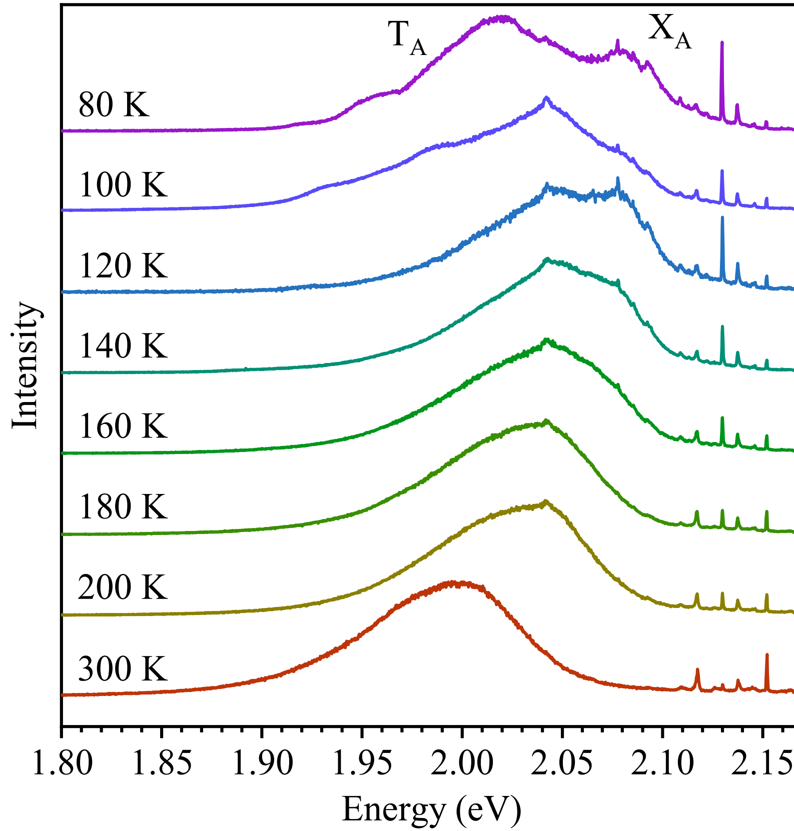

Figure 6.11. PL measurements of H1 close to the emission from WS_2 measured with a 2.18 eV laser for temperatures in the range of 80 to 300 K.

In order to observe the coupling between layers, we change the temperature to observe how the interlayer interaction is tuned, since as the temperature increases, the excitonic transition shifts to lower energies, making the laser at 2.18 eV come out of resonance. Figure 6.10(a) shows the Raman spectrum of H1 in the range of 160 to 440 cm^{-1} for some temperatures in the range between 80 to 320 K. At 80 K, the E_M band is expressively intense, much different from the results observed for the single flake of $MoSe_2$ in Figure 6.4(a), where its intensity is over one hundred times smaller than the intensity of the A_M band. However, as we increase the temperature, two effects can be observed: first, the intensity of the E_M band decreases back to the single flake case in Figure 6.4(a); second, the observed frequency of the E_M band presents a bigger slope as a function of temperature.

Figure 6.10(b) presents the positions of the first-order bands of WS_2 and $MoSe_2$ in the spectra of H1 as a function of temperature. The same experiments were carried with H2 and similar results were found, therefore, we choose to omit the results from H2. The A_W and the E_W bands of WS_2 follow the same exact behavior observed in a single layer, presented in sections 5.2 and 5.3. The E_M band of $MoSe_2$ presents a much higher dispersion though, where

the slope is almost twice as big as the one observed in Figure 6.6(b). Unlike what was observed before, it seems that a mix of the LO and TO phonons appears as if the degeneracy of the E' band is recovered, leading to a substantial increment in the slope of the E' band.

The intensity of the first-order bands is presented in Figure 6.10(c) for WS_2, where a similar behavior between a single flake and the heterostructure is observed. Figure 6.10(d) presents the intensity of the first-order modes for $MoSe_2$, where the intensity profile of the E' band follows, approximately, the same behavior of the first-order bands of WS_2. Therefore, we can assume from this result that the interlayer interaction is responsible for the observed phenomena around the E' band of $MoSe_2$ in the heterostructure.

We move now to the new band observed at approximately 1130 cm^{-1}, which we call *N*. Figure 6.11 shows the PL spectrum of H1 for a few temperatures in the range of 80 to 300 K. At 80 K, the most prominent feature appears close to the position of 2.03 eV, and as temperature is increased, the main PL features become broad and convoluted, until 300 K, where only 1 main peak can be observed. This result is similar to the reported behavior of the PL spectrum of WS_2 under gate tension, where the induced charges contribute to the enhancement of the

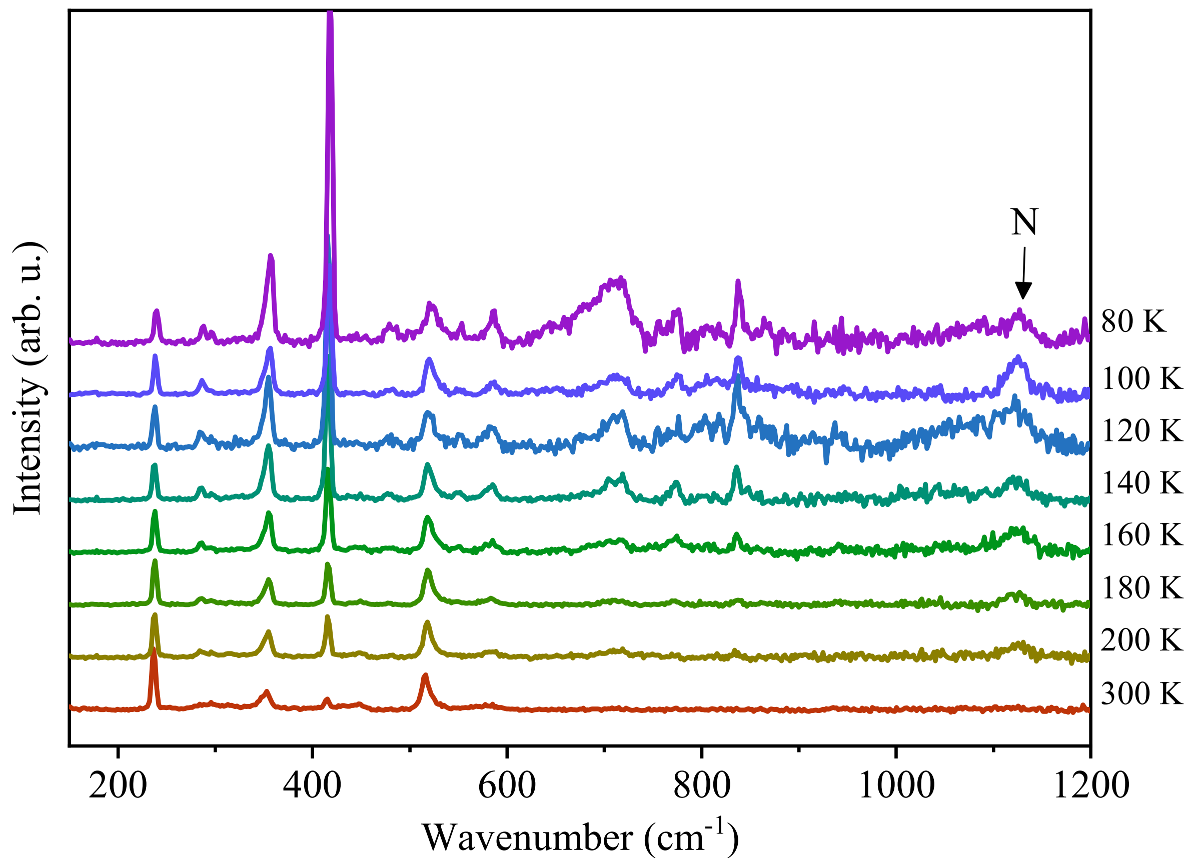

Figure 6.12. (a) Raman spectrum extracted from Figure 6.11, where the intensity is normalized by the intensity of the silicon peak. (b) The intensity and (c) position of *N* as a function of temperature. The solid line in (c) corresponds to the linear function 1129.5 - 0.04T.

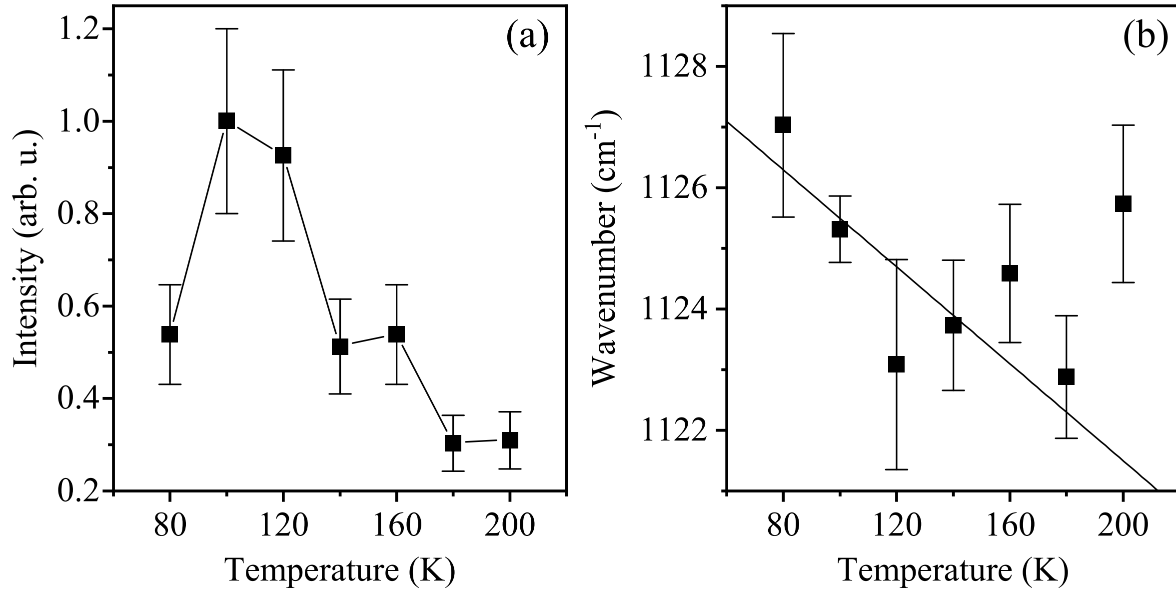

Figure 6.13. (a) The intensity and (b) position of *N* as a function of temperature. The solid line in (c) corresponds to the linear function 1129.5 - 0.04T.

trion and biexciton peaks [272]. This behavior can be possibly attributed to the interlayer interaction, which would contribute with charge transfer from one flake to the other, resulting in a high charge concentration for the monolayer. This behavior can actually explain the higher intensity of the *N* band intensity since, from Figure 6.8(a), the intensity of *N* is stronger for higher contributions of T_A to the PL spectrum.

Figure 6.12 shows the extracted Raman spectrum from Figure 6.11, where the *N* band is more clearly observed. Starting at 80 K, the *N* band is not very strong, however, at 100 and 120 K the intensity of *N* is quite noticeable, to the point where it is equal to the intensity of the silicon peak at 100 K. Moving to higher temperatures, the band becomes smaller, until it vanishes at 300 K. The intensity profile as a function of temperature is displayed in Figure 6.13(b), where the maximum intensity measured is for the 100 K spectrum. Comparing the behavior of the PL emission in Figure 6.11 to the intensity of *N*, we observe a similar trend, where the *N* peak becomes smaller as the T_A peak becomes smaller as well.

Figure 6.12(c) shows the position of the *N* band as a function of temperature. The behavior as a function of the temperature of the *N* band follows an approximately linear behavior between the temperatures of 80 and 180 K, which could be approximately fit with the expression 1129.5 - 0.04T. The slope of -0.04 cm^{-1}/K is very close to the sum of the slopes of the components of the band that we proposed before, $2A_W+E_M$, where the added slope can be found to be -0.036 cm^{-1}/K.

In summary, we conclude this chapter saying that the possible interlayer interactions in the heterostructures composed of TMDs are observable by the optical techniques when the excitation energy is in resonance with the electronic transition energies of the components, such as it was reported by ref. [266]. Recently it was reported that in $WS_2/MoSe_2$ heterostructures, just like the ones reported here, the electronic structure of the new metamaterial depends on the stacking angle up to an angle of 9°, or for angles bigger than 45° [273], and it is independent of the stacking angle in a large range of angles in between. In our case, since the observed PL intensities of the separated components vary by position and also by laser energy, we believe we're observing the interlayer interaction in a variety of angles, both small and large. Therefore we can contribute to significant statistics of the observation of Raman bands induced by the interlayer interaction in the heterostructures at different stacking angles.

7. Conclusion

In this work, we explored the PL and Raman spectra of three different types of TMDs belonging to the H-MX_2 phase, where we also observed the spectrum of few-layers and bulk crystals. We observed the temperature dependence of the resonant Raman spectra under the illumination of lasers with energy in resonance with the excitonic transition energies. It was observed how the first-order, second-order and double-resonance bands of MoS_2, for both monolayer and bulk, behave as a function of temperature. We also observe how the resonance with different laser energies was capable of affecting the double-resonance bands, where we can extract the purely resonant effects from the double resonance bands that are affected by the resonance with the excitonic transition. The PL spectra measured as a function of temperature revealed how the excitonic transition energies are affected by temperature. From the combination of resonance effects from excitonic transition as a function of temperature and the purely resonant behavior of the double-resonance bands as a function of the laser excitation energy, we can extract the temperature dependence of the acoustic phonons in MoS_2. Further, we can combine the information provided by the difference between the laser energy and the excitonic transition to complete the frequency profile of the double resonance bands.

We also presented the frequency dependence of the lower frequency double-resonance bands which were not treated in the literature before, as a function of both the laser energy and temperature. These bands are investigated for bulk MoS_2 samples, where the resonance with the indirect bandgap becomes more relevant than for the monolayer case. Based on the behavior presented by each band as a function of the laser energy, we could associate each band to specific two-phonon combinations near the **K** and **M** points in the Brillouin zone. We observed how the Stokes/Anti-Stokes band behaves near the resonance with the B exciton as a function of the laser energy and temperature, where we observe that for bulk, the resonance with the excitonic transition is extremely important to describe the intensity of the band.

Finally, for monolayer MoS_2, we observe the defect-induced and subtractive bands for different laser energies and temperatures, where the intensities of the defect-induced bands are heavily affected by temperature, decreasing massively near room temperature. We also observed the subtractive band as a function of temperature, where at room temperature, the frequency range containing the defect-induced bands is dominated by the subtractive bands.

In WS_2, we observed the tuning of the double-resonance bands for laser energies near the A and B excitons, where we recover the resonance with the excitonic transitions by

decreasing the temperature. We observe that the resonance with the A exciton intensifies the double resonance bands involving zone-center phonons, while the resonance with the B exciton intensifies the double resonance bands involving the zone-edge phonons.

In the case $MoSe_2$, we observed the behavior of the intensity of the first-order bands as a function of the laser energy and temperature as well, where we could extract the excitonic transition energy of the C exciton as a function of temperature for the A_1' and E' bands. It was also observed that the transition energy extracted from the intensity profile for each mode is different, and we attributed the difference to the coupling of each phonon with two components of the excitonic transition observed in the literature.

Finally, for the $WS_2/MoSe_2$ heterostructure, we were able to observe the interlayer interaction in different points in the flake displaying different relative PL intensities for each monolayer component, which we attributed to different stacking angles of the heterostructure. We investigated the interlayer interaction further by measuring the PL spectrum with a laser excitation energy closer to the A exciton of WS_2, revealing a strong change in the relative PL intensities for the components of the heterostructure. The analysis of the Raman spectrum near the resonance of WS_2 revealed the enhancement of the first-order mode of $MoSe_2$, along with the appearance of a new Raman band that could be associated with the combination of three phonons, two belonging to WS_2 and one belonging to $MoSe_2$.

We would like to add here that it could be possible to observe similar exciton-phonon and phonon-phonon processes in heterostructures formed by other TMDs components, provided that we excite the sample in resonance with the excitonic transition.

Appendix A: Temperature effects in the optical spectra

In order to calculate the electronic and vibrational properties of materials, the lattice motion must be decoupled from the electronic motion in order to make the calculations feasible. Although this is a good approximation, in reality, there are some effects that come from electron-phonon and phonon-phonon interactions that are relevant to the electronic and vibrational properties of the material. The effects induced by electron-phonon and phonon-phonon interactions appear when macroscopic parameters such as temperature are changed. Here, we use a relation that describes the phonon-phonon interactions and that is based on the anharmonic terms in the lattice potential.

In our case, since the focus of our work is the study of the Raman process, we are interested in the process of inelastically scattering of light, which involves the creation of a zone center phonon of frequency ω_0. After light absorption, the electron-hole pair recombines and a scattered photon is emitted along with the emission of a phonon. The phonon will decay into other phonons in the material, respecting energy and momentum conservation [274]. We consider in our treatment the three-phonon process, in which the phonon created through the interaction of light with the material decays into two thermal phonons. The lineshape of the Raman features, in first-order, is given by the Lorentzian distribution

$$I_R \times \frac{\Gamma}{[\omega - \Omega(\boldsymbol{k}, j)]^2 + \Gamma^2} \qquad \text{(A.4)},$$

Where I_R is the Raman intensity and is given by equation 3.2, and the distribution is centered in the resonant frequency $\Omega(\boldsymbol{k}, j)$, and the broadening parameter Γ is the reciprocal of the lifetime of the phonon. The resonant frequency is given by $\Omega(\boldsymbol{k}, j) = \omega_{\boldsymbol{k},j} + \Delta(\boldsymbol{k}, j)$, where $\omega_{\boldsymbol{k},j}$ is the value of the vibrational frequency under the harmonic approximation, and the term $\Delta(\boldsymbol{k}, j)$ comes from the terms beyond the harmonic approximation [274]. For the calculation of these terms, we use the changes in the population of phonons for a simple, yet powerful method to obtain relations between the energy of the phonon and the temperature.

Under thermal equilibrium, if a phonon ω_0 is created and it decays into two phonons ω_1 and ω_2 afterward, we may write the condition

$$(n_0 + 1)n_1 n_2 = n_0(n_1 + 1)(n_2 + 1) \qquad \text{(A.1)},$$

where n_i is the occupation for the phonon with frequency ω_i given the Bose-Einstein distribution. If we consider a small variation δn_0 from the occupation of ω_0 due to the decay of

an optical phonon unto two other phonons, the decay rate of δn_0 will be proportional to the difference of occupations after and before the decay given by

$$(\delta n_0 + n_0)(n_1 + 1)(n_2 + 1) - (\delta n_0 + n_0 + 1)n_1 n_2 \qquad \text{(A.2).}$$

Therefore, we may write the following kinetic equation [274,275]

$$\frac{d}{dt}(\delta n_0) = -a\left[(\delta n_0 + n_0)(n_1 + 1)(n_2 + 1) - (\delta n_0 + n_0 + 1)n_1 n_2\right] \qquad \text{(A.3),}$$

where a is a fitting parameter. Combining equations A.1 and A.2, we reach

$$\frac{d}{dt}(\delta n_0) = -a\left[1 + n_1 + n_2\right]\delta n_0 = -a\left(1 + \frac{2}{e^{\frac{\langle\hbar\omega\rangle}{K_B T}} - 1}\right)\delta n_0 \qquad \text{(A.4),}$$

which is the correction introduced by the three-phonon scattering process for the temperature dependence of the eigenvalues of the vibrational frequencies. We apply a trick to use the average phonon energy to describe the rate of change since there is a continuum of phonons that can satisfy the condition of A.4. Equation A.4 is a decay law related to the lifetime, τ_0, of the phonon and for increasing temperatures, the lifetime of the phonon is also decreased. The quantity related to the lifetime measured experimentally is the linewidth at half maximum, Γ, which is the inverse of the lifetime, according to the uncertainty relation between time and energy. The formal definition is given by

$$\Gamma = \frac{1}{\tau_0} = -\frac{1}{\delta n_0}\frac{d}{dt}\delta n_0 = a\left(1 + \frac{2}{e^{\frac{\langle\hbar\omega\rangle}{K_B T}} - 1}\right) \qquad \text{(A.5).}$$

Equation A.5 gives the dependence of the linewidth at half maximum, expected to increase as the temperature is increased [274,275].

Just like Γ, the value of Δ also changes with temperature, generally decreasing when the temperature increases. We may use the same reasoning applied to Γ to obtain the relation

$$\Delta(\boldsymbol{k}, j) = b\left(1 + \frac{2}{e^{\frac{\langle\hbar\omega\rangle}{K_B T}} - 1}\right) \qquad \text{(A.6),}$$

Which is analog of A.5 and is in good agreement with the changes in the vibrational frequency as a function of temperature, for a negative value of b, up to a certain temperature that depends on the thermal properties of the material [274].

In reality, the range of validity of 2.24 and 2.25 is limited since we are only considering a three-phonon process, and a complete analysis would also need to consider a four-phonon process, beyond the scope of our text [274]. For the range of temperature measurements that were used in our work, the three-phonon process is enough.

Since this process has been used for the changes in the vibrational properties, we may also consider a similar decay for the bandgap, where the electron-phonon interaction will be dominant. Since we are dealing with effects that are small compared to the measured values, we may deal with the contributions from electron-phonon interactions by the expansion of the electron-lattice potential in terms of the normal coordinate of vibration. For a crystal with κ atoms at sites $\boldsymbol{R}(\boldsymbol{l},\kappa)$ that have displacements $\boldsymbol{u}(\boldsymbol{l},\kappa)$, we may write that the temperature correction $\Delta E_{\boldsymbol{k},n}$ to the electronic state $\boldsymbol{k},n$ will be [244]

$$\Delta E_{\boldsymbol{k},n} = \sum_{\boldsymbol{l}\kappa,\boldsymbol{l}'\kappa'} \sum_{\boldsymbol{k}'n'} \frac{\left\langle \boldsymbol{k}n \middle| \frac{\partial V}{\partial R_i} \middle| \boldsymbol{k}'n' \right\rangle \left\langle \boldsymbol{k}'n' \middle| \frac{\partial V}{\partial R_j} \middle| \boldsymbol{k}n \right\rangle}{E_{\boldsymbol{k}n} - E_{\boldsymbol{k}'n'}} \Big[u_i(\boldsymbol{l}\kappa) u_j(\boldsymbol{l}'\kappa') - \frac{1}{2} u_i(\boldsymbol{l}\kappa) u_j(\boldsymbol{l}\kappa) - \frac{1}{2} u_i(\boldsymbol{l}'\kappa') u_j(\boldsymbol{l}'\kappa') \Big] \quad \text{(A.7)},$$

where $\frac{\partial V}{\partial R_i}$ will be the change in the electron-lattice potential per unit displacement of the atom κ in direction i. A sum over i and j, the cartesian components, is implicit. We can make use of the creation and annihilation operators in order to rewrite the displacement $\boldsymbol{u}$ as

$$\boldsymbol{u}(\boldsymbol{l},\kappa) = \sum_{\boldsymbol{Q},\alpha} \left(\frac{\hbar}{2NM_\kappa \omega_{\boldsymbol{Q},\alpha}} \right)^{\frac{1}{2}} \boldsymbol{\epsilon}(\boldsymbol{Q},\alpha,\kappa) e^{i\boldsymbol{Q}\cdot(l+\tau_\kappa)} \phi_{\boldsymbol{Q},\alpha} \quad \text{(A.8)},$$

where $\boldsymbol{Q}$ and α are the phonon wavevector and branch while $\omega_{\boldsymbol{Q},\alpha}$ is its frequency, M_κ is the mass of the κ-th atom located and position $\boldsymbol{\tau}_\kappa$ in the unit cell, N is the number of unit cells in the crystal and $\phi_{\boldsymbol{Q},\alpha} = a^\dagger_{\boldsymbol{Q},\alpha} + a_{-\boldsymbol{Q},\alpha}$. The polarization vector $\boldsymbol{\epsilon}(\boldsymbol{Q},\alpha,\kappa)$ will obey the completeness relations

$$\begin{aligned} \sum_{\kappa} \epsilon_i(-\boldsymbol{Q},\alpha,\kappa)\epsilon_i(\boldsymbol{Q},\beta,\kappa) &= \delta_{\alpha\beta} \\ \sum_{\alpha} \epsilon_i(-\boldsymbol{Q},\alpha,\kappa)\epsilon_j(\boldsymbol{Q},\beta,\kappa') &= \delta_{ij}\delta_{\kappa\kappa'} \end{aligned} \quad \text{(A.9)}.$$

When all is put together, we can use a thermal average, yielding [244]

$$\Delta E_{\boldsymbol{k},n}(T) = \sum_{\boldsymbol{Q},\alpha} \frac{\partial E_{\boldsymbol{k},n}}{\partial n_{\boldsymbol{Q},\alpha}} \left(n_{\boldsymbol{Q},\alpha} + 1 \right) \quad \text{(A.10)}.$$

$$\frac{\partial E_{\boldsymbol{k},n}}{\partial n_{\boldsymbol{Q},\alpha}} = \frac{1}{N}\sum_{\kappa\kappa' n'}\left(\frac{\left\langle \boldsymbol{k}n\left|\frac{\partial V}{\partial R_i(\kappa)}\right|\boldsymbol{k}+\boldsymbol{Q}n'\right\rangle\left\langle \boldsymbol{k}+\boldsymbol{Q}n'\left|\frac{\partial V}{\partial R_j(\kappa')}\right|\boldsymbol{k}n\right\rangle}{E_{\boldsymbol{k}n}-E_{\boldsymbol{k}+\boldsymbol{Q}n'}} - \frac{\left\langle \boldsymbol{k}n\left|\frac{\partial V}{\partial R_i(\kappa)}\right|\boldsymbol{k}n'\right\rangle\left\langle \boldsymbol{k}n'\left|\frac{\partial V}{\partial R_j(\kappa')}\right|\boldsymbol{k}n\right\rangle}{E_{\boldsymbol{k}n}-E_{\boldsymbol{k}n'}}\right)\frac{e^{-\boldsymbol{Q}\bullet(\tau_\kappa-\tau_{\kappa'})}\hbar\epsilon_i(-\boldsymbol{Q},\alpha,\kappa)\epsilon_j(\boldsymbol{Q},\alpha,\kappa')}{\left(M_\kappa M_{\kappa'}\omega^2_{\boldsymbol{Q},\alpha}\right)^{\frac{1}{2}}}$$

Now, we must also take into account the electron-phonon interaction, which will select the most relevant phonons that will affect the electronic state $\boldsymbol{k}n$. In the end, the result from A.10 can be resumed into

$$\Delta E_{\boldsymbol{k}n} = -a'\left(\frac{1}{2}+\frac{1}{e^{\frac{\langle\hbar\omega\rangle}{K_BT}}-1}\right) = -a\left(1+\frac{2}{e^{\frac{\langle\hbar\omega\rangle}{K_BT}}-1}\right) \quad \text{(A.11)},$$

where a will be a fitting parameter and $\langle\hbar\omega\rangle$ is the average phonon energy [244]. Since this result is similar to the one obtained at A.6, we manipulated the first outcome of A.11 to yield similar results. One remark though is that $\langle\hbar\omega\rangle$ for A.6 and for A.11 do not necessarily need to be the same. Same as with A.6 and A.11, the relation between the lifetime for the electronic state $\boldsymbol{k}n$ and T will be given by

$$\Delta\Gamma_{\boldsymbol{k}n} = b\left(1+\frac{2}{e^{\frac{\langle\hbar\omega\rangle}{K_BT}}-1}\right) \quad \text{(A.12)}.$$

In summary, for an energy dispersion relation, we may write that the temperature dependence of the state E and its lifetime Γ will be

$$E(T) = E(T=0) - a\left(1+\frac{2}{e^{\frac{\langle\hbar\omega\rangle}{K_BT}}-1}\right) \quad \text{(A.13)},$$

$$\Gamma(T) = \Gamma(T=0) + b\left(1+\frac{2}{e^{\frac{\langle\hbar\omega\rangle}{K_BT}}-1}\right) \quad \text{(A.14)}.$$

Thus, we may use the same type of equation to fit the dependence of the phonon and electronic transition energies. Care must be taken though, for the fitting parameters present in these equations is not always the same.

Appendix B: Double resonance Raman processes in graphene

Graphene was the first isolated 2D material, and it is regarded as the strongest material due to its in-plane double sp^2 bonding [276]. At the same time, it was one of the first 2D materials to have its Raman spectra measured [128].

The electronic properties of graphene can be well described by the tight-binding approach considering two p_z orbitals [277]. Thus, the one-electron dispersion of graphene is characterized by the presence of Dirac cones near the **K** point in the Brillouin zone, where the valence and conduction bands touch each other, making graphene be considered a zero bandgap semiconductor [278]. In a first approximation, the electronic band structure around the **K** point can be regarded as linear and, consequently, the dependence of the electronic density of states present a linear behavior near the Fermi level [279]. The optical transitions in graphene are characterized by vertical transitions from the valence band to the conduction band close to the **K** point, with constant light absorption in the near-infrared (NIR) and visible spectral regions [280]. As for the vibrational properties of graphene, there are six phonon branches at the **Γ** point, three acoustic and three optical phonon branches, named longitudinal acoustic (LA), transversal acoustic (TA) and out of plane transversal acoustic (ZA), out of plane transversal optic (ZO), longitudinal optic (LO) and transversal optic (TO). Among these phonon branches, only the LO and TO modes at the **Γ** point are Raman active and correspond to a degenerate E_{2g} representation (the G band). Thus, the expected Raman spectrum should consist of a single first-order band.

Nevertheless, the Raman spectrum of pristine graphene is characterized by the presence of mostly four bands, named as G, D+D", 2D and 2D' in frequency order (Figure B.0.1(a)) [130]. In the presence of defects, new features arise in the Raman spectrum of graphene, thus, besides the four Raman bands observed in pristine graphene, three other bands are also observed, named as D, D' and D+D' (see Figure B.0.1(a)).

The G band (the E_{2g} mode) originates from a first-order Raman process, as shown in Figure 2.9(a). As a first-order process, it will be present in the Raman spectrum of pristine and defective samples regardless of the excitation laser energy and the number of layers [128,129,156,205–207]. An interesting aspect of the G band is its classical behavior for the scattering process across the visible range, where its intensity is proportional to the fourth power of the laser frequency [178]. The other bands are related to a double or triple resonance process discussed before.

The bands that arise from double or triple resonance may be affected not only by excitation laser energy and defect density but also by the number of layers as well, where an increasing number of layers will affect the number of allowed processes due to changes in the electronic structure [128,129]. Although we name the double or triple resonance processes as intervalley and intravalley, we must remember that graphene presents Dirac cones in its electronic structure, not parabolic bands. For the sake of comparison between materials, though, we will stick with this name. The intervalley scattering process (see Figure B.0.1(b)) occurs when the excited electron is scattered from the conduction band near **K** point to the conduction band near **K'** point, whereas the intravalley scattering process (see Figure B.0.1(c)) scatters the electron along the same valley. Once the excited electron is scattered, it can return to its original band via another phonon or a defect, and then it recombines with the hole in the valence band emitting a scattered photon.

The 2D (or G') band in graphene, appearing between 2600 and 2800 cm^{-1} in Figure B.0.1(d), is an example of a band originated from the electron-hole intervalley scattering. This process is mediated by two TO phonons (one for the excited electron and one for the hole)

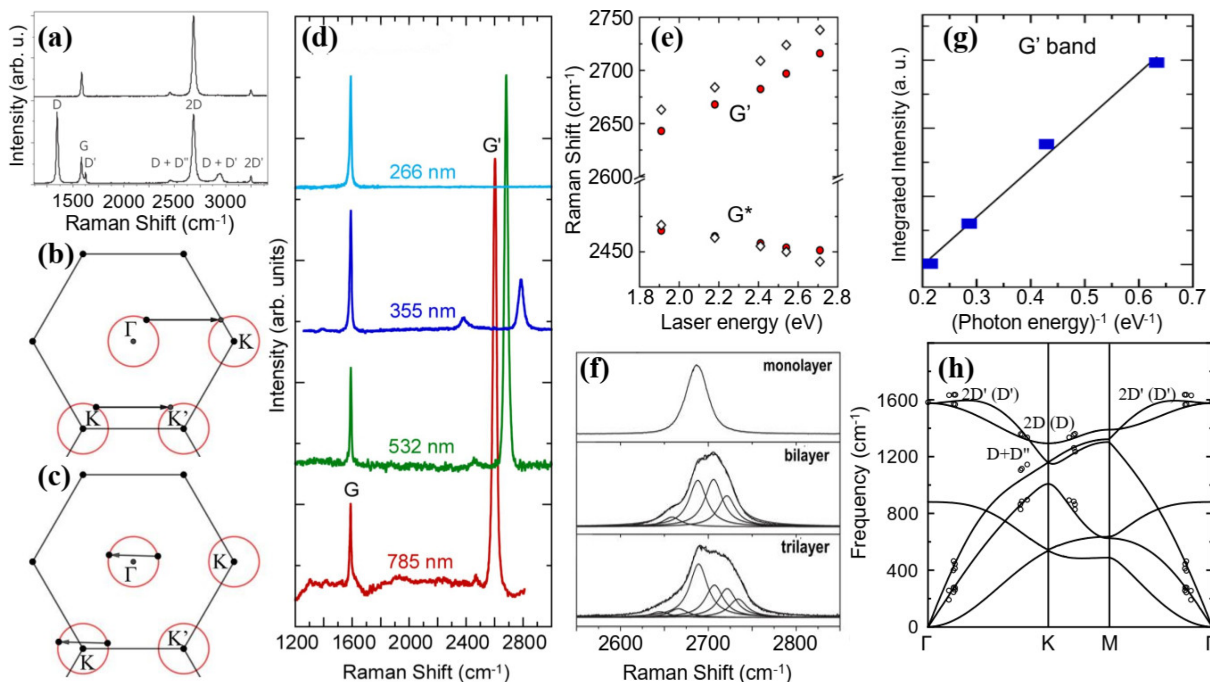

Figure B.0.1. The Raman scattering process in graphene. (a) Raman spectrum of pristine graphene (top) and defective graphene (bottom). (b) intervalley and (c) intravalley wave vector scattering processes. (d) Raman spectrum of graphene collected at different excitation wavelengths from NIR to UV. (e) Frequencies of the 2D and D + D" (G' and G*) bands as a function of the laser energy. (f) Raman spectra of monolayer, bilayer and trilayer graphene at the same energy showing the differences in the observed intervalley processes of the 2D band. (g) The intensity of the 2D band as a function of the inverse of the laser energy. (h) Phonon dispersion of single-layer graphene with the phonons that participate in the intervalley and intravalley bands. Adapted from ref. [176].

around the **K** point in the phonon dispersion and the recombination happens around the **K'** point [129,155,157]. This association is made because the phonon wavevector is around the length of the distance between **K** and **K'** points, corresponding to the approximate distance between the **Γ** and **K** points (see Figure B.0.1(b)), which can be mapped to the phonon dispersion. Additionally, the 2D band frequency presents a high dispersion as the excitation laser energy is tuned (around 100 cm^{-1}/eV, see Figure B.0.1(d) and (e)). The reason for this comes from both the linear electronic dispersion near **K** point of graphene and the Kohn anomaly, which manifests as strongly dispersive LO branch in the vicinity of the **Γ** and **K** points [281]. Thus, for laser energies close to the linear regime of the electronic dispersion, the intensity of the 2D band is greatly enhanced.

When a graphene sheet presents a significative defect density, a band with approximately half the frequency of the 2D band appears, and it is called D band [149]. The D band is a double resonance process, and its intensity is strongly bound to the defect density [156,206]. The 2D band, on the other hand, decreases in intensity for increasing defect density [156], which could be argued as a preference for the phonon-defect process instead of the phonon-phonon process of recombination. We mention that as the number of graphene layers increases, the number of intervalley processes increases as well, in accordance with the changes in the electronic structure (see Figure B.0.1(f)) [129,179]. Also, as the excitation laser energy approaches the UV range, the 2D band intensity considerably decreases (with the first-order process prevailing), such that its intensity is inversely proportional to the excitation laser energy (see Figure B.0.1(d) and (g)) [178]. The D+D" band, also known in the literature as G* band, is associated with an intervalley scattering involving phonons from TO (D) and LA (D") branches. Contrarily to the 2D band, the D+D" presents a negative dispersion due to the behavior of the LA phonon branch around the **K** point (Figure B.0.1(e)) [129,155,282].

The 2D' band is an example of a phonon-phonon intravalley scattering process [283]. The scattering of the excited electron happens along the **K** cone through the emission of two LO phonons close to the **Γ** point [283]. Analogously, one can also see a D' band, which is a phonon-defect intravalley scattering [283]. Interestingly, the 2D' band does not present a strong enhancement of its intensity, showing an intensity smaller than that of a first-order mode. This could be related to the strong interaction between electrons and LO phonons near the **K** point, such that the numerator is also an important factor. Therefore, the electron-phonon interaction is an important factor for the double (or triple) resonance process.

The D’ and 2D’ bands are not very dispersive, i.e. their frequency position does not change much when tuning the excitation laser energy, but they are related to phonon dispersion points where the LO phonon branches are maximum [284].

We comment that combinations of intravalley and intervalley scattering are also possible. For instance, the D+D’ band comes from the scattering of an electron to the **K'** point mediated by a TO phonon close to the **K** point and, then scattered back by a TO phonon close to the **Γ** point. Afterward, electron and hole recombine mediated by a defect [130,156].

Figure B.0.1(h) shows the phonon dispersion of graphene depicting all the contributions from the double resonance Raman bands associated with their specific points [284]. In summary, the ability to probe phonons away from the **Γ** point in such a way that they can be mapped out by their wavevectors is one of the most interesting features of the double Raman resonance bands in a layered material.

The Raman spectrum of a defective graphene sample presents three new features assigned as D, D’ and D+D’ bands, as it is shown in Figure B.0.2(a) [156]. These new Raman bands are the result of intervalley and intravalley electron scattering and the combination of both processes where the conservation of momentum is preserved by the presence of a defect.

In Figure B.0.2(a), we can notice that the D band is the most intense one of the defect induced Raman features in graphene. It has half the frequency of the 2D band and shows a dispersive behavior as the excitation laser energy is tuned [156]. Additionally, the D band also depends on the average defect distance, L_D, since its intensity increases as the L_D value decreases (see Figure B.0.1(a)). Notice that D band intensity can even surpass the G band intensity. The intensity ratio of both bands (I_D/I_G) provides a route to characterize the sample quality [156]. The relationship between the I_D/I_G intensity ratio can be expressed as a function of L_D given by [156,206]

$$\frac{I_D}{I_G} = C_A \frac{\left(r_A^2 - r_S^2\right)}{\left(r_A^2 - 2r_S^2\right)} \left[\exp\left(-\pi \frac{r_S^2}{L_D}\right) - \exp\left(-\pi \frac{r_A^2}{L_D} + \pi \frac{r_S^2}{L_D}\right)\right] \qquad \text{(B.1).}$$

The parameters r_A and r_S are length scales related to either the regions that contribute to the scattering of the electron to form the D band or to the disorder caused by defect formation. C_A is a weight parameter that depends on the laser energy. By Equation B.1, it is possible to observe the behavior of the intensity of the D band as a function of both laser energy and defect length. A laser independent relationship can also be obtained by multiplying the left side of Equation B.1 by E_L^4, as it is shown in Figure B.0.2(b) [156]. This new expression allows us to monitor

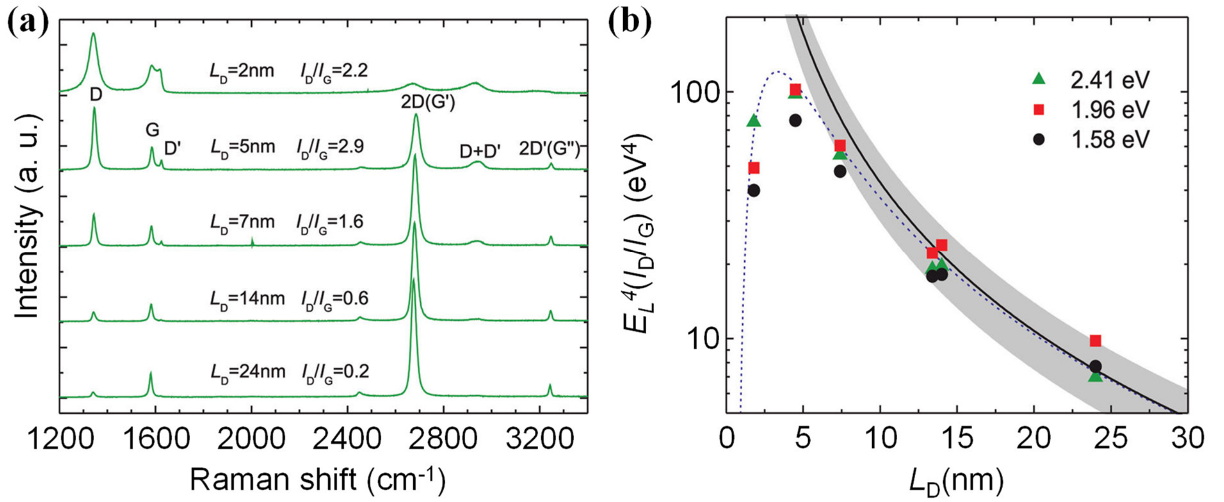

Figure B.0.2. One-phonon-defect Raman spectrum of defective graphene. (a) Raman spectrum of monolayer graphene for different values of inter-defect density (L_D) collected with a 2.41 eV laser. (b) Intensity ratio of D to G band multiplied by the fourth power of the laser energy as a function of L_D. Adapted from ref. [156].

and control the defect density in graphene for its applications, independently of the laser line used.

It is worthy of note that after the threshold of the defects amounts is reached, i.e. the L_D is considerably small, there is a change in the crystallinity of the sample becoming increasingly rich in sp^3 amorphous carbon [130,156]. At this point, several changes in the Raman spectrum are observed, including the broadening and asymmetry of the bands, shifts in the frequency of the first-order modes, among others [130,156,205,206].

Appendix C: Phonon dispersion and list of critical points for WS_2 and $MoSe_2$

Here, we show the phonon dispersion for WS_2 and $MoSe_2$, we also list all the phonon energies at the critical points for WS_2 in order to list all the second-order and double resonance bands. In the process of naming the phonon branches in the **K** and **M** points in chapter 5, we used the irreducible representations of the phonon branches at the **Γ** point for simplicity, as we do in this appendix.

Figure C.0.1 presents the phonon dispersion relations for WS_2 and $MoSe_2$. The irreducible representations at the **Γ** point are the same for 1L MoS_2 and they are given by

$$\Gamma_{vib} = \Gamma_{eq} \otimes \Gamma_{vec} = A_1{}' \oplus 2E' \oplus 2A_2{}'' \oplus E''.$$

Therefore, we expect the presence of 3 non-degenerate modes and 3 doubly degenerate modes. Since there are 3 acoustic phonons and the LA and TA phonon branches are degenerate at the **Γ** point, we expect that the representations A_2” and E' can be associated with the ZA, LA and TA branches, respectively, which is also justified due to the fact that the *x*, *y*, and *z* functions

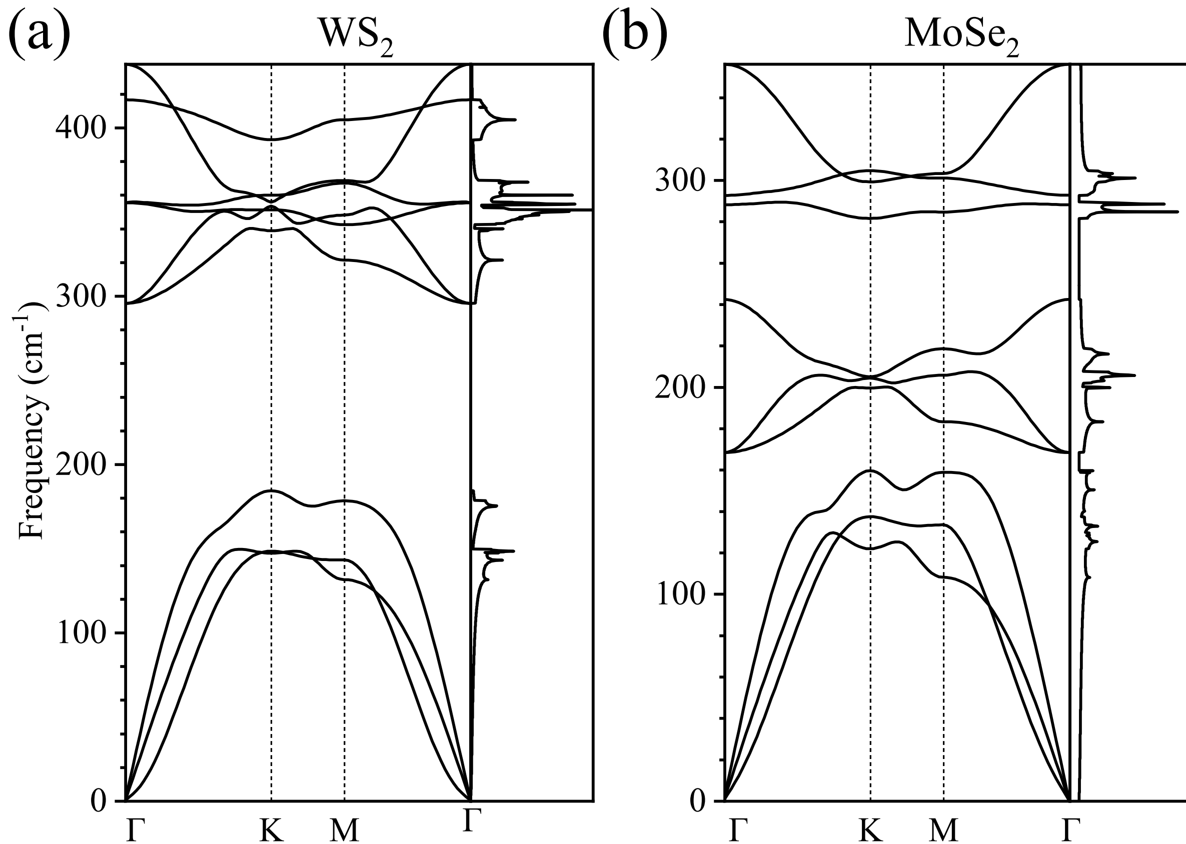

Figure C.0.1. Phonon dispersions of (a) WS_2 and (b) $MoSe_2$, with their respective density of states.

belong to the A_2'' and E' representations. From the out-of-resonance Raman spectrum of WS_2, we can find the irreducible representations A_1' and E', at 420 cm^{-1} and 358 cm^{-1} for WS_2 and at 242 and 286 to 291 cm^{-1} for $MoSe_2$. The remaining irreducible representations can be directly related to the phonon branches in the phonon dispersion relations of each material in Figure C.0.1.

We now move to the table of phonon frequencies at the critical points, using the irreducible representations at the **Γ** point. At the **K** point, only one mode is expected to be degenerate, while at the **M** point, the phonon branches are expected to be non-degenerate [110]. Where the degenerate phonon branches of the **Γ** split, we designate the phonon as E'_1 or E'_2 for the higher and lower energy branches.

Table C.0.1. Frequency of the phonon branches at the critical points of WS_2.

Γ	ω_{Ph} (cm^{-1})	**K**	ω_{Ph} (cm^{-1})	**M**	ω_{Ph} (cm^{-1})
A_2'' (ZO)	438	A_2'' (ZO)	356	A_2'' (ZO)	369
A_1' (ZO)	418	A_1' (ZO)	393	A_1' (ZO)	405
E' (TO, LO)	356	E'_1 (TO, LO)	360	E'_1 (TO, LO)	367
		E'_2 (TO, LO)	351	E'_2 (TO, LO)	342
E'' (TO, LO)	296	E''_1 (TO, LO)	353	E''_1 (TO, LO)	348
		E''_2 (TO, LO)	339	E''_2 (TO, LO)	321
E' (TA, LA)	0	E' (LA)	184	E' (LA)	178
		E' (TA)	147	E' (TA)	143
A_2'' (ZA)	0	A_2'' (ZA)	148	A_2'' (ZA)	132

Appendix D: Functions used for the fitting procedures of Chapter 5

The Modded Gaussian function

The definition of the modded Gaussian function we used to fit the δ band is the following:

$$f(x) = \frac{A}{t_0} e^{\frac{1}{2}\left(\frac{w}{t_0}\right)^2 - \frac{x-x_c}{t_0}} \int_{-\infty}^{z} \frac{1}{(2\pi)^{1/2}} e^{\frac{y^2}{2}} dy \tag{D.1}$$

Where A is the area under the curve, x_c is the peak center, w is the width and t_0 is a fitting parameter.

The BiGaussian function

The definition of the biGaussian function we used in the fitting of the LA band is the following:

$$f(x) = \begin{cases} He^{-\frac{1}{2}\left(\frac{x-x_c}{w_1}\right)}, & x < x_c \\ He^{-\frac{1}{2}\left(\frac{x-x_c}{w_2}\right)}, & x > x_c \end{cases} \tag{5.2}$$

Where H is the height of the peak, w_1 is the width of the peak when $x < x_c$ and w_2 is the width of the peak when $x > x_c$.

8. References

[1] K. S. Novoselov, Science **306**, 666 (2004).

[2] P. Miró, M. Audiffred, and T. Heine, Chem. Soc. Rev. **43**, 6537 (2014).

[3] M. Ashton, J. Paul, S. B. Sinnott, and R. G. Hennig, Phys. Rev. Lett. **118**, 106101 (2017).

[4] C. Ataca, H. Şahin, and S. Ciraci, J. Phys. Chem. C **116**, 8983 (2012).

[5] K. S. Novoselov, A. Mishchenko, A. Carvalho, and A. H. Castro Neto, Science **353**, aac9439 (2016).

[6] J. A. Wilson and A. D. Yoffe, Adv. Phys. **18**, 193 (1969).

[7] K. F. Mak and J. Shan, Nat. Photonics **10**, 216 (2016).

[8] Y. Guo, C. Dun, J. Xu, P. Li, W. Huang, J. Mu, C. Hou, C. A. Hewitt, Q. Zhang, Y. Li, D. L. Carroll, and H. Wang, ACS Appl. Mater. Interfaces acsami.8b10720 (2018).

[9] D. De Fazio, I. Goykhman, D. Yoon, M. Bruna, A. Eiden, S. Milana, U. Sassi, M. Barbone, D. Dumcenco, K. Marinov, A. Kis, and A. C. Ferrari, ACS Nano **10**, 8252 (2016).

[10] B. W. H. H. Baugher, H. O. H. H. Churchill, Y. Yang, and P. Jarillo-Herrero, Nat. Nanotechnol. **9**, 262 (2014).

[11] D.-H. Kang, M.-S. Kim, J. Shim, J. Jeon, H.-Y. Park, W.-S. Jung, H.-Y. Yu, C.-H. Pang, S. Lee, and J.-H. Park, Adv. Funct. Mater. **25**, 4219 (2015).

[12] W. Choi, N. Choudhary, G. Hee Han, J. Park, D. Akinwande, and Y. Hee Lee, Mater. Today **20**, (2017).

[13] F. Withers, O. Del Pozo-Zamudio, S. Schwarz, S. Dufferwiel, P. M. Walker, T. Godde, A. P. Rooney, A. Gholinia, C. R. Woods, P. Blake, S. J. Haigh, K. Watanabe, T. Taniguchi, I. L. Aleiner, A. K. Geim, V. I. Fal'Ko, A. I. Tartakovskii, and K. S. Novoselov, Nano Lett. **15**, 8223 (2015).

[14] Z. Xia and S. Guo, Chem. Soc. Rev. (2019).

[15] B. Chen, X. Zhang, K. Wu, H. Wang, J. Wang, and J. Chen, Opt. Express **23**, 26723 (2015).

[16] H. H. Li, Z. Yin, Q. He, H. H. Li, X. Huang, G. Lu, D. W. H. Fam, A. I. Y. Tok, Q. Zhang, and H. Zhang, Small **8**, 63 (2012).

[17] J. H. Lee, H. Z. Gul, H. Kim, B. H. Moon, S. Adhikari, J. H. Kim, H. Choi, Y. H. Lee, and S. C. Lim, Nano Lett. **17**, 673 (2017).

[18] Y. Zhu, Z. Li, L. Zhang, B. Wang, Z. Luo, J. Long, J. Yang, L. Fu, and Y. Lu, ACS Appl. Mater. Interfaces **10**, 43291 (2018).

[19] L. M. Xie, Nanoscale **7**, 18392 (2015).

[20] D. Wang, Z. Pan, Z. Wu, Z. Wang, and Z. Liu, J. Power Sources **264**, 229 (2014).

[21] X. Ge, M. Minkov, S. Fan, X. Li, and W. Zhou, Npj 2D Mater. Appl. **3**, 16 (2019).

[22] H. Ichimiya, M. Takinoue, A. Fukui, T. Yoshimura, A. Ashida, N. Fujimura, and D. Kiriya, ACS Appl. Mater. Interfaces **11**, 15922 (2019).

[23] Y. Ye, Z. J. Wong, X. Lu, X. Ni, H. Zhu, X. Chen, Y. Wang, and X. Zhang, Nat. Photonics **9**, 733 (2015).

[24] Z. Yin, H. Li, H. Li, L. Jiang, Y. Shi, Y. Sun, G. Lu, Q. Zhang, X. Chen, and H. Zhang, ACS Nano **6**, 74 (2012).

[25] H. Liang, Z. Cao, F. Ming, W. Zhang, D. H. Anjum, Y. Cui, L. Cavallo, and H. N. Alshareef, Nano Lett. **19**, 3199 (2019).

[26] D. B. Velusamy, R. H. Kim, S. Cha, J. Huh, R. Khazaeinezhad, S. H. Kassani, G. Song, S. M. Cho, S. H. Cho, I. Hwang, J. Lee, K. Oh, H. Choi, and C. Park, Nat. Commun. **6**, 8063 (2015).

[27] M. Bernardi, M. Palummo, and J. C. Grossman, Nano Lett. **13**, 3664 (2013).

[28] D.-H. Kang, S. R. Pae, J. Shim, G. Yoo, J. Jeon, J. W. Leem, J. S. Yu, S. Lee, B. Shin, and J.-H. Park, Adv. Mater. **28**, 7799 (2016).

[29] N. Zibouche, A. Kuc, J. Musfeldt, and T. Heine, Ann. Phys. **526**, 395 (2014).

[30] B. Liu, L. Chen, G. Liu, A. N. Abbas, M. Fathi, and C. Zhou, ACS Nano **8**, 5304 (2014).

[31] M. Xiao, S. Wei, Y. Li, J. Jasensky, J. Chen, C. L. Brooks, and Z. Chen, Chem. Sci. **9**, 1769 (2018).

[32] S. Yu, J. S. Kim, P. J. Jeon, J. Ahn, J. C. Park, and S. Im, Adv. Funct. Mater. **27**, 1603682 (2017).

[33] S.-H. Jo and J.-H. Park, ECS Trans. **75**, 73 (2016).

[34] Z. Wang, Y. Shen, S. Ning, Y. Ito, P. Liu, Z. Tang, T. Fujita, A. Hirata, and M. Chen, ACS Appl. Mater. Interfaces **9**, 29438 (2017).

[35] A. Dathbun, Y. Kim, Y. Choi, J. Sun, S. Kim, B. Kang, M. S. Kang, D. K. Hwang, S. Lee, C. Lee, and J. H. Cho, ACS Appl. Mater. Interfaces acsami.9b03078 (2019).

[36] T.-Y. Kim, J. Ha, K. Cho, J. Pak, J. Seo, J. Park, J.-K. Kim, S. Chung, Y. Hong, and T. Lee, ACS Nano **11**, 10273 (2017).

[37] W. Gao, F. Zhang, Z. Zheng, and J. Li, ACS Appl. Mater. Interfaces acsami.9b03709 (2019).

[38] J. Ma, K.-Y. Choi, S. H. Kim, H. Lee, and G. Yoo, Appl. Phys. Lett. **113**, 013102 (2018).

[39] Y. Liu, X. He, D. Hanlon, A. Harvey, U. Khan, Y. Li, and J. N. Coleman, ACS Nano **10**,

5980 (2016).

[40] N. Kumar, E. Fosso-Kankeu, and S. S. Ray, ACS Appl. Mater. Interfaces **11**, 19141 (2019).

[41] C.-H. Liu, G. Clark, T. Fryett, S. Wu, J. Zheng, F. Hatami, X. Xu, and A. Majumdar, Nano Lett. **17**, 200 (2017).

[42] L. Britnell, R. M. Ribeiro, A. Eckmann, R. Jalil, B. D. Belle, A. Mishchenko, Y.-J. Kim, R. V Gorbachev, T. Georgiou, S. V Morozov, A. N. Grigorenko, A. K. Geim, C. Casiraghi, A. H. C. Neto, and K. S. Novoselov, Science **340**, 1311 (2013).

[43] F. Ersan, S. Cahangirov, G. Gökoğlu, A. Rubio, and E. Aktürk, Phys. Rev. B **94**, 155415 (2016).

[44] H. He, P. Lu, L. Wu, C. Zhang, Y. Song, P. Guan, and S. Wang, Nanoscale Res. Lett. **11**, 330 (2016).

[45] L. Liu, J. Wu, L. Wu, M. Ye, X. Liu, Q. Wang, S. Hou, P. Lu, L. Sun, J. Zheng, L. Xing, L. Gu, X. Jiang, L. Xie, and L. Jiao, Nat. Mater. **17**, 1108 (2018).

[46] J. van Baren, G. Ye, J.-A. Yan, Z. Ye, P. Rezaie, P. Yu, Z. Liu, R. He, and C. H. Lui, 2D Mater. **6**, 025022 (2019).

[47] S. Zhang, N. Zhang, Y. Zhao, T. Cheng, X. Li, R. Feng, H. Xu, Z. Liu, J. Zhang, and L. Tong, Chem. Soc. Rev. **47**, 3217 (2018).

[48] A. Molina-Sánchez, K. Hummer, and L. Wirtz, Surf. Sci. Rep. **70**, 554 (2015).

[49] L. M. Malard, T. V. Alencar, A. P. M. Barboza, K. F. Mak, and A. M. de Paula, Phys. Rev. B **87**, 201401 (2013).

[50] D. H. Kim and D. Lim, J. Korean Phys. Soc. **66**, 816 (2015).

[51] J. Klein, J. Wierzbowski, A. Steinhoff, M. Florian, M. Rösner, F. Heimbach, K. Müller, F. Jahnke, T. O. Wehling, J. J. Finley, and M. Kaniber, Nano Lett. **17**, 392 (2017).

[52] R. N. Gontijo, A. Gadelha, O. J. Silveira, B. R. Carvalho, R. W. Nunes, L. C. Campos, M. A. Pimenta, A. Righi, and C. Fantini, J. Raman Spectrosc. **50**, 1867 (2019).

[53] B. R. Carvalho, Y. Wang, S. Mignuzzi, D. Roy, M. Terrones, C. Fantini, V. H. Crespi, L. M. Malard, and M. A. Pimenta, Nat. Commun. **8**, 14670 (2017).

[54] S. Fang, R. Kuate Defo, S. N. Shirodkar, S. Lieu, G. A. Tritsaris, and E. Kaxiras, Phys. Rev. B **92**, 205108 (2015).

[55] D. Y. Qiu, F. H. da Jornada, and S. G. Louie, Phys. Rev. Lett. **111**, 216805 (2013).

[56] J. Silva-Guillén, P. San-Jose, and R. Roldán, Appl. Sci. **6**, 284 (2016).

[57] A. R. Beal and H. P. Hughes, J. Phys. C Solid State Phys. **12**, 881 (1979).

[58] R. Coehoorn, C. Haas, and R. A. de Groot, Phys. Rev. B **35**, 6203 (1987).

[59] N. Scheuschner, O. Ochedowski, M. Schleberger, and J. Maultzsch, Phys. Status Solidi **249**, 2644 (2012).

[60] P. Soubelet, A. E. Bruchhausen, A. Fainstein, K. Nogajewski, and C. Faugeras, Phys. Rev. B **93**, 155407 (2016).

[61] E. del Corro, A. Botello-Méndez, Y. Gillet, A. L. Elias, H. Terrones, S. Feng, C. Fantini, D. Rhodes, N. Pradhan, L. Balicas, X. Gonze, J.-C. Charlier, M. Terrones, and M. A. Pimenta, Nano Lett. **16**, 2363 (2016).

[62] T. Sekine, T. Nakashizu, M. Izumi, and K. Toyoda, in *Proc. 15th Int. Conf. Phys. Semicond.* (1980), pp. 551–554.

[63] Y. Li, A. Chernikov, X. Zhang, A. Rigosi, H. M. Hill, A. M. van der Zande, D. A. Chenet, E.-M. Shih, J. Hone, and T. F. Heinz, Phys. Rev. B **90**, 205422 (2014).

[64] A. R. Klots, A. K. M. Newaz, B. Wang, D. Prasai, H. Krzyzanowska, J. Lin, D. Caudel, N. J. Ghimire, J. Yan, B. L. Ivanov, K. A. Velizhanin, A. Burger, D. G. Mandrus, N. H. Tolk, S. T. Pantelides, and K. I. Bolotin, Sci. Rep. **4**, 6608 (2015).

[65] D. Kozawa, R. Kumar, A. Carvalho, K. Kumar Amara, W. Zhao, S. Wang, M. Toh, R. M. Ribeiro, A. H. Castro Neto, K. Matsuda, and G. Eda, Nat. Commun. **5**, 4543 (2014).

[66] B. Han, C. Robert, E. Courtade, M. Manca, S. Shree, T. Amand, P. Renucci, T. Taniguchi, K. Watanabe, X. Marie, L. E. Golub, M. M. Glazov, and B. Urbaszek, Phys. Rev. X **8**, 031073 (2018).

[67] R. Kumar, I. Verzhbitskiy, F. Giustiniano, T. P. H. Sidiropoulos, R. F. Oulton, and G. Eda, 2D Mater. **5**, 041003 (2018).

[68] Z. Y. Zhu, Y. C. Cheng, and U. Schwingenschlögl, Phys. Rev. B **84**, 153402 (2011).

[69] D. Xiao, G. Bin Liu, W. Feng, X. Xu, and W. Yao, Phys. Rev. Lett. **108**, 196802 (2012).

[70] G.-B. Liu, W.-Y. Shan, Y. Yao, W. Yao, and D. Xiao, Phys. Rev. B **88**, 085433 (2013).

[71] A. Kuc and T. Heine, Electronics **5**, 1 (2015).

[72] A. Kormányos, G. Burkard, M. Gmitra, J. Fabian, V. Zólyomi, N. D. Drummond, and V. Fal'ko, 2D Mater. **2**, 022001 (2015).

[73] M. A. Khan, M. Erementchouk, J. Hendrickson, and M. N. Leuenberger, Phys. Rev. B **95**, 245435 (2017).

[74] L. Sun, J. Yan, D. Zhan, L. Liu, H. Hu, H. Li, B. K. Tay, J.-L. L. Kuo, C.-C. C. Huang, D. W. Hewak, P. S. Lee, and Z. X. Shen, Phys. Rev. Lett. **111**, 126801 (2013).

[75] G. Wang, C. Robert, A. Suslu, B. Chen, S. Yang, S. Alamdari, I. C. Gerber, T. Amand, X. Marie, S. Tongay, and B. Urbaszek, Nat. Commun. **6**, 10110 (2015).

[76] J. W. Christopher, B. B. Goldberg, and A. K. Swan, Sci. Rep. **7**, 14062 (2017).

[77] Y. Chen, W. Wen, Y. Zhu, N. Mao, Q. Feng, M. Zhang, H.-P. Hsu, J. Zhang, Y.-S. Huang, and L. Xie, Nanotechnology **27**, 445705 (2016).

[78] R. C. Miller and D. A. Kleinman, J. Lumin. **30**, 520 (1985).

[79] A. D. Yoffe, Adv. Phys. **42**, 173 (1993).

[80] Y. Y. Yu, Y. Y. Yu, Y. Cai, W. Li, A. Gurarslan, H. Peelaers, D. E. Aspnes, C. G. Van De Walle, N. V Nguyen, Y.-W. Zhang, and L. Cao, Sci. Rep. **5**, 16996 (2015).

[81] J. D. E. McIntyre and D. E. Aspnes, Surf. Sci. **24**, 417 (1971).

[82] J. S. Ross, S. Wu, H. Yu, N. J. Ghimire, A. M. Jones, G. Aivazian, J. Yan, D. G. Mandrus, D. Xiao, W. Yao, and X. Xu, Nat. Commun. **4**, 1474 (2013).

[83] F. Wu, F. Qu, and A. H. MacDonald, Phys. Rev. B **91**, 075310 (2015).

[84] K. Wei, Y. Liu, H. Yang, X. Cheng, and T. Jiang, Appl. Opt. **55**, 6251 (2016).

[85] J. Huang, T. B. Hoang, and M. H. Mikkelsen, Sci. Rep. **6**, 22414 (2016).

[86] M. Koperski, M. R. Molas, A. Arora, K. Nogajewski, A. O. Slobodeniuk, C. Faugeras, and M. Potemski, Nanophotonics **6**, 1289 (2017).

[87] J. Jadczak, J. Kutrowska-Girzycka, P. Kapuściński, Y. S. Huang, A. Wójs, and L. Bryja, Nanotechnology **28**, 395702 (2017).

[88] L. P. McDonnell, C.-C. C. Huang, Q. Cui, D. W. Hewak, and D. C. Smith, Nano Lett. **18**, 1428 (2018).

[89] L. Du, T. Zhang, M. Liao, G. Liu, S. Wang, R. He, Z. Ye, H. Yu, R. Yang, D. Shi, Y. Yao, and G. Zhang, Phys. Rev. B **97**, 165410 (2018).

[90] H.-V. Han, A.-Y. Lu, L.-S. Lu, J.-K. Huang, H. Li, C.-L. Hsu, Y.-C. Lin, M.-H. Chiu, K. Suenaga, C.-W. Chu, H.-C. Kuo, W.-H. Chang, L.-J. Li, and Y. Shi, ACS Nano **10**, 1454 (2016).

[91] F. Cadiz, S. Tricard, M. Gay, D. Lagarde, G. Wang, C. Robert, P. Renucci, B. Urbaszek, and X. Marie, Appl. Phys. Lett. **108**, 251106 (2016).

[92] P. K. Gogoi, Z. Hu, Q. Wang, A. Carvalho, D. Schmidt, X. Yin, Y.-H. Chang, L.-J. Li, C. H. Sow, A. H. C. Neto, M. B. H. Breese, A. Rusydi, and A. T. S. Wee, Phys. Rev. Lett. **119**, 077402 (2017).

[93] K. P. Dhakal, S. Roy, S. J. Yun, G. Ghimire, C. Seo, and J. Kim, J. Mater. Chem. C **5**, 6820 (2017).

[94] K. F. Mak, K. He, C. Lee, G. H. Lee, J. Hone, T. F. Heinz, and J. Shan, Nat. Mater. **12**, 207 (2013).

[95] J. S. Ross, P. Klement, A. M. Jones, N. J. Ghimire, J. Yan, D. G. Mandrus, T. Taniguchi, K. Watanabe, K. Kitamura, W. Yao, D. H. Cobden, and X. Xu, Nat. Nanotechnol. **9**, 268

(2014).
[96] J. Shang, X. Shen, C. Cong, N. Peimyoo, B. Cao, M. Eginligil, and T. Yu, ACS Nano **9**, 647 (2015).
[97] H. S. Lee, M. S. Kim, H. Kim, and Y. H. Lee, Phys. Rev. B **93**, 140409 (2016).
[98] G. Moody, J. Schaibley, and X. Xu, J. Opt. Soc. Am. B **33**, C39 (2016).
[99] M. R. Molas, K. Nogajewski, A. O. Slobodeniuk, J. Binder, M. Bartos, and M. Potemski, Nanoscale **9**, 13128 (2017).
[100] Q. Zhang, C. H. Naylor, Z. Gao, R. Wu, I. H. Abidi, M.-Q. Q. Zhao, Y. Ding, A. A. Cagang, M. Zhuang, X. Ou, and Z. Luo, ACS Nano **11**, 10808 (2017).
[101] P. Nagler, M. V. Ballottin, A. A. Mitioglu, M. V. Durnev, T. Taniguchi, K. Watanabe, A. Chernikov, C. Schüller, M. M. Glazov, P. C. M. Christianen, and T. Korn, Phys. Rev. Lett. **121**, 57402 (2018).
[102] H. Liu, J. Lu, K. Ho, Z. Hu, Z. Dang, A. Carvalho, H. R. Tan, E. S. Tok, and C. H. Sow, Nano Lett. **16**, 5559 (2016).
[103] Z. Wu, W. Zhao, J. Jiang, T. Zheng, Y. You, J. Lu, and Z. Ni, J. Phys. Chem. C **121**, 12294 (2017).
[104] Q.-H. Tan, S.-L. Ren, T. Shen, X.-L. Liu, W. Shi, Y.-J. Sun, H.-X. Deng, P.-H. Tan, and J. Zhang, J. Phys. Chem. C **123**, 4433 (2019).
[105] Y. You, X.-X. X. Zhang, T. C. Berkelbach, M. S. Hybertsen, D. R. Reichman, and T. F. Heinz, Nat. Phys. **11**, 477 (2015).
[106] F. Cadiz, C. Robert, G. Wang, W. Kong, X. Fan, M. Blei, D. Lagarde, M. Gay, M. Manca, T. Taniguchi, K. Watanabe, T. Amand, X. Marie, P. Renucci, S. Tongay, and B. Urbaszek, 2D Mater. **3**, 045008 (2016).
[107] A. Chernikov, T. C. Berkelbach, H. M. Hill, A. Rigosi, Y. Li, O. B. Aslan, D. R. Reichman, M. S. Hybertsen, and T. F. Heinz, Phys. Rev. Lett. **113**, 076802 (2014).
[108] H. M. Hill, A. F. Rigosi, C. Roquelet, A. Chernikov, T. C. Berkelbach, D. R. Reichman, M. S. Hybertsen, L. E. Brus, and T. F. Heinz, Nano Lett. **15**, 2992 (2015).
[109] N. W. Ashcroft and N. D. Mermin, *Solid State Physics* (Cengage Learning, 2011).
[110] J. Ribeiro-Soares, R. M. Almeida, E. B. Barros, P. T. Araujo, M. S. Dresselhaus, L. G. Cançado, and A. Jorio, Phys. Rev. B **90**, 115438 (2014).
[111] E. Del Corro, H. Terrones, A. Elias, C. Fantini, S. Feng, M. A. Nguyen, T. E. Mallouk, M. Terrones, and M. A. Pimenta, ACS Nano **8**, 9629 (2014).
[112] C. Ruppert, O. B. Aslan, and T. F. Heinz, Nano Lett. **14**, 6231 (2014).
[113] B. Amin, T. P. Kaloni, and U. Schwingenschlögl, RSC Adv. **4**, 34561 (2014).

[114] C. Lee, H. Yan, L. E. Brus, T. F. Heinz, J. Hone, and S. Ryu, ACS Nano **4**, 2695 (2010).

[115] H. Li, Q. Zhang, C. C. R. Yap, B. K. Tay, T. H. T. Edwin, A. Olivier, and D. Baillargeat, Adv. Funct. Mater. **22**, 1385 (2012).

[116] M. Placidi, M. Dimitrievska, V. Izquierdo-Roca, X. Fontane, A. Castellanos-Gomez, A. Perez-Tomas, N. Mestres, M. Espindola-Rodriguez, S. Lopez-Marino, M. Neuschitzer, V. Bermudez, A. Yaremko, A. Perez-Rodriguez, X. Fontané, A. Castellanos-Gomez, A. Pérez-Tomás, N. Mestres, M. Espindola-Rodriguez, S. López-Marino, M. Neuschitzer, V. Bermudez, A. Yaremko, and A. Pérez-Rodríguez, 2D Mater. **2**, 10 (2015).

[117] I. Bilgin, A. S. Raeliarijaona, M. C. Lucking, S. C. Hodge, A. D. Mohite, A. de Luna Bugallo, H. Terrones, and S. Kar, ACS Nano **12**, 740 (2018).

[118] K. Kim, J. U. Lee, D. Nam, and H. Cheong, ACS Nano **10**, 8113 (2016).

[119] A. Berkdemir, H. R. Gutiérrez, A. R. Botello-Méndez, N. Perea-López, A. L. Elías, C.-I. Chia, B. Wang, V. H. Crespi, F. López-Urías, J.-C. Charlier, H. Terrones, and M. Terrones, Sci. Rep. **3**, 1755 (2013).

[120] X. Luo, Y. Zhao, J. Zhang, M. Toh, C. Kloc, Q. Xiong, and S. Y. Quek, Phys. Rev. B **88**, 195313 (2014).

[121] L. Du, M. Liao, J. Tang, Q. Zhang, H. Yu, R. Yang, K. Watanabe, T. Taniguchi, D. Shi, Q. Zhang, and G. Zhang, Phys. Rev. B **97**, 235145 (2018).

[122] M. Fox, *Optical Properties of Solids, 2nd Ed* (Oxford university press, 2010).

[123] M. Amani, D.-H. Lien, D. Kiriya, J. Xiao, A. Azcatl, J. Noh, S. R. Madhvapathy, R. Addou, S. KC, M. Dubey, K. Cho, R. M. Wallace, S.-C. Lee, J.-H. He, J. W. Ager, X. Zhang, E. Yablonovitch, and A. Javey, Science **350**, 1065 (2015).

[124] K. F. Mak, C. Lee, J. Hone, J. Shan, and T. F. Heinz, Phys. Rev. Lett. **105**, 136805 (2010).

[125] S. Dubey, S. Lisi, G. Nayak, F. Herziger, V.-D. Nguyen, T. Le Quang, V. Cherkez, C. González, Y. J. Dappe, K. Watanabe, T. Taniguchi, L. Magaud, P. Mallet, J.-Y. Veuillen, R. Arenal, L. Marty, J. Renard, N. Bendiab, J. Coraux, and V. Bouchiat, ACS Nano **11**, 11206 (2018).

[126] S. Shree, M. Semina, C. Robert, B. Han, T. Amand, A. Balocchi, M. Manca, E. Courtade, X. Marie, T. Taniguchi, K. Watanabe, M. M. Glazov, and B. Urbaszek, Phys. Rev. B **98**, 035302 (2018).

[127] C. M. Chow, H. Yu, A. M. Jones, J. R. Schaibley, M. Koehler, D. G. Mandrus, R. Merlin, W. Yao, and X. Xu, Npj 2D Mater. Appl. **1**, 33 (2017).

[128] A. C. Ferrari, J. C. Meyer, V. Scardaci, C. Casiraghi, M. Lazzeri, F. Mauri, S. Piscanec,

D. Jiang, K. S. Novoselov, S. Roth, and A. K. Geim, Phys. Rev. Lett. **97**, 1 (2006).

[129] L. M. Malard, M. A. Pimenta, G. Dresselhaus, and M. S. Dresselhaus, Phys. Rep. **473**, 51 (2009).

[130] A. C. Ferrari and D. M. Basko, Nat. Nanotechnol. **8**, 235 (2013).

[131] H. B. Ribeiro, M. A. Pimenta, and C. J. S. de Matos, J. Raman Spectrosc. **49**, 76 (2018).

[132] S. Reich, A. C. Ferrari, R. Arenal, A. Loiseau, I. Bello, and J. Robertson, Phys. Rev. B **71**, 205201 (2005).

[133] Q. Cai, D. Scullion, A. Falin, K. Watanabe, T. Taniguchi, Y. Chen, E. J. G. Santos, and L. H. Li, Nanoscale **9**, 3059 (2017).

[134] C. Attaccalite, L. Wirtz, A. Marini, and A. Rubio, Sci. Rep. **3**, 2698 (2013).

[135] M. A. Pimenta, E. del Corro, B. R. Carvalho, C. Fantini, and L. M. Malard, Acc. Chem. Res. **48**, 41 (2015).

[136] R. Saito, Y. Tatsumi, S. Huang, X. Ling, and M. S. Dresselhaus, J. Phys. Condens. Matter **28**, 353002 (2016).

[137] C. H. Lui, Z. Ye, C. Ji, K.-C. Chiu, C.-T. Chou, T. I. Andersen, C. Means-Shively, H. Anderson, J.-M. Wu, T. Kidd, Y.-H. Lee, and R. He, Phys. Rev. B **91**, 165403 (2015).

[138] B. R. Carvalho, L. M. Malard, J. M. Alves, C. Fantini, and M. A. Pimenta, Phys. Rev. Lett. **114**, 136403 (2015).

[139] X. Zhang, X.-F. Qiao, W. Shi, J.-B. Wu, D.-S. Jiang, and P.-H. Tan, Chem. Soc. Rev. **44**, 2757 (2015).

[140] A. A. Puretzky, L. Liang, X. Li, K. Xiao, K. Wang, M. Mahjouri-Samani, L. Basile, J. C. Idrobo, B. G. Sumpter, V. Meunier, and D. B. Geohegan, ACS Nano **9**, 6333 (2015).

[141] M.-H. Chiu, M.-Y. Li, W. Zhang, W.-T. Hsu, W.-H. Chang, M. Terrones, H. Terrones, and L.-J. Li, ACS Nano **8**, 9649 (2014).

[142] G. W. Shim, K. Yoo, S.-B. Seo, J. Shin, D. Y. Jung, I.-S. Kang, C. W. Ahn, B. J. Cho, and S.-Y. Choi, ACS Nano **8**, 6655 (2014).

[143] Y. Gong, S. Lei, G. Ye, B. Li, Y. He, K. Keyshar, X. Zhang, Q. Wang, J. Lou, Z. Liu, R. Vajtai, W. Zhou, and P. M. Ajayan, Nano Lett. **15**, 6135 (2015).

[144] K. Zhang, T. Zhang, G. Cheng, T. Li, S. Wang, W. Wei, X. Zhou, W. Yu, Y. Sun, P. Wang, D. Zhang, C. Zeng, X. Wang, W. Hu, H. J. Fan, G. Shen, X. Chen, X. Duan, K. Chang, and N. Dai, ACS Nano **10**, 3852 (2016).

[145] R. C. Miller, D. A. Kleinman, and A. C. Gossard, Solid State Commun. **60**, 213 (1986).

[146] F. Cerdeira, E. Anastassakis, W. Kauschke, and M. Cardona, Phys. Rev. Lett. **57**, 3209 (1986).

[147] A. Alexandrou, M. Cardona, and K. Ploog, Phys. Rev. B **38**, 2196 (1988).

[148] S. I. Gubarev, T. Ruf, and M. Cardona, Phys. Rev. B **43**, 1551 (1991).

[149] C. Thomsen and S. Reich, Phys. Rev. Lett. **85**, 5214 (2000).

[150] A. Grüneis, R. Saito, T. Kimura, L. G. Cançado, M. A. Pimenta, A. G. Jorio, A. G. Souza Filho, G. Dresselhaus, and M. S. Dresselhaus, Phys. Rev. B **65**, 1 (2002).

[151] S. Reich and C. Thomsen, Philos. Trans. R. Soc. A Math. Phys. Eng. Sci. **362**, 2271 (2004).

[152] J. Maultzsch, S. Reich, and C. Thomsen, Phys. Rev. B **70**, 155403 (2004).

[153] L. G. Cançado, M. A. Pimenta, B. R. A. Neves, M. S. S. Dantas, and A. Jorio, Phys. Rev. Lett. **93**, 5 (2004).

[154] A. C. Ferrari, Solid State Commun. **143**, 47 (2007).

[155] D. L. Mafra, G. Samsonidze, L. M. Malard, D. C. Elias, J. C. Brant, F. Plentz, E. S. Alves, and M. A. Pimenta, Phys. Rev. B **76**, 233407 (2007).

[156] L. G. Cançado, A. Jorio, E. H. M. Ferreira, F. Stavale, C. A. Achete, R. B. Capaz, M. V. O. Moutinho, A. Lombardo, T. S. Kulmala, and A. C. Ferrari, Nano Lett. **11**, 3190 (2011).

[157] I. Kupčić, J. Raman Spectrosc. **43**, 1 (2012).

[158] D. Yoon, Y. W. Son, and H. Cheong, Phys. Rev. Lett. **106**, 1 (2011).

[159] P. Venezuela, M. Lazzeri, and F. Mauri, Phys. Rev. B **84**, 1 (2011).

[160] T. Sekine, K. Uchinokura, T. Nakashizu, E. Matsuura, and R. Yoshizaki, J. Phys. Soc. Japan **53**, 811 (1984).

[161] A. M. M. Stacy and D. T. T. Hodul, J. Phys. Chem. Solids **46**, 405 (1985).

[162] C. Sourisseau, F. Cruege, M. Fouassier, and M. Alba, Chem. Phys. **150**, 281 (1991).

[163] N. T. McDevitt, J. S. Zabinski, M. S. Donley, and J. E. Bultman, Appl. Spectrosc. **48**, 733 (1994).

[164] G. L. Frey, R. Tenne, M. J. Matthews, M. S. Dresselhaus, and G. Dresselhaus, Phys. Rev. B **60**, 2883 (1999).

[165] T. Livneh and E. Sterer, Phys. Rev. B **81**, 195209 (2010).

[166] K. Gołasa, M. Grzeszczyk, K. P. Korona, R. Bożek, J. Binder, J. Szczytko, A. Wysmołek, and A. Babiński, Acta Phys. Pol. A **124**, 849 (2013).

[167] A. A. Mitioglu, P. Plochocka, G. Deligeorgis, S. Anghel, L. Kulyuk, and D. K. Maude, Phys. Rev. B **89**, 245442 (2014).

[168] H.-L. Liu, H. Guo, T. Yang, Z. Zhang, Y. Kumamoto, C.-C. Shen, Y.-T. Hsu, L.-J. Li, R. Saito, and S. Kawata, Phys. Chem. Chem. Phys. **17**, 14561 (2015).

[169] H. Guo, T. Yang, M. Yamamoto, L. Zhou, R. Ishikawa, K. Ueno, K. Tsukagoshi, Z. Zhang, M. S. Dresselhaus, and R. Saito, Phys. Rev. B **91**, 205415 (2015).

[170] W. Shi, M.-L. Lin, Q.-H. Tan, X.-F. Qiao, J. Zhang, and P.-H. Tan, 2D Mater. **3**, 025016 (2016).

[171] Q. Qian, Z. Zhang, and K. J. Chen, Phys. Rev. B **97**, 165409 (2018).

[172] J. Kutrowska-Girzycka, J. Jadczak, and L. Bryja, Solid State Commun. **275**, 25 (2018).

[173] Z. Lin, B. R. Carvalho, E. Kahn, R. Lv, R. Rao, H. Terrones, M. A. Pimenta, and M. Terrones, 2D Mater. **3**, 022002 (2016).

[174] Z. Hu, Z. Wu, C. Han, J. He, Z. Ni, and W. Chen, Chem. Soc. Rev. **47**, 3100 (2018).

[175] M. Cardona, *Light Scattering in Solids I*, 2nd ed. (Springer Berlin Heidelberg, Berlin, Heidelberg, 1983).

[176] R. N. Gontijo, G. C. Resende, C. Fantini, and B. R. Carvalho, J. Mater. Res. **34**, 1976 (2019).

[177] S. Mignuzzi, A. J. Pollard, N. Bonini, B. Brennan, I. S. Gilmore, M. A. Pimenta, D. Richards, and D. Roy, Phys. Rev. B **91**, 195411 (2015).

[178] H. L. Liu, S. Siregar, E. H. Hasdeo, Y. Kumamoto, C. C. Shen, C. C. Cheng, L. J. Li, R. Saito, and S. Kawata, Carbon N. Y. **81**, 807 (2015).

[179] L. M. Malard, D. L. Mafra, M. H. D. Guimarães, M. S. C. Mazzoni, and A. Jorio, Phys. Rev. B **79**, 125426 (2008).

[180] B. R. Carvalho, L. M. Malard, J. M. Alves, C. Fantini, and M. A. Pimenta, Phys. Rev. Lett. **116**, 089904 (2016).

[181] D. Nam, J.-U. Lee, and H. Cheong, Sci. Rep. **5**, 17113 (2015).

[182] A. Kumara, P. K. Ahluwalia, A. Kumar, and P. K. Ahluwalia, Eur. Phys. J. B **85**, 186 (2012).

[183] H.-P. Komsa and A. V Krasheninnikov, J. Phys. Chem. Lett. **3**, 3652 (2012).

[184] A. P. S. Gaur, S. Sahoo, J. F. Scott, and R. S. Katiyar, J. Phys. Chem. C **119**, 5146 (2015).

[185] J. M. Chen and C. S. Wang, Solid State Commun. **14**, 857 (1974).

[186] T. Livneh and J. E. Spanier, 2D Mater. **2**, 035003 (2015).

[187] Y. Gillet, S. Kontur, M. Giantomassi, C. Draxl, and X. Gonze, Sci. Rep. **7**, 7344 (2017).

[188] G. Wang, M. Glazov, C. Robert, T. Amand, X. Marie, and B. Urbaszek, Phys. Rev. Lett. **115**, 1 (2015).

[189] H.-L. Liu, T. Yang, Y. Tatsumi, Y. Zhang, B. Dong, H. Guo, Z. Zhang, Y. Kumamoto, M.-Y. Li, L.-J. Li, R. Saito, and S. Kawata, Sci. Rep. **8**, 11398 (2018).

[190] K. Gołasa, M. Grzeszczyk, P. Leszczyński, C. Faugeras, A. A. L. Nicolet, A. Wysmołek,

M. Potemski, and A. Babiński, Appl. Phys. Lett. **104**, 092106 (2014).

[191] H. Zeng, J. Dai, W. Yao, D. Xiao, and X. Cui, Nat. Nanotechnol. **7**, 490 (2012).

[192] K. F. Mak, K. He, J. Shan, and T. F. Heinz, Nat. Nanotechnol. **7**, 494 (2012).

[193] G. Kioseoglou, A. T. Hanbicki, M. Currie, A. L. Friedman, and B. T. Jonker, Sci. Rep. **6**, 25041 (2016).

[194] P. Dey, J. Paul, Z. Wang, C. E. Stevens, C. Liu, A. H. Romero, J. Shan, D. J. Hilton, and D. Karaiskaj, Phys. Rev. Lett. **116**, 127402 (2016).

[195] W. Zhou, X. Zou, S. Najmaei, Z. Liu, Y. Shi, J. Kong, J. Lou, P. M. Ajayan, B. I. Yakobson, and J. C. Idrobo, Nano Lett. **13**, 2615 (2013).

[196] Z. Wu, Z. Luo, Y. Shen, W. Zhao, W. Wang, H. Nan, X. Guo, L. Sun, X. Wang, Y. You, and Z. Ni, Nano Res. **9**, 3622 (2016).

[197] W. M. Parkin, A. Balan, L. Liang, P. M. Das, M. Lamparski, C. H. Naylor, J. A. Rodríguez-Manzo, A. T. C. C. Johnson, V. Meunier, and M. Drndić, ACS Nano **10**, 4134 (2016).

[198] W. Shi, X. Zhang, X.-L. Li, X.-F. Qiao, J.-B. Wu, J. Zhang, and P.-H. Tan, Chinese Phys. Lett. **33**, 057801 (2016).

[199] H.-P. Komsa, J. Kotakoski, S. Kurasch, O. Lehtinen, U. Kaiser, and A. V. Krasheninnikov, Phys. Rev. Lett. **109**, 035503 (2012).

[200] J. Lu, A. Carvalho, X. K. Chan, H. Liu, B. Liu, E. S. Tok, K. P. Loh, A. H. Castro Neto, and C. H. Sow, Nano Lett. **15**, 3524 (2015).

[201] H. Fang, M. Tosun, G. Seol, T. C. Chang, K. Takei, J. Guo, and A. Javey, Nano Lett. **13**, 1991 (2013).

[202] K. Dolui, I. Rungger, C. Das Pemmaraju, and S. Sanvito, Phys. Rev. B **88**, 1 (2013).

[203] N. Saigal, I. Wielert, D. Čapeta, N. Vujičić, B. V Senkovskiy, M. Hell, M. Kralj, and A. Grüneis, Appl. Phys. Lett. **112**, 121902 (2018).

[204] E. Asari, I. Kamioka, K. G. Nakamura, T. Kawabe, W. A. Lewis, and M. Kitajima, Phys. Rev. B **49**, 1011 (1994).

[205] E. H. Martins Ferreira, M. V. O. Moutinho, F. Stavale, M. M. Lucchese, R. B. Capaz, C. A. Achete, and A. Jorio, Phys. Rev. B **82**, 125429 (2010).

[206] M. M. Lucchese, F. Stavale, E. H. M. Ferreira, C. Vilani, M. V. O. Moutinho, R. B. Capaz, C. A. Achete, and A. Jorio, Carbon N. Y. **48**, 1592 (2010).

[207] A. Eckmann, A. Felten, A. Mishchenko, L. Britnell, R. Krupke, K. S. Novoselov, and C. Casiraghi, Nano Lett. **12**, 3925 (2012).

[208] H. Richter, Z. P. Wang, and L. Ley, Solid State Commun. **39**, 625 (1981).

[209] I. H. Campbell and P. M. Fauchet, Solid State Commun. **58**, 739 (1986).

[210] K. Ishioka, K. G. Nakamura, and M. Kitajima, Phys. Rev. B **52**, 2539 (1995).

[211] C. Lee, B. G. Jeong, S. J. Yun, Y. H. Lee, S. M. Lee, and M. S. Jeong, ACS Nano **12**, 9982 (2018).

[212] A. McCreary, J. R. Simpson, Y. Wang, D. Rhodes, K. Fujisawa, L. Balicas, M. Dubey, V. H. Crespi, M. Terrones, and A. R. Hight Walker, Nano Lett. **17**, 5897 (2017).

[213] D. Wolverson, S. Crampin, A. S. Kazemi, A. Ilie, and S. J. Bending, ACS Nano **8**, 11154 (2014).

[214] X. Wang, N. Mao, W. Luo, H. Kitadai, and X. Ling, J. Phys. Chem. Lett. **9**, 2830 (2018).

[215] A. Favron, F. A. Goudreault, V. Gosselin, J. Groulx, M. Côté, R. Leonelli, J. F. Germain, A. L. Phaneuf-L'Heureux, S. Francoeur, and R. Martel, Nano Lett. **18**, 1018 (2018).

[216] J. Sun, X. Li, W. Guo, M. Zhao, X. Fan, Y. Dong, C. Xu, J. Deng, and Y. Fu, Crystals **7**, 1 (2017).

[217] S. B. Desai, S. R. Madhvapathy, M. Amani, D. Kiriya, M. Hettick, M. Tosun, Y. Zhou, M. Dubey, J. W. Ager, D. Chrzan, and A. Javey, Adv. Mater. **28**, 4053 (2016).

[218] M. Velický, G. E. Donnelly, W. R. Hendren, S. McFarland, D. Scullion, W. J. I. Debenedetti, G. C. Correa, Y. Han, A. J. Wain, M. A. Hines, D. A. Muller, K. S. Novoselov, H. D. Abruna, R. M. Bowman, E. J. G. Santos, and F. Huang, ACS Nano (2018).

[219] M. R. Molas, K. Nogajewski, M. Potemski, and A. Babiński, Sci. Rep. **7**, 5036 (2017).

[220] Y. Zhang, Y. Yao, M. G. Sendeku, L. Yin, X. Zhan, F. Wang, Z. Wang, and J. He, Adv. Mater. **31**, 1901694 (2019).

[221] M. Samadi, N. Sarikhani, M. Zirak, H. Zhang, H.-L. Zhang, and A. Z. Moshfegh, Nanoscale Horizons **3**, 90 (2018).

[222] M. K. Jana and C. N. R. Rao, Philos. Trans. R. Soc. A Math. Phys. Eng. Sci. **374**, 20150318 (2016).

[223] J. You, M. D. Hossain, and Z. Luo, Nano Converg. **5**, 26 (2018).

[224] X. Song, Z. Guo, Q. Zhang, P. Zhou, W. Bao, and D. W. Zhang, Small **13**, 1700098 (2017).

[225] J. Yu, J. Li, W. Zhang, and H. Chang, Chem. Sci. **6**, 6705 (2015).

[226] Z. Cai, B. Liu, X. Zou, and H.-M. Cheng, Chem. Rev. **118**, 6091 (2018).

[227] X. Huang, Y. Gao, T. Yang, W. Ren, H.-M. Cheng, and T. Lai, Sci. Rep. **6**, 32236 (2016).

[228] K. Almeida, M. Wurch, A. Geremew, K. Yamaguchi, T. A. Empante, M. D. Valentin, M. Gomez, A. J. Berges, G. Stecklein, S. Rumyantsev, J. Martinez, A. A. Balandin, and

L. Bartels, ACS Appl. Mater. Interfaces **10**, 33457 (2018).

[229] J. Robertson, D. Blomdahl, K. Islam, T. Ismael, M. Woody, J. Failla, M. Johnson, X. Zhang, and M. Escarra, Appl. Phys. Lett. **114**, 163102 (2019).

[230] J. Chen, K. Shao, W. Yang, W. Tang, J. Zhou, Q. He, Y. Wu, C. Zhang, X. Li, X. Yang, Z. Wu, and J. Kang, ACS Appl. Mater. Interfaces **11**, 19381 (2019).

[231] J. B. Renucci, R. N. Tyte, and M. Cardona, Phys. Rev. B **11**, 3885 (1975).

[232] H. R. Philipp, J. Appl. Phys. **43**, 2835 (1972).

[233] V. Carozo, Y. Wang, K. Fujisawa, B. R. Carvalho, A. McCreary, S. Feng, Z. Lin, C. Zhou, N. Perea-López, A. L. Elías, B. Kabius, V. H. Crespi, and M. Terrones, Sci. Adv. **3**, e1602813 (2017).

[234] X. Wang, Y. Gong, G. Shi, W. L. Chow, K. Keyshar, G. Ye, R. Vajtai, J. Lou, Z. Liu, E. Ringe, B. K. Tay, and P. M. Ajayan, ACS Nano **8**, 5125 (2014).

[235] A. L. Elías, N. Perea-López, A. Castro-Beltrán, A. Berkdemir, R. Lv, S. Feng, A. D. Long, T. Hayashi, Y. A. Kim, M. Endo, H. R. Gutiérrez, N. R. Pradhan, L. Balicas, T. E. Mallouk, F. López-Urías, H. Terrones, and M. Terrones, ACS Nano **7**, 5235 (2013).

[236] S. Tongay, W. Fan, J. Kang, J. Park, U. Koldemir, J. Suh, D. S. Narang, K. Liu, J. Ji, J. Li, R. Sinclair, and J. Wu, Nano Lett. **14**, 3185 (2014).

[237] H. Fang, C. Battaglia, C. Carraro, S. Nemsak, B. Ozdol, J. S. Kang, H. A. Bechtel, S. B. Desai, F. Kronast, A. A. Unal, G. Conti, C. Conlon, G. K. Palsson, M. C. Martin, A. M. Minor, C. S. Fadley, E. Yablonovitch, R. Maboudian, and A. Javey, Proc. Natl. Acad. Sci. **111**, 6198 (2014).

[238] L. F. Huang, P. L. Gong, and Z. Zeng, Phys. Rev. B **90**, 045409 (2014).

[239] Z.-Y. Cao and X.-J. Chen, Appl. Phys. Lett. **114**, 052102 (2019).

[240] N. A. Lanzillo, A. Glen Birdwell, M. Amani, F. J. Crowne, P. B. Shah, S. Najmaei, Z. Liu, P. M. Ajayan, J. Lou, M. Dubey, S. K. Nayak, and T. P. O'Regan, Appl. Phys. Lett. **103**, 093102 (2013).

[241] A. Taube, J. Judek, C. Jastrzębski, A. Duzynska, K. Świtkowski, M. Zdrojek, C. Jastrzębski, A. Duzynska, K. Świtkowski, and M. Zdrojek, ACS Appl. Mater. Interfaces **6**, 8959 (2014).

[242] R. Yan, J. R. Simpson, S. Bertolazzi, J. Brivio, M. Watson, X. Wu, A. Kis, T. Luo, A. R. Hight Walker, and H. G. Xing, ACS Nano **8**, 986 (2014).

[243] S. Sahoo, A. P. S. Gaur, M. Ahmadi, M. J.-F. Guinel, and R. S. Katiyar, J. Phys. Chem. C **117**, 9042 (2013).

[244] P. B. Allen and M. Cardona, Phys. Rev. B **23**, 1495 (1981).

[245] J. Oishi and T. Kimura, Metrologia **5**, 50 (1969).

[246] R. Murray and B. Evans, J. Appl. Crystallogr. **12**, 312 (1979).

[247] C. Bousige, F. Balima, D. Machon, G. S. Pinheiro, A. Torres-Dias, J. Nicolle, D. Kalita, D. N. Bendiab, L. Marty, V. Bouchiat, G. Montagnac, A. G. Souza Filho, P. Poncharal, and A. San-Miguel, Nano Lett. **17**, 21 (2017).

[248] D. Machon, C. Bousige, R. Alencar, A. Torres-Dias, F. Balima, J. Nicolle, G. de Sousa Pinheiro, A. G. Souza Filho, and A. San-Miguel, J. Raman Spectrosc. **49**, 121 (2018).

[249] G. Plechinger, F.-X. Schrettenbrunner, J. Eroms, D. Weiss, C. Schüller, and T. Korn, Phys. Status Solidi - Rapid Res. Lett. **6**, 126 (2012).

[250] H. J. Conley, B. Wang, J. I. Ziegler, R. F. Haglund, S. T. Pantelides, and K. I. Bolotin, Nano Lett. **13**, 3626 (2013).

[251] M. Cardona, R. K. Chang, G. Güntherodt, M. B. Long, and H. Vogt, *Light Scattering in Solids II* (Springer Berlin Heidelberg, Berlin, Heidelberg, 1982).

[252] B. Chakraborty, H. S. S. R. Matte, A. K. Sood, and C. N. R. Rao, J. Raman Spectrosc. **44**, 92 (2013).

[253] A. Molina-Sánchez and L. Wirtz, Phys. Rev. B **84**, 155413 (2011).

[254] R. Addou, L. Colombo, and R. M. Wallace, ACS Appl. Mater. Interfaces **7**, 11921 (2015).

[255] G. H. Han, N. J. Kybert, C. H. Naylor, B. S. Lee, J. Ping, J. H. Park, J. Kang, S. Y. Lee, Y. H. Lee, R. Agarwal, and A. T. C. Johnson, Nat. Commun. **6**, 6128 (2015).

[256] C. H. Naylor, N. J. Kybert, C. Schneier, J. Xi, G. Romero, J. G. Saven, R. Liu, and A. T. C. Johnson, ACS Nano **10**, 6173 (2016).

[257] C. H. Ho, C. S. Wu, Y. S. Huang, P. C. Liao, and K. K. Tiong, J. Phys. Condens. Matter **10**, 9317 (1998).

[258] T. M and D. J. Late, ACS Appl. Mater. Interfaces **6**, 1158 (2014).

[259] H. G. Park, T. J. Kim, F. Ullah, V. L. Le, H. T. Nguyen, Y. S. Kim, and Y. D. Kim, Sci. Rep. **8**, 3173 (2018).

[260] R. Gillen and J. Maultzsch, IEEE J. Sel. Top. Quantum Electron. **23**, 219 (2017).

[261] S. Horzum, H. Sahin, S. Cahangirov, P. Cudazzo, A. Rubio, T. Serin, and F. M. Peeters, Phys. Rev. B **87**, 125415 (2013).

[262] D. J. Late, S. N. Shirodkar, U. V. Waghmare, V. P. Dravid, and C. N. R. R. Rao, ChemPhysChem **15**, 1592 (2014).

[263] M. Yang, X. Cheng, Y. Li, Y. Ren, M. Liu, and Z. Qi, Appl. Phys. Lett. **110**, 093108 (2017).

[264] S. H. El-Mahalawy and B. L. Evans, J. Appl. Crystallogr. **9**, 403 (1976).

[265] A. Righi, S. D. Costa, H. Chacham, C. Fantini, P. Venezuela, C. Magnuson, L. Colombo, W. S. Bacsa, R. S. Ruoff, and M. A. Pimenta, Phys. Rev. B **84**, 241409 (2011).

[266] C. Jin, J. Kim, J. Suh, Z. Shi, B. Chen, X. Fan, M. Kam, K. Watanabe, T. Taniguchi, S. Tongay, A. Zettl, J. Wu, and F. Wang, Nat. Phys. **13**, 127 (2016).

[267] M.-L. Lin, Q.-H. Tan, J.-B. Wu, X.-S. Chen, J.-H. Wang, Y.-H. Pan, X. Zhang, X. Cong, J. Zhang, W. Ji, P.-A. Hu, K.-H. Liu, and P.-H. Tan, ACS Nano **12**, 8770 (2018).

[268] G. S. N. Eliel, M. V. O. Moutinho, A. C. Gadelha, A. Righi, L. C. Campos, H. B. Ribeiro, P.-W. Chiu, K. Watanabe, T. Taniguchi, P. Puech, M. Paillet, T. Michel, P. Venezuela, and M. A. Pimenta, Nat. Commun. **9**, 1221 (2018).

[269] P. K. Nayak, Y. Horbatenko, S. Ahn, G. Kim, J. U. Lee, K. Y. Ma, A. R. Jang, H. Lim, D. Kim, S. Ryu, H. Cheong, N. Park, and H. S. Shin, ACS Nano **11**, 4041 (2017).

[270] D. Kozawa, A. Carvalho, I. Verzhbitskiy, F. Giustiniano, Y. Miyauchi, S. Mouri, A. H. Castro Neto, K. Matsuda, and G. Eda, Nano Lett. **16**, 4087 (2016).

[271] S. Huang, X. Ling, L. Liang, J. Kong, H. Terrones, V. Meunier, and M. S. Dresselhaus, Nano Lett. **14**, 5500 (2014).

[272] G. Plechinger, P. Nagler, J. Kraus, N. Paradiso, C. Strunk, C. Schüller, and T. Korn, Phys. Status Solidi - Rapid Res. Lett. **9**, 457 (2015).

[273] E. M. Alexeev, D. A. Ruiz-Tijerina, M. Danovich, M. J. Hamer, D. J. Terry, P. K. Nayak, S. Ahn, S. Pak, J. Lee, J. I. Sohn, M. R. Molas, M. Koperski, K. Watanabe, T. Taniguchi, K. S. Novoselov, R. V. Gorbachev, H. S. Shin, V. I. Fal'ko, and A. I. Tartakovskii, Nature **567**, 81 (2019).

[274] M. Balkanski, R. F. Wallis, and E. Haro, Phys. Rev. B **28**, 1928 (1983).

[275] P. G. Klemens, Phys. Rev. **148**, 845 (1966).

[276] C. Lee, X. Wei, J. W. Kysar, and J. Hone, Science **321**, 385 (2008).

[277] S. Reich, J. Maultzsch, C. Thomsen, and P. Ordejón, Phys. Rev. B **66**, 1 (2002).

[278] T. O. Wehling, A. M. Black-Schaffer, and A. V. Balatsky, Adv. Phys. **63**, 1 (2014).

[279] A. H. Castro Neto, F. Guinea, N. M. R. Peres, K. S. Novoselov, and A. K. Geim, Rev. Mod. Phys. **81**, 109 (2009).

[280] K. F. Mak, L. Ju, F. Wang, and T. F. Heinz, Solid State Commun. **152**, 1341 (2012).

[281] S. Piscanec, M. Lazzeri, F. Mauri, A. C. Ferrari, and J. Robertson, Phys. Rev. Lett. **93**, 1 (2004).

[282] P. May, M. Lazzeri, P. Venezuela, F. Herziger, G. Callsen, J. S. Reparaz, A. Hoffmann, F. Mauri, and J. Maultzsch, Phys. Rev. B **87**, 075402 (2013).

[283] D. M. Basko, S. Piscanec, and A. C. Ferrari, Phys. Rev. B **80**, 165413 (2009).

[284] S. Bernard, E. Whiteway, V. Yu, D. G. Austing, and M. Hilke, Phys. Rev. B **86**, 085409 (2011).